ISSN
2224-7270 (Online)
0378-8121 (Print)

JOURNAL OF
BANGLADESH ACADEMY OF SCIENCES

Volume 50 Issue 1 March 2026

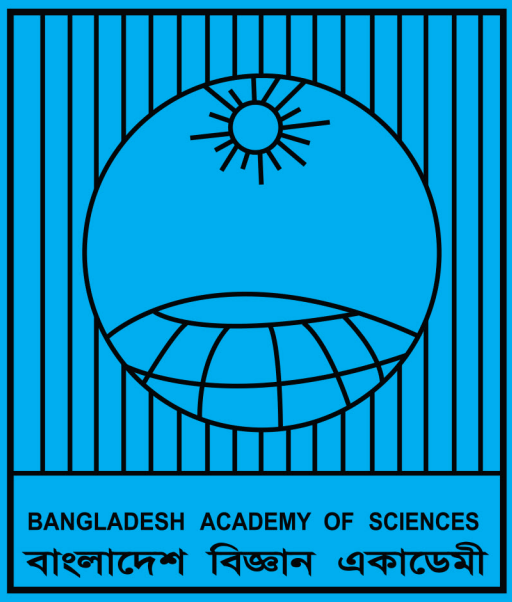

A Publication of Bangladesh Academy of Sciences
http://www.bas.org.bd

COUNCIL OF
THE BANGLADESH ACADEMY OF SCIENCES
(July 2025 - June 2028)

Prof. Dr. Zahurul Karim	-	President
Prof. Dr. Z N Tahmida Begum	-	Vice-President
Prof. Dr. Md. Abdur Rashid	-	Vice-President
Prof. Dr. Shariff Enamul Kabir	-	Treasurer
Prof. Dr. Yearul Kabir	-	Secretary
Prof. Dr. M. Tofazzal Islam	-	Associate Secretary
Prof. Dr. Liaquat Ali	-	Member
Maj Gen. Prof. Dr. ASM Matiur Rahman (Retd)	-	Member
Prof. Dr. Haseena Khan	-	Member
Prof. Dr. M. Jahiruddin	-	Member
Prof. Dr. Md. Abu Bin Hasan Susan	-	Member
Prof. Dr. Md. Anwar Hossain	-	Member
Prof. Dr. Md. Shahdat Hossain	-	Member

JOURNAL OF
BANGLADESH ACADEMY OF SCIENCES

EDITORIAL BOARD

J. Bangladesh Acad. Sci. Volume 50, Issue 1, March 2026

ISSN 2224-7270 (Online), 0378-8121 (Print)

Journal of Bangladesh Academy of Sciences is published four times a year (March, June, September and December comprising one volume) in English. Original research articles, review articles, and short communications of all branches of Science and Technology are considered for publication in this journal. Review articles are generally by invitation.

Disclaimer

The opinions, analysis and conclusions expressed or implied in this journal are those of the authors and do not represent the views of Bangladesh Academy of Sciences.

Submission

All correspondence regarding contributions for publication in the journal should be addressed to the *Editor, Journal of Bangladesh Academy of Sciences* <jbas.editor@yahoo.com>. Authors should consult the contributor's guideline at the back of the journal before submitting their manuscripts.

Published by

Bangladesh Academy of Sciences, National Science and Technology Complex, Agargaon, Dhaka-1207.

Design and Printed by

Sucharu Desktop Publishing, 1/E/1, Paribagh, Dhaka-1000, Bangladesh

Annual Subscription: Tk. 500.00 (Bangladesh); US $ 60.00; £ 21.50 plus postage.

Single Copy: Tk. 250.00 (Bangladesh); US $ 30.00; £ 11.25 plus postage.

JOURNAL OF BANGLADESH ACADEMY OF SCIENCES

Volume 50, Issue 1, March 2026
ISSN 0378-8121 eISSN 2224-7270
Available at: http://www.bas.org.bd/publications/jbas.html

Journal of Bangladesh Academy of Sciences is currently indexed in the following online scholarly journal database:

JOURNAL OF
BANGLADESH ACADEMY OF SCIENCES

VOLUME 50 **ISSUE 1** **MARCH 2026**

CONTENTS

J. Bangladesh Acad. Sci. 50(1); 1-13: March 2026 DOI:https://doi.org/10.3329/jbas.v50i1.88260

Journal of Bangladesh Academy of Sciences

Journal homepage: http://www.bas.org.bd/publications/jbas.html

Review Article

Micronutrient deficiency in food crops and humans in Bangladesh and strategies for mitigation

Mohammad Jahiruddin

Department of Soil Science

Bangladesh Agricultural University (BAU), Mymensingh

ARTICLE INFO

Article History

Received: 03 March 2026

Revised: 11 March 2026

Accepted: 12 March 2026

Keywords: Anaemia, Biofortification, Food fortification, Hidden hunger, Micronutrient deficiency.

ABSTRACT

Micronutrients are substances required in trace amounts for the growth and metabolism of living organisms. In human nutrition, micronutrients include both vitamins and minerals, whereas in plant science, the term generally refers only to minerals. Thus, from a nutritional perspective, micronutrient deficiency denotes a lack of essential vitamins and minerals in the diet. Micronutrient deficiency is a major global health concern, affecting over two billion people worldwide, particularly children under five years of age and pregnant and lactating women. The most common deficiencies involve iron (leading to anaemia), zinc, vitamin A, and vitamin D. These deficiencies contribute to stunted growth, weakened immunity, cognitive impairment, and increased susceptibility to disease. This article aims to review the status of micronutrient deficiencies in both food crops and human populations in Bangladesh, and to advocate strategies for their mitigation. For normal growth and development, humans require 10 essential trace elements (minerals) and 14 vitamins. The trace elements include iron (Fe), zinc (Zn), manganese (Mn), copper (Cu), iodine (I), selenium (Se), molybdenum (Mo), chromium (Cr), fluorine (F), and silicon (Si). Vitamins are classified into two groups: (a) water-soluble vitamins (e.g., ascorbic acid, biotin, cobalamin, folic acid, niacin, pantothenic acid, pyridoxine, riboflavin, and thiamin), and (b) fat-soluble vitamins (e.g., retinoic acid, calciferol, tocopherol, phylloquinone, and menaquinone). In plants, the essential micronutrients include iron (Fe), manganese (Mn), zinc (Zn), copper (Cu), boron (B), molybdenum (Mo), chlorine (Cl), and nickel (Ni). The health impacts of micronutrient deficiencies are often not immediately visible; hence, they are commonly referred to as "hidden hunger." In many rural areas, cereal-based diets—while providing the majority of caloric intake—are relatively low in essential vitamins and minerals, contributing to this condition. Poverty further exacerbates the problem by limiting access to nutrient-rich foods such as meat, milk, fish, fruits, and vegetables. Addressing human micronutrient deficiencies requires a multifaceted approach, including supplementation, food fortification, biofortification, and dietary diversification. Additionally, homestead gardening (for fruits and vegetables) and nutrition education programs can play a crucial role in achieving long-term nutritional resilience. Future research should explore diverse and integrated strategies, particularly in fortification, biofortification, and public awareness, to effectively combat micronutrient deficiencies.

Introduction

Micronutrient deficiency is a global health concern. The present establishes a clear dichotomy between food security (caloric intake) and nutritional security (micronutrient adequacy). While the global agricultural system has succeeded in producing adequate carbohydrates through cereal crops, it fails

*Corresponding author: <m_jahiruddin@yahoo.com>

to meet the physiological demands for trace elements and vitamins (FAO et al., 2023; Ahmed et al., 2021). This discrepancy is particularly acute for vulnerable demographics—children under five and pregnant women—whose developmental stages create a heightened biological "demand" for minerals like iron (Fe) and zinc (Zn).

The synthesis of data regarding Bangladesh reveals a population of 177 million (as of 2026) caught in a nutritional transition. Despite ranking 8th globally in population, the country struggles with a diet heavily reliant on rice, which is naturally low in Zinc (15-16 $\mu g\ g^{-1}$). The text identifies two primary barriers to nutritional health: Economic barriers**:** High prices for pulses, fruits, and vegetables render a "healthy diet" unaffordable for 66% of the population, and Biological barriers: The presence of antinutrients like phytic acid in cereal grains actively inhibits the absorption of minerals in the human gut (White and Broadley, 2009). Access to food is not enough; access to nutritious food is important for a healthy nation. The RDA (recommended daily allowance) of different minerals for humans is: Fe 8.0-18.0, Zn 8.0-11.0, Mn 1.8-2.3, Cu 0.9, I150, Se 55, Mo 45, Cr 25-35, and F 3-4 mg (White and Broadley, 2009).

There is a notable tension between the country's "significant progress" and its remaining challenges. On one hand, stunting levels dropped from 42% in 2013 to 28% in 2019 (Hossain, 2022). On the other hand, the 2019-20 National Micronutrient Survey paints a sobering picture. Anaemia has affected 40-50% of women and children, and vitamin deficiencies have affected 21-23% of preschool children, who suffer from Vitamin A and D deficiencies. Recent research by Nguyen et al. (2025) highlights that while adequacy is improving, significant inequities persist, particularly among children aged 2 to 5.

The text moves beyond identifying problems to suggesting dietary and agricultural shifts. It highlights the untapped potential of indigenous biodiversity, noting that small fish species like *mola* and *dhela* contain 50 to 100 times the micronutrient content of larger commercial fish (Hossain, 2022). Furthermore, it contrasts the Recommended Daily Allowance (RDA) for humans with the suboptimal levels currently found in crops, suggesting a need to shift agricultural priorities from "yield-only" to "nutrient-sensitive" farming. The argument implies that meeting the UN Sustainable Development Goals (SDGs) by 2030 will require bridging the "knowledge gap" between soil health, crop nutrient density, and human intake.

Although in the recent past many initiatives have been taken to address micronutrient deficiencies in food crops and humans in Bangladesh, some knowledge gaps remain, which this article addresses. Thus, this article aims to review the status of micronutrient deficiencies in food crops and humans in Bangladesh and advocate effective strategies for their mitigation.

Concept of micronutrients

Malnutrition can arise in three forms (Ritchie and Roser, 2020): (a) hunger and under nourishment, (b) obesity or over nourishment, and (c) micronutrient deficiencies. In this article, micronutrient deficiency has been addressed. Micronutrient refers to a substance that is essential in trace amounts for the growth and metabolism of a living organism.To a human nutritionist micronutrient could be a vitamin or a mineral,while plant scientists mean it only minerals. So, nutritionally micronutrient deficiency is a dietary deficiency of minerals and vitamins.

Essential micronutrients

Humans need 10 trace elements (minerals) and 14 vitamins for their normal growth and development. The trace elements include Fe, Zn, Mn, Cu, I, Se, Mo, Cr, F, and Si. The vitamins are of two types: (a) water-soluble vitamins, *viz*., ascorbic acid, biotin, cobalamin, folic acid, niacin, pantothenic acid, pyridoxine, riboflavin, and thiamin, and (b) fat-soluble vitamins, *viz*., retinoic acid, calciferol, tocopherol, phylloquinone, and menaquinone (Graham et al., 2001).

Unlike humans, both animals and plants require eight essential trace elements, but not all the same. The essential trace elements for animals are Co, Cu, Fe, Mn, Zn, I, Se, & Si, and those for plants are Fe, Mn,

Zn, Cu, B, Mo, Cl, and Ni. Four micronutrients, viz. Fe, Mn, Zn, and Cu are common in humans, animals, and plants. Nutrient Mo is common for humans & plants and Se & Si are common for humans and animals. Other nutrients such as B, Cl, and Ni are essential only to plants. A list of minerals required by humans, livestock and crops is shown in Table 1 and the human requirement are presented in Table 2.

Table 1. **Essential micronutrients for humans, livestock and crops.**

Life	Micronutrients
Humans	Fe, Zn, Mn, Cu, I, Se, Mo, Cr, F, Si
Livestock	Fe, Zn, Mn, Cu, Co, I, Se, Si
Plants	Fe, Zn, Mn, Cu, B, Mo, Cl, Ni

Source: Bell and Dell, 2008.

Table 2. Amount of essential micronutrients required for humans

Element	RDA	RNI	UL	SUL
Fe (mg)	8.0-18.0	11.4	45.0	17.0
Zn (mg)	8.0-11.0	9.5	40.0	25.0
Mn (mg)	1.8-2.3	>1.4	11.0	4.0
Cu (mg)	0.9	1.2	10.0	10.0
I (µg)	150	140	1100	500
Se (µg)	55	75	400	450
Mo (µg)	45	50-400	2000	NS
Cr (µg)	25-35	>25	NS	NS
F (mg)	3-4	NS	10.0	NS
Si (mg)	NS	NS	NS	1500

Source: White and Broadley, 2009. NS=Non specified; RDA=Recommended daily allowance (US recommendation); RNI=Reference nutrient intake (UK recommendation) (Amount enough for atleast 97% in a group); UL=Upper intake level (US recommendation); SUL=Safe upper level (UK recommendation).

Of the essential micronutrients, the most frequently reported deficiencies for human health are Fe, Zn, I and vitamin A (Welch and Graham, 2004), the reason can be attributed to the smaller amount of micronutrients in cereal grains (Garg et al., 2018) which the people usually more consume and the higher amount of antinutrient substances e.g. phytic acid (Whiteand Broadley, 2009), a substance that inhibits the ab- sorption of mineral elements by the gut.

Functions of micronutrients

Each mineral nutrient has a definite role in humans, animals and plants (Tables 3 and 4; Fig. 1).

Hidden hunger

Hidden hunger is a form of malnutrition in which individuals consume enough calories but lack essential vitamins and minerals (micronutrients) like iron, zinc, iodine, and Vitamin A. The health impact of micronutrient deficiency is not always visible; it is therefore called ‘hidden hunger’. Swaminathan (2014) states, ‘Hidden hunger is one form of hunger which arises from lack of micronutrients’. Poor diet is a major cause of hidden hunger. Cereal-based diets, the primary source of energy (calories) for rural people, are relatively low in vitamins and minerals, leading to hidden hunger. In addition, poverty is a major factor limiting access to nutritious foods, such as meat, milk, fish, fruits, and vegetables (Bouis et al., 2011a). About 800 million people worldwide are chronically hungry (calorie deficiencies) (FAO et al., 2017) and more than 2 billion people are affected by hidden hunger (micronutrient deficiencies), the vast majority from developing countries (WHO, 2006; McGuire, 2015; Hodge, 2016). Based on Disability-Adjusted Life Years (DALYs) data, Gödecke et al. (2018) observed that all country-level determinants have a larger effects on the burden of chronic hunger (calorie deficiencies) than on the burden of hidden hunger (micronutrient deficiencies), and complementary micro-level interventions are required to end hidden hunger. The Hidden Hunger Index (HHI) for countries in South Asia and Southeast Asia is shown in Table 5.

Table 3. Functions of micronutrients in plants.

Micronutrients	Key functions
Iron	Component of cytochromes, ferrodoxins and leghaemoglobin; involved in the nitrogenase and nitrate reductase enzymatic reactions, associated with chlorophyll formation, protein synthesis.
Manganese	Involved in the oxidation-reduction processes of photosynthetic electron transfer system, acts as a bridge for ATP and enzyme complex (phosphokinase), activates IAA oxidases.
Zinc	Synthesis of tryptophane needed for the production of auxins; activation of dehydrogenase and carbonic anhydrase enzymes; helps in protein synthesis, high P interferes with Zn uptake by plants.
Copper	Acts as an electron carrier in photosynthesis and respiration; part of enzymes e.g. cytochrome oxidase; involved in protein and carbohydrate metabolism and N_2 fixation, helps in pollination and seed set, involved in the desaturation and hydroxylation of fatty acids.
Boron	Regulates carbohydrate metabolism; involved in protein synthesis; helps in transport of photosynthetic sugars to meristematic (growing) tissues; good role in pollen viability and seed formation.
Molybdenum	Constituent of nitrate reductase and nitrogenase enzymes; role in Fe absorption and translocation in plants.
Chlorine	Involved in the evolution of O_2 in photosynthesis; increases cell osmotic pressure, stomatal regulation, increases hydration of plant tissues.
Nickel	Works as a co-factor to enable urease to catalyze the conversion of urea into the ammonium ion, which plants can use as a source of N.

Source: BARC, 2024.

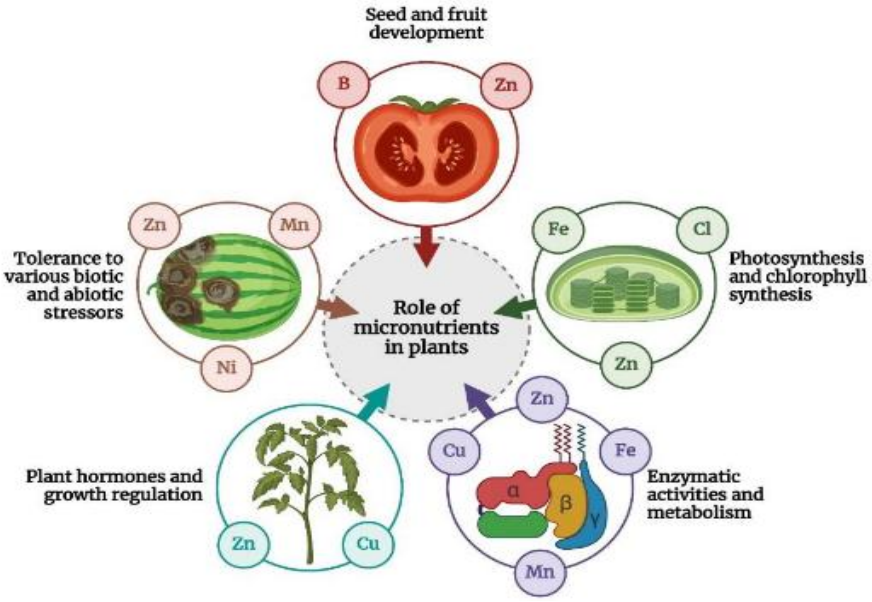

Fig. 1. Role of micronutrients in plants (Behera et al., 2025).

Table 4. Functions of micronutrients for humans and their food sources.

Micronutrient	Key functions	Key food sources
Vitamin A (Retinoids/Carotenoids)	Vision, immune system, cellular communication, skin health	Liver, fish, eggs, carrots, spinach, sweet potatoes, cantaloupe
Vitamin B1 (Thiamine)	Glucose breakdown, energy metabolism	Whole grains, nuts, seeds, legumes, pork, fortified foods
Vitamin B2 (Riboflavin)	Cell function, growth, development, metabolism	Liver, dairy products, eggs, meat, leafy greens
Vitamin B3 (Niacin)	Converts food into energy, DNA repair	Meat, fish, poultry, legumes, peanuts
Vitamin B6 (Pyridoxine)	Metabolism, brain development, immune function	Fish, poultry, legumes, nuts, whole grains
Vitamin B9 (Folate/Folic Acid)	Cell division, DNA production, nerve function	Leafy greens, beans, asparagus, peanuts, fortified grains
Vitamin B12 (Cobalamin)	Red blood cell formation, neurological function, DNA synthesis	Meat, fish, eggs, dairy, shellfish
Vitamin C (Ascorbic Acid)	Antioxidant, collagen production, immune support	Citrus fruits, berries, peppers, broccoli, tomatoes
Vitamin D	Calcium absorption, bone health, immune function	Fatty fish, egg yolks, fortified milk, sunlight exposure
Vitamin E	Antioxidant, protects cells from free radicals	Vegetable oils, nuts, seeds, spinach
Vitamin K	Blood clotting, bone metabolism	Leafy greens (kale, spinach), broccoli, vegetable oils
Calcium (Mineral)	Bone structure, muscle contraction, nerve transmission	Dairy (milk, cheese, yogurt), leafy greens, fish with bones
Iron (Mineral)	Oxygen transport, energy metabolism	Red meat, lentils, beans, spinach, fortified cereals
Zinc (Mineral)	Immune function, wound healing, protein synthesis	Shellfish, beef, pumpkin seeds, nuts, whole grains
Iodine (Mineral)	Thyroid hormone production, brain development	Iodized salt, seafood, dairy products
Magnesium (Mineral)	Bone health, over 300 metabolic reactions, nerve function	Nuts, spinach, legumes, whole grains
Selenium (Mineral)	Thyroid health, antioxidant protection	Brazil nuts, seafood, eggs, meat

Source: Gombart et al., 2020.

Table 5. Hidden Hunger Index (HHI) and micronutrient deficiencies in South Asia and Southeast Asia.

Region	Country	Deficiency prevalence (%)			
		HHI score	Zn[1]	Fe[2]	Vitamin[3]
South Asia	Afghanistan	47.7	59.3	19.0	64.5
	India	48.3	47.9	34.7	62.0
	Pakistan	26.7	42.0	25.5	12.5
	Bangladesh	29.3	43.0	23.5	21.7
	SriLanka	22.3	19.2	12.6	35.3
	Nepal	35.3	49.3	24.2	32.3
	Bhuttan	33.3	37.5	40.3	22.0
	Maldives	30.0	31.9	48.9	9.4
Southeast Asia	Indonesia	27.3	40.1	22.3	19.6
	Thailand	14.7	15.7	12.6	15.7
	Philippines	30.7	33.8	18.2	40.1
	Malaysia	11.7	15.6	16.2	3.5
	Singapore	NA	4.4	11.3	NA
	Vietnam	24.0	43.3	17.1	12.0
	Myanmar	36.3	40.6	31.6	36.7
	Cambodia	31.0	39.5	31.0	22.3
	Laos	38.7	47.6	24.1	44.7
	Brunei	NA	11.6	14.5	NA
	Timor-Leste	39.0	55.7	15.8	45.8

Source: Muthayya et al., 2013. NA=Data not available, HHI score= [Stunting (%) + Anaemia (%) + Low serum retinol (%)]/3, three components equally weighted; [1]Stunting as proxy for Zn; [2]Anemia as proxy for Fe; [3]Low serum retinol, <0.7 µmol L^{-1}

The situation of Fe and Zn deficiency is worse in South and southeast Asia, where a high proportion of cereal crops, such as rice and wheat, are consumed as a staple food (Cakmak, 2008; Stein, 2009). Cereals contribute about 60% for Zn and 55% for Fe to the daily intake of these minerals by Bangladeshi people (Islam et al., 2014). Ahmed et al.(2016) reviewed micronutrient deficiencies among children and women in Bangladesh. Their view states that, as per the National Micronutrients Status Survey report (2011-2012), among the preschool-age children, 20.5% are deficient in vitamin A, 44·5% in Zn and 10.7% in Fe. About 57% of non- pregnant and non-lactating women are anemic, and 25% women are Fe deficient, and nearly 50% pregnant and lactating women are anaemic, induced by Fe deficiency.

Soil as a source of micronutrients

A link exists between the health of soil and the health of people who consume foods produced on soils (Friedrichsen et al., 2018). Healthy soils continuously provide ecosystem services, such as sustaining plant and animal productivity, increasing biodiversity, and maintaining or enhancing the qualities of air and water, thereby supporting human health (Anonymous, 2018). Plants depend on soil for nutrients, and both humans and animals depend on plants for food. So, soil can be regarded as the basis of life. Jahiruddin (2020a) has reviewed how soil health affects human health. When

soil is healthy, plants grown on healthy soil are healthy, reviewed how soil health affects human health. When soil is healthy, plants grown on healthy soil are healthy, and consequently, man eating plant food is healthy. As reported by Hasan et al. (2020), 55-60% soils of Bangladesh are deficient in two micronutrients, viz., zinc & boron, and farmers are advised to apply zinc sulphate and boric acid fertilizers. We do not fully understand the complex interactions among soil, crops and human health. For a thorough understanding of safe and nutritious food production grown on soil and its broadly impact on human health, a multidisciplinary approach is needed. Contributions from experts in agriculture, human nutrition and social sciences are important for addressing micronutrient deficiencies in food crops and human health issues.

Biofortification

Biofortification is a biological process of adding micronutrients to food crops through breeding or an agronomic approach. It is recognized as a good means of improving the diet of the malnourished rural population (Bouis, 2013; Garg et al., 2018). A number of studies have been done and are in progress regarding biofortification of cereals, such as in rice (Behura et al., 2011; Mubarak et al., 2015; Jahiruddin and Islam, 2018), wheat (Cakmak et al., 2010; Guzmán et al., 2014; Jahiruddin and Islam, 2018), and maize (Qin et al., 2012; Šimic´ et al., 2011).

Breeding approach includes conventional breeding and genetic engineering (transgenic). The agronomic approach covers fertilizer management, variety screening and crop diversification. The HarvestPlus Challenge Programme on 'Biofortified Crops for Improved Human Nutrition' was initiated in 2004 with the objective of developing cultivars of staple food crops that are rich in Fe, Zn, and vitamin A (β-carotene). The target crops include 7 food crops: rice, wheat, maize, cassava, pearl millet, beans and sweet potato. Those crops have been chosen based on the observation that those foods are consumed as staple foods by the world's poor. The HarvestPlus programme is carried on in south Asia for rice Zn (target 28 µg g^{-1}) in Bangladesh and India, for wheat Zn (target 28 µg g^{-1}) (& Fe secondary) in India and Pakistan, and for lentil Fe (target 70 mg g^{-1}) (& Zn secondary) in Bangladesh, Nepal and India (HarvestPlus, 2014).

The success of biofortification programme depends on three factors, as outlined by Bouis et al. (2011b). The factors are: (i) the biofortified crop must be high yielding and profitable to the farmer, (ii) the biofortified crop must be as efficacious and effective in reducing micronutrient malnutrition of humans, and (iii) the biofortified crop must be acceptable to both farmers and consumers in the regions where people are afflicted by micronutrient deficiency. For example, BRRI dhan62 (Zn-enriched rice variety) has not been popularized among the farmers in Bangladesh due to low yield potential (4.0-4.5 tha^{-1}). However, the later varieties, notably BRRI dhan74, 84, 100, and 102 have addressed this problem with high yield potential and high Zn content. These bio-fortified, non-GMO varieties offer high zinc content (ranging from 22.8–27.6 µg g^{-1} Zn content) (Table 6).

Table 6. Zinc enriched BRRI rice varieties.

Variety	Season	Zinc content (µg g^{-1})	Yield potential (t ha^{-1})	Key feature
BRRI dhan102	Boro	25.5	8.1	Long slender grain
BRRI dhan100	Boro	25.7	7.7	Slender, non-sticky
BRRI dhan84	Boro	27.6	6.5	Red-colored grain
BRRI dhan74	Boro	24.2	7.1	Coarse grain, high yield
BRRI dhan72	Aman	22.8	6.0	Tidal flood tolerant
BRRI dhan64	Boro	24.0	6.5	Mediumcoarse grain
BRRI dhan62	Aman	19.0	4.5	Shortest duration (100 days)

BRRI, 2025.

Recently, Jahiruddin (2020b) has comprehensively reviewed biofortification of food crops, with greater emphasis on micronutrient malnutrition in South Asia. Apart from the breeding approach of biofortification, the fertilization strategy (agronomic method) is a rapid way to achieve micronutrient-dense foods without incurring yield loss. An increment of 4-8 µg g^{-1} Zn in wheat grain and 2-4 µg g^{-1} Zn in rice grain is possible through Zn fertilization (Jahiruddin and Islam, 2018). Farmers of South Asian countries commonly use N, P and K fertilizers; use of micronutrient fertilizers is limited (Jahiruddin, 2019). Efficient management of N and Zn fertilizers would help enhance the grain Fe and Zn concentrations, as evidenced by positive correlation of seed Fe and Zn with N contents in several crops (Cakmak et al., 2010; Kutman et al., 2010). Siddika (2019) observed a synergistic relationship between N and Zn concentrations of rice. However, the success rate and acceptability of the genetic engineering technique (transgenic) appear to be much lower compared to conventional breeding. Furthermore, the globally introduction of GMO food crops is a subject of debate, and in fact, their consumption is very low. In breeding programs, breaking the negative relationship between grain yield and Zn or Fe concentration is a challenging for enhanced micronutrient density in cereal grains (Zhao and McGrath, 2009; Bouis and Welch, 2010; Waters and Sankaran, 2011). Processing of food grain is also important in the context of the biofortification strategy. Minerals such as iron, zinc, and copper, which are highest in rice bran, are lost during milling and polishing. This is not a problem for Se and S, since they reach maximum levels in the embryo (Gregorio et al., 2000). In the past, nutrient supplementation, food fortification, and dietary diversification were widely used to reduce micronutrient deficiency (Casey et al., 2009; Eneroth et al., 2010; Ritchie and Roser, 2020). However, these approaches had limited success (Ssemakula and Pfeiffer, 2011). Child mortality from diarrhoea and pneumonia was reduced significantly in Bangladesh with the use of the‘baby zinc’ tablet developed by ICDDR,B (Baqui, 2002; Brooks et al., 2005). However, fortification and supplementation programs could complement biofortification for better use by urban people, not by rural people.

Mitigation of micronutrient deficiencies in Bangladesh is primarily driven by the National Strategy on Prevention and Control of Micronutrient Deficiencies (2015-2024), which employs a multi-sectoral approach combining food fortification, supplementation, and food-based dietary diversification. These strategies aim to address high rates of deficiencies (iron, vitamin A, zinc, iodine) by focusing on vulnerable groups, including children, women of reproductive age, and pregnant women.

When a soil is critically deficient in micronutrients, the benefits of biofortified varieties cannot be achieved. Thus, biofortification should be considered as an integrated approach in which both breeding and agronomic approaches are equally important for the question of sustainability (Mubarak et al., 2015). In cultivation of micronutrient biofortified varieties, the application of micronutrient fertilizers can be regarded as a sustainable strategy to boost the crop

Strategies for micronutrient deficiency mitigation

There are four possible ways to address mitigation of micronutrient deficiency in humans.

➢ Supplementation	Use of concentrated micronutrients in pill, powder or liquid form
➢ Food fortification:	Addition of micronutrients to food products during processing such as ri milling, wheat flours
➢ Biofortification:	Addition of micronutrients to food crops by breeding or agronomic method.
➢ Diet diversification:	Consumption of micronutrient rich diet, e.g. fruits, vegetables, pulses.

Ritchie and Roser, 2020.

yield with higher mineral concentrations in edible parts (White and Broadley, 2005; Graham et al., 2007; Pfeiffer and McClafferty, 2007). Concurrently, it is also needed to enhance the concentrations of 'promoter'substances such as ascorbate (vitamin C), which stimulates the absorption of mineral elements by the gut, and to lower the concentrations of 'antinutrients', such as phytate, which interferes with their absorption (White and Broadley, 2009). Agronomic biofortification complements the breeding approach. Thus, neither breeding nor an agronomic approach alone can adequately and sustainably solve the problem of micronutrient malnutrition. For an effective and sustainable strategy, agronomic biofortification needs to be complemented by breeding for micronutrient enrichment of food crops.

Agricultural and community-based nutrition programs in Bangladesh

These programs focus on enhancing food security through homestead food production (HFP), dietary diversification, and nutrition education to combat micronutrient deficiencies, particularly benefiting women and children. There are several programs and models aligned with the community-based nutrition and Homestead Food Production (HFP) programs to increase micronutrient-rich food consumption among vulnerable households. There is ample evidence that the HFP program in Bangladesh has improved food security for more than 5 million vulnerable people across diverse agro-ecological zones (Ahmed and Chowdhury, 2016). Rahman et al. (2025) advocate promoting nutrient-dense crop production and homestead gardening with green leafy vegetables & fruits and awareness programs to change dietary behaviors in order to attain long-term nutritional resilience in Bangladesh.

Helen Keller International (HKI) HFP Program: The foundational model introduced over two decades ago to combat vitamin A deficiency by promoting year-round production of nutrient-rich fruits and vegetables.

BARI "Palima" Model: Initiated in 1998 by the On-Farm Research Division (OFRD) of the Bangladesh Agricultural Research Institute (BARI), focusing on homestead vegetable and fruit production based on local ecological niches.

SI-MFS (Sustainable Intensification of Mixed Farming Systems): Since 2022, this initiative has supported over 9,000 farmers in northern/southern Bangladesh, often using the "Saidpur Model" for year-round intensive vegetable, fruit, and small livestock production.

Floating Garden (Baira) Agriculture: FAO-supported initiatives that use traditional hydroponic techniques in waterlogged areas to produce vegetables like okra, brinjal, and gourds.

Community-Based Initiatives: Programs like those in Rangpur and Nilfamari (JANO initiative) teach climate-smart agriculture and nutrition education.

Rohingya Camp Homestead Gardening: A specialized program in Cox's Bazar utilizing cash-based transfers to motivate participation in gardening activities.

Key research gaps

Widespread vitamin D and B12 deficiencies: There is a huge gap in knowledge regarding Vitamin D and Vitamin B12 deficiencies, with limited intervention strategies targeting these deficiencies.

Evaluation of fortification compliance: There is a lack of data on consumer compliance, actual nutrient intake, and the bioavailability of these fortified foods in rural, low-income settings.

Climate change and nutritional security: There is a critical need to understand how climate change (flooding, salinity, heat) impacts nutrient-dense food production.

Impact of infectious disease and sanitation: Research is needed on how diarrhoeal diseases and parasitic infections in slum areas affect nutrient absorption and on the effectiveness of supplementation programs.

Urban vs. rural disparities: There is a limited study tracking the shifting prevalence of hidden hunger in urban slum dwellers compared to rural, coastal, and haor-affected populations.

Thus, these knowledge gaps need to be addressed through productive research and interventions.

Conclusion

Micronutrient deficiency is a global health problem affecting over 2 billion people, particularly children and pregnant women, causing several health consequences like stunted growth, cognitive impairment, and weakened immunity. Common deficiencies are iron, zinc, vitamin A, and vitamin D, which results mainly from a cereal (rice) based diet of poor people living in rural areas. Young children (under five) and pregnant and lactating women are at particular risk of micronutrient deficiencies. Key strategies to combat this problem include food fortification (e.g., iodization of salt), biofortification, dietary diversification, and nutrient supplementation. Homestead food production programs encouraging small-scale, nutrient-dense gardening (fruits/vegetables) could be introduced to improve dietary diversity. Biofortification, such as the introduction of zinc-enriched rice (e.g., BRRI dhan 84, 100 & 102) and Golden Rice (Vitamin A), can increase the nutrient density of crops. This chapter provides an excellent foundation by establishing the Economic Barrier (the price of pulses/vegetables) and the Biological Barrier (phytic acid), making a compelling case that "access to food is not enough." Future research should explore diverse avenues to effectively address micronutrient deficiency through fortification, biofortification, and awareness programs. Contributions of experts from agriculture, human nutrition and social science fields are important to address the micronutrient deficiency of food crops and human health issues in this country.

Conflict of interest

Regarding the publication of this paper, the author has no conflict of interest.

References

Ahmed F, Prendiville N and Narayan A. Micronutrient deficiencies among children and women in Bangladesh: progress and challenges. *J. Nutr. Sci.*,2016; 5: e46.

Ahmed M and Chowdhury MAT. Homestead food production (HFP) in Bangladesh: An Approach to improve diet quality and enhance micronutrients-rich sustainable food security. *OIDAInt. J. Sustain. Dev.* 2016; 9(10): 51-57.

Ahmed F, Khosravi-Boroujeni H, Khan MR, Roy AK and Raqib R. Prevalence and predictors of vitamin D deficiency and insufficiency among pregnant rural women in Bangladesh, 2021; 13(2): 449.

Anonymous. *Conference on Connections between Soil Health and Human Health*. October 16-17, 2018. Silver Spring, Maryl and USA.

Baqui AH. Effect of zinc supplementation started during diarrhoea on morbidity and mortality in Bangladeshi children: community randomized trial. *Br. Med. J.* 2002; 325: 1059-1059.

BARC. *Fertilizer Recommendation Guide-2024*. Bangladesh Agricultural Research Council (BARC), Farmgate, Dhaka, 2024.

Behera SR, Bhatt M, Gairola A, Rana S, Mohapatra A. Joshi D and Tripathy A. A comprehensive review of micronutrients and their implications on vegetable quality. *J. Adv. Biol. Biotechnol.* 2025; 28(5): 284-299.

Behura N, Sen P and Kar MK. Introgression of yellow stem borer (Scirpophaga incertulus) resistance genes into cultivated rice (Oryza sp.) from wild species. *Indian J. Agric. Sci.,* 2011; 81: 359-362.

Bell RW and Dell B. *Micronutrients for Sustainable Food, Feed, Fibre and Bioenergy Production*. International Fertilizer Industry Association (IFA), Paris, France, 2008.

Bouis HE, Hotz C, McClafferty B, Meenakshi JV and Pfeiffer WH. Biofortification: A new

tool to reduce micronutrient malnutrition. *Food Nutr. Bull*. 2011; 32(1 Suppl): S31-40.

Bouis HE and Welch RM. Biofortification – A sustainable agricultural strategy for reducing micronutrient malnutrition in the global south. *Crop Sci.* 2010; 50: S20-S32.

Bouis HE, Eozenou P and Rahman A. Food prices, household income, and resource allocation: Socioeconomic perspectives on their effects on dietary quality and nutritional status. *Food Nutr Bull.* 2011a; 32: S14-S23.

Bouis HE, Hotz C, McClafferty B, Meenakshi JV and Pfeiffer WH. Biofortification: A new tool to reduce micronutrient malnutrition. *Food Nutr. Bull.* 2011b; 32: S31-S40.

Broadley MR, White PJ, Hammond JP, Zelko I and Lux A. Zinc in plants. *New Phytologist*, 2007; 173: 677-702.

Brooks WA, Santosham M, Naheed A, Goswami D, Wahed MA, Diener-West M, Faruque ASG and Black RE. Effect of weekly zinc supplements on incidence of pneumonia and diarrhoea in children younger than 2 years in an urban, low-income population in Bangladesh: Randomised controlled trial. *The Lancet*, 2005; 366:999-1004.

BRRI (Bangladesh Rice Research Institute). Modern Rice Cultivation, 25th Edition, 2025; p 128.

Cakmak I, Pfeiffer WH and McClafferty B. Biofortification of durum wheat with zinc and iron. *Cereal Chem.*, 2010; 87: 10-20.

Cakmak I. Enrichment of cereal grains with zinc: Agronomic or genetic biofortification? *Plant Soil*, 2008; 302: 1-17.

Casey GJ, Phuc TQ, MacGregor L, Montresor A, Mihr- shahi S, Thach TD, Tien NT and Biggs BA. A free weekly iron-folic acid supplementation and regular deworming program is associated with improved hemoglobin and iron status indicators in Vietnamese women. *BMC Public Health*, 2009; 9:261.

Eneroth H, Arifeen S, Persson LA, Lonnerdal B, Hossain MB, Stephensen CB and Ekstrom EC. Maternal multiple micronutrient supplementation has limited impact on micronu trient status of Bangladeshi infants compared with standard iron and folic acid supplementation. *J. Nutr*. 2010; 140: 618-624.

FAO, IFAD, UNICEF, WFP, WHO. The State of Food Security and Nutrition in the World 2023: *Urbanization, agrifood systems transformation, and healthy dietsacross the rural-urban continuum*. Rome, Italy, 2023.

FAO, IFAD, UNICEF, WFP, WHO. The State of Food Security and Nutrition in the World 2017: *Building resilience for peace and food security*. *World Food Programme*, FAO, Rome, Italy, 2017.

Friedrichsen CN, Daroub SH, Monroe MC, Stepp JR and Wani SP. Mental models of soil management for food security in peri-urban india. *Urban Agric. Region. Food Syst.,* 2018; 3(1):170002.

Garg M, Sharma N, Sharma S, Kapoor P, Kumar A, Chunduri V and Arora P. Biofortified crops generated by breeding, agronomy, and trans- genic approaches are improving lives of millions of people around the world. *Front. Nutr.* 2018; 5: 12.

Gödecke T, Stein AJ and Qaim M. The global burden of chronic and hidden hunger: Trends and determinants.*Glob. Food Secur.* 2018; 17: 21-29.

Gombart AF, Pierre A and Maggini S. A review of micronutrients and the immune system-working in harmony to reduce the risk of infection. *Nutr.* 2020; 16; 12(1): 236.

Graham RD, Welch RM and Bouis HE. Addressing micronutrient malnutrition through enhancing the nutritional quality of staple foods: Principles, perspectives and knowledge gaps. *Adv. Agron*. 2001; 70: 77-142.

Graham RD, Welch RM, Saunders DA, Ortiz-Monasterio I, Bouis HE, Bonierbale M, deHaan S, Burgos G, Thiele G, Liria R, Meisner CA,

Beebe SE, Potts MJ, Kadian M, Hobbs PR, Gupta R and Twomlow S. Nutritious subsistence foodsystems. *Adv. Agron.* 2007; 92: 1-74.

Gregorio GB, Senadhira D, Htut H and Graham RD. Breeding for trace mineral density in rice. *Food Nutr. Bull.* 2000; 21: 382-386.

Guzmán C, Medina-Larqué AS, Velu G, González-Santoyo H, Singh RP, Huerta-Espino J, Ortiz-Monasterio I and Peña RJ. Use of wheat genetic resources to develop biofortified wheat with enhanced grain zinc and iron con centrations and desirable processing quality. *J. Cereal Sci.* 2014; 60: 617-622.

HarvestPlus. Better Crop. Better Nutrition. HarvestPlus, Washington, DC, USA. 2014.

Hasan MN, Bari MA and Lutfar MR. Soil fertility trends in Bangladesh 2010 to 2020. *SRSRF project*. Soil Resource Development Institute, Ministry of Agriculture. The Government of the People's Republic of Bangladesh. 2020; pp 84.

Hodge J. Hidden hunger: Approaches to tack- ling micronutrient deficiencies. In: *Gillespie S, Hodge J, Yosef S, Pandya-Lorch R (Eds)*, Nourishing Millions: Stories of Change in Nutrition. International Food Policy Research Institute (IFPRI), Washington DC, USA, 2016.

Hossain M. Fighting malnutrition and food insecurity in Bangladesh with micronutrient-rich small fish. In: Grow Further, www.growfurther.org. 2022.

Islam M, Jahiruddin M, Islam M, Alim M and Akhtaruzzaman M. Consumption of unsafe foods: Evidence from heavy metal, mineral and trace element contamination. *FAO Project Completion Report*, Department of Soil Science, Bangladesh Agricultural University, Mymensingh, Bangladesh, 2014.

Jahiruddin M and Islam MR. Biofortification of zinc and iron in cereals by fertilizer use and variety selection. Funded by BAS-USDA, *Project Completion Report.* of Soil Science, Bangladesh Agricultural University, Mymensingh, Bangladesh, 2018.

Jahiruddin M. Research and development on natural resource management in south Asia. In: *Shrestha RB, Bokhtiar SM, Khetarpal R and Thapa YB (Eds)*, Agricultural Policy and Program Framework: Priority Areas for research and Development in South Asia. SAC, Dhaka, Bangladesh, 2019.

Jahiruddin M. Soil health and human well-being: areview. *Fundam. Appl. Agric.* 2020a; 5(4): 443-452.

Jahiruddin M. Biofortification of food crops: A novel strategy for reducing micronutrient mal-nutrition. *Fundam. Appl. Agric.* 2020b; 9: 10.

Kutman UB, Yildiz B, Ozturk L and Cakmak I. Biofortification of durum wheat with zinc through soil and foliar applications of nitrogen. *Cereal Chem. J.* 2010; 87: 1-9.

McGuire S. FAO, IFAD, and WFP. the state of food insecurity in the world 2015: Meeting the 2015 international hunger targets: Taking stock of uneven progress. *Adv. Nutr.*, 2015; 6: 623-624.

Mubarak T, Sheikh FA and Bangroo SA. Role of rice in tackling hidden hunger: The biofortification approach. *Res. J. Agric. Sci.*, 2015; 6: 1-7.

Muthayya S, Rah JH, Sugimoto JD, Roos FF, Kraemer K and Black RE. The global hidden hunger indices and maps: An advocacy tool for action. *PLoS ONE,*2013; 8: e67860.

Nguyen PH, Ali M, Ghostlaw J, Tran LM, Parvin A, Bakhtiar MM and Ahmed AU. Trends and inequities in adequacy of micronutrient intakes in rural Bangladesh. *J. Nutr.* 2025; 155(2): 492-508.

Pfeiffer WH and McClafferty B. HarvestPlus: Breeding crops for better nutrition. *Crop Sci.* 2007; 47: S88-S105.

Qin H, Cai Y, Liu Z, Wang G, Wang J, Guo Y and Wang H. Identification of QTL for zinc and iron concentration in maize kernel and cob. *Euphytica*, 2012; 187: 345-358.

Rahman MZ, Amjath-Babu TS, Robbani M, Rashid MM, Dipok, Choudhury K and Hasan MF. Mitigating micro-nutrient deficiencies in the

diets of rural farm households on the south-central coast of Bangladesh: What roles do the markets and homestead play? *J. Agri. Food Res.*2025; 23: 102193.

Ritchie H and Roser M. Micronutrient Deficiency. Our World in Data, 2020.

Siddika A. Biofortification of zinc in ricegrain through nitrogen and zinc fertilizer ap- plication. MS Thesis, Department of Soil Science, Bangladesh Agricultural University, Mymensingh, 2019.

Šimic´ D, Drinic´ SM, Zdunic´ Z, Jambrovic´ A, Ledenc˘an T, Brkic´ J, Brkic´ A and Brkic´ I. Quantita- tive trait loci for biofortification traits in maize grain. *J. Here.*, 2011; 103: 47-54.

Ssemakula G and Pfeiffer W. Considerations for implementation of biofortification in develop- ing countries: The case of Sub-Saharan Africa. Symposia Brief: Progress, Challenges, and the Way Forward in Breeding and Gene Discovery: Vitamin A. *First Global Conference on Biofortification*. November 9-11, 2011. Washington DC, USA.

Stein AJ. Global impacts of human mineral malnutrition. *Plant Soil*, 2009; 335: 133-154.

Swaminathan MS. Bring more women farmers on board to eliminate hunger. The Times of India, November 6, 2014.

Waters BM and Sankaran RP. Moving micronu- trients from the soil to the seeds: Genes and physiological processes from a biofortification perspective. *Plant Sci.,* 2011; 180: 562-574.

Welch RM and Graham RD. Breeding for micronu- trients in staple food crops from a human nutri- tion perspective. *J. Exp. Bot.* 2004; 55: 353-364.

White P and Broadley M. Biofortifying crops with essential mineral elements. *Trends Plant Sci.,* 2005; 10: 586-593..

White PJ and Broadley MR. Biofortification of crops with seven mineral elements often lacking in human diets - iron, zinc, copper, calcium, magnesium, selenium and iodine. *New Phy.* 2009; 182: 49-84.

WHO. Guidelines on Food Fortification with Micronutrients. Allen L, de Benoist B, Dary O, Hurrell R, eds., World Health Organization, Geneva, Switzerl and; 2006.

Zhao FJ and McGrath SP. Biofortification and phytoremediation. *Curr. Opin. Plant Biol.,* 2009; 12: 373-380.

J. Bangladesh Acad. Sci. 50(1); 15-22: March 2026 DOI:https://doi.org/10.3329/jbas.v50i1.81291

Journal of Bangladesh Academy of Sciences

Journal homepage: http://www.bas.org.bd/publications/jbas.html

Research Article

A novel nonlinear stochastic differential equation model with quadratic and logarithmic drift

Ampitan Kehinde Ronald*, Agwuegbo Samuel Obi-Nnamdi, Akintunde Abosede Adelola and Basirat Adetona

Department of Statistics, Federal University of Agriculture, Abeokuta, Nigeria

ARTICLE INFO

Article History

Received: 25 April 2025
Revised: 27 November 2025
Accepted: 29 January 2026

Keywords: Nonlinear models, Quadratic drift term, Logarithmic drift term, Stochastic differential equations.

ABSTRACT

This study introduces a new class of nonlinear stochastic differential equations (SDEs) with a logarithmic drift term, given by $dX_t = (\propto X_t + \beta X_t^2 + \gamma log X_t)dt + \sigma dW_t$. Assuming a lognormal distribution, we derive expressions for the mean and variance and also determine the stationary distribution. Furthermore, the proposed model is compared with existing SDE models using economic data, including exchange rates, inflation rates, and interest rates. Model performance is evaluated using the Akaike Information Criterion (AIC) and the Bayesian Information Criterion (BIC). The results show that the proposed SDE outperforms the competing models.

Introduction

Stochastic processes have become an important foundation in modern applied mathematics and quantitative finance due to their capability to model systems influenced by uncertainty and randomness. The use of Stochastic Differential Equations (SDEs) has expanded significantly over the years as researchers seek more realistic representations of phenomena with inherent randomness, structural complexity, and temporal dependence (Liao, 2024; Mahmoud et al., 2023). This expansion showcases a broader recognition that deterministic models, although analytically convenient, are often limited in capturing the dynamic variability observed in empirical data.

Modeling Financial data mostly requires the use of Stochastic Differential Equations (SDEs) to describe the dynamics of interest rates, asset prices, inflation rates, exchange rates, and other financial quantities. Most Stochastic Differential Equations (SDEs) are assumed to follow linear models. Nevertheless, financial data often exhibit nonlinear characteristics that linear models alone cannot capture.

Stochastic Differential Equations can be linear or nonlinear, depending on the nature of the system being modeled. Linear Models have the advantage of being analytically tractable, allowing for closed-form solutions. Nonlinear Models, on the other hand, require numerical methods for estimation and analysis. (McCamley et al., 2018). These models are particularly valuable for analyzing longitudinal data with unequally spaced measurement occasions (Hecht and Zitzmann, 2020).

One of the critical aspects of SDEs is their ability to incorporate randomness into deterministic models, which is essential for accurately representing real-world phenomena. For instance, stochastic models have been shown to provide more realistic insights into biological processes, such as the dynamics of infectious diseases, where traditional ordinary differential equations (ODEs) often fall short due to their deterministic nature (Marwa et al., 2019). The stochasticity introduced into these models can be achieved through various methods, including adding random noise or using stochastic perturbations to

*Corresponding author: <ampitanronaldkehinde@gmail.com>

capture environmental fluctuations. (Marwa et al., 2019).

The theoretical foundation of continuous-time stochastic modelling traces back to Ito's development of stochastic calculus, which provided a mathematically coherent framework for integrating randomness into dynamic systems. Building upon these early contributions, contemporary research has extended SDEs to include path-dependence, memory effects, and non-standard noise structures, giving rise to Stochastic Delay Differential Equations (SDDEs) and related generalizations (Caraballo et al., 2024; de Feo et al., 2023). These models have proven valuable, particularly for capturing delayed responses, regime changes, and structural nonlinearities that occur in finance, economics, engineering, and biological systems.

In modelling financial data, SDEs have proven to be among the most important tools for characterizing the evolution of asset prices, interest rates, exchange rates and volatility. Recent studies have shown that classical linear drift formulations, such as Geometric Brownian Motion (GBM) and Ornstein – Uhlenbeck (OU) process, are limited in capturing key facts of financial markets, including heavy – tailed distributions, volatility clustering, asymmetric mean reversion, and structural breaks (Coulibaly et al., 2024; Nagarajan et al., 2025; Shen and Tang, 2025). These limitations have motivated the development of richer nonlinear SDE specifications, including regime-switching, fractional-order dynamics, and nonlinear drift structure (Chumpong et al., 2024; Oduselu-Hassan, 2025). Akintunde et al. (2020) introduced a Logarithmic mean reverting sine diffusion (LMRSD) process for modelling dynamics of nonlinear dynamical systems. The model was tested on two empirical datasets and compared with existing models; the study showed that it outperformed them, with the lowest values of the information criterion.

Motivated by these previous methodological and empirical considerations, this paper proposes a new class of nonlinear SDEs in which the drift term consists of a combination of linear, quadratic, and logarithmic terms. This proposed model captures a broader range of behaviors observed in financial markets, including volatility clustering, heavy tails, and skewness. This combination also introduces rich dynamics not present in traditional models such as the Geometric Brownian Motion (GBM) and the Ornstein-Uhlenbeck process and allows the model to capture diverse behaviors observed in empirical data. We derive the stationary distribution using the Fokker–Planck equation, while the mean and variance for this model are derived under the assumption that the process follows a lognormal distribution, which is common in financial applications.

Materials and method

Model Description

In this chapter, we present the proposed methodological framework. We begin with the nonlinear SDE. The SDE was formulated by adding a logarithmic term $\gamma log X_t$ to the drift term.

$$dX_t = (\propto X_t + \beta X_t^2 + \gamma log X_t)dt + \sigma dW_t \quad (1)$$

Where:

X_t is the process of interest.

$\propto$, β, γ, σ are constants that oversee the drift and volatility of the process.

W_t is a Weiner process (or Brownian motion).

The noise term is assumed to follow standard Brownian motion, with constant volatility σ.

Mean

We assumed the distribution of X_t is stationary, so the time derivative of the mean is zero:

$$\frac{d}{dt} E[X_t] = 0 \quad (2)$$

$$E(\propto X_t + \beta X_t^2 + \gamma log X_t)dt = 0 \quad (3)$$

This gives the equation:

$$\propto \mathrm{E[X]} + \beta \mathrm{E}[X^2] + \gamma \mathrm{E[logX]} = 0 \quad (4)$$

We assumed a log-normal moment distribution:

Assume $X_t \sim LogNormal(\mu, \sigma_X^2)$, then:

$$E[X] = e^{\mu+\frac{\sigma_X^2}{2}} \quad (5)$$

$$\mathrm{E}[X^2] = e^{2\mu+2\sigma_X^2} \quad (6)$$

$$\mathrm{E}[\log X] = \mu \quad (7)$$

Substituting 5,6, and 7 into equation (3), we have

$$\propto e^{\mu+\frac{\sigma_X^2}{2}} + \beta e^{2\mu+2\sigma_X^2} + \gamma\mu = 0 \quad (8)$$

The mean in terms of (μ, σ_X^2) is,

$$E[X] = e^{\mu+\frac{\sigma_X^2}{2}} \quad (9)$$

Where μ satisfies $\propto e^{\mu+\frac{\sigma_X^2}{2}} + \beta e^{2\mu+2\sigma_X^2} + \gamma\mu = 0$

Variance

Assuming $X_t \sim LogNormal(\mu, \sigma_X^2)$ of equation 5 and 6, the variance is, $Var(X_t) = \mathrm{E}[X^2] - (E[X])^2$

$$e^{2\mu+2\sigma_X^2} - (e^{\mu+\frac{\sigma_X^2}{2}})^2 \quad (10)$$

$$Var(X_t) = e^{2\mu+2\sigma_X^2} - e^{2\mu+\sigma_X^2} \quad (11)$$

Factor out $e^{2\mu+\sigma_X^2}$, $Var(X_t) = e^{2\mu+\sigma_X^2}(e^{\sigma_X^2} - 1)$ (12)

Stationary Distribution

We used the Fokker–Planck equation to find the stationary distribution of our nonlinear SDE. We begin with the Fokker–Planck equation for general SDE,

$$dX_t = \mu X_t dt + \sigma dW_t \quad (13)$$

The Fokker – Planck equation for the probability density $\pi(x,t)$ is, $\frac{\partial \pi(x,t)}{\partial \mathrm{t}} = -\frac{\partial}{\partial \mathrm{x}}[\mu(x)\pi(x,t)] + \frac{1}{2}\sigma^2 \frac{\partial^2 \pi(x,t)}{\partial \mathrm{x}^2}$ (14)

For a stationary distribution $\frac{\partial \pi}{\partial \mathrm{t}} = 0$, the equation becomes,

$$\frac{d}{dx}\left[-\mu(x)\pi(x) + \frac{1}{2}\frac{d}{dx}\{\sigma^2\pi(x)\}\right] = 0 \quad (15)$$

Integrating once, and assuming probability flux goes to zero at boundaries (natural boundary conditions), we get,

$$\mu(x)\pi(x) = \frac{1}{2}\frac{d}{dx}\{\sigma^2\pi(x)\} \quad (16)$$

For constant diffusion $\sigma(x) = \sigma$, this simplifies to,

$$\mu(x)\pi(x) = \frac{\sigma^2}{2}\frac{d\pi(x)}{dx} \quad (17)$$

Now, plugging in the drift of our nonlinear SDE

$$\mu(x) = \propto x + \beta x^2 + \gamma log x \quad (18)$$

So, we solve,

$$(\propto x + \beta x^2 + \gamma log x)\pi(x) = \frac{\sigma^2}{2}\frac{d\pi(x)}{dx} \quad (19)$$

Rewriting,

$$\frac{d\pi(x)}{dx} = \frac{2}{\sigma^2}(\propto x + \beta x^2 + \gamma log x)\pi(x) \quad (20)$$

This is a first-order linear ODE in $\pi(x)$, and it can be solved via an integrating factor,

$$\frac{d\pi(x)}{dx} = f(x), \pi(x) \quad (21)$$

Where $f(x) = \frac{2}{\sigma^2}(\propto x + \beta x^2 + \gamma log x)\pi(x)$ (22)

$$\pi(x) = Cexp(\int f(x)dx) \quad (23)$$

Now, computing the integral, we have,

$$\int f(x)dx = \frac{2}{\sigma^2}(\int \propto x dx + \int \beta x^2 dx \int \gamma log x dx) \quad (24)$$

$$\frac{2}{\sigma^2}(\frac{\propto}{2}x^2 + \frac{\beta}{3}x^3 + \gamma log x - \gamma x) \quad (25)$$

So, the stationary density is,

$$\pi(x) = C \exp\left[\frac{2}{\sigma^2}\left(\frac{\propto}{2}x^2 + \frac{\beta}{3}x^3 + \gamma log x - \gamma x\right)\right] \quad (26)$$

Now we normalize the density to get the final form, we write,

$$\pi(x) = \frac{1}{Z}\exp\left[\frac{2}{\sigma^2}\left(\frac{\propto}{2}x^2 + \frac{\beta}{3}x^3 + \gamma log x - \gamma x\right)\right] \quad (27)$$

Where Z is the normalizing constant,

$$\mathrm{Z} = \int_0^\infty \exp\left[\frac{2}{\sigma^2}\left(\frac{\propto}{2}x^2 + \frac{\beta}{3}x^3 + \gamma log x - \gamma x\right)\right] \quad (28)$$

In conclusion, the stationarity density is,

$$\pi(x) = \alpha \exp\left[\frac{2}{\sigma^2}\left(\frac{\propto}{2}x^2 + \frac{\beta}{3}x^3 + \gamma log x - \gamma x\right)\right], x > 0 \quad (29)$$

Results and Discussion

The proposed model was applied, and compared with existing models, such as GBMP, LMRSL, MRP, and LMRP. Three data sets were used in this study. The data sets used are Nigerian Interest rate data (1970-2020), Nigerian Inflation rate data (1970-2020), and Nigerian Naira-to-US Dollar data (1970-2020). Figs. 1, 2, and 3 show the plots of the realizations of Nigerian Interest rate data, Nigerian Inflation rate data and Nigerian Naira-to-US Dollar data, respectively.

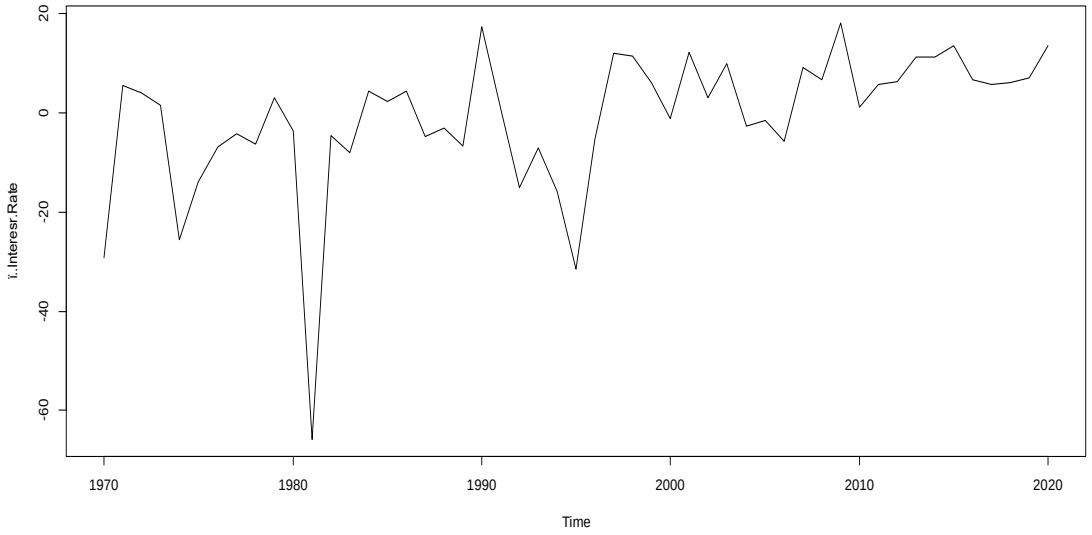

Fig. 1. Time plot of interest rate (1970-2020).

Table 1. Performance of the proposed model in comparison with the other existing models for interest rate.

Models	Theta 1	Theta 2	Theta 3	Theta 4	AIC	BIC
Geometric Brownian Motion Process (GBMP)	18.708535	4.307083	-	-	264.1226	267.9863
Vasicek Model	0.7334604	-0.0523150	13.1486770	-	405.5259	407.3895
Hull-White (extended Vasicek) Model	0.1525242	0.3283890	4.6961937	-	599.5245	601.3882
Mean Reverting Process (MRP)	-5.374235	4.114894	-	-	261.5663	265.4299
Mean Reverting Square Root Process (MRSRP)	-0.9374107	5.6694366	-	-	230.0693	233.9329
Mean Reverting Logarithmic Process (MRLP)	-7.006559	3.968649	-	-	259.5399	263.4036
Logarithmic Mean Reverting Processs (LMRP)	0.8416127	17.8034951	-	-	260.5464	264.41
Sine Diffusion Process	18.708535	4.307083	3.000000	-	266.1226	267.9863
Quadratic Loglinear Drift	-3.2325344	2.4831770	0.7823936	-1.2508919	8	7.863651

AIC: Akaike Information Criterion; BIC: Bayesian Information Criterion

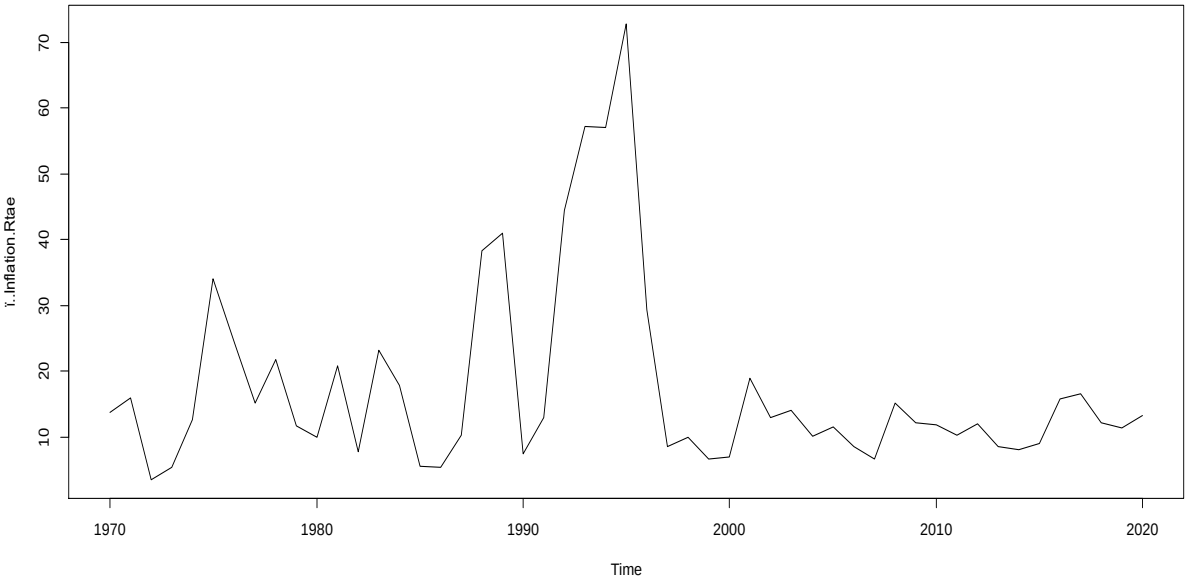

Fig. 2. Time plot of inflation rate (1970-2020).

Table 2. Performance of the proposed model in comparison with the other existing models for inflation rate.

Models	Theta 1	Theta 2	Theta 3	Theta 4	AIC	BIC
Geometric Brownian Motion Process (GBMP)	-1.3432274	0.8292275	-	-	381.5209	385.3449
Vasicek Model	0.3665149	17.4512875	11.3959955	-	383.5145	385.3386
Hull-White (extended Vasicek) Model	0.02879194	3.14479405	2.05850401	-	504.9414	506.7655
Mean Reverting Process (MRP)	45.117354	-1.080304	-	-	4	7.824046
Mean Reverting Square Root Process (MRSRP)	13.89840	2.99128	-	-	378.8435	382.6675
Mean Reverting Logarithmic Process (MRLP)	5.6024125	0.7526916	-	-	372.0306	375.8547
Logarithmic Mean Reverting Process (LMRP)	15.579575	3.904813	-	-	367.8736	371.6976
Sine Diffusion Model	-1.3432274	0.8292275	3.0000000	-	383.5209	385.3449
Quadratic Loglinear Drift	-0.4050182	0.7480697	0.6592802	-15.3437646	8	7.824046

AIC: Akaike Information Criterion; BIC: Bayesian Information Criterion

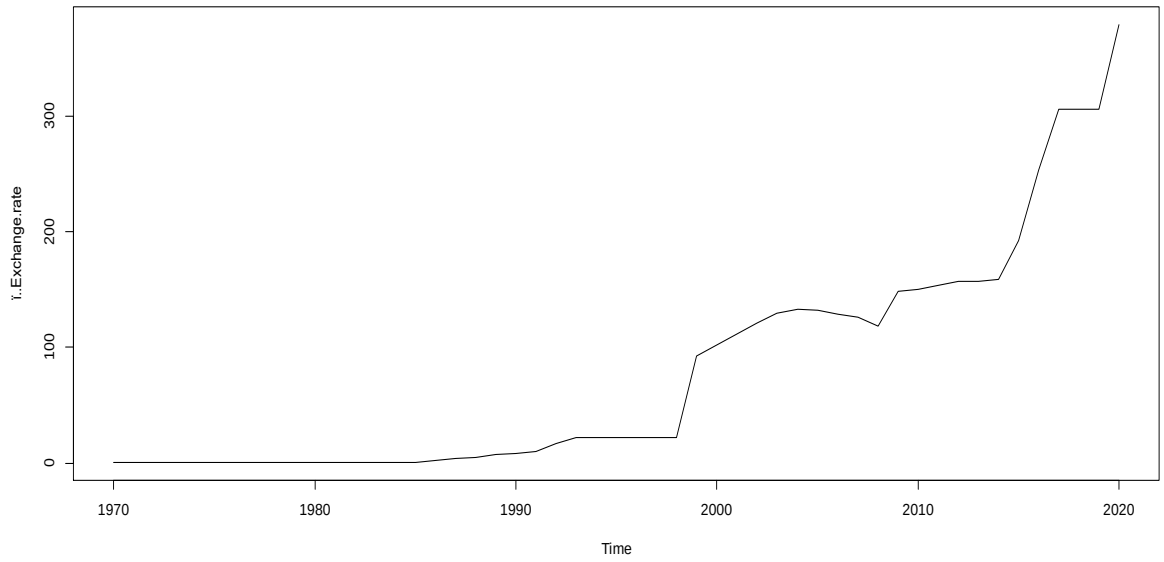

Fig. 3. Time plot of exchange rate.

Table 3. Performance of the proposed model in comparison with the other existing models for interest rate.

Exchange rate

Models	Theta 1	Theta 2	Theta 3	Theta 4	AIC	BIC
Geometric Brownian Motion Process (GBMP)	-0.5878979	0.5414701	-	-	345.2912	349.1153
Vasicek Model	-0.08521805	-15.58572705	16.66794661	-	420.7778	422.6018
Hull-White (extended Vasicek) Model	-0.02714862	1.04255587	-0.09606881	-	6	7.824046
Mean Reverting Process (MRP)	0.773846	1.118084	-	-	416.3496	420.1737
Mean Reverting Square Root Process (MRSRP)	2.379130	9.697673	-	-	496.878	500.7021
Mean Reverting Logarithmic Process (MRLP)	-0.5835662	-0.1563665	-	-	4	7.824046
Logarithmic Mean reverting Processs (LMRP)	-0.607859	4.895924	-	-	297.3123	301.1363
Logarithmic Mean Reverting Sine Diffusion (LMRSD)	-0.5878979	0.5414701	3.0000000	-	347.2912	349.1153
Quadratic Loglinear Drift	0.567964995	0.001940176	1.006402410	1.639346889	8	7.824046

AIC: Akaike Information Criterion; BIC: Bayesian Information Criterion

Conclusion

This study proposes a new class of nonlinear SDEs characterized by a drift function that incorporates linear, quadratic, and logarithmic terms. In extension beyond traditional linear models such as the Geometric Brownian Motion and the Ornstein-Uhlenbeck process, the proposed framework captures a richer set of dynamic behaviors commonly observed in financial and economic time series, including nonlinear mean reversion, heavy tails, asymmetry, and volatility clustering. The derivation of the Fokker-Planck equation, along with analytical expressions for the mean and variance under lognormality assumptions, provides deeper theoretical insight into the long-run properties of the model.

Future research may investigate parameter estimation using Bayesian, likelihood-based, or filtering methods; assess the model's empirical performance across diverse financial datasets; and extend the formulation to incorporate jumps, stochastic volatility or structural breaks.

Acknowledgment

I would like to express my sincere appreciate to my supervisor, Agwuegbo S.O.N., for his invaluable guidance, continuous support, and constructive feedback throughout this research. I am also deeply grateful to my co-supervisor, Akintunde A.A., for generously sharing her depth of knowledge, as well as for her insightful discussions and meaningful contributions to the development of this work. Finally, I extend my heartfelt thanks to my friend and colleague, Basirat A., for her encouragement and support during the course of this research.

Authors contribution

Ampitan K.R. conducted all experiments and was responsible for drafting, revising, and approving the final manuscript. Agwuegbo S.O.N. supervised the research work. Akintunde A.A. performed the data analysis. Basirat A. contributed to data collection.

Conflict of interest

The authors declare that there is no conflict of interest regarding the publication of this article.

References

Akintunde AA, Agwuegbo SON, Olayiwola OM, Dawodu GA, Soyinka AT and Wale-Orojo OA. Sine diffusion model for nonlinear dynamical systems. *Pac. J. Sci. Technol*. 2020; 21(2): 152-158.

Caraballo T, Ezzine F and Hammami MA. Practical stability of stochastic differential delay equations driven by G-Brownian motion with general decay rate. *Electron. J. Differ. Equ*. 2024; (70): pp. 1-26.

Chumpong K, Mekchay K, Nualsri F andSutthimat P. Analytical formula for fractional-order conditional moments of nonlinear drift CEV process with regime switching:Hybrid approach with applications. *arXiv*: 2411.13937, 2024.

Coulibaly BD, Ghizlane C and Khomssi ME. An approach to stochastic differential equations for long-term forecasting in the presence of α-stable noise: An application to gold prices. *Math. Model. Numer. Simul. Appl.* 2024; 4(2): 165-192.

de Feo F, Federico S and Święch A. Optimal control of stochastic delay differential equations and applications to path-dependent financial and economic models. *arXiv*: 2302.08809, 2023.

Hecht M and Zitzmann S. A computationally more efficient bayesian approach for estimating continuous-time models. *Struct. Equ. Model. Multidiscip. J.* 2020; 27(6): 829-840.

Liao L. The application and stability analysis of stochastic differential equations infinancial mathematics. *Acad. J. Math. Sci.* 2024; 5(3): 137-141.

Mahmoud AM, Adewumi AO and Ademola AT. Stochastic stability of solutions for a fourth-order stochastic differential equation with constant delay. *J. Inequal. Appl.* 2023; 148: 1-15.

Marwa Y, Mbalawata I, Mwalili S and Charles W. Stochastic dynamics of cholera epidemic model: formulation, analysis and numerical simulation. *J. Appl. Math. Phys*.2019;07(05): 1097-1125.

McCamley J, Denton W, Arnold A, Yentes J andYentes J. On the calculation of sample entropy using continuous and discrete human gait data. *Entropy*, 2018; 20(10): 764.

Nagarajan R, Rajendran M and Chandrasekaran V. Stock return model using stochastic delay differential equation in finance. *Math. Model. Eng. Probl.* 2025; 2(1): 91-99.

Oduselu-Hassan EO. Advancing hybrid numerical methods for nonlinear stochastic differential equations: Applications in complex systems. *Asian J. Res. Comput. Sci.*2025; 18(1): 124-132.

Shen L and Tang H. Stochastic differential equation model for detecting digital-currency market manipulation: A systematic review. *Adv. Differ. Equ. Contr. Process.*2025; 32(3): 45-62.

J. Bangladesh Acad. Sci. 50(1); 23-34: March 2026 DOI:https://doi.org/10.3329/jbas.v50i1.84634

Journal of Bangladesh Academy of Sciences

Journal homepage: http://www.bas.org.bd/publications/jbas.html

Research Article

A comparative study on flow-induced phenomena of servo-valve for realizable $k-\varepsilon$ and spalart-allmaras turbulence model under malfunction

Md. Shah Najmus Shakib[1] and Bijan Krishna Saha[*]

Department of Mathematics, Faculty of Science, University of Barishal, Barishal, Bangladesh

ARTICLE INFO

Article History

Received: 28 September 2025
Revised: 27 January 2026
Accepted: 29 January 2026

Keywords: Deflector jet servo-valve (DJSV), Computational fluid dynamics (CFD), Electro-hydraulic servo-valve (EHSV), Pressure and flow distribution, Cavitation.

ABSTRACT

Servo-valves are widely used in the aerospace, mechanical, and aeronautics sectors, where precise control of missile fins and aircraft components is essential. This study presents a details comparison between the Realizable $k-\varepsilon$ turbulence model and the Spalart-Allmaras turbulence model to evaluate flow behavior and its impact on servo-valve malfunction. This article highlights the critical role of electrohydraulic servo-valves in ensuring the performance and reliability of the servo control systems. Computational fluid dynamics (CFD) is employed to analyze pressure distribution, velocity patterns, and flow behaviors within the pilot stage of the servo-valves. Additionally, mesh refinement techniques are applied to achieve optimal accuracy and computational efficiency in capturing flow physics. Significant variations in pressure and velocity fields are observed, demonstrating the differing predictive capabilities of the turbulence models in capturing flow-induced effects. Therefore, this study provides valuable insights for improving servo-valve design and mitigating performance degradation caused by flow-related malfunctions..

Introduction

The EHSV affects the efficiency and dependability of the servo control system and is among the most prone parts to malfunction. For cost and performance, Tamburrano et al. (2018) assessed computational fluid dynamics analysis of electro-hydraulic servo-valves, novel control strategies, and smart material combinations. Because of its excellent contamination resistance, rapid dynamic response, improved flow control, and dependability, DJSV is used in many technological fields. Conversely, flow cavitation arising from the dynamic and static performance of the deflector jet servo-valve could compromise the accuracy of the hydraulic servo control system. It generates power loss, vibration, noise, and component deterioration of hydraulic valves. In a water-hydraulic valve, Liang et al. (2016) examined input pressure variations and unstable cavitation conditions. Their results showed that while a groove at the port of the valve can minimize cavitation severity during initial pressure changes, raising or lowering the frequency can help diminish cavitation enhancement. For a water poppet valve, Han et al. (2017) computed the cavitation and flow force. Their results revealed that valve cavitation can be avoided with a special valve-opening and outlet-pressure arrangement. A spool valve having U-grooves showed more severe cavitation as the valve opening and groove depth increased, claims Zou et al. (2008). Investigating the vortex and flow stream during metering in a spool valve with varying valve apertures, Gao (2009) used finite element and PIV approaches. Chen et al. (2019) sought the source of self-excited noise in the flapper-nozzle servo-valve pilot stage. Numerical models and experimental flow

[*]Corresponding author: <bksaha@bu.ac.bd>

[1]*Department of Mathematics, University of Global Village (UGV), Barishal, Bangladesh*

data suggest that the cavitation increases as oil viscosity decreases. Their studies also showed that noise was produced by unstable cavitation in the pilot stage. Other studies, in the meantime, studied the directional control valve and servo-valve spool pressure losses and flow characteristics using numerical simulations. Using pure water flowing through the valve port, Zhang et al. (2012) focused on energy loss, cavitation erosion, and spiral vortices. Sandor and Suan-Resiga found that more severe and destructive cavitation followed by increased input pressure (Sandor and Suan-Resiga, 2012). The flow profile and cavitation events within hydraulic servo-valve pilot stages have been investigated theoretically and experimentally on several occasions. The pilot-stage flow field of a dual nozzle-flapper servo-valve was investigated by Jacob et al. (2011) using CFD. They demonstrated the stability of the conventional turbulence model for incompressible steady fluid flow profile in a servo-valve pilot stage. Li et al. (2013) assessed cavitation in the pilot stage of a flapper-nozzle servo-valve at Reynolds numbers between 630 and 2500. Also, the hollow, cloud-like shape on the flapper's curved surface was examined. Aung and Li (2014) designed a special rectangular flapper form to prevent cavitation. The efficiency of the new flapper form was shown by its identical flow characteristics to those of the traditional flapper form. Using three flapper geometries, Yang et al. (2015) examined cavitation effects under four flow conditions and changing input pressures with two flapper-nozzle null clearances (0.2 mm and 0.1 mm). The researchers found that in the pilot valve, flutter-nozzle null clearance and intake pressure improved turbulent jets and cavitation. Finally, rectangular flappers reduce cavitation between the pilot valve and the flapper nozzle. Several researchers have recently examined electrohydraulic servo-valve cavitation to improve pilot-stage performance. Yang et al. (2019a) studied cavitation reduction using microjets surrounding the main jets of the flapper-nozzle servo-valve. Their results showed that continuous micro-jets greatly decreased flapper-nozzle valve cavitation. Yang et al. (2019b) investigated the flapper-nozzle pilot stage cavity and flow forces in a hydraulic servo-valve at multiple supply pressures using continuous microjets. To avoid cavitation in the nozzle-flapper servo-valve, Yang et al. (2019c) argued for replacing circular nozzles with diamond ones. They found that, in numerical simulations, a modified nozzle structure might reduce cavitation without compromising servo-valve performance. Wu et al. (2018) investigated cavitation intensity using LES and snapshots. The results revealed that whilst raising the deflection angle stabilizes the flow field, increasing the jet pipe input pressure generates turbulent components with smaller vortices. Using two usually closed two-way two-position valves operated by two piezoelectric ring benders, Tamburrano et al. (2020) created a pilot stage flapper-nozzle servo-valve to control quiescent flow when the main stage is stationary. Numerical models and experiments are compared to guarantee consistent findings. The model-based work of Ren et al. (2022) on servo-values validated the hypotheses of jet theory about the design of the deflector jet valve. Emphasizing the importance of inlet pressure on performance, Abdallah et al. (2023a) examined pressure oscillation and structural factors.

To better grasp the internals of the deflector jet servo-valve, Yan et al. (2019) created a computational model. Additionally, Abdallah et al. (2023b) examined erosion events. They advised performance improvements and focused on the shunt wedge. Chu et al. (2021) examined oil-contaminated performance degradation with multi-physics simulation correction and theoretical analysis. To maximize jet-pipe servo-valve dynamics, Chen et al. (2022) applied a mathematical model and a hierarchical particle swarm optimization genetic technique. The dynamic erosion wear of the nozzle flapper pressure servo-valve of an aircraft braking system was investigated in another paper by Chu et al. (2020). Yan et al. (2020) quantitatively investigated erosion wear in a hydraulic amplifier of a deflector jet servo-valve and derived failure criteria and a lifespan prediction formula depending on hydraulic oil contamination.

Electrohydraulic servo-valves are an inseparable element of systems in the aerospace, automotive, and industrial sectors, where hydraulic fluids are controlled to ensure processes run smoothly and with accuracy. However, typical deviations include irregular flow and pressure fluctuations, which occur due to malfunctions and thereby affect the performance of the whole system, leading to complete failure. A thorough understanding of these concerns forms a decisive part of the quest to increase the reliability and efficiency of the servo-valve.

While previous studies have extensively examined turbulence models, including the Realizable $k-\varepsilon$ and Spalart-Allmaras models in general nozzle flows or convergent-divergent jets, a direct comparison with electro-hydraulic servo-valves, especially deflector-jet systems under conditions of malfunction, is evidently lacking. As a result, measurements of model-specific predictions applicable to pilot-stage reliability are restricted. The vast majority of previous research has focused on valves in an ideal, neutral state or during steady-state erosion, leaving an essential knowledge gap about the behavior of turbulence models in the presence of an asymmetric pressure gradient and local flow separation caused by the physical misalignment. When the flapper is positioned in the middle position, the flow is symmetric. However, when the flapper is misaligned due to mechanical failure or excessive use, the flow becomes assymmetric. In that case, it requires the comparative use of two models as it transforms this stable jet into a highly non-linear flow field.

This paper attempts to fill this gap by proposing a rotational malfunction as an exemplar of a failure mode, thereby providing a more general model for considering valve reliability under non-ideal mechanical conditions. The study compares the Spalart-Allmaras and realizable $k-\varepsilon$ models in a deflector jet servo-valve (DJSV) under malfunction and reveals distinct changes in the pressure and velocity fields, which guide optimal model selection to enhance the reliability of the valve in high-pressure aerospace applications. A 5-degree rotation is used to induce significant changes in flow behavior, with smaller angles yielding trivial changes that cannot allow a sound conclusion.

The essence of the study phenomenon is its coverage of this gap by clarifying the effect of model choice on predicting changes in flow components caused by malfunctions and by complying with the practical imperative to gain accessy to efficient servo-control apparatus in areas that indeed demand precision. The findings can be used to design better valves in conditions where the valve malfunctions, as they identify the type of turbulence model that better reflects the flow phenomena. At the same time, as a practical application of improvement, the research is expected to enhance the efficiency and reliability of critical systems that utilize servo-valves.

Operating principle and flow field

As shown in Fig. 1, a two-stage deflection flapper servo-valve typically has a pilot and main stage. Electromagnetic torque drives the pilot stage. As an electromechanical converter, the motor and hydraulic amplifier ensure proper movement of the main stage (spool) and proper performance of the pilot stage. The amplifier jet disk is established, and a deflection flapper with a V-shaped guiding groove is meticulously placed between the supply nozzle and two receiving ports during the pilot stage. Fig. 1 shows the amplifier disk and deflection flapper in close-up. Its term is considered as coil current. A slight current applied to the electromagnetic torque motor induces the flapper to rotate at a limited angle.

From the fixed intake, the flapper grooves direct fluid flow to one of two receiving ports. The main spool in the port is driven in the opposite direction to the flapper's movement by a pressure difference created there. The feedback rod links the flapper and spool to balance forces. The flapper is in the null state when the torque motor voltage is zero, therefore dispersing fluid equally between two receiving ports from the supply nozzle. Should both receiving ports

have the same energy consumption, the pressure differential between them will be zero (Saha et al., 2020). Further, for rotational movement of the servo-valve, the valve's components include a rotary actuator, rotary wheel, rotary flapper, receiver ports, and a supply nozzle. The rotary actuator generates electrical torque that drives the flapper to rotate. The fluid goes to the receiving ports, which regulate the main stage flow in the valve. To provide precise control, a feedback rod connects the flapper to the spool. Rotational motion reduces damage and improves control precision, hence allowing small, long-lasting devices (Saha et al., 2024).

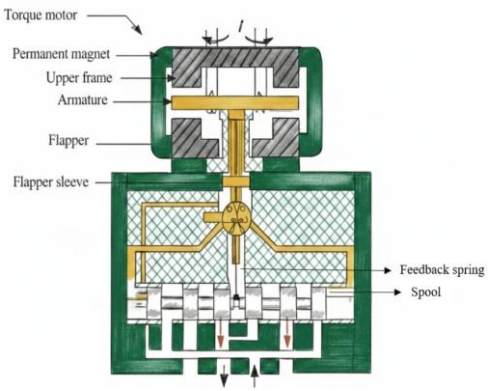

Fig. 1. Schematic of a two-stage deflection flapper servo-valve with pilot and main stage.

Execution of CFD analysis

The implementation of this numerical analysis is based on the coupling of mechanical failure suppositions and the resulting fluid-structure interaction. One of the fundamental assumptions of this study is that the deflector jet undergoes a 5-degree rotational malfunction under non-linear operating conditions. Physically, such a condition requires a specialized model formulation to capture the intricate flow phenomena.

A. Simplification of geometric models

As seen in Fig. 2, the flow channel inside the initial stage of the servo-valve has a complex geometry. Fig. 2(a) shows the amplifier disk, and Fig. 2(b) shows the CAD model of this study.

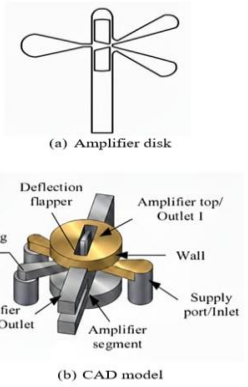

(a) Amplifier disk (b) CAD model

Fig. 2. Computational domain of the flapper pilot stage.

The dimensions of the amplifier disk for this study are based on the model developed earlier by Saha et al. (2020). By limiting the simulation to the nearest part of the pilot stage, we may improve computing performance and conserve memory.

B. Grid independence test

Mesh quality in CFD simulations has a significant impact on the numerical solution to a specific problem. Three distinct grid sizes, Grid E, Grid F, and Grid G, are used for the validation of the grid. It is abundantly evident that numerical convergence with numerous grids has significant obstacles. Using many grids, the surface average for both models is approximated to explore the dependency of the grid on the simulation results, as given in Table 1. Grid E and Grid F have a relative error of less than 3%; Grid F and Grid G have less than 2%. Grid F is employed in this study for numerical simulations to compromise computational expense with numerical accuracy.

Table 1. Findings from the grid independence test.

Grid	Cells	Faces	Vertices	Surface average (Realizable k-ε)	Surface average (Spalart-Allmaras)
Grid E	101336	314313	108731	5.63 MPa	6.17 MPa
Grid F	131425	382725	152792	5.76 MPa	6.33 MPa
Grid G	152942	422768	186765	5.62 MPa	6.21 MPa

C. Grid distribution

Grid distribution uses the Star-CCM+ program's built-in mesh generator, along with the trimmer, surface remesher, and prism layer meshing models. In addition, we have used a two-layer prism component and a block having a base size of only 0.00002 m. Refined meshing was applied to the region around the flapper's V-groove to improve accuracy. There are 131425 cells, 382725 faces, and 152792 vertices, which are shown in Fig. 3. Fig. 3(a) shows mesh model of the pilot stage and 3(b) represents the derived part of the pilot stage.

The precision of convergence is 1×10^{-5}. You may create orthogonal prismatic cells near the edges of walls by combining the prism layer's mesh. A mesh system's maximum skewness angle is one of the key metrics for gauging its quality. A skews angle of 90 degrees or greater is problematic in STAR-CCM+ and can occur in concave cells. According to Fig. 4, every single study ensures that the majority of the skewness angle remains below 45 degrees.

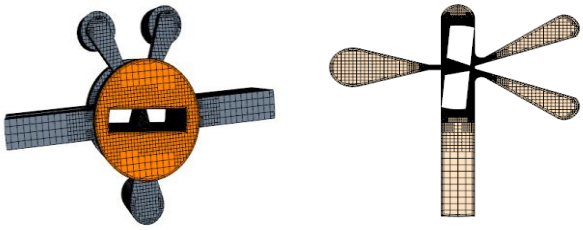

(a) Mesh model **(b) Derived part**

Fig. 3. Meshing model of the deflector jet pilot stage and its plane section.

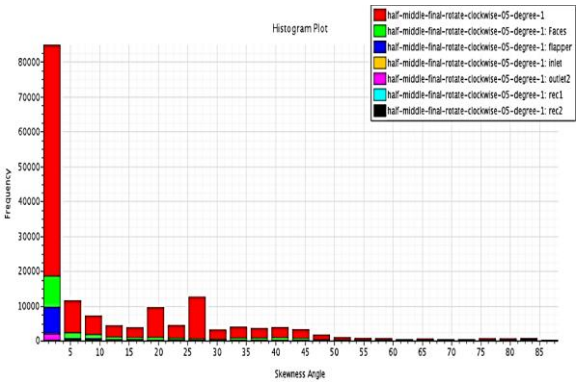

Fig. 4. Histogram of skewness angle.

D. Rationale for turbulence model selection

Two different turbulence models have been selected to account for the particularities of a malfunctioning DJSV. The Spalart-Allmaras model is a one-equation model that solves a transport equation for the modeled turbulent eddy viscosity. It was chosen because it has proven reliable in aerospace applications involving wall-bounded flow and adverse pressure gradient. At an inclined angle in the V-groove, this occurs when the jet strikes the groove at an oblique angle, leading to local flow separation. The Spalart-Allmaras model is computationally efficient and uniquely designed to account for layer offsets at the boundaries, where two-equation models overdo turbulence. Further, realizable $k-\varepsilon$ was selected because it introduces a dissipation rate term in the turbulent transport equation and a critical coefficient that varies with the mean flow and turbulence characteristics. Higher curvature and rotation can be found in the flow of a malfunctioning servo-valve with a 5-degree malfunction. Specifically, the realizable formulation addresses all these conditions better than the usual $k-\varepsilon$ model, thereby ensuring the mathematical consistency (realizability) of the normal stresses.

E. Boundary conditions

In Fig. 2, we can see the design that dictates the boundary conditions of the servo-valve construction. The input, wall, and output boundaries are the three types of boundaries that define the computational domains. All other surfaces have wall-type boundaries that demarcate the regions around the fluid or solid. The presence of viscous flow automatically enforces the no-slip wall criterion. Temperature changes are not considered. The inlet boundary condition of pressure is defined as the supply point. Pressure acts on the amplifier's upper and lower surfaces. There is a pressure differential of 20 MPa to 24 MPa at the input and 1 MPa at the output.

Result and Discussion

This section analyzes the pressure and velocity distribution of a servo-valve for a 5-degree rotational malfunction. This work compares the realizable k-ε model and Spalart-Allmaras turbulence models to better understand how they capture flow-induced changes. The effects of varying supply pressure on pressure distribution, velocity patterns, and system response are studied to highlight model-specific performance.

A. Pressure distribution

When the supply pressure rises from 20 MPa to 24 MPa, the pressure of receivers A and B increases. Because the greater supply pressure drives more fluid into the servo-valve, pressure throughout the system increases. Also, it is notable that the effective orifice size decreases when the flapper is at 5 degrees clockwise; pressure drops in receiver B and increases in receiver A. The Spalart-Allmaras model generates more pressure in receiver A than the realizable k-ε model. This demonstrates the Spalart-Allmaras model's capacity to capture turbulence and flow separation in high-pressure environments. Particularly in places where the flow has significant rotation and complicated behavior, the Spalart-Allmaras model offers a more comprehensive result of turbulent viscosity than the realizable k-ε model. The model correctly forecasts localized high-pressure zones as supply pressure rises, generating higher pressures in receiver A. This observation is shown in Fig. 5.

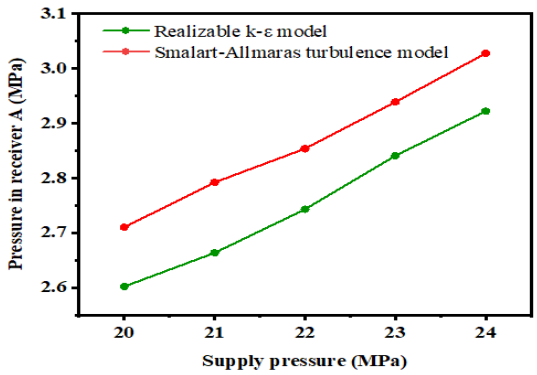

Fig. 5. Comparison of pressure distribution in receiver A for Spalart-Allmaras and realizable k-ε models.

The realizable k-ε model has a higher pressure than the Spalart-Allmaras model in receiver B. The realizable k-ε model is well-suited to handling complex flow dynamics and pressure losses because it imposes additional constraints that ensure the turbulence representation remains realistic. Its equation structure enables more accurate modeling of pressure decreases and flow stability, particularly in areas with complex interactions. As supply pressure increases, this model better captures the intricacies of fluid behavior, leading to higher pressure measurements in receiver B, as shown in Fig. 6.

For both the Spalart-Allmaras and realizable k-ε models, analyzing the scalar scene of pressure distribution is crucial. It physically shows how pressure varies across valve surfaces and helps identify localized high-pressure zones, flow separation, and turbulence.

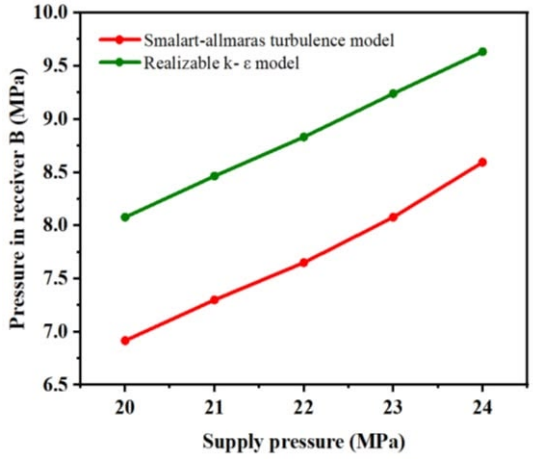

Fig. 6. Comparison of pressure distribution in receiver B for Spalart-Allmaras and realizable k-ε models.

At a traditional neutral position (without malfunction), the pilot stage of the DJSV is in a state of complete hydrodynamic symmetry. The jet of supply leaving the nozzle impacts directly on the shunt wedge, thus creating a stagnation point in the center of the fluid, which converts the kinetic energy of the fluid into a static pressure. Since the geometry is perfectly aligned, the pressure field is reflected with respect to the vertical axis of the valve. As a result, the pressure recovery in the two receivers is equivalent, resulting

in a zero differential pressure as shown in Fig. 7(c) (Saha et al., 2024). The pressure gradients in this regime are smooth and predictable, and there are no localized regions of low pressure commonly referred to as hot spots, indicative of flow separation or cavitation. Although the traditional setup maintains a balanced pressure field, the addition of a 5-degree malfunction introduces complex non-linear pressure remnant changes that require a dual-model verification. The Spalart-Allmaras model is used to trace the adverse pressure gradient and the likely separation at the receiver walls due to the steep angle of impingement, which direct effects the efficiency of pressure recovery. At the same time, the realizable k-ε model is also essential for addressing streamline curvature and rotational pressure variation in the V-groove, as mathematical restrictions limit the over-representation of turbulence kinetic energy in swirling flow.

Comparing the scalar landscapes of different models reveals how each forecast behaves and experiences turbulence under similar conditions, thereby informing model selection for maximum performance in hydraulic systems. The scalar scene of pressure distribution is shown in Figs. 7(a) and 7(b).

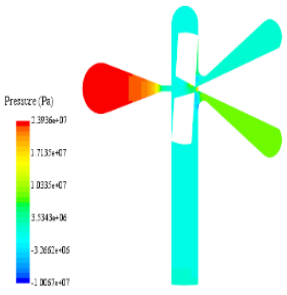

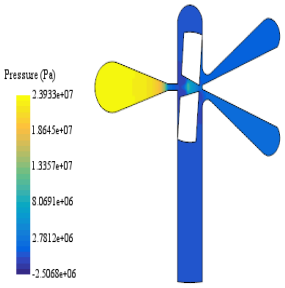

(a) Spalart-Allmaras **(b) Realizable k-ε**

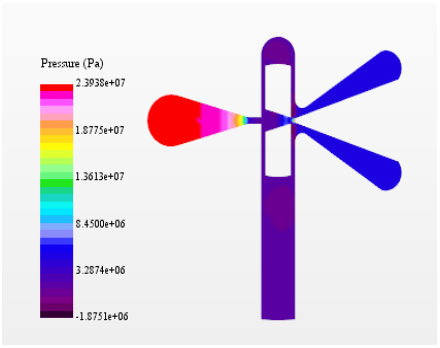

(c) Middle flapper position for the traditional model.

Fig. 7. Scaler scene of pressure distribution.

Also, pressure in the cross-sectional area for both models has been calculated and compared with the traditional model (Saha et al., 2024) to understand how fluid forces distribute within the valve, as illustrated in Fig. 8.

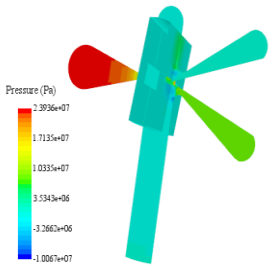

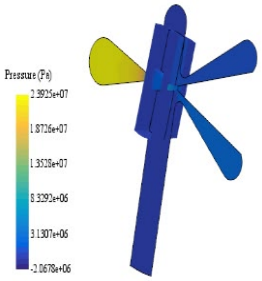

(a) Spalart-Allmaras **(b) Realizable k-ε**

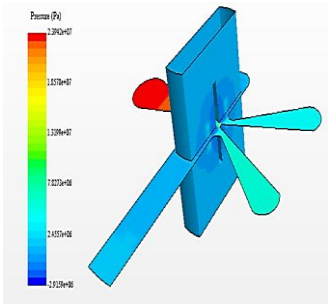

(c) Traditional model

Fig. 8. Pressure comparison in the cross-sectional area.

To sum up, the differences between the models are clearly important relative to the traditional neutral position, where the two models agree on the same outcomes because of a symmetrical, predictable flow-field and no separation. Nevertheless, when

the state becomes malfunctioning, the symmetry that is broken sparks two different phenomena requiring the application of different mathematical approaches. The models that forecast high pressure in Receiver A include the Spalart-Allmaras model, which is designed to solve only wall-bounded flow; thus, it successfully predicts the stagnation pressure at the rear part of the jet striking the inlet at an acute angle. On the other hand, the realizable k-ε model is more stable in the shadow areas of Receiver B due to the realizability constraint, which prevents excessive generation of turbulent kinetic energy in the rotating vortices developed within the V-groove. It shows that to measure the entire extent of performance deterioration in a malfunctioned valve, a dual-model method is necessary.

B. Surface average

Increasing supply pressure from 20 MPa to 24 MPa in a servo-valve system increases surface average pressure according to the Spalart-Allmaras and realizable k-ε turbulence models. This increase is caused by higher fluid energy in the system resulting from increased supply pressure. The motion of the fluid increases with increasing pressure, thereby generating greater force on the surfaces of the valve. As the fluid moves through the system, these dynamics raise average surface pressures. In high-pressure conditions, the Spalart-Allmaras model more precisely forecasts turbulent viscosity and flow dynamics than the realizable k-ε turbulence model. Therefore, it produces a surface average pressure higher than that of the realizable k-ε turbulence model. Particularly in regions with significant areas of high rotation and separation, the Spalart-Allmaras model effectively captures the complex interactions in turbulent flows, thereby producing significant surface pressure build-up, as shown in Fig. 9.

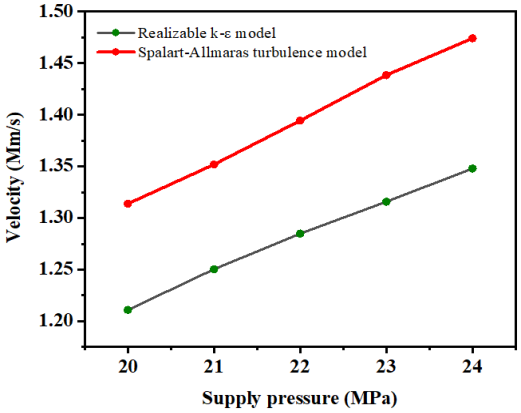

Fig. 9. Comparison of surface average for Spalart-Allmaras and realizable k-ε models.

C. Velocity distribution

Increasing supply pressure increases fluid velocity in both models, as flow rate and pressure are strongly related to velocity. Increased pressure from 20 to 24 MPa accelerates the fluid through the valve orifice. The Spalart-Allmaras turbulence model exhibits greater velocity while the supply pressure is increased, as illustrated in Figure 10. This is because this model better captures flow separation and rotational effects. The split-Allmaras turbulence model provides a finer resolution of turbulent viscosity near walls and therefore simulates fast, confined flow patterns more accurately than the realizable k-ε model, which averages turbulence effects over a larger region.

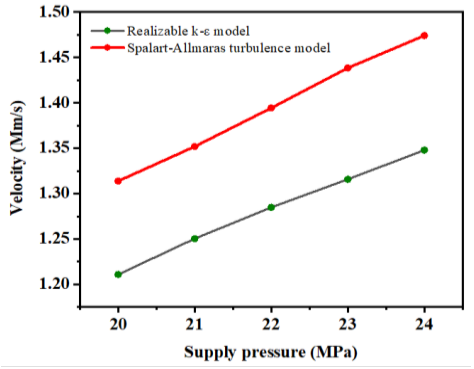

Fig. 10. Comparison of velocity distribution for Spalart-Allmaras and realizable k-ε models.

To visualize flow patterns and velocity variations across different models, scalar and vector scenes of the velocity distribution shown in Figs. 11 and 12,

respectively, compared with the traditional middle position of the flapper (Saha et al., 2024). During the neutral position of the flapper, the velocity field is observed to be entirely symmetrical, with the jet core cutting in half at the shunt wedge, thus yielding an equilibrium kinetic energy distribution. The emergence of the malfunction, however, involves the comparative implementation of two turbulence models, which are considered because they cause the otherwise stable jet to become a highly non-linear flow field with skewed momentum flux and centrifugal influence. Physically, the failure forces the jet to hit the receiver wall at an oblique angle, creating a high- velocity impingement zone unique to each model. The Spalart-Allmaras model is essential for solving steep velocity gradients and fully describing boundary-layer attachment at the receivers. On the other hand, the realizable k-ε model is to correctly capture rotational energy and streamline curvature, as the fluid is driven into the V-groove. With the assistance of both models, it is possible possible to verify the theoretical velocity losses in the receivers.

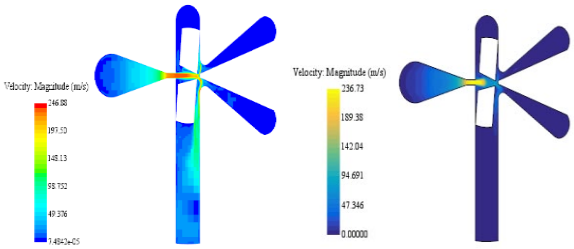

(a) Spalart-Allmaras **(b) Realizable k-ε**

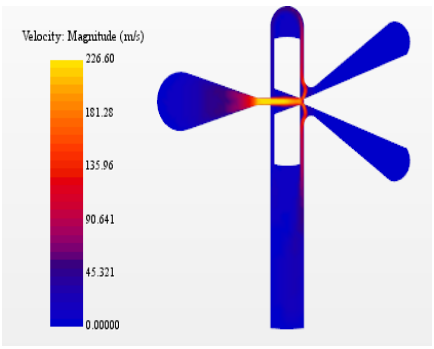

(c) Middle position without malfunction.

Fig. 11. Scalar scene of velocity distribution.

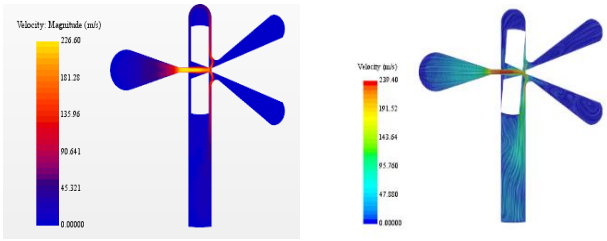

(a) Spalart-Allmaras **(b) Realizable k-ε**

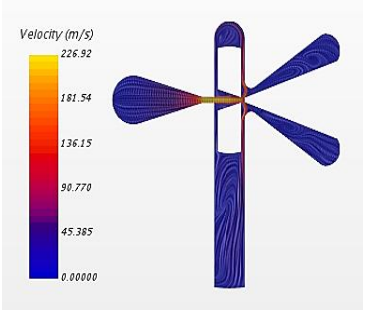

(c) Middle position without malfunction for the traditional model

Fig. 12. Vector scenes of velocity distribution.

Moreover, to visualize both the magnitude and direction of flow, vector contour for both models are shown in Fig.13.

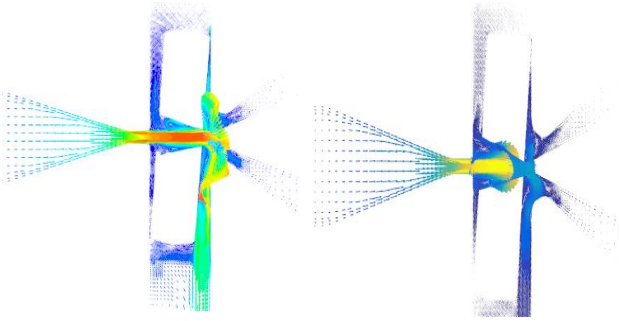

(a) Spalart-Allmaras **(b) Realizable k-ε**

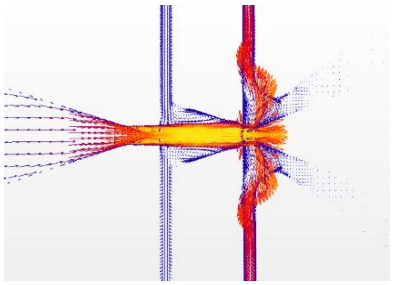

(c) Traditional models for neutral flapper positions.

Fig. 13. Vector contour of velocity distribution.

Also, velocity across the cross-sectional area is observed in both models, as illustrated in Fig. 14.

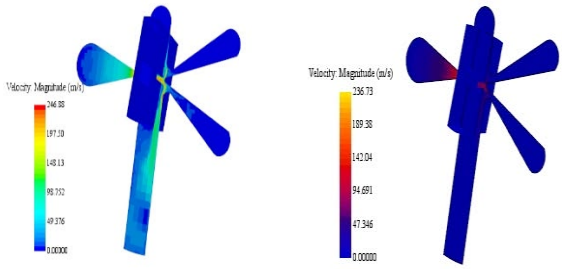

(a) Spalart-Allmaras **(b) Realizable k-ε**

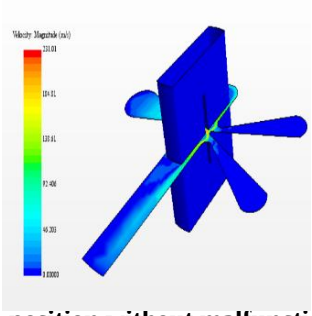

(c) Middle position without malfunction for the traditional model

Fig. 14. Velocity comparison of cross-sectional area.

Implementation of the study

This study provides a key finding: selection models of turbulence to analyze the operation of electro-hydraulic servo-valves (EHSV) under specified malfunctioning conditions. This result emphasizes the relationships among several significant physical parameters in deflector-jet servo-valves (DJSVs) during malfunction, and these results are beneficial for computational fluid dynamics (CFD) methods. Specifically, the supply pressure is directly related to the jet velocity, which, in turn, amplifies the pressure distributions and creates an asymmetry between receivers A and B with increasing deflector angle. Boundary-layer effects do control the shape of the velocity profiles, amplifying kinetic energy and decreasing it in V-grooves than in nozzles, and hence correlate with differences in pressure, which lead to spool movement and systems reliability. The intensity of turbulence varies the effective viscosity; high supply pressure increases the effect of jet forces and oscillations, a point that shows some correlatability with erosion alleviation in the air aircraft scenario. The implications of this study state the relationship of supply pressure, jet velocity, and pressure asymmetry in the DJSVs, where the model-specific abilities are reflected: the Spalart-Allmaras model is well equipped to deal with wall-bounded velocity fields, whereas the realizable k-ε model is more competent in shear-driven losses and can help in the model selection of accurate malfunctioning prediction. The application of such results to broader processes involves optimizing resistance to contamination and the dynamical response, as the revealed parameter relationships can be used to improve the design of the model, such as altered nozzle shapes, to achieve flow equilibrium. In the field of mechanical engineering, the results are valuable for predictive maintenance strategies, as they establish a correlation between supply pressure and vibrations caused by uneven pressure distribution.

Despite the detailed comparison of the two analyses, the current study has several limitations. First, the research is only focused on a specific malfunction condition; as such phenomena are caused by flow, they are not studied at other angles. Secondly, whereas the pressure and velocity differences are described, the effects of cavitation, which is often involved in erosion and noise disturbances in DJSVs, are not measured. In addition, the thermal effects and the full interaction between the pilot and main stages have not been considered in the simulation due to a simplified geometry model, prioritizing pilot-stage fidelity over increased computational efficiency. In future studies, multiphase cavitation modeling and thermal analysis will be needed to provide a more comprehensive representation of servo-valve failure modes.

Conclusion

We analyzed pressure distribution, surface-average, and velocity distributions using the Spalart-Allmaras and realizable k-ε turbulence models for a 5-degree clockwise servo-valve malfunction. The goal was to investigate how each model captured flow behavior and turbulence under varying supply pressures and rotational movements. For the increase of supply pressure, pressure in receivers A and B increases for

both the Spalart-Allmaras and the realizable k-ε turbulence model. Moreover, for a 5-degree malfunction, the Spalart-Allmaras model shows higher pressure in receiver A when the supply pressure increases due to better handling of flow separation. However, the realizable k-ε model captures pressure more effectively in receiver B, likely due to differences in turbulence averaging. Both models show an increase in surface average as supply pressure increases. The Spalart-Allmaras model produces higher surface averages, reflecting its better ability to anticipate localized flow changes.

Increased supply pressure increases fluid velocity in both models. The Spalart-Allmaras model exhibits higher velocities when the supply pressure is increased due to improved resolution of rotational effects and wall-bound flows.

Acknowledgment

The following support is gratefully acknowledged: Professor Songjing Li, Head of the Department of Fluid Control and Automation, Harbin Institute of Technology (HIT), Harbin, China, and the National Natural Science Foundation of China (No. 51675119).

Authors contribution

Md Shah Najmus Shakib: Conceptualization; methodology; software; validation; visualization; investigation; drafting the original manuscript; revision; formal analysis. Bijan Krishna Saha: Supervision; critical review and editing; original manuscript; formal analysis; validation; software; visualization.

Conflict of interest

The authors have no financial or personal relationships that could have influenced the study.

References

Saha BK, Peng J and Li S. Numerical and experimental investigations of cavitation phenomena inside the pilot stage of the deflector Jet Servo-Valve, *IEEE Access*, 2020; 8: 64238-64249.

Gao D. Finite element numerical simulation and PIV measurement of the flow field inside metering-in spool valve. *Chin. J. Mech. Eng.* 2009; 22(1): 102-108.

Abdallah HK, Peng J and Li S. Analysis of pressure oscillation and structural parameters on the performance of deflector jet Servo-valve. *Alex. Eng. J.* 2023a; 63: 675-692.

Abdallah HK, Ben-Mansour R and Li S. Numerical study of erosion phenomena with the presence of cavitation at deflector jet servo-valve. *Arab. J. Sci. Eng.* 2023b; 49(2): 15.

Yan H, Li J, Cai C and Ren Y. Numerical investigation of erosion wear in the hydraulic amplifier of the deflector jet Servo-valve. *Appl. Sci. (Switzerland)*, 2020; 10(4): 1299.

Yan H, Ren Y, Yao L and Dong L. Analysis of the internal characteristics of a deflector jet servo-valve. *Chin. J. Mech. Eng.* 2019; 32: 31.

Yang H, Wang W and Lu K. Cavitation and flow forces in the flapper-nozzle stage of a hydraulic servo-valve manipulated by continuous minijets. *Adv. Mech. Eng.* 2019a; 11(5): 168781401985143.

Yang H, Wang W and Lu K. Numerical simulations on flow characteristics of a nozzle-flapper Servo-valve with diamond nozzles. *IEEE Access*, 2019b; 7: 28001-28010.

Yang H, Wang W, Lu K and Chen Z. Cavitation reduction of a flapper nozzle pilot valve using continuous microjets. *Int. J. Heat Mass Transf.* 2019c; 133:1099-1109.

Sandor IB and Suan-Resiga R. Numerical model for cavitational flow in Hydraulic poppet valve. *model. Simul. Eng.* 2012; 2012: 742162.

Chen J, Li F, Yang Y and Gao Y. Mathematical modelling and hierarchical encourage particle swarm optimization genetic algorithm for jet pipe servo-valve. *Comput. Intell. Neurosci*. 2022; 2022(7): 9155248.

Liang J, Luo X, Liu Y, Li X and Shi T. A numerical investigation in effects of inlet pressure

fluctuations on the flow and cavitation characteristics inside water hydraulic poppet valves.*Int. J. Heat Mass Transf.* 2016; 103: 684-700.

Saha BK, Peng J, Shakib MSN, Li S and Jihan JI. A numerical analysis of pressure characteristics in the deflector jet pilot stage valve with an innovative deflector deflection. *Flow Meas. Instrum.* 2024; 99: 102674.

Zou J, Fu X, Du XW, Ruan XD, Ji H, Ryu S and Ochiai M. Cavitation in a non-circular opening spool valve with U-grooves. *Proc. Inst. Mech. Eng. A, J. Power Energy*, 2008; 222(4): 413-420.

Jacob M, Mchenya S, Zhang and Li S. A study of flow-field distribution between the flapper and nozzle in a hydraulic servo- valve.In:*Proc. Int. Conf. Fluid Power Mechatronics, Beijing, China*, 2011; pp. 658-662.

Wu L, Chen K and Zhan C. Snapshot POD analysis of transient flow in the pilot stage of a jet pipe Servo-valve. *J. Turbulence*, 2018; 19(10); 889-909.

Zhang L, Luo J, Yuan R and He M. The CFD analysis of twin flapper nozzle valve in pure water hydraulic. *Int. Conf. Adv. Comput. Model. Simul., Proc. Eng.* 2012; 31: 220-227.

Chen M, Aung NZ, Li S and Zou C. Effect of oil viscosity on self-excited noise production inside the pilot stage of a two-stage electrohydraulic servo-valve. *J. Fluids Eng.* 2019; 141(1): 011106.

Han M, Liu Y, Wu D, Zhao X and Tan H. A numerical investigation in characteristics of flow force under cavitation state inside the water hydraulic poppet valves. *Int. J. Heat Mass Transf.* 2017; 111: 1-16.

Aung NZ and Li S. A numerical study of cavitation phenomenon in a flapper- nozzle pilot stage of an electrohydraulic servo-valve with an innovative flapper shape. *Energy Convers. Manage.* 2014; 77:31-39.

Tamburrano P, Plummer AR, Distaso E and Amirante R. A review of electrohydraulic servo-valve research and development. *Int. J. Fluid Power*, 2018; 201: 53-98.

Tamburrano P, Plummer AR, Palma PD, Distaso E and Amirante R. A novel servo-valve pilot stage actuated by a piezo-electric ring bender: A numerical and experimental analysis. *Energies*, 2020; 13(3): 671.

Yang Q, Aung NZ and Li S. Confirmation on the effectiveness of rectangle-shaped flapper in reducing cavitation in flapper–nozzle pilot valve. *Energy Convers. Manage.*, 2015; 98: 184-198.

Li S, Aung NZ, Zhang S, Cao J and Xue X. Experimental and numerical investigation of cavitation phenomenon in flapper–nozzle pilot stage of an electrohydraulic servo-valve. *Comput. Fluids*, 2013; 88: 590-598.

Chu Y, Yuan Z and Chang W. Research on the dynamic erosion wear characteristics of a nozzle flapper pressure servo-valve used in aircraft brake system. *Math. Probl. Eng.* 2020; 2020: 136412.

Chu Y, Yuan Z, He X. and Dong Z. Model construction and performance degradation characteristics of a deflector jet pressure servo-valve under the condition of oil contamination. *Int. J. Aerosp. Eng.* 2021; 2021(5): 8840084.

Ren Y, Yan H, Mao Q, Zuo Z and Hao H. A model-based investigation of the performance robustness of the deflector jet servo-valve. *Appl. Sci.* 2022; 12(20): 10428.

J. Bangladesh Acad. Sci. 50(1); 35-50: March 2026 DOI:https://doi.org/10.3329/jbas.v50i1.86069

Journal of Bangladesh Academy of Sciences

Journal homepage: http://www.bas.org.bd/publications/jbas.html

Research Article

Development of novel blast-resistant wheat lines via X-ray induced mutation breeding

Hossain Sohrawardy[#], Sanjoy Kumar Paul[#], Nur Uddin Mahmud[#], Paritosh Chandra Roy, Abdullah Al Mahbub Rahat, Dipali Rani Gupta and Tofazzal Islam[*]

Institute of Biotechnology and Genetic Engineering, Gazipur Agricultural University, Gazipur, Bangladesh

ARTICLE INFO

Article History

Received: 04 November 2025
Revised: 21 December 2025
Accepted: 29 January 2026

Keywords: X-ray, Physical mutagenesis, Loss-of-function mutants, Blast-resistant variety.

ABSTRACT

Wheat blast, caused by the fungus *Magnaporthe oryzae Triticum* (MoT), poses a severe and escalating threat to global food security, particularly as conventional breeding struggles due to scarce genetic resources and the pathogen's rapid adaptation. In this study, X-ray irradiation-induced mutation breeding was employed to develop novel and durable resistance. Seeds of three high-yielding wheat varieties from Bangladesh: BARI Gom 27 (BG27), BARI Gom 29 (BG29), and BARI Gom 33 (BG33), were treated with a single acute dose of 180 Gy. Following irradiation, preliminary screening of the M2 generation using a Detached Leaf Assay (DLA) identified thirty fully resistant lines. To assess the stability and durability of resistance, fourteen selected M2 lines were advanced to the M3 generation and subject to rigorous field screening under artificial MoT inoculation in a blast-endemic environment. This critical field evaluation identified eight superior mutant lines, including BG27(X180)-8-4, BG27(X180)-8-5, and four lines derived from the BG33(X180)-98 series, all of which exhibited complete immunity (0% disease incidence and 0% disease severity) to MoT. To the best of our knowledge, this is the first report of completely blast-resistant M3 wheat lines identified through large-scale, open-field screening using X-ray induced mutagenesis of three high-yielding varieties. These resistant M3 lines represent an invaluable and readily deployable genetic resource for the rapid development of durable, blast-resistant wheat cultivars. Such advancements are crucial for mitigating the growing threat of wheat blast in high-risk regions, including Bangladesh, Zambia, and parts of South America. A further multi-location field trials and genomic analyses of the mutant lines are essential to ensure their stability for deployment as blast-resistant wheat variety, and identify the loss-of-function mutation(s) useful for marker development for molecular breeding.

Introduction

Wheat (*Triticum aestivum* L.) is one of the most important cereal crops worldwide, serving as a primary food source for billions of people. However, its productivity is increasingly threatened by diverse biotic and abiotic stresses. Among these, wheat blast caused by the *Magnaporthe oryzae Triticum* (MoT) pathotype has emerged as a rapidly spreading and highly destructive fungal disease, posing a major challenge to global food security (Islam et al., 2016; 2020). First reported in Brazil in 1985 (Igarashi et al., 1986), the disease spread aggressively throughout

[*]Corresponding author: tofazzalislam@gau.edu.bd, [#]Equally contributed.

South America (Bhattacharjee et al., 2025). A major shift occurred in 2016 when a severe epidemic hit Bangladesh, inflicting up to 100% yield losses on 15,000 hectares of wheat fields (Islam et al., 2016). By 2018, MoT was also detected in Zambia (Tembo et al., 2020). Genomic studies confirmed that the Bangladesh and Zambia outbreaks were caused by the South American B71 clonal lineage, indicating long-distance transboundary introduction through grain trade and highlighting the pathogen's alarming capacity for intercontinental spread (Latorre et al., 2023).

Conventional breeding programs have achieved some progress toward wheat blast resistance; however, the frequent emergence of new pathogen races and MoT's high evolutionary potential continue to undermine the development of durable resistance. Currently, only a limited number of partial resistance sources are available, many of which are temperature- or race-sensitive and thus lack resilience (Islam et al., 2020). To date, only a single major resistance gene, *Rmg8*, has been successfully cloned (Asuke et al., 2024), and identifying new resistance genes in wheat remains a major challenge due to its large and complex genome, significantly slowing down progress and increasing cost (Wang et al., 2025). Therefore, the diversification of the resistance gene pool is not only important but also urgently required to secure global wheat production in vulnerable regions, particularly across South Asia and Africa (Anh et al., 2018).

Induced mutagenesis represents a powerful and promising alternative for rapidly generating novel blast-resistant germplasm. Physical mutagenesis methods, such as X-ray irradiation, have long been recognized for their ability to introduce a broad spectrum of genetic alterations, including point mutations, deletions, insertions, inversions, and chromosomal rearrangements, ultimately creating useful phenotypic diversity for crop improvement (Bordoloi et al., 2024). Globally, mutation breeding has already contributed to the release of more than 3,000 crop cultivars (FAO/IAEA**,** 2018). Importantly, this approach facilitates the development of improved varieties without genetic transformation, making it particularly relevant for regions with strict genetically modified organism (GMO) regulatory frameworks. Furthermore, desired traits can emerge rapidly in the M2 generation, significantly shortening the breeding timeline for improved resistance and agronomic performance (Chavez and Kohli, 2020).

In Bangladesh, where most high-yielding wheat cultivars remain alarmingly susceptible to blast, the development of durable MoT resistance is critically vital to sustain national wheat production and prevent future catastrophic yield losses as the disease spreads to major wheat-growing areas. Based on this compelling regional and global need to diversify genetic resistance sources, the present study employed X-ray irradiation to induce genetic variation in three elite wheat varieties of Bangladesh, viz. BARI Gom 27 (BG27), BARI Gom 29 (BG29), and BARI Gom 33 (BG33). The primary objective of this work was to screen and identify stable mutant lines exhibiting complete and durable blast resistance through rigorous field-based artificial inoculation with MoT fungus. By expanding the functional resistance gene pool, this work aims to directly contribute to the development of resilient wheat varieties suitable for MoT-endemic agro-ecosystems in Bangladesh and elsewhere.

Materials and Methods

Mutagenesis of wheat seeds

Three elite wheat varieties developed by the Bangladesh Agricultural Research Institute (BARI), namely BARI Gom 27, BARI Gom 29, and BARI Gom 33, were selected for mutation breeding to develop blast-resistant lines. In November 2019, X-ray irradiation was utilized as a physical mutagenic agent, provided by the International Atomic Energy Agency (IAEA) in Vienna, Austria. Based on established literature and prior experimental results, a single 180 Gy dose was applied to the seeds of three wheat varieties. This dosage was selected because levels exceeding 200 Gy are known to be lethal for wheat (Ylli et al., 2024).

Exactly, 500 seeds from each of the three varieties were treated with X-ray. The mutagenesis and screening scheme for blast-resistant mutant lines is depicted in Fig. 1. Wheat seeds obtained from the Bangladesh Agricultural Research Institute (BARI) were transported to the International Atomic Energy Agency (IAEA) in Vienna, Austria, for X-ray irradiation. Following treatment, the M1 seeds were returned to the Institute of Biotechnology and Genetic Engineering (IBGE) at Gazipur Agricultural University (GAU), Gazipur. The seeds were shipped in dry condition and maintained at room temperature throughout transit.

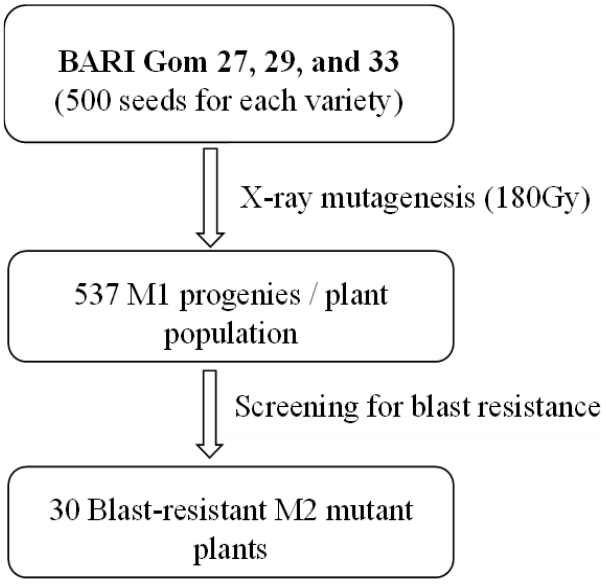

Fig. 1. Scheme of mutagenesis and development of blast-resistant M2 wheat mutant lines.

Research site, breeding methods and agronomic practices

Field experiments were conducted at the research field of Gazipur Agricultural University (GAU) (24.0360° N, 90.3962° E), Bangladesh, and a farmer's field in the blast-prone area of Meherpur (23.7750°N, 88.6417°E) district in south-western Bangladesh. Laboratory work was carried out at the Institute of Biotechnology and Genetic Engineering Laboratory at GAU. The single spike-to-line sowing method was employed for advancing generations. Seeds were sown annually in November, which marks the wheat-growing season in Bangladesh. For the M1 population, seeds were sown with a 3 cm spacing. For the M2 generation, plant spacing was set at 20 cm, and row-to-row distance was maintained at 25 cm. Recommended doses of fertilizers, including Urea (220 kg/ha), TSP (150 kg/ha), MP (100 kg/ha), and Gypsum (100 kg/ha), were applied (BARC, 2012). Two-thirds of the urea and all other fertilizers were applied as basal at the final land preparation. In contrast, the remaining one-third of the urea was top-dressed during the first irrigation (17-20 days after sowing). The first irrigation was light, with excess water drained immediately. Second and third irrigations were applied at the maximum tillering stage (50-55 DAS) and the early stage of grain filling (70-80 DAS), respectively. Weeding was performed manually throughout the wheat growing period. To protect the mutant population from avian damage, a significant risk due to variation in maturity rates, nylon netting was installed as a physical barrier.

Field bioassay

For the bioassay, *M. oryzae Triticum* (MoT) isolate, BTJP-4(5) cultures were incubated for 6 days at 25°C (Gupta et al. 2020). Subsequently, mycelium was gently scraped from the culture plate to promote conidia formation. Twenty-four hours later, the plate was washed with 3–5 mL of sterile distilled water, to which two drops of Tween 20 per liter were added to release the spores. The resulting conidial suspension was filtered through two layers of cheesecloth and adjusted to a concentration of 5×10^4 conidia mL^{-1}.

Recording of data, measurement of disease intensity and severity

Germination rates were recorded from M1 progenies. M2 resistant lines were selected using Detach Leaf Assay (DLA) while disease intensity and severity were assessed in M3 mutant progenies. Data on the number of total tillers, effective tillers, infected tiller $hill^{-1}$, entire length, and infected part of spike, seeds $spike^{-1}$, 1000 grain weight, and grain yield $hill^{-1}$ were gathered during the reproductive period of M3 progenies. During the vegetative phase, data were recorded for the total number of seedlings, the number of infected seedlings per pot, total leaf length, and the length of the infected leaf area. To

evaluate disease intensity, wheat blast, a devastating fungal infection caused by MoT, was scored.

The disease intensity (DI) was calculated using the formula:

DI=(Total number of infected plants)/
(Total number of plants observed) × 100

Similarly, blast disease severity was assessed on a five-scale basis, representing the percentage of infection affecting the length of the spike: 0 = No lesions; 1 = 1–25% infection; 2 = 26–50% infection; 3 = 51–75% infection; 4 = 76–100% of the length of the spikes infected by the blast (Suryadi et al., 2013; Goddard et al., 2020). Disease Severity (DS) was calculated as:

$DS = (n \times v)/(N \times V) \times 100\%$

Where, DS = disease severity, n = number of spikes infected by the blast, v = value score corresponding to the category of attack, N = total number of spikes observed, and V = value representing the highest score.

Detached Leaf Assay (DLA)

Wheat leaves were detached from five-leaf stage seedlings and placed in plates lined with moist paper towels. Then, detached leaves were inoculated with 1 µl of a conidial suspension containing 1×10^5 MoT conidia/mL, followed by incubation of the plates at 25˚C under 100% relative humidity in the dark for the first 24 h, and thereafter at 24 ℃ under a 16 h/8 h light-dark photoperiod. At 6 days post inoculation [dpi] leaves were scored for disease symptoms using a 0–6 scale (0 = no visible symptoms, 1 = pin-point brown necrotic lesions, 2 = brown necrotic lesions across the leaf, 3 = brown necrotic lesions and mild chlorosis of the leaf, 4 = grey lesions ringed with necrosis and chlorosis, 5 = extensive grey lesions and chlorosis across the leaf, 6 = grey sporulating lesions and water soaking across the entire leaf. The test was performed three times independently, with 3 replicate samples per run. The resulting length of wheat blast lesions, MoT, was measured from 3 leaves per experiment for each treatment.

Design of experiment and statistical analysis

The experiments in the laboratory and field conditions were performed using a completely randomized design (CRD) and a randomized complete block design (RCBD), respectively, to identify resistant mutant lines against wheat blast compared to parental lines. Data analysis and visualization were performed using RStudio 2025.05.1 and Microsoft Office Excel 2015, which provided a flexible and powerful environment for handling datasets and generating informative graphical representations.

Results

Germination of X-ray irradiated seeds

Five hundred X-ray irradiated seeds for each variety (BARI Gom 27, BARI Gom 29 and BARI Gom 33) were sown in the field. Among these, BARI Gom 27, BARI Gom 29 and BARI Gom 33 of X-ray irradiated seeds were germinated with 32, 75, and 430 seeds, respectively. In total 537 M1 plants (35.8%) successfully survived, indicating that the irradiation doses effectively induced viable mutants. The remaining plants succumbed to lethal doses. Observable variations among surviving plants compared to the control further confirmed the successful induction of mutations by X-ray irradiation, as shown in Fig. 2.

As depicted in Fig. 3, control plants consistently exhibited the highest seed germination (98%) rates compared to all mutant populations. Among the treated varieties, BARI Gom 27, irradiated with 180 Gy, showed the lowest germination rate (6%). On the other hand, 15% and 86% of M1 seeds of BARI Gom 29 and BARI Gom 33, respectively, were germinated under field conditions. Despite the overall reduction, a considerable number of seeds germinated at 180 Gy highlighting the potential for successful mutagenesis without complete loss of viability. Genotypic variations in tolerance to irradiation were clearly observed. For instance, BARI Gom 33 maintained significantly higher seed germination rate (86%) of M1 seeds.

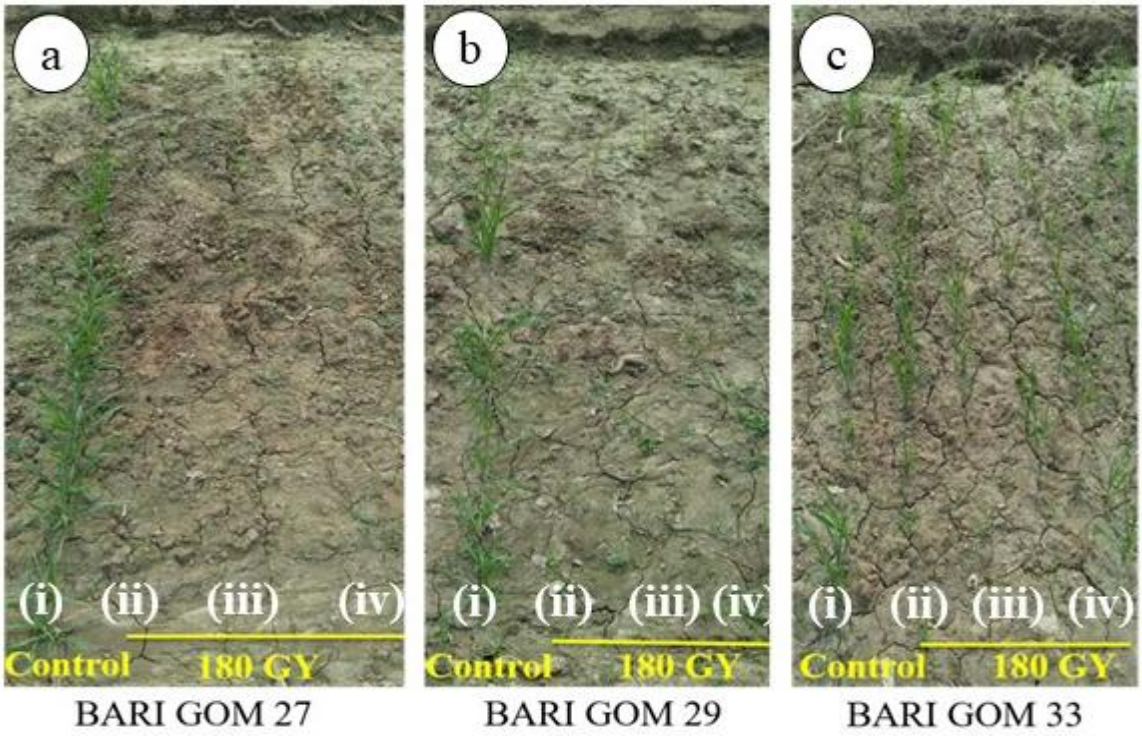

Fig. 2. Germination percentage of M0 (control) and M1 of wheat varieties. (a) BARI Gom 27, (b) BARI Gom 29, (c) and BARI Gom 33 under field conditions, 14 days after sowing. i) M0 seeds (Control), ii), iii) and iv) M1 seeds irradiated at 180Gy.

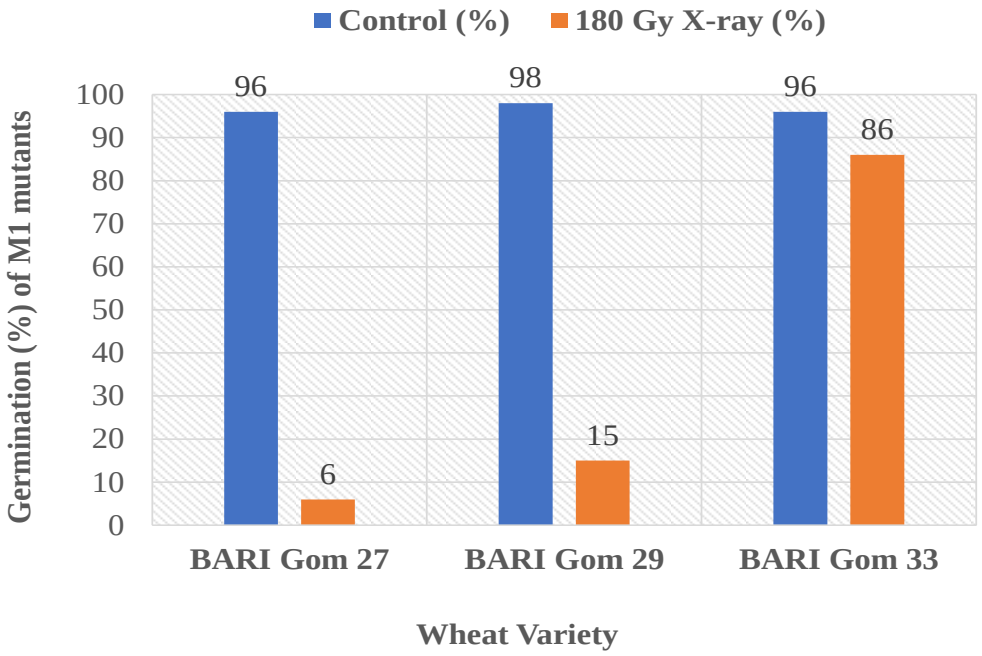

Fig. 3. Germination percentages of 180Gy dose of X-ray irradiation applied to wheat seeds of three varieties of Bangladesh.

Screening for resistance against wheat blast in X-ray irradiated M2 progenies using the Detach Leaf Assay (DLA) technique

A disease assay was performed on the M2 population derived from 180 Gy X-ray irradiation of three wheat varieties to evaluate initial resistance to the wheat blast pathogen under controlled conditions. From the previously selected lines, 537 individual plants were selected for *in vitro* screening using the Detached Leaf Assay (DLA) based on superior phenotypes. The majority of the tested progenies exhibited susceptibility. Specifically, BARI Gom 27 showed 67.7% susceptibility and 32.3% resistance. BARI Gom 29 recorded 86.7% susceptible and 13.3% resistant plants. BARI Gom 33 displayed the highest level of vulnerability, with 97.7% of plants categorized as susceptible and only 2.3% as resistant. Notably, no plants showed a moderately resistant reaction across any of the tested varieties. Detailed DLA results for these 537 M2 mutant progenies are summarized in Table 1.

The overall results suggested that although the frequency of resistance was low, irradiation generated useful variability and enabled the identification of resistant individuals within the M2 populations. These resistant plants were advanced for further phenotypic evaluation and stability testing in subsequent generations. A visual representation of the DLA is illustrated in Fig. 4.

Table 1. The results of DLA of X-ray (180Gy) irradiated M2 progenies grown in the field and bioassayed for disease resistance of leaves in controlled conditions.

Wheat Varieties	Number of Plant Screened	Susceptible (S)	Moderately Resistant (MR)	Resistant (R)
BARI Gom 27	32	21	0	10
BARI Gom 29	75	65	0	10
BARI Gom 33	430	421	0	10

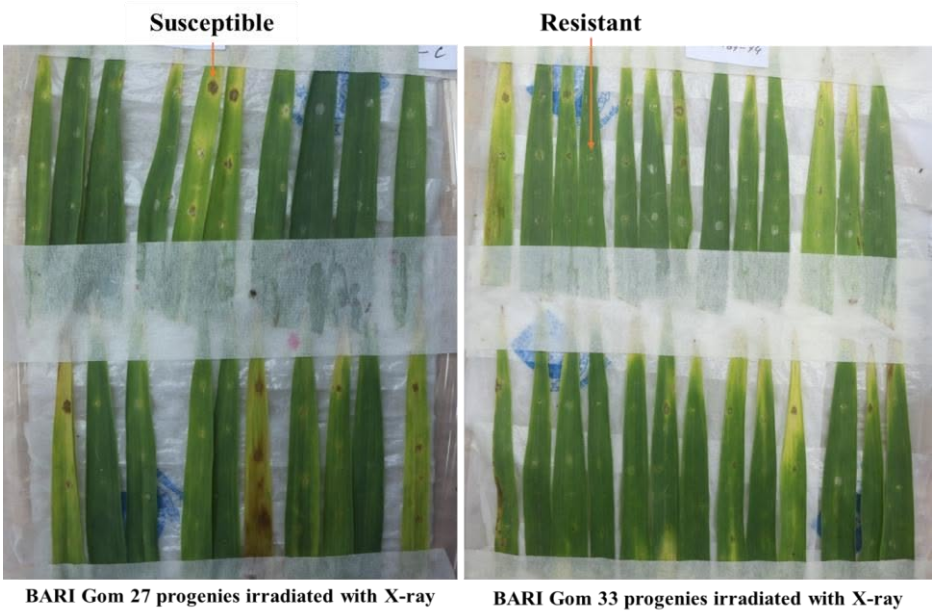

Fig. 4. Leaf-assay of X-ray irradiated M2 progenies in the laboratory.

Field evaluation of X-ray induced mutants of BARI Gom 27 against wheat blast

Field screening under artificial inoculation conditions revealed a wide range of variation among the M2 mutants of BARI Gom 27 in relation to blast disease response and agronomic performance (Table 2). The control variety BARI Gom 27 exhibited high susceptibility, with a disease incidence (DI) of 84.21% and disease severity (DS) of 50%, indicating strong pathogen pressure in the test environment. In contrast, all evaluated X-ray mutants showed complete resistance to wheat blast, as demonstrated by 0% infected spikes, DI, and DS values. Among the resistant mutants, several lines displayed significant improvement in yield-contributing traits. Mutants BG27(X180)-28 and BG27(X180)-31 exhibited the highest number of total and effective tillers per hill (43 and 47 tillers, respectively), whereas BG27(X180)-14 recorded the tallest plants (107 cm). Additionally, spike length ranged from 11 cm to 18 cm, with BG27(X180)-11 producing the longest spikes. These findings confirm that X-ray mutagenesis successfully generated wheat blast-resistant genotypes while simultaneously improving yield-related traits. Such elite mutants represent promising materials for advancement through subsequent generations and potential inclusion in future varietal development pipelines.

Table 2. X-ray irradiated M2 mutants of BARI Gom 27 showed in suppression of wheat blast disease development in artificially inoculated wheat field.

Sl. No.	Control/ Mutant	Plant height (cm)	Total tillers/hill	Effective tillers/hill	Spike length (cm)	Infected spike	DI (%)	DS (%)
1	BARI Gom 27	93	19	16	10	8	84.21	50
2	BG27(X180)-8	80	16	14	15	0	0	0
3	BG27(X180)-9	82	12	8	16	0	0	0
4	BG27(X180)-10	94	30	30	11	0	0	0
5	BG27(X180)-11	83	14	12	18	0	0	0
6	BG27(X180)-14	107	23	20	11	0	0	0
7	BG27(X180)-16	90	14	12	15	0	0	0
8	BG27(X180)-21	98	29	27	11	0	0	0
9	BG27(X180)-28	94	43	43	12	0	0	0
10	BG27(X180)-30	77	12	10	16	0	0	0
11	BG27(X180)-31	88	47	47	12	0	0	0

DI: Disease Intesity; DS: Disease Severity.

Field evaluation of X-ray induced mutants of BARI Gom 29 under artificial inoculation

The M2 mutants derived from BARI Gom 29 showed substantial improvement in wheat blast disease suppression along with desirable agronomic characteristics under artificially inoculated field conditions (Table 3). The control variety BARI Gom 29 exhibited high disease incidence (80%) and moderate disease severity (37.5%), confirming susceptibility to blast pressure in the screening environment. In contrast, all evaluated X-ray mutants expressed complete resistance to wheat blast, reflected by zero infected tillers, DI, and DS values. Significant improvements in tiller productivity and spike traits were also observed. Mutant BG29(X180)-17 recorded the highest total tiller count (31) and effective tiller count (29), while BG29(X180)-58 also produced a remarkably high total tiller count (36). Spike length varied between 11 cm and 21 cm, with BG29(X180)-43 producing the longest spikes.

Improved plant height was noted in multiple mutants, especially in BG29(X180)-23 and BG29(X180)-17 (108 cm and 107 cm, respectively), surpassing the control. These findings suggest that X-ray mutagenesis effectively generated resistant, high-performing genotypes with enhanced yield attributes. Such elite M2 mutants demonstrate promising potential for further evaluation and varietal development.

Table 3. X-ray irradiated M2 mutants of BARI Gom 29 showed in suppression of wheat blast disease development in artificially inoculated wheat field.

Sl. No.	Control /Mutant	Plant height (cm)	Total tillers/hill	Effective tillers/hill	Spike length (cm)	Infected tillers	DI (%)	DS (%)
1	BARI Gom 29	94	20	16	10	6	80	37.5
2	BG29(X180)-17	107	31	29	11	0	0	0
3	BG29(X180)-19	86	13	9	15	0	0	0
4	BG29(X180)-23	108	25	23	13	0	0	0
5	BG29(X180)-29	83	12	9	16	0	0	0
6	BG29(X180)-30	88	24	23	18	0	0	0
7	BG29(X180)-31	101	21	18	14	0	0	0
8	BG29(X180)-43	80	12	9	21	0	0	0
9	BG29(X180)-47	80	13	10	15	0	0	0
10	BG29(X180)-48	96	23	23	11	0	0	0
11	BG29(X180)-58	94	36	36	13	0	0	0

DI: Disease Intesity; DS: Disease Severity.

Field Performance of X-ray induced mutants of BARI Gom 33 under wheat blast inoculation

The M2 population of BARI Gom 33 developed through X-ray irradiation exhibited substantial improvements in wheat blast resistance and agronomic traits under artificial inoculation (Table 4). The control BARI Gom 33 showed noticeable susceptibility, recording 16.67% disease incidence and 6.39% disease severity, confirming that the environment was suitable for disease expression.

However, all eleven evaluated mutants demonstrated complete resistance, as reflected by zero infected tillers, DI, and DS values. Enhanced agronomic performance was also evident among several mutants. The maximum plant height was observed in BG33(X180)-347 (117 cm) and BG33(X180)-365 (116 cm). Whereas, BG33(X180)-13 and BG33(X180)-15 were comparatively shorter. Spike length varied between 12 cm and 21 cm, with BG33(X180)-33 producing the longest spikes. Additionally, BG33(X180)-365 produced the highest number of effective tillers (9) among the evaluated mutants. These results indicate that X-ray mutagenesis successfully generated multiple resistant mutants with improved yield-related features. The identified mutants are promising candidates for future selection and advancement in wheat blast-resistant breeding programs.

Table 4. X-ray irradiated M2 mutants of BARI Gom 33 showed in suppression of wheat blast disease development in artificially inoculated wheat field.

Sl. No.	Control/ Mutant	Plant height (cm)	Total tillers/hill	Effective tillers/hill	Spike length (cm)	Infected tillers	DI (%)	DS (%)
1	BARI Gom 33	107	8	6	15	1	16.67	6.39
2	BG33(X180)-13	87	9	7	17	0	0	0
3	BG33(X180)-15	87	8	7	15	0	0	0
4	BG33(X180)-33	104	9	6	21	0	0	0
5	BG33(X180)-34	97	8	6	19	0	0	0
6	BG33(X180)-98	114	9	7	16	0	0	0
7	BG33(X180)-137	104	9	7	12	0	0	0
8	BG33(X180)-279	97	8	8	18	0	0	0
9	BG33(X180)-322	112	9	6	17	0	0	0
10	BG33(X180)-347	117	8	7	15	0	0	0
11	BG33(X180)-365	116	9	9	14	0	0	0

DI: Disease Intesity; DS: Disease Severity.

Stability and yield trials of X-ray irradiated M3 progenies

To assess the performances of the M3 mutant lines, a field trial was conducted compared with the unmutated parent. These findings highlight the potential of forward mutagenesis for improving wheat blast resistance and emphasize the importance of advancing selected lines to later generations (M3) for stability and yield trials. Based on bioassay result, we selected fourteen suitable mutant lines from 750 mutants of BARI Gom 27, BARI Gom 29, and BARI Gom 33. The rest of the mutants from BARI Gom 27, BARI Gom 29, and BARI Gom 33 were discarded due to their susceptibility against wheat blast. The field views of screening for resistance to wheat blast, as well as the yield trial of Gy-irradiated M3 progenies, are shown in Fig. 5. At the end of the experiment, crop residues were burnt to prevent further unexpected expansion of the devastating disease. Crucially, fourteen M3 plants demonstrated resistance against blast infection e.g., BG27(X180)-8-4, BG27(X180)-8-5, BG27(X180)-30-3, BG27(X180)-30-10, BG29(X180)-17-5, BG29(X180)-17-6, BG29(X180)-17-7, BG29(X180)-58-5, BG33(X180)-98-4, BG33(X180)-98-5, BG33(X180)-98-6, BG33(X180)-98-7, BG33(X180)-347-8, and BG33(X180)-347-9.

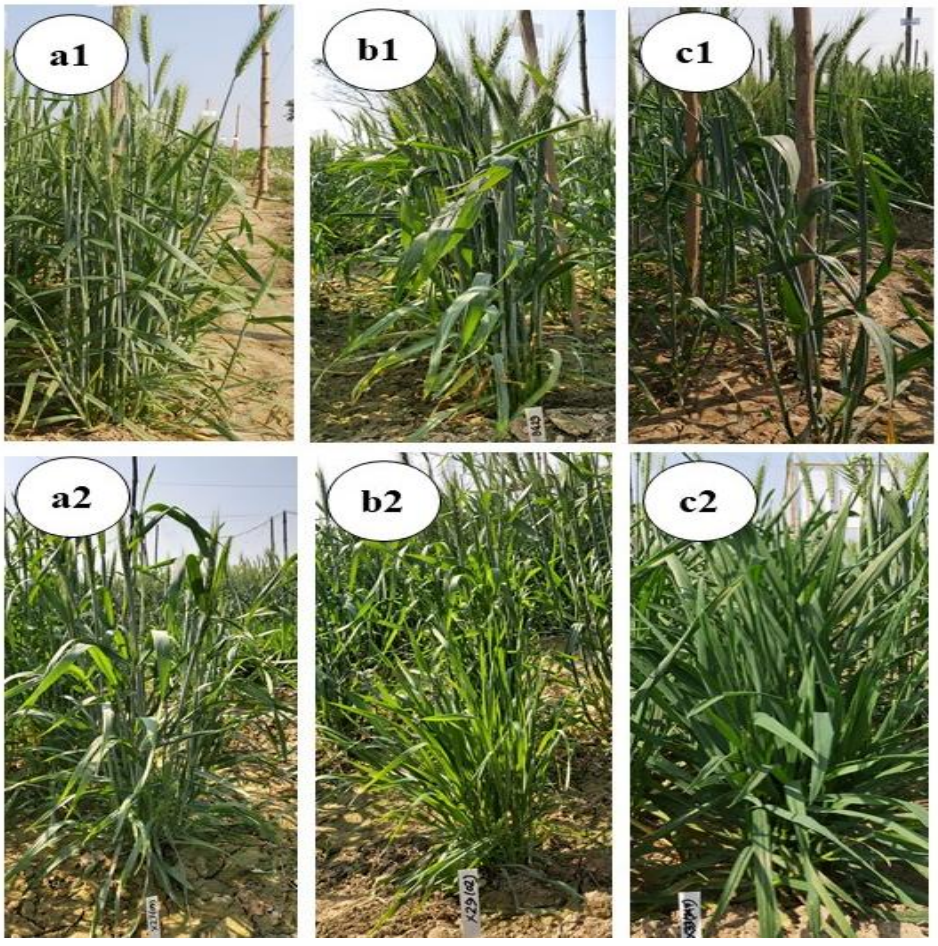

Fig. 5. Variations in plant height and tillering morphology in X-ray mediated wheat mutant populations during M2 generation in field condition. a2, b2, and c2 are mutants of BARI Gom 27, BARI Gom 29, and BARI Gom 33 respectively. a1, a2, and c1 represent as parental lines of BARI Gom 27, BARI Gom 29, and BARI Gom 33 respectively.

Infection manifested as whitening of the spike, usually from the top, on the growing heads of wheat plants during the pre-heading stage in the farmer's fields of Meherpur. On the developing head, infection also occurred at random in various locations, such as the centre, next the tip, or at the base. It was frequently noted that bleaching happened from top to bottom, regardless of the infection site. This indicates that an infection at the base would cause the entire spike to bleach, an infection close to the top would bleach the spike from the top to the point of infection, and an infection in the centre would bleach half of the spike from the top. However, over time, the entire spike in all cases turned silvery white, i.r., completely bleached, as shown in Fig. 6.

Effect of X-ray irradiation on the yield components of the selected plants at the M3 generation

Seventeen wheat genotypes, including three checks (BARI Gom 27, BARI Gom 29, and BARI Gom 33) and fourteen X-ray induced mutant lines, were evaluated for their agronomic and blast disease response traits (Table 5). Significant variation was observed among the genotypes for all studied parameters.

Plant height ranged from 82 cm to 121 cm, where the mutant line BG33(X180)-347-8 and BG33(X180)-347-9 exhibited the tallest plants (121 cm), while BG27(X180)-30-10 produced the shortest plants (82 cm). Variation in tillering ability was also prominent. The highest total and effective tiller counts per hill were recorded in BG27(X180)-8-5 (24 and 22, respectively), indicating improved tiller productivity compared with its control BARI Gom 27. Spike length varied from 12 cm in BG33(X180)-98-7 to 23 cm in BG33(X180)-347-9**,** with several mutant lines showing longer spikes than their corresponding controls. Thousand-grain weight displayed marked improvements in mutants, with BG27(X180)-30-3 and BG33(X180)-347-9 recordeding the highest values (53.89 g and 49.63 g, respectively), outperforming the control varieties.

A substantial reduction in infected tillers was observed in most mutants of BARI Gom 27 and BARI Gom 33, where multiple genotypes showed complete absence of infected tillers and zero blast infection (DI = 0% and DS = 0%). Notably, BG27(X180)-8-4**,** BG27(X180)-8-5**,** BG27(X180)-30-3**,** BG27(X180)-30-10**,** and four mutants of BARI Gom 33 revealed complete resistance to wheat blast under field conditions. On the other hand, the control varieties exhibited high susceptibility to blast disease, particularly BARI Gom 27 with DI 91.67% and DS 79.80%. Among the BARI Gom 29 mutants, disease incidence and severity were reduced but not completely eliminated; BG29(X180)-58-5 showed the lowest infection within this cluster (DI 14.29%, DS 1.28%). Overall, the study identified several promising mutant lines combining higher yield-related traits with improved blast resistance. Specifically, BG27(X180)-8-5**,** BG27(X180)-30-3**,** and BG33(X180)-98-5 were noteworthy for superior tillering, spike length, grain weight, and complete disease resistance, indicating their strong potential in future breeding and varietal advancement programs.

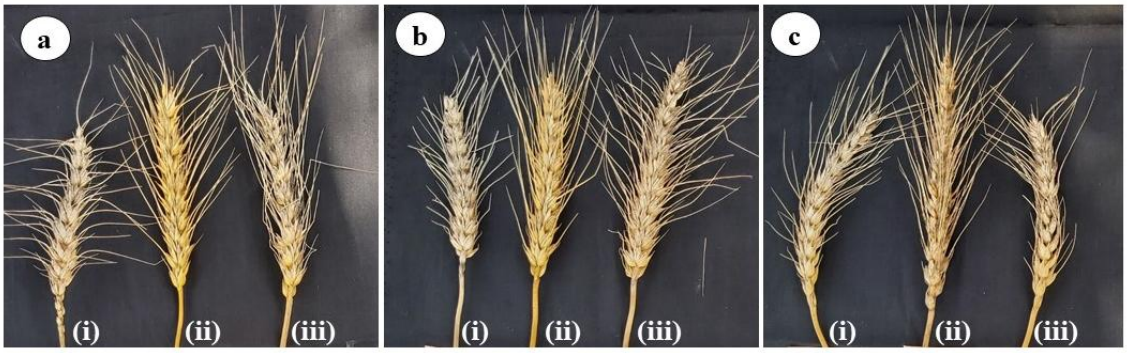

Fig. 6. Pictorial comparison of mutant lines with untreated parents. Resistant reaction indicates by the bright golden color free from gray colored conidial presence in the spikelets. (a), (b) and (c) shows BARI Gom 27, BARI Gom 29, and BARI Gom 33 respectively. In each case, middle one (ii) is the mutant. Conversely, (i) and (iii) are the parental lines.

Table 5. Effect of X-ray irradiation on yield components and suppression of wheat blast disease development of the selected plants from the M3 generation of the BARI Gom 27, BARI Gom 29, and BARI Gom 33 respectively under field conditions.

Sl. No.	Control/ Mutant	Plantheight (cm)	Total tillers/hill	Effective tillers/hill	Spike length(cm)	Infected tillers/hill	1000grain weight	DI (%)	DS (%)
1	**BARI Gom 27**	**98**	**16**	**12**	**15**	**11**	**30.45**	**91.67**	**79.80**
2	BG27(X180)-8-4	87	19	18	14	0	47.46	0.00	0.00
3	BG27(X180)-8-5	93	24	22	13	0	49.54	0.00	0.00
4	BG27(X180)-30-3	91	21	20	16	0	53.89	0.00	0.00
5	BG27(X180)-30-10	82	19	19	15	0	51.23	0.00	0.00
6	**BARI Gom 29**	**100**	**19**	**18**	**16**	**14**	**32.17**	**77.78**	**65.14**
7	BG29(X180)-17-5	96	15	12	16	3	46.15	25.00	3.08
8	BG29(X180)-17-6	98	13	11	15	4	46.35	36.36	4.52
9	BG29(X180)-17-7	88	18	16	17	4	42.16	25.00	4.38
10	BG29(X180)-58-5	84	14	14	17	2	48.97	14.29	1.28
11	**BARI Gom 33**	**110**	**7**	**6**	**19**	**3**	**38.58**	**50.42**	**47.69**
12	BG33(X180)-98-4	102	8	7	18	0	42.48	0.00	0.00
13	BG33(X180)-98-5	105	9	7	18	0	47.58	0.00	0.00
14	BG33(X180)-98-6	101	9	6	17	0	45.63	0.00	0.00
15	BG33(X180)-98-7	100	8	6	12	0	49.25	0.00	0.00
16	BG33(X180)-347-8	121	11	11	20	3	46.26	27.27	1.81
17	BG33(X180)-347-9	121	12	11	23	2	49.63	18.18	0.93

DI: Disease Intesity; DS: Disease Severity.

Principal Component Analysis (PCA) for X-ray irradiated M3 progenies

In the present study, principal component analysis was conducted using seven agromorphological and disease-related traits of wheat genotypes to determine their contribution to overall phenotypic variation. The first two principal components (PC1 and PC2) explained 46.6% and 35.4% of the total variation, respectively, accounting for 82.0% of the cumulative variability (Fig. 7).

PC1 was strongly and positively associated with disease index (DI), disease severity (DS), and infected tillers, indicating that genotypes positioned on the positive axis of PC1 were more susceptible to blast disease. Conversely, effective tillers and total tillers showed a negative loading toward PC1, suggesting these yield-related traits contributed to tolerance. PC2 was primarily influenced by plant height and spike length, which were positively loaded, while thousand-grain weight contributed less strongly along this axis. Genotypes with higher PC2 scores were characterized by better plant architecture traits.

The biplot separated the genotypes into distinct groups. Several mutant lines were positioned in the negative PC1 and positive PC2 quadrants, exhibiting desirable agronomic traits, such as increased effective tillers and improved spike length, while maintaining reduced blast infection levels. In contrast, a few genotypes located on the positive PC1 axis showed higher disease incidence, indicating susceptibility (Fig. 7).

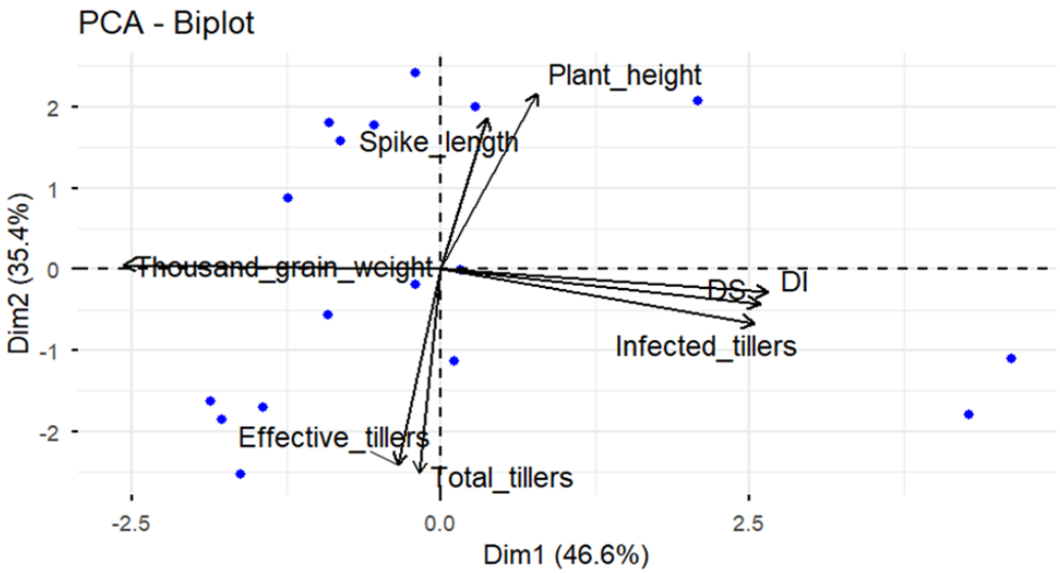

Fig. 7. Principal component analysis for X-ray irradiated M3progenies.

Discussion

The success of mutation breeding hinges on balancing the rate of mutation induction with subsequent plant survival and fertility (Bado et al., 2015; Hassine et al., 2023). In the current study, we demonstrated that X-ray irradiation at 180 Gy effectively induced genetic variation in three elite wheat varieties of Bangladesh for the critical trait of blast resistance. Consistent with established literature on radiation mutagenesis (Hassine et al., 2023), we observed a drastic decline in seed germination and survival across wheat varieties due to irradiation of seeds with 180Gy of X-ray, except BARI Gom 33 (Verma et al., 2017), suggesting that the dose successfully approached the lethal threshold necessary to induce significant chromosomal and genetic alterations. The observed genotypic variation in tolerance, exemplified by BARI Gom 33 maintaining relatively higher germination, underscores the importance of optimizing mutagenic doses on a cultivar-specific basis for a robust mutation breeding program. The resulting phenotypic variability among the surviving M1 and M2 progeny confirmed the successful induction of heritable mutations in wheat for screening for blast resistance (Bado et al., 2015; Hassine et al., 2023; Rana et al., 2025). The current study, encompassing both field and laboratory screening, represents the first identification of several blast-resistant, high-yielding M3 mutant lines. These promising lines serve as valuable genetic resources for developing durable resistance against the destructive wheat blast disease.

Field-validated complete resistance and novelty in M3 genotypes

The ultimate goal of our study was to identify mutant lines with stable, durable resistance to the highly destructive wheat blast fungus, *M. oryzae Triticum* (MoT). The initial M2 Detached Leaf Assay (DLA) served as a high-throughput, preliminary screen (Suryadi et al., 2013), identifying individuals with strong seedling-stage resistance, albeit at a low frequency (e.g., only 2.3% resistance in BARI Gom 33). The identification of these resistant lines in the M2 population, which is a typically segregating generation, suggested the action of stable, strong-effect induced mutations. To rigorously validate the stability and durability of this resistance, 14 selected lines were advanced to field screening at high artificial MoT inoculation pressure in the M3 generation.

Our M3 field trial results represent the most significant novelty of this study: eight superior mutant lines derived from BARI Gom 27 and BARI Gom 33 [e.g., BG27(X180)-8-4, BG33(X180)-98-7, and others] exhibited complete immunity, recording 0% disease incidence (DI) and 0% disease severity (DS) against MoT (Table 5). This outcome contrasts sharply with the high susceptibility observed in the control parents, where BARI Gom 27 showed a DI of 91.67% and a DS of 79.80%. This achievement is a landmark, as it is the first reported successful identification of completely immune M3 plants generated from a large-scale, open-field screen utilizing X-ray-induced mutagenesis in these elite wheat varieties of Bangladesh. This complete, stable, field-level immunity is critical for developing durable resistant varieties, especially given the history of devastating outbreaks in blast-prone regions like Meherpur, Bangladesh (Islam et al. 2016). While physical mutagenesis has been successfully applied to develop resistance to other fungal diseases, such as powdery mildew in blackgram (Tamilzharasi et al., 2023), our success in generating absolute field resistance to MoT provides a uniquely powerful genetic resource.

Simultaneous improvement of resistance and agronomic performance

A core objective of mutation breeding is to ensure that the induced resistance is not linked to detrimental agronomic traits. Our combined M3 screening demonstrated that the resistance was often integrated with superior yield-contributing characters. We used Principal Component Analysis (PCA) to evaluate both disease resistance and yield traits simultaneously, a proven multivariate approach for identifying key selection criteria. The PCA biplot positioned desirable mutants in the quadrant characterized by high agronomic performance (positive PC2, influenced by plant height and spike length) and low disease metrics (negative PC1, strongly associated with total and effective tillers, and inversely related to DI and DS). Specifically, several promising mutant lines successfully combined these desirable traits. For instance, the completely resistant line BG27(X180)-8-5 recorded the highest number of total and effective tillers (24 and 22, respectively), significantly outperforming the control. Furthermore, BG27(X180)-30-3 and BG33(X180)-347-9 recorded the highest thousand-grain weight (53.89 g and 49.63 g, respectively), demonstrating that the induced mutations resulted in beneficial pleiotropic effects or tightly linked positive traits.

In a global context, our findings strongly validate the power of physical mutagenesis as a tool for creating novel resistance in wheat, offering a critical alternative to traditional breeding methods constrained by a limited number of resistance genes (Surovy et al., 2024), such as the recently cloned *Rmg8* (Asuke et al., 2024). The identified M3 mutant lines, which possess complete, stable, field-level immunity, provide an invaluable and immediate genetic resource for national and international wheat breeding programs. The complete resistance observed in these lines offers a unique opportunity for future genomic studies, including targeted transcriptomic analysis of back-crossed populations to map and identify the induced resistance gene(s), providing new insights into the genetic basis of durable resistance against the evolving threat of MoT. Further advancement through selfing and multi-location field trials is the next essential step for developing these elite lines into resilient, commercially viable varieties. Crucially, the discovery of this absolute resistance phenotype offers a unique opportunity for future genomic studies (e.g., MutMap or transcriptomics) to precisely map and identify the underlying induced resistance gene(s), providing new, essential insights into the genetic basis of durable resistance against the evolving global threat of MoT (Wang et al. 2025).

Conclusion

In a global context, our findings strongly validate the power of physical mutagenesis (specifically X-ray irradiation) as a highly effective tool for generating novel and vital resistance traits in elite wheat

cultivars, supporting its long-standing contribution to mutant variety development worldwide. While previous studies have successfully used physical mutagens to engineer resistance to other diseases, such as yellow rust, our research represents a significant step forward: the successful induction and stable identification of eight completely immune M3 mutant lines to the devastating wheat blast fungus (*M.oryzae Triticum*) under rigorous, high-pressure field conditions. These promising M3 lines, which demonstrated 0% disease incidence and 0% disease severity, provide an invaluable and immediate genetic resource for national and international wheat breeding programs. Their stable, complete field resistance will enable the rapid development of durable blast-resistant varieties through continued selfing and/or backcrossing. Comprehensive genomic analysis of the candidate mutants and their respective parents could facilitate the discovery of susceptibility (S) genes and loss-of-function mutations. These findings are essential for developing molecular markers that enable rapid, marker-assisted breeding of blast-resistant wheat varieties.

Acknowledgment

This research article forms part of the PhD dissertation of HS. The author gratefully acknowledges Gazipur Agricultural University for its institutional support. HS also expresses sincere gratitude to the Government of Bangladesh for awarding the prestigious Prime Minister Fellowship, which made this study possible. The authors are thankful to the International Atomic Energy Agency (IAEA) for generously facilitating the irradiation treatment of wheat seeds at its Vienna laboratory. Financial support provided by the IAEA/FAO through a Coordinated Research Contract No. R23030 to TI is also gratefully acknowledged.

Authors contribution

Conceptualization, writing-review, editing, and supervision, TI; investigation, visualization, writing-original draft, and editing, HS, SKP, NUM; methodology and software, HS, AAMR; investigation and formal analysis, HS, SKP, PKP, NUM, DRG; writing-review and editing, project administration, and funding acquisition. All authors read and approved the final manuscript.

Conflict of interest

The authors declare no conflict of interest.

References

Anh VL, Inoue Y, Asuke S, Vy TT, Anh NT, Wang S, Chuma I and Tosa Y. *Rmg8* and *Rmg7*, wheat genes for resistance to the wheat blast fungus, recognize the same avirulence gene *AVR-Rmg8*. *Mol. Plant Pathol.* 2018; 19: 1252-1256.

Asuke S, Morita K, Shimizu M, Abe F, Terauchi R, Nago C, Takahashi Y, Shibata M, Yoshioka M, Iwakawa M and Kishi-Kaboshi M. Evolution of wheat blast resistance gene *Rmg8* accompanied by differentiation of variants recognizing the powdery mildew fungus. *Nat. Plants.* 2024**;** 10: 971-983.

Bado S, Forster BP, Nielen S, Ali AM, Lagoda PJL, Till BJ and Laimer M. Plant mutation breeding: current progress and future assessment. *Plant Breed. Rev.* 2015; 39: 23-88.

Bangladesh Agricultural Research Council (BARC).Fertilizer Recommendation Guide-2012. BARC, Dhaka; 2012.

Bhattacharjee P, Ali J and Islam T. Management of wheat blast disease in Bangladesh caused by *Magnaporthe oryzae* pathotype *Triticum*. *Plant Health Cases*, 2025; phcs20250025.

Bordoloi D, Sarma Dand Das BK. Comparative sensitivity and relative biological effectiveness of gamma-rays, X-rays and electron beams in aromatic Joha rice derived from different locations in Assam state. *Cereal Res. Commun.* 2024; 52: 57-71.

Chavez A and Kohli MM. Screening wheat germplasm for blast resistance: methods and protocols. In: *Wheat Blast*. 1st eds. *CRC Press*; 2020. pp. 149-162.

FAO/IAEA Joint Division. FAO/IAEA international symposium on plant mutation breeding and

biotechnology.Book of Abstracts (IAEA-CN-263). Vienna, Austria, 27-31 August, 2018.

Goddard R, Steed A, Chinoy C, Ferreira JR, Scheeren PL, Maciel JL, Caierão E, Torres GA, Consoli L, Santana FMand Fernandes JM. Dissecting the genetic basis of wheat blast resistance in the Brazilian wheat cultivar BR 18-Terena. *BMC Plant Biol.* 2020; 20(1): 398.

Gupta DR, Surovy MZ, Mahmud NU, Chakraborty M, Paul SK, Hossain MS, Bhattacharjee P, Mehebub MS, Rani K, Yeasmin Rand Rahman M. Suitable methods for isolation, culture, storage and identification of wheat blast fungus *Magnaporthe oryzae Triticum* pathotype. *Phytopathol. Res.* 2020; 2: 30.

Hassine M, Baraket M, Marzougui Nand Slim-Amara H. Screening of the effect of mutation breeding on biotic stress tolerance and quality traits of durum wheat. *Gesunde Pflanzen.* 2023; 75: 837-846.

Igarashi S,Utiamada CM, Igarashi LC, Kazuma AHand Lopes RS. Occurrence of *Pyricularia* sp. in wheat (*Triticum aestivum* L.) in the State of Paraná. *Fitopatol. Bras.*1986; 11: 351-352.

Islam MT, Croll D, Gladieux P, Soanes DM, Persoons A, Bhattacharjee P, Hossain MS, Gupta DR, Rahman MM, Mahboob MGand Cook N. Emergence of wheat blast in Bangladesh was caused by a South American lineage of *Magnaporthe oryzae*. *BMC Biol.* 2016; 14(1): 84.

Islam MT, Gupta DR, Hossain A, Roy KK, He X, Kabir MR, Singh PK, Khan MA, Rahman M and Wang GL. Wheat blast: a new threat to food security. *Phytopathol. Res.* 2020; 2: 28.

Latorre SM, Were VM, Foster AJ, Langner T, Malmgren A, Harant A, Asuke S, Reyes-Avila S, Gupta DR, Jensen Cand Ma W. Genomic surveillance uncovers a pandemic clonal lineage of the wheat blast fungus. *PLoS Biol.* 2023; 21(7): e3002052.

Rana A, Rana V, Bakshi Sand Kumar Sood V. Isolation and characterization of gamma rays induced mutants for improved agro-morphological performance and harder grain texture in wheat (*Triticum aestivum* L.). *Int. J. Radiat. Biol.* 2025; 101: 85-100.

Surovy MZ, Dutta S, Mahmud NU, Gupta DR, Farhana T, Paul SK,Win J, Dunlap C, Oliva R, Rahman Mand Sharpe AG. Biological control potential of worrisome wheat blast disease by the seed endophytic bacilli. *Front. Microbiol.* 2024; 15: 1336515.

Suryadi Y, Susilowati DN, Riana E and Mubarik NR. Management of rice blast disease (*Pyricularia oryzae*) using formulated bacterial consortium. *Emir. J. Food Agric.* 2013; 25: 349-357.

Tamilzharasi M, Kumaresan D, Thiruvengadam V, Jegadeesan, Souframanien J, Latha TKS, Boopathi N Mand Jayamani P. Development and characterization of gamma ray and EMS induced mutants for powdery mildew resistance in blackgram. *Int. J. Radiat. Biol.* 2023; 99(8): 1267-1284.

Tembo B, Mulenga RM, Sichilima S, M′siska KK, Mwale M, Chikoti PC, Singh PK, He X, Pedley KF, Peterson GL, Singh RP and Braun HJ. Detection and characterization of the fungus (*Magnaporthe oryzae* pathotype *Triticum*) causing wheat blast disease on rain-fed wheat (*Triticum aestivum* L.) in Zambia. *PLoS One.* 2020; 15**:** e0238724.

Verma AK, Reddy KS, Dhansekar P and Singh B. Effect of acute gamma radiation exposure on seed germination, survivability and seedling growth in cumin cv. Gujarat Cumin-4. *Int. J. Seed Spices*, 2017; 7: 23-28.

Wang Y, Wang X, Zhang L, Zhakupova K, Ayala F, Ouyang Y, Lu J, Athiyannan N, Wulff BB and Krattinger SG. An optimized disease resistance gene cloning work flow for wheat. *Nat. Commun.* 2025; 16(1): 4904.

Ylli A, Mitrushi F, Elezi F and Ylli F. Optimization of X-ray irradiation dose for induced mutation in bread wheat varieties cultivated in Albania. *Rap Proc.* 2024; 9: 57-62.

J. Bangladesh Acad. Sci. 50(1); 51-58: March 2026 DOI:https://doi.org/10.3329/jbas.v50i1.88771

Journal of Bangladesh Academy of Sciences

Journal homepage: http://www.bas.org.bd/publications/jbas.html

Research Article

Management of legume pod borer, *Maruca vitrata* (Lepidoptera: Crambidae) on yardlong bean using some new generation insecticides

Shammi Aktar, Hasan Fuad El Taj, Md. Abdul Alim and Md. Alamgir Hossain*

Department of Entomology, Faculty of Agriculture, Hajee Mohammad Danesh Science and Technology University, Dinajpur, Bangladesh

ARTICLE INFO

Article History

Received: 07 January 2026
Revised: 29 January 2026
Accepted: 02 February 2026

Keywords: Yardlong bean, Pod borer, Bio-pesticides, Potency.

ABSTRACT

Yard-long bean (*Vigna unguiculata* subsp. *sesquipedalis*) is a protein-rich vegetable widely cultivated in Bangladesh; however, its production is severely hampered by the legume pod borer, *Maruca vitrata*. A field experiment was conducted from February to June 2024 at the Entomology Research Field of Hajee Mohammad Danesh Science and Technology University (HSTU), Dinajpur, using a randomized complete block design (RCBD) to evaluate four selected new-generation insecticides against this pest. The treatments included Spinosad (Tracer 45 SC), Bio-chamak 1% EW (*Celastrus angulatus*), Spinetoram (Delegate 11.7 SC), Azadirachtin 1% EC, and an untreated control. Among the treatment, Spinetoram (Delegate 11.7 SC) @ 0.3 ml L^{-1} consistently resulted in the lowest pod infestation after three applications, reduced infestation by up to 80.56% compared to the control. It also produced the highest yield (9.15 t/ha), with a yield increase of 80.19% and the highest benefit-cost ratio (2.59). Therefore, Spinetoram proved to be an effective and economically viable option for sustainable management of pod borer in yard-long bean cultivation.

Introduction

Legumes are an excellent source of protein in the human diet and are often referred to as the "poor man's meat" (Maphosa and Jideani, 2017). They also serve as valuable green manure crops, high-quality livestock feed, and contribute nitrogen to the soil through atmospheric nitrogen fixation (Cook et al., 2005). Among food legumes, yard long bean (*Vigna unguiculata* subsp. *sesquipedalis*) is widely consumed in Southeast Asia, West Africa, Europe, Oceania, and North America (Malacrino et al., 2019). In Bangladesh, it is extensively cultivated, especially during vegetable shortages, occupying 17,307 ha and producing 28,469 MT in 2018-2019 (BBS, 2024). A 100-g serving provides 50 calories, 9 g carbohydrates, 3 g protein, 0.2 g fat, and is rich in vitamins A, C, thiamin, and riboflavin (Jayasinghe et al., 2015).

Although a summer vegetable, the yard long bean is grown year-round in Bangladesh to meet strong market demand. The crop also has potential for export in both fresh and frozen forms (Mian et al., 2016). Despite this, overall production remains low, failing to meet both domestic demand and international standards. Its cultivation is threatened by multiple insect pests, causing significant economic losses (Oliveira et al., 2014). Among them, the legume pod borer, *Maruca vitrata* F. (Lepidoptera: Crambidae), is the most destructive, causing up to 80% yield losses due to its wide host range, high damage potential, and global distribution (Ali, 2019; Aktar et al., 2020; Margam et al., 2011). Farmers in Bangladesh frequently rely on indiscriminate chemical pesticide applications to rapidly knock down this pest (Ahmed et al., 2020; Aktar et al., 2020).

*Corresponding author: <alamgirhstu@gmail.com>

However, conventional chemical control poses major problems, including ecological imbalance, pesticide resistance, pest resurgence, outbreaks, phytotoxicity, and environmental hazards (Ambethar, 2009; Mweke et al., 2020). Consequently, there is a global shift toward safer, newly formulated insecticides. These modern pesticides are highly selective, effective at low doses, biodegradable, less harmful to beneficial insects, and environmentally safer, making them suitable for sustainable agriculture (Kodandaram et al., 2014). However, research on the use of biorational insecticides for suppressing the yard-long bean pod borer in Bangladesh remains limited. Hence, considering the economic significance of pod borer, a field study was conducted to evaluate four newly formulated insecticides of Spinosad (Tracer 45 SC), Bio-Chamak 1% EW (*Celastrus angulatus*), Azadirachtin 1% EC, and Spinetoram (Delegate 11.7 EC) against *M. vitrata* on yardlong bean.

Materials and Methods

Experimental site and soil preparation

The experiment was conducted at the Research Field of the Department of Entomology, Hajee Mohammad Danesh Science and Technology University (HSTU), Dinajpur, Bangladesh, from February to June 2024. The experimental field was located on medium-high land in Agro-Ecological Zone AEZ-1 (Old Himalayan Piedmont Plain) and characterized by clay loam soil with a pH of 5.52, electrical conductivity (EC) of 2.0 mS m^{-1}, and medium organic matter content (Shil et al., 2016). Seeds of a dwarf yard-long bean variety were procured from the local market of Sadar Upazila, Dinajpur.

The land was ploughed and cross-ploughed several times using a power tiller to achieve a fine tilth, followed by laddering and spading. Before planting, the field was thoroughly leveled, and weeds and crop residues were eliminated. To provide sufficient soil moisture for germination, three seeds were planted in each pit and lightly irrigated. Thinning was done fifteen days after seeding, leaving one healthy plant per pit. A bamboo stick was used to support each plant to prevent lodging. Weeding, irrigation, and plant protection techniques were among the intercultural tasks carried out as needed. Fertilizers were applied according to the Fertilizer Recommendation Guide's suggested dosages (FRG, 2012). A randomized complete block design (RCBD) with three replications, five treatments, and an untreated control was used to set up the experiment. The field was divided into 15 plots. Each unit plot had a single pit measuring 1.0 m × 0.5 m. Plots were kept 0.35 m apart.

Treatments and data collection

The treatments evaluated were T_1 = Spinosad (Tracer 45 SC) @ 0.4 ml L^{-1} of water, T_2 = Bio-Chamak 1% EW (*Celastrus angulatus*) @ 1.5 ml L^{-1} of water, T_3 = Spinetoram (Delegate 11.7 SC) @ 0.3 ml L^{-1} of water, T_4 = Azadirachtin 1% EC @ 1.0 ml L^{-1} of water as well as an untreated control that received just water. A backpack sprayer was used to apply each treatment three times at 15 days intervals. Spraying was done in the late afternoon (about 4:00 pm) to assure pollinator safety. Ten days after flowering, the first spray was applied. During the podding stage, individual pods were harvested 5, 10, and 15 days after each spray. After each spray, data were recorded on the number of healthy pods, the weight of healthy pods, and the percent of pod protection relative to the untreated control.

Economic analysis and benefit-cost ratio

To evaluate the economic feasibility of the treatments, marketable yield data were collected from each pit at every harvest. Based on market-quality attributes, harvested pods were graded, including size, shape, and freedom from defects. Gross return was calculated by multiplying the marketable yield by the prevailing local market price. The benefit-cost ratio (BCR) was computed using the following formula:

BCR = Gross return / Total cost of production (treatment costs + common cost)

Statistical analysis

The LSD test ($p<0.05$) was used to separate the means after the data were statistically examined using Statistix 10 software to determine the significance of variation among the treatments.

Results and Discussion

Effect of treatments against *M. vitrata* on yard long bean after 1st spray

All tested biopesticides significantly reduced *Maruca vitrata* infestation on pods compared with the untreated control after the first spray (Table 1). Among the treatments, spinetoram 11.7% SC applied at 0.3 ml L^{-1} of water recorded the lowest number of infested pods at 1, 5, and 10 days after spraying (DAS), with mean values of 1.93, 1.70, and 1.57, respectively. Conversely, the untreated control showed the highest levels of infestation, with 5.03, 6.80, and 8.57 infested pods during the corresponding observation periods. Statistical analysis revealed highly significant differences among treatments at all intervals (1 DAS: $p < 0.01$, $F = 122.32$, $df = 4$; 5 DAS: $p < 0.01$, $F = 202.61$, $df = 4$; 10 DAS: $p < 0.01$, $F = 332.76$, $df = 4$). After the 1st spray, spinetoram 11.7% SC @ 0.3 ml L^{-1} produced the greatest overall reduction in pod infestation, with a 74.55% over the untreated control.

The current study's findings on spinetoram align with earlier scholars' findings. The best treatment for pod borer, according to Bhuva and Patel (2023), was spinetoram (0.010%), which reduced larval density to 0.33 larvae per plant, limited pod damage to 3.02%, and increased grain output by 46.78% above the control. Similarly, Akbar et al. (2018) reported that spinetoram caused the highest larval mortality (85.71%) of pod borers in chickpea, reducing larval populations to 0.33 per plant and pod damage to 4.62%. These findings confirm the rapid and effective action of Spinetoram against lepidopteran pod borers.

Table 1. Efficacy of tested bio-rational pesticides against *M. vitrata* after 1st spray on yardlong bean.

Treatments	Dose (ml L^{-1}) water	Number of infested pods $plant^{-1}$ after 1st spray				Decrease (%) over control
		1 DAS	5 DAS	10 DAS	Mean	
T_1	0.4	2.46^{c}	2.23^{c}	2.40^{d}	2.37^{c}	65.15
T_2	1.5	3.10^{b}	2.83^{b}	3.13^{c}	3.02^{b}	55.44
T_3	0.3	1.93^{d}	1.70^{d}	1.57^{e}	1.73^{d}	74.55
T_4	1.0	3.30^{b}	2.73^{b}	3.70^{b}	3.24^{b}	52.35
Control	-	5.03^{a}	6.80^{a}	8.57^{a}	6.80^{a}	-
CV (%)	-	5.81	7.58	6.72	4.26	-

T_1 = Spinosad, T_2 = *Celastrus angulatus*, T_3 = Spinetoram, T_4 =Azadirachtin, DAS = Days after spray. Different superscripts indicate differences among the treatment.

Effect of treatments against *M. vitrata* on yardlong bean after the 2nd spray

Following the second spray, all tested biorational insecticides again significantly suppressed pod borer infestation compared with the untreated control (Table 2). Spinetoram 11.7% SC applied at 0.3 ml L^{-1} recorded the lowest number of infested pods at 1, 5, and 10 DAS, with mean values of 1.37, 1.16, and 1.03, respectively. Conversely, the untreated control exhibited the highest infestation levels (5.40, 6.37, and 6.47 pods). These differences were statistically highly significant (1 DAS: $p < 0.01$, $F = 50.64$, $df = 4$; 5 DAS: $p < 0.01$, $F = 147.08$, $df = 4$; 10 DAS: $p < 0.01$, $F = 209.49$, $df = 4$). After the second spray, spinetoram reduced overall pod infestation by 80.56% compared to the control, suggesting increased efficacy with repeated treatment.

These findings agree with those of Abbas et al. (2021), who reported that spinetoram reduced pod borer larval populations by 70.0% at 3 days, 59.67% at 7 days, and 49.10% at 14 days after application, demonstrating its sustained effectiveness. Likewise,Kumar and Muthukrishnan (2018) found that spinetoram 12 SC applied at 45 g a.i. ha^{-1} reduced pod borer infestation to 4.4%, corresponding to an 82.9% reduction over the untreated control. Nur et al. (2020) also reported similar results using Spinosad against *M. vitrata*. The present findings also align with Kumar and Pavviya (2018), who reported that Spinetoram 12 SC effectively reduced *M. vitrata* incidence on pigeon pea when applied three times at 36-45 g a.i. ha^{-1} intervals.

Effect of treatments against *M. vitrata* on yardlong bean after the 3rd spray

After the third spray, tested biorational insecticides continued to show promising efficacy in reducing *M. vitrata* infestation (Table 3). Spinetoram 11.7% SC @ 0.3 ml L^{-1} again recorded the lowest number of infested pods at 1, 5, and 10 DAS (1.50, 1.13, and 1.33 pods, respectively), whereas the untreated control showed the highest infestation levels. Overall, spinetoram achieved a 66.24% reduction in pod infestation compared with the untreated control after the third spray.

The consistent superiority of Spinetoram across all three sprays highlights its strong, reliable efficacy against *M. vitrata*. Similar results were reported by Srinivasan et al. (2025), who found that spinetoram 6% w/v + methoxyfenozide 30% w/v SC applied at 144 g a.i. ha^{-1} reduced *M. vitrata* and *Lampides boeticus* larval populations by 86.97% and 85.75%, respectively, and reduced pod damage by 73.78%. Patel et al. (2023a) also reported that spinetoram 11.7% SC significantly reduced pod borer larval populations in chickpea, ranking among the most effective insecticides tested. The present results are comparable to those of Hossain et al. (2025). They reported that the lowest number of infested pods (1.33, 1.11, and 1.22) $plant^{-1}$ was observed in Spinosad- treated plants. Additionally, Patel et al. (2023b) observed effective suppression of *M. vitrata* on cowpea, with only 1.53 larvae per plant and 14.24% pod damage.

Table 2. Efficacy of tested bio-rational pesticides against *M. vitrata* after the 2nd spray on yardlong bean.

Treatments	Dose (ml L^{-1}) water	Number of infested pods/plant				Decrease (%) over control
		2nd spray				
		1 DAS	5 DAS	10 DAS	Mean	
T_1	0.4	2.20^{c}	2.13^{c}	2.43^{c}	2.25^{c}	62.93
T_2	1.5	3.13^{b}	2.97^{b}	3.03^{b}	3.04^{b}	49.92
T_3	0.3	1.37^{d}	1.16^{d}	1.03^{d}	1.18^{d}	80.56
T_4	1.0	$2.87b^{c}$	2.73^{b}	$2.83b^{c}$	2.81^{b}	53.70
Control	-	5.40^{a}	6.37^{a}	6.47^{a}	6.07^{a}	-
CV (%)	-	12.27	9.15	7.60	6.37	-

T_1 = Spinosad, T_2 = *Celastrus angulatus*, T_3 = Spinetoram, T_4 =Azadirachtin, DAS= Days after spray. Different superscripts indicate differences among the treatment.

Table 3. Efficacy of tested bio-rational pesticides against *M. vitrata* after 3rd spray on yardlong bean.

Treatments	Dose (ml L^{-1}) water	Number of infested pods $plant^{-1}$ after 3rd spray				Decrease (%) over control
		1 DAS	5 DAS	10 DAS	Mean	
T_1	0.4	$1.83c^{d}$	1.90^{c}	2.27^{c}	2.00^{c}	48.85
T_2	1.5	$2.16b^{c}$	2.06^{c}	$2.53b^{c}$	$2.25b^{c}$	42.45
T_3	0.3	1.50^{d}	1.13^{d}	1.33^{d}	1.32^{d}	66.24
T_4	1.0	2.50^{b}	2.73^{b}	2.90^{b}	2.71^{b}	30.69
Control	-	3.77^{a}	3.83^{a}	4.13^{a}	3.91^{a}	-
CV (%)	-	12.77	12.32	11.31	10.41	-

T_1 = Spinosad, T_2 = *Celastrus angulatus*, T_3 = Spinetoram, T_4 =Azadirachtin, DAS= Days after spray. Different superscripts indicate differences among the treatment.

Effect of treatments on the yields of yardlong bean

Yield data further substantiated Spinetoram's effectiveness. All treatments resulted in significantly higher yields than the untreated control (Table 4). Spinetoram 11.7% SC @ 0.3 ml L^{-1} produced the highest yield per harvest and also the highest cumulative yield (9.15 ton/ ha), while the untreated control recorded the lowest cumulative yield (1.81 ton ha^{-1}). The Spinetoram treatment resulted in an 80.19% increase in yield over the control, clearly demonstrating its contribution to enhanced productivity. Similar yield improvements with spinetoram have been reported by Srinivasan et al. (2025), Patel et al. (2023b), Bhuva and Patel (2023), and Kumar and Muthukrishnan (2018). Novel research demonstrates that newly formulated insecticides have been successfully evaluated by multiple researchers against various pod borer species (Haripriya et al., 2019). The present findings are consistent with those of Dahal et al. (2020), who reported the lowest pod damage and higher cowpea yield in Spinosad-treated plots compared with pod-borer treatments.

Effect of tested bio-rational pesticides on Benefit Cost Ratio (BCR)

According to the economic analysis (Table 5), the most economical treatment was Spinetoram (Delegate 11.7% SC), which achieved the highest benefit-cost ratio (BCR) of 2.59, while the untreated control had the lowest BCR (0.54). Parallel results were also reported by Mrong et al. (2024), who observed that the lowest pod infestation, along with the highest marketable yield (10.7 ton/ha) and marginal benefit-cost ratio (7.7), was achieved using a management approach involving Tracer 45 SC (Spinosad) applied at 0.4 g L^{-1} of water for the effective suppression of pod borer in yardlong bean. These results are consistent with reports of positive economic returns for spinetoram-based management techniques by Khan et al. (2025), Bhuva and Patel (2023), and Patel et al. (2023a). Sharma et al. (2023) also reported that spinetoram, as a widely used insecticide for fall armyworm management, proved economically viable in Nepal.

Table 4. Effect of tested biorational insecticides on the yield of yardlong bean at different harvesting time.

Treatments/dose (ml L^{-1}) water		Yield (g pit^{-1}) at different harvesting						Yield (ton/ha)	Increase yield (%) over control
		1st	2nd	3rd	4th	5th	6th		
T_1	0.4	68.68^b	61.25^b	40.63^b	28.83^b	18.01^b	23.41^b	4.81^b	62.40
T_2	1.5	42.91^c	41.57^c	22.43^c	17.73^c	30.96^a	19.10^c	3.49^c	48.17
T_3	0.3	128.02^a	87.53^a	144.21^a	35.72^a	34.32^a	27.47^a	9.15^a	80.19
T_4	1.0	42.01^c	51.92^b	46.98^b	11.99^d	17.44^b	13.31^d	3.67^c	50.69
Control	-	17.60^d	30.80^d	13.16^b	10.42^d	10.73^c	7.84^e	1.81^d	-
CV (%)	-	5.55	10.00	7.66	10.89	8.22	10.99	5.03	-

T_1 = Spinosad, T_2 = *Celastrus angulatus*, T_3 = Spinetoram, T_4 =Azadirachtin. Different superscripts indicate differences among the treatment.

Table 5. Effectiveness of tested bio-pesticides on the economics and benefit cost ratio.

Treatments	Yield (ton/ha)	Gross return (Tk/ha)	Cost of production (Tk/ha)			Net return (Tk/ha)	BCR
			Common cost	Treatment cost	Total		
T_1	4.81	192664	135000	5020	140020	52644	1.37
T_2	3.49	139768	135000	2000	137000	2768	1.02
T_3	9.15	365800	135000	6165	141165	224635	2.59
T_4	3.67	146920	135000	4350	139350	7570	1.05
Control	1.81	72440	135000	-	135000	-62560	0.54

Here, T_1 = Spinosad, T_2 = *Celastrus angulatus*, T_3 = Spinetoram, T_4 = Azadirachtin. BCR: Benefit Cust Ratio.

Conclusion

The field experiment on yard long bean was evaluated against *M. vitrata* using four new-generation insecticides: Spinosad, Bio-chamak 1% EW, Spinetoram, and Azadirachtin. All evaluated biorational pesticides demonstrated promising efficacy compared to the untreated control. However, Spinetoram consistently resulted in reduced pod infestation (up to 80.56% over the control) and produced the highest yield (9.15 t/ha) and benefit-cost ratio (2.59). Spinetoram is a foliar spray containing the semisynthetic spinosyn, broad-spectrum, contact, stomach poison, and exhibits translaminar activity, which effective against borers and caterpillars. The insecticide acts on the insect's nervous system to cause rapid cessation of feeding, paralysis, and death. Owing to its high selectivity, lower environmental impact, and novel mode of action, spinetoram can be used as a reliable and

effective option for managing *M. vitrata* and enhancing yard-long bean productivity.

Acknowledgment

We thank the IRT of HSTU for supporting this study with a research grant, and Corteva Agriscience Bangladesh Limited for providing Spinetoram. We also thank the anonymous reviewer for their critical review of the manuscript and for contributing to its improvement.

Authors contribution

MAH conceived and designed the experiment. MAH supervised the study, and MAA analyzed the data. SA performed the experiments, collected the data, and drafted the manuscript. MAH, MAA, and HFE revised both the initial and final versions of the manuscript. All authors read and approved the final manuscript.

Conflict of interest

The authors declare no conflicts of interest.

References

Abbas A, Wang Y, Muhammad, U and Fatima A. Efficacy of different insecticides against gram pod borer (*Helicoverpa armigera*) and their safety to the beneficial fauna. *Int. J. Biosci*. 2021; 18: 82-88.

Ahmed RN, Uddin MM, Haque MA and KS. Effectiveness of insect growth regulators for management of legume pod borer, *Maruca vitrata* F. in yard long bean. *Fundam. Appl. Agric*.2020; 5(2): 248-255.

Akbar WA, Asif, MU, Memon RM, Moula Bux MB and Sohail S. Validation of some new chemistry and conventional insecticides against gram pod borer (*Helicoverpa armigera*) in chickpea. *Pak. Entomol*. 2018; 40(1): 45-49.

Aktar S, Uddin MM and Ahmed KS. Bio-efficacy of some novel insecticides and biopesticides for managing bean pod borer, *Maruca vitrata Geyer*. *J. Bangladesh Agric. Univ*. 2020; 18(2): 221-226.

Ali S. The efficacy of botanical extract on pest control and yield of yard long bean. South *Asian J. Biol. Res*. 2019; 2(01): 6-13.

Ambethar V. Potential of entomopathogenic fungi in insecticide resistance management (IRM): A review. *J. Biopestic.* 2009; 2 (2): 177-193.

BBS (Bangladesh Bureau of Statistics). *Year book of Agricultural Statistics of Bangladesh*. Ministry of Planning, Government of the People's Republic of Bangladesh. Dhaka. 2024; pp. 50.

Bhuva KJ and Patel SD. Bio-efficacy of insecticides against spotted pod borer, *Maruca vitrata* (Fabricius) in Greengram. *Int. J. Stat. Appl. Math*. 2023; 8(6S): 950-956.

Cook BG, Pengelly BC, Brown SDJ, Donnelly L, Eagles DA, Franco MA, Hanson J, Mullen BF, Partridge IJ, Peters M and Schultze-Kraft R. Differential aphid colony establishment in Dolichos lablab varieties correlated with some plant specific factors that impact on aphid fecundity. *Am. J. Plant Sci*. 2005; 8(4): 754-769.

Dahal S, Gautamb B, Sharma, B, Neupanea K., Kandel S, Sedhaia S, Tiwaria G. and Ojha LN. Management options against pod borer (*Maruca testulalis* Geyer) and pod sucking bugs (*Riptorus dentipes*) of cowpea [*Vigna unguiculata* (L.) Walp.]. *Trop. Agrobi*. (TRAB). 2020; 1(1): 24-30

FRG (Fertilizer Recommendation Guide). Bangladesh Agricultural Research Council, Farmgate, Dhaka, 2012. p. 274.

Haripriya KS. Jeyarani S. Mohankumar and Soundararajan RP. Field evaluation of biocontrol agents and biopesticides against spotted pod borer, *Maruca vitrata* on lablab. *Indian J. Agric. Res*. 2019; 53(5): 599-603.

Hossain MA, Hasin T, Rashedi M, El Taj HF and Alim MA. Influence of novel formulated insecticides against *Maruca vitrata* F. (Lepidoptera: Crambidae) on yard long bean. *Mun. Ent. Zool.* 2025; 20(1): 1728-1735.

Jayasinghe RC, Premachandra D and Neilson R. A study on *Maruca vitrata* infestation of Yard-long beans (*Vigna unguiculata* subsp. *sesquipedalis*). *Heliyon*, 2015; 1(1): e00014.

Khan AM, Saljoqi AR, Amin SA, Ullah M, Ali M, Shah I, Hamad SH and Akhtar FU. Field efficacy of various insecticides and *Trichogramma chilonis* (Ishii) against tomato fruit borer *Helicoverpaarmigera* (*Hübner) (Lepidoptera: Noctuidae). Pure Appl. Biol*, 2025; 14(1): 69-81.

Kodandaram MH, Halder J and Rai AB. New insecticide molecules and entomopathogens against hadda beetle, *Henosepilachna vigintioctopunctata* infesting vegetable cowpea. *Indian J. Plant Prot.* 2014; 42(4): 333-337.

Kumar AS and Muthukrishnan N. Field evaluation of spinetoram 12 SC mixture against *Spodoptera litura* (Fabricius) on onion. *Indian J. Ent.* 2018; 80(1): 137-140.

Kumar AS. and Pavviya A. Field evaluation of spinetoram 12 SC against *Maruca vitrata* on pigeonpea. *Legume Res*. 2018; 41 (3): 447-453

Malacrino A, Seng KH, An C, Ong S and Rourke MEO. Integrated pest management for yard-longbean (*Vigna unguiculata* subsp. *sesquipedalis*) in Cambodia. *Crop Prot*. 2019; 135: 104811.

Maphosa Y and Jideani VA. The role of legumes in human nutrition. In:*Functional Food-Improve Health Through Adequate Food*. Hueda MC, ed. 2017; pp. 103-122.

Margam VM, Coates BS, Ba MN, Sun W, Binso-dabire CL, Baoue I, Ishiyaku MF, Shukle JT, Hellmich RL, Covas FG, Ramasamy S, Armstrong J, Pittendrigh BR and Murdock LL. Geographic distribution of phylogenetically distinct legume pod borer, *Maruca vitrata* (Lepidoptera: Pyraloidea: Crambidae). *Mol. Biol. Rep*. 2011; 38: 893-903.

Mian MY, Hossain MS and Karim ANMR. Integrated pest management of vegetable crops in Bangladesh. In: R. Muniappan, E. Heinrichs (Eds), *Integrated Pest Management of Tropical Vegetable Crops.* Springer, Dordrecht, Germany. 2016. pp. 235-349.

Mrong A, Amin MR, Kayesh E, Sutradhar P and Hossain MS. Effectiveness of bio-rational insecticides against pod borer of yard long bean and their effect on natural enemies. *Ann. Bangladesh Agric*. 2024; 28(1): 39-47

Mweke A, Akutse KS, Ulrichs C, Fiaboe KKM, Maniania NK and Sunday ES. Integrated management of Aphis craccivora in cowpea using intercropping and entomopathogenic fungi under field conditions. *J. Fungi*. 2020; 60(6): 60.

Nur MW, Miah MRU and Amin MR. Management of aphid and pod borer of country bean using bio-rational pesticides. *Bangladesh J. Ecol*. 2020; 2(1): 1-5.

Oliveira CM, Auad AM, Mendes SM and Frizzas MR. Crop losses and the economic impacts of insect pests on Brazilian agriculture. *J. Crop Prot*. 2014; 56: 50-54.

Patel RM, Patel HC and Mohapatra AR. Evaluation of different insecticides against spotted pod borer, *M. vitrata* infesting vegetable cowpea. *Env. Ecol*. 2023b; 41: 2516-2525.

Patel S, Garg VK and Balpande S. Bio-efficacy of newer insecticides against gram pod borer *Helicoverpa armigera* (Hubner) on chickpea (*Cicer arietinum* L.). *Int. J. PlantSci*. 2023a; 18 (1): 10-13.

Sharma S, Thapa RB, Pokhrel S. Neupane S, Tiwari S and Adhikari C. Evaluation on the efficacy of synthetic insecticides for the management of fall armyworm, *Spodoptera frugiperda* (Lepidoptera: Noctuidae) in maize. *J. Plant Prot. Soc.* 2023; 8: 14-20.

Shil NC, Saleque MA, Islam MR and Jahiruddin M. Soil fertility status of some of the intensive crop growing areas under major agroecological zones of Bangladesh. *Bangladesh J. Agric. Res*. 2016; 41(4): 735-757.

Srinivasan G, Shanthi M and Naveena K. Bio-efficacy of Spinetoram 6% W/V (5.66% W/W) + Methoxyfenozide 30% W/V (28.3% W/W) SC against pod borers infesting green gram, *Vigna radiata* (L.) Wilczek. *Legume Res*. 2025; 48(6): 1057-1062.

J. Bangladesh Acad. Sci. 50(1); 59-69: March 2026 DOI:https://doi.org/10.3329/jbas.v50i1.83124

Journal of Bangladesh Academy of Sciences

Journal homepage: http://www.bas.org.bd/publications/jbas.html

Research Article

From orchard to bedside: Prospective, real-world study exploring the utility of Indian gooseberry (amlaki) in end stage hepatocellular carcinoma

Md. Rezwanur Rahman[1], Sheikh Mohammad Noor E Alam[2], Rezaul Karim[3], Rakibul Hasan[3], Debabrata Karmakar[3], Manas Saha[4], Rabinarayan Acharya[5], Anagha Ranade[5], Chowdhury Faiz Hossain[6], Gazi Nurun Nahar Sultana[7], Sitesh Chandra Bachar[8], Md. Zakir Sultan[7], Md. Abdur Rahim[9], Dulal Chandra Das[2], Rokshana Begum[10], Md Enayet Ali Pramanik[11], Sheikh Zahir Raihan[12], Ahmed Lutful Moben[13], M. Shahabuddin K. Choudhuri[14], Noureen Amin[18], Musarrat Mahtab[16], Sakirul Khan[17], Sheikh Mohammad Fazle Akbar[18] and Mamun Al Mahtab[2]

[1]National Gastroliver Institute and Hospital, Dhaka, Bangladesh

ARTICLE INFO

Article History

Received: 21 July 2025
Revised: 25 January 2026
Accepted: 29 January 2026

Keywords: *Phyllanthus emblica*, End-stage hepatocellular carcinoma, Performance status, Survival, Best supportive care.

ABSTRACT

Hepatocellular carcinoma (HCC) remains a leading cause of cancer-related mortality worldwide, despite significant advances in its treatment. In Bangladesh, as in many other countries, most patients present at an advanced stage when curative options are no longer feasible. Therefore, it is essential to explore locally available, homegrown solutions to address this growing health challenge. A total of sixty patients with end-stage HCC were enrolled in this study and randomly assigned into 2 groups, each comprising 30 patients. Both groups received best supportive care. In addition, patients in Group A were received 1000 mg of *Phyllanthus emblica* extract in powder formulation in capsules. The study included drug collection, preparation, extraction, protein isolation, molecular docking, data analysis, and ultimately a clinical trial. The baseline characteristics of patients in both groups were comparable. The findings demonstrated a survival benefit and improvement in quality of life among patients treated with *Phyllanthus emblica* compared to the control group; however, these results were not statistically significant. Overall, the study established the safety and suggested limited efficacy of *Phyllanthus emblica* in patients with end-stage HCC. These findings may well pave the way for future research on repurposing and repositioning traditional medicines into modern medical practice.

Introduction

Hepatocellular carcinoma (HCC) is the 6th most common diagnosed cancer and the 3rd leading cause of cancer deaths globally (Ganjalikhaniet al., 2020). Annually, there are morethan 800,000 new cases of HCC resulting in 700,000 deaths per year globally (Ganjalikhani et al., 2020). Further adding to our worries, the incidence of HCC is on the rise across the globe, which has been attributed to

*Corresponding author: <shwapnil@agni.com>

[2]Department of Hepatology, Bangladesh Medical University, Dhaka, Bangladesh; [3]Institute of Technology Transfer and Innovation, Bangladesh Council of Scientific and Industrial Research, Dhaka, Bangladesh; [4]Department of Hepatology, Khulna Medical College, Khulna, Bangladesh; [5]Central Council for Research in Ayurvedic Sciences, New Delhi, India; [6]Department of Pharmacy. East West University, Dhaka, Bangladesh, [7]Centre for Advanced Research in Sciences (CARS), University of Dhaka, Dhaka, Bangladesh; [8]Department of Pharmacy, University of Dhaka, Dhaka, Bangladesh; [9]Department of Hepatology, International Medical College, Gazipur, Bangladesh; [10]Department of Hepatology, Shaheed Suhrawardy Medical College, Dhaka, Bangladesh; [11]On-Farm Research Division, Bangladesh Agricultural Research Institute, Rajshahi, Bangladesh; [12]Department of Clinical Pharmacy and Pharmacology, University of Dhaka, Dhaka, Bangladesh;[13]Department of Hepatology, Kurmitola General Hospital, Dhaka, Bangladesh; [14]Department of Pharmacy, Jahangirnagar University, Dhaka, Bangladesh; [15]Department of Nephrology, National Institute of Kidney Diseases and Urology, Dhaka, Bangladesh; [16]Clinical Research Organization Ltd., Dhaka, Bangladesh; [17]Research Center for Global and Local Infectious Diseases, Oita University, Yufu, Oita, Japan; [18]Department of Gastroenterology and Metabolism, Ehime University Graduate School of Medicine, Ehime, Japan; Miyakawa Memorial Research Foundation, Tokyo, Japan.

increasing prevalence of chronic viral hepatitis B (HBV) and C (HCV), alcohol, and metabolic dysfunction associated fatty liver diseases and cirrhosis (Cho et al., 2023). Despite recent advances in therapeutics, overall survival in HCC remains dismal, with a 5-year survival rate of less than 15% (Yousef et al., 2020).

In Bangladesh, the picture is even gloomier as most of our HCC patients are diagnosed with end-stage disease. The reasons are multi-factorial, including a lack of effective surveillance for HCC and liver cirrhosis. We are hardly left with any option whatsoever, as at diagnosis, most HCC patients in Bangladesh are beyond indications for surgery, ablation, chemotherapy, chemoembolization, or a combination of these therapeutic approaches. The challenge is therefore to find homegrown remedies that offer some benefit to our end-stage HCC patients, who constitute the bulk of our HCC burden in this resource-constrained country.

With an array of shortcomings, right from a lack in funding to research infrastructure, research attitude, and appropriate human resources, finding the correct answer to this ever-imposing challenge is not any easy task for us. We simply cannot embark on the drug discovery and development race, as it is still not our dish of rice. Our focus is therefore on what is doable for us. We hypothesized that our traditional medical practice can be a game-changer. Despite having a rich heritage of traditional medical practice, the harsh reality is that most of our traditional medical literature is lost, with few exceptions.

Phyllanthus emblica is an important medicinal plant in Ayurveda and Unani medicine and is a key constituent of many herbal formulations. In the Indian subcontinent, it is known as *Amalaki* in Bengali and Sanskrit and Amla in Hindi (Fig.1). *Phyllanthus emblica* has been extensively studied for its phytoconstituents, biological activities, and therapeutic potential, and has been shown to possess anti-diabetic, anti-inflammatory, antioxidant, hepato-protective, radio-modulatory, and immune-modulatory properties (Yadav et al., 2017).

Fig. 1. *Phyllanthus emblica* (amlaki).

Phyllanthus emblica is rich in polyphenols and hydrolysable tannin-derived compounds, which prevent mutagenesis and lipid peroxidation induced by carcinogens. The therapeutic potential of different components of *Phyllanthus emblica* has been extensively studied. Most of its active constituents, namely tannins, chebulagic acid, ellagic acid, etc., have pro-apoptotic and anti-proliferative activity against cancer cells. Its phytoconstituents act synergistically to make *Phyllanthus emblica* a strong free-radical scavenger, which protects DNA damage from reactive oxygen species (Ngamkitidechakul et al., 2010). *Phyllanthus emblica* extracts inhibit the proliferation of various cancer cell lines, including A549, HepG2, HeLa, MDA-MB-231. (Ahmad et al., 2021).

It has been demonstrated that *Phyllanthus emblica* reduces serum transaminases (ALT and AST), TNF-α, serum triglyceride (TG), IL-1β, and hepatic triglyceride (HTG) and increases the viability of hepatocytes following ethanol-induced liver injury in rats (Pramyothin et al., 2006). *Phyllanthus emblica* also exerts hepato-protective effects against anti-tubercular drugs as well as in carbon-tetrachloride (CCl4) and thioacetamide-induced hepatic fibrosis in rat models (Ahmad et al., 2021; Jose and Kuttan, 2000). In this article, we describe our recent, prospective, real-world experience with *Phyllanthus emblica* in patients with end-stage HCC.

Materials and Methods

Preparation and dose of the study drug

In this study, we used capsules containing a powder formulation of *Phyllanthus emblica* extract. The study determined the drug collection, preparation, extraction, protein preparation, molecular docking analysis and chemical content of *Phyllanthus emblica* extract capsules using high-performance liquid chromatography (HPLC) at the Institute of Technology Transfer and Innovation (ITTI), Bangladesh Council of Scientific and Industrial Research (BCSIR). ITTI also ensured that the powder formulation was pharmaceutical-grade and in compliance with the pharmacopoeia. Pharmaceutical-grade capsules were then manufactured by Beacon Pharmaceuticals PLC. Each capsule contained 500 mg *Phyllanthus emblica* extract.

Collection, extraction, and storage of the study drug

Phyllanthus emblica was collected from different super-shops in Dhaka city. The fruits were cleaned with running tap water, then immersed in a fruit and vegetable washing solution for 30 minutes. Washing was repeated in deionized water. The fruits were then chopped into small pieces and oven-dried at 60°C for 24 hours. After 24 hours, the dried fruits were ground into a powder and stored at room temperature in a dark place.

About 40 g of dried powder was added to 200 mL of analytical-grade methanol and incubated for 5 days at room temperature in the dark. After 5 days, the dissolved methanolic powder was filtered by Whatman Filter Paper No 1. Residues were collected in another jar, evaporated under reduced pressure, and dried using a rotary evaporator at 70°C for 3 days. The dried extracts were labeled and stored in sterile screw-capped bottles at 4°C in a refrigerator for further use.

Chromatographic investigation

Flavonoids were quantitatively analyzed using a reverse-phase HPLC system with a UV system. A C18 column (25 cm x 4.6 mm, 5 µm) was used to separate the compounds. Column temperature and flow rate were maintained at 35 °C and 1 mL/min, respectively. The injection volume was 10 µL, and detection was at 350 nm. The mobile phase was composed of 0.5% acetic acid in water and acetonitrile. Kaempferol concentration was 268.5485 mg/g in *Phyllanthus emblica* (Fig. 2).

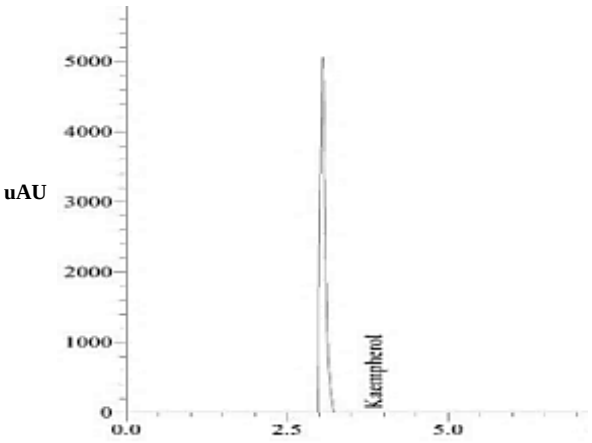

Fig. 2. HPLC Chromatogram of Kaempferol.

Anti-oxidant assay

Radical scavenging action of *Phyllanthus emblica* against the stable 2, 2-diphenyl-2-picrylhydrazyl (DPPH) radical was measured spectrophotometrically. In order to measure the DPPH scavenging activity of *Phyllanthus emblica*, a DPPH solution was prepared by adding DPPH (12.5 mg) to 50 mL of methanol. Absorbance of this stock solution was measured at 517 nm. The DPPH solution was diluted with methanol to an absorbance of 0.98 and stored in an amber-colored bottle ready for use. An aliquot of 200 µL of *Phyllanthus emblica* at different concentrations (120, 140, 160, 180, and 200 µg/mL prepared in methanol) was added to 1 mL of DPPH solution. The reaction mixture was incubated at 37 °C in the dark for 20–30 min. Absorbance decrease was determined at 517 nm. Ascorbic acid was used as a standard. The reaction was performed in triplicate. Scavenging activity was calculated by using the following equation, where Q represents DPPH scavenging activity.

$$Q\,(\%) = \frac{\text{Absorbance of control} - \text{Absorbance of sample}}{\text{Absorbance of control}} \times 100$$

Protein preparation, molecular docking, analysis, and visualization

The 3D crystal structure of ornithine amino-transferase, OAT (PDB ID: 6OIA) was obtained from the Protein Data Bank (PDB) in PDB format. Heteroatoms and water molecules were deleted from the protein chain using the Discovery Studio (Version 4.1) software package and subsequently reinserted for energy minimization, using the conjugate gradient technique to remove bad contacts between protein atoms, in Swiss-PDB Viewer (Version 4.1.0). Finally, the optimized structures were subjected to molecular docking against the active phytocompounds (chebulagic acid, quercetin, ellagic acid, kaempferol, chebulic acid, gallic acid, and ascorbic acid) retrieved from the PubChem database. Docking was done using the PyRx (Version 0.8) software package. Flexible docking was performed with a center grid box size of 30.4498, 24.1222, and 34.2317 Å along the x, y, and z directions, respectively, where the entire protein was covered by the grid box. Moreover, Discovery Studio (Version 4.1) was used for nonbonded interaction calculation and to analyze and visualize docking results (Table 1 and Fig. 3).

Table 1. Docking score of different phytochemicals of *Phyllanthus emblica* with standard drug.

Compound name	Binding affinity (kcal/mol)
Chebulagic acid	-9.5
Quercetin	-8
Ellagic acid	-8
Kaempferol	7.8
Chebulic acid	-6.9
Gallic acid	-6
Ascorbic Acid	-5.8
Cabozantinib(Std)	-8.6

Patient selection

Ethical approval of this observational study was obtained from the Institutional Review Board of Bangladesh Medical University (BMU) (approval no. 4460). The study commenced on July 15, 2023, and was completed on August 14, 2024. Patients with HCC (BCLC-D), irrespective of etiology, with ECOG performance status >2 or CTP score C, age >18 years, and both genders attending the Department of Hepatology, BMU for treatment were included in the study. Patients diagnosed with another cancer in addition to HCC and

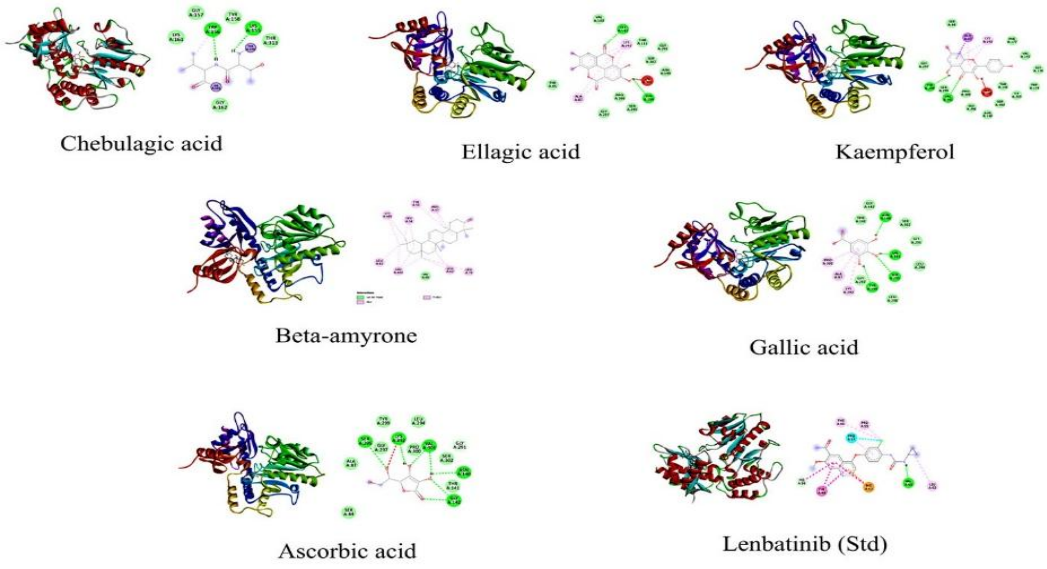

Fig. 3. Docking of different phytochemicals of *Phyllanthus emblica* with standard drug.

patients with co-morbid conditions like severe congestive cardiac failure (CCF), ischemic heart diseases (IHD), recent myocardial infarction (MI), chronic obstructive pulmonary disease (COPD), chronic kidney disease (CKD) etc. were excluded.

Baseline clinical evaluation and several investigations were done to meet inclusion and exclusion criteria namely, complete blood count (CBC), serum bilirubin, serum albumin, serum alanine aminotransferase (ALT), prothrombin time, serum creatinine, random blood sugar (RBS), urine routine microscopic examination (RME), alpha feto-protein (AFP) from Departments of Clinical Pathology, Biochemistry, Hematology and Microbiology, HBsAg (ELISA), Anti HBc (total) (ELISA) and Anti-HCV (ELISA) from Department of Virology, Chest X-ray (P/A view), ultrasonogram of whole abdomen and triphasic computed tomography (CT) scan of hepato-biliary system (HBS) from Radiology and Imaging Department and endoscopy of upper gastrointestinal (UGIT) at the Hepatology Department of BMU. Fine needle aspiration (FNA) from hepatic space-occupying lesions was performed in patients where indicated.

After diagnosis of end-stage HCC, the potential benefits and risks of the use of *Phyllanthus emblica* extract in capsule form were explained to the patients. They were properly informed and explained about the study's purpose and procedures. After obtaining written informed consent, 60 patients with end-stage HCC were enrolled in the study. The sample size was determined using Morgan's table for sample size. The patients were randomized into 2 groups by block randomization. Half of them (Group A, 30 patients) were selected for *Phyllanthus emblica* therapy plus best supportive care (BSC), and the other half (Group B, 30 patients) were selected for BSC only. Group A received *Phyllanthus emblica* 1000 mg daily and were followed up at 1 and 3 months or up to death. Group B patients were also followed up in a similar manner. BSC, included maintenance of nutritional status and palliative care, including but not restricted to management of pain, weakness, anorexia, insomnia, respiratory distress, ascites, coagulopathy, encephalopathy, etc. The objective of the study was to compare survival and performance status between *Phyllanthus emblica* and BSC groups.

Monitoring and compliance

The study was conducted at the Department of Hepatology of BMU between 2023 and 2024. Close communication was maintained with all patients. Permanent and present addresses and landline/cell phone numbers of all patients were kept on record. To improve patient compliance, a telephone survey was done every 2 weeks. Attendants or relatives were requested to monitor patients'drug intake. Patients were asked to bring empty capsule strips during each visit. All patients were advised to contact the study team immediately in case of any adverse event. Each patient was followed up at 1 and 3 months from initiation of treatment. Patients were encouraged to consume healthy foods as much as possible, if needed in smaller quantities, and on multiple occasions, with special emphasis on animal protein.

Results

All data were presented as mean±standard deviation (SD) and analyzed using the statistical package SPSS (version 26.0, IBM Corp., Armonk NY, USA). Qualitative data were analyzed by the Chi-square test, and quantitative data were analyzed by the Student´s t-test. The Wilcoxon rank sum was used to compare laboratory parameters and measurements before and after treatment. A statistically significant result was considered when the p-value was less than 0.05.

Comparison of demographic characteristics between the *Phyllanthus emblica* group and the BSC groups revealed that age and sex distribution were similar between the two groups. The mean age of the *Phyllanthus emblica* group was 53.5±12.1 years,

compared to the BSC group's mean age of 49.9±12.87 years, which was not statistically significant (p=0.260). Regarding sex distribution, both groups were predominantly male, with 96.7% of the *Phyllanthus emblica* group and 93.3% of the BSC group being males. The difference in sex distribution between the groups was also not statistically significant (p=0.554) (Table 2).

Jaundice was universal in both groups, present in 100% of the *Phyllanthus emblica* group and 96.7% of the BSC group. Ascites was also prevalent, observed in 96.7% of the *Phyllanthus emblica* group and 100% of the BSC group. Similarly, hepatic encephalopathy was observed in 23.3% of *Phyllanthus emblica*groupcompared to 26.7% of BSC group (Table 2).

Biochemical parameters between the two groups were also similar (Table 3). Imaging showed similar numbers of space-occupying lesions, portal vein thrombus, and extrahepatic metastases in both groups. The same goes for the aetiology of end-stage HCC, with HBV the leading cause in both groups (Table 4).

At 1 month follow-up, hepatic encephalopathy was

Table 2. Baseline demographic and clinical characteristics of the study subject

Variable	Study Subject		*p* value
	Phyllanthus emblica (n=30), n(%)	BSC (n=30), n (%)	
Age (year)[a]	53.5±12.1 (Range: 30-80)	49.9±12.87 (Range: 27-75)	0.260
Age distribution (yr.)			
< 40	6 (20.0)[b]	8 (26.7)	NS
> 40	24 (80.0)	22 (73.3)	
Gender			
Male	29 (96.7)	28 (93.3)	0.554
Female	1 (3.3)	2 (6.7)	
Physical examination			
Jaundice	30 (100)	29 (96.7)	0.313
Presence of ascites	29 (96.7)	30 (100)	0.313
Hepatic encephalopathy	7 (23.3)	8 (26.7)	0.766
Imaging findings			
Number of space occupying lesion (SOL)			
1	0 (0.0)	3 (10.0)	0.076
2-3	2 (6.7)	0 (0.0)	0.150
>3	28 (93.3)	27 (90.0)	0.640
Portal vein thrombosis	23 (76.7)	17 (56.7)	0.100
Extrahepatic metastasis	7 (23.3)	9 (30.0)	0.559

[a]Mean±SD; [b]Numbers in parentheses show percentage; CN, not significant; Unpaired t-test and Chi-square test were performed. A $p<0.05$ was considered as significant.

Table 3. Baseline biochemical characteristics and etiology of the study sujbect

Variable	*Phyllanthus emblica* (n=30)	BSC (n=30)	*p*-value
Haemoglobin (gm/dl)	11.5±2.1	10.7±1.7	0.119
Platelet (10^9/L)	208.0±78.2	230.0±119.9	0.401
ALT (U/L)	103.5±80.7	95.6±61.4	0.672
S. Bilirubin (mg/dl)	7.75±10.02	10.5±10.3	0.303
S. Albumin (g/dl)	3.24±4.50	2.65±0.63	0.479
INR	1.41±0.49	1.39±0.37	0.868
S. Creatinine (mg/dl)	0.92±0.31	1.09±0.40	0.075
Na (mmol/L)	129.5±5.3	130.9±5.3	0.308
K (mmol/L)	4.55±0.84	4.37±0.95	0.425
AFP (ng/ml)	17328.4±37116.8	8218.0±19229.2	0.237
≤200	8(26.7%)	13(43.3%)	
201-400	2(6.7%)	2(6.7%)	
>400	20(66.7%)	15(50.0%)	
Child-Turcotte-Pugh score(CTP)	10.1±0.8	10.17±1.46	0.913

[a]Mean±SD; [b]Numbers in parentheses show percentage; Unpaired t-test and Mann-Whitney testwere performed. A $p<0.05$ was considered as significant.

Table 4. Etiology of the study subject.

Variables	Study Subject		*p* value
	Phyllanthus emblica (n=30) n (%)	BCS (n=30) n(%)	
Hepatitis B virus (HBV)	18 (60.0)	17 (56.7)	
Hepatitis C virus (HCV)	4 (13.3)	4 (13.3)	
Non-alcoholic steatohepatitis(NASH)	3 (10.0)	3 (10.0)	0.3
Occult hepatitis B virus infection (OBI)	4 (13.3)	1 (13.3)	
Others	1 (13.3)	5 (16.7)	
Total	30 (100)	30 (100)	

Numbers in parentheses show percentages; Chi-square test was performed; A p-value <0.05 was considered as significant.

reported in 35.7% BSC group, but absent in *Phyllanthus emblica* group, with a statistically significant difference (p=0.014) (Table 5). CTP value was also significantly lower in the *Phyllanthusemblica* group (10.00 ± 0.96) compared to the BSC group (11.07±1.21) (p = 0.015) (Table 6).

Table 5. Physical examination of the study subjects at 1 month (n=29).

Variables	Study Subject		*p* value
	Phyllanthus emblica (n=30) n (%)	BCS (n=30) n(%)	
Jaundice	14 (93.3)	13 (92.9)	0.960
Presence of ascites	14 (100)	14 (100)	1.00
Hepatic encephalopathy	0 (0.0)	5 (35.7)	0.014

Numbers in parentheses show percentages; Chi-square test was performed; A p-value <0.05 was considered as significant.

At the 3-months follow-up, the CTP value was slightly lower in the *Phyllanthus emblica* group (10.00±1.41) compared to BSC group (11.33±2.08), but the difference was not statistically significant (p=0.355) (Table 6).

Table 6. Etiology of the study subject.

CTP Value	Study Subject		*p* value
	Phyllanthus emblica (n=30), n (%)	BCS (n=30), n(%)	
Baseline	10.1 ± 0.8	10.2±1.5	0.913
1st follow up (1st month)	10.0±1.0 (n=15)	11.1±1.2 (n=14)	0.015
2nd follow up (3rd month)	10.0±1.4 (n=4)	11.3±2.1 (n=3)	0.355

[a]Mean±SD; Chi-square and Fisher Exact test were performed; A p-value <0.05 was considered as significant.

At the 3-month follow-up, 75.0% patients in the *Phyllanthus emblica* group and 33.3% of the BSC group were classified as Eastern Cooperative Oncology Group (ECOG) performance status (PS) 3, indicating a better performance status in the *Phyllanthus emblica* group, though the difference was not statistically significant (p=0.270) (Table 7).

Table 7. Distribution of the study patients by Eastern Cooperative Oncology Group.

ECOG	Study Subject		*p* value
	Phyllanthus emblica (n=30), n (%)	BCS (n=30), n(%)	
Baseline			
ECOG PS2	0 (0.0)	3 (10.0)	
ECOG PS3	21 (70.0)	17 (56.7)	0.176
ECOG PS4	9 (30.0)	10 (33.3)	
1st follow up (1st month)	(n=15)	(n=14)	
ECOG PS2	2 (13.3)	1 (7.1)	
ECOG PS3	10 (66.7)	7 (50.0)	0.453
ECOG PS4	3 (20.0)	6 (42.9)	
2nd follow up (3rd month)	(n=4)	(n=3)	
ECOG PS3	3 (75.0)	1 (33.3)	0.270
ECOG PS4	1 (25.0)	2 (66.7)	

[a]Mean±SD; Chi-square and Fisher Exact test were performed; A p-value <0.05 was considered as significant.

At 1-month follow-up, 50.0% of patients in the *Phyllanthus emblica* group and 53.3% of patients in the BSC group expired. Although more patients survived in *Phyllanthus emblica* group, it was not statistically significant. At 3-month follow-up, 73.3% in the *Phyllanthus emblica* group and 78.6% in the BSC group died, once again showing statistically non-significant survival benefit in the *Phyllanthus emblica* group (Fig. 4).

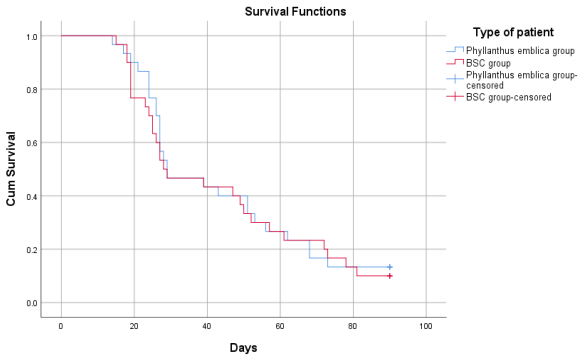

Fig. 4. Kaplan-Meier curve for survival of HCC patients.

Discussion

A review of the literature reveals that several nutrients and herbs have been used in HCC, mainly with preventive intent. Consuming fish rich in n-3 polyunsaturated fatty acids, or supplementing with n-3 polyunsaturated fatty acids, was protective against HCC development in patients with chronic HBV and HCV infection (Sawada et al., 2012). Similarly, studies suggest that fresh fruits and vegetables rich in polyphenols regulate multiple intracellular signaling pathways and reduce the risk of HCC development (Cazarolli et al., 2008; Kiruthiga et al., 2020). The protective role of coffee, which is rich in polyphenols and contains antioxidants and anti-mutagenic compounds, against HCC is also well established (Tao et al., 2008; Kennedyet al., 2017).

However, our focus was more on treatment. Earlier, we worked with herbal medicines produced in the West for the management of end-stage HCC. We conducted two clinical trials with a combination of *Camellia sinensis* (green tea), *Cinnamomum verum* (cinnamone) and *Glycyrrhiza glabra* (glycyrrhizin),

among others, in 29 and 60 patients (Matsui et al., 2002; Morihara et al., 2012). In vitro studies have shown that this combination inhibits HCC cell line proliferation by inducing cell cycle arrest, inhibiting cancer cell proliferation, differentiation,angiogenesis, invasion and metastasis and by stimulating apoptosis (Al-Mahtab et al., 2015). Both studies revealed no significant short-time survival or quality of life benefits. Similarly, our third study with rice bran, which is known for its chemopreventive effect by increasing apoptosis, reducing cell cycle proliferation, and alteration of cancer cell cycle, (Henderson et al., 2012) also showed a non-significant survival benefit and improvement of quality of life in end-stage HCC (Ashrafujjaman et al., 2023). Similarly, other researchers have shown a beneficial role for nutrients in end-stage HCC (Matsui et al., 2002; Morihara et al., 2012).

Our present study revealed a non-statistically significant survival benefit among end-stage-HCC patients treated with locally developed *Phyllanthus emblica* capsules. Similarly, although patients in the *Phyllanthus emblica* group had better outcomes, the difference was not statistically significant. These findings are similar to those of our previous studies on food supplements in end-stage HCC (Matsui et al., 2002; Morihara et al., 2012;Ashrafujjaman et al., 2023). It is well known that end-stage HCC has a very poor outcome with a median survival of 3 to 4 months (Kumar and Panda, 2014).

Limitations

Our sample size was modest. However, having said so, it is also a reality that this type of study with terminally ill patients with end-stage HCC is challenging anywhere in the world, which is why studies involving such patients are not plentiful in the literature. We found that several other phytochemicals in *Phyllanthus emblica*, such as chebulagic acid and ellagic acid, were also effective according to our docking results, but we unfortunately couldn't extract them due to our limitations.

Conclusion

Although we couldn't demonstrate significant improvements in quality of life or survival in end-stage HCC patients treated with *Phyllanthus emblica*, our study is significant for several reasons. It established the safety and limited efficacy of *Phyllanthus emblica* in end-stage HCC. It is one of the early attempts to establish traditional medical knowledge with a modern scientific approach from Bangladesh, where review of traditional medical literature and identifying a prospective remedy, collection of ingredient, laboratory based research and finally human study - the 'bench to bed side' exercise was performed through collaboration between basic and medical scientists belonging to multiple centres with maximum utilization of available resources and with minimum costs involved. It is also an example of academia-industry collaboration. This study may well open a new era of research into repurposing and repositioning our traditional medicines for modern medical practice.

Acknowledgment

The authors gratefully acknowledge Beacon Pharmaceuticals PLC for manufacturing the Amlaki capsules used in this study.

Authors contribution

Md. Rezwanur Rahman: Conducted the study. Manas Saha: Assisted in the study.Mamun Al Mahtab, Md. Abdur Rahim, Sheikh Mohammad Noor E Alam and Dulal Chandra Das: Supervised the study.Rezaul Karim, Rakibul Hasan, Debabrata Karmakar: Performed molecular docking & stimulation and prepared amlaki powder for capsules.Gazi Nurun Nahar Sultana, Sitesh Chandra Bachar, Md. Zakir Sultan and Sheikh Mohammad Fazle Akbar: High Performance Liquid Chromatography. M Shahabuddin K. Choudhuri, Noureen Amin, Musarrat Mahtab: Helped in literature search. Mamun Al Mahtab, Chowdhury Faiz Hossain: Drafted the manuscript. Md. Rezwanur Rahman, Manas Saha, Rokshana Begum, Md. Enayet Ali Pramanik, Sheikh Zahir Raihan, and Ahmed Lutful

Moben: Reviewed the manuscript and did statistical analysis. Rabinarayan Acharya, Anagha Ranade: Revised the manuscript. Mamun Al Mahtab, Sakirul Khan, Rabinarayan Acharya, Sheikh Mohammad Fazle Akbar: Conceptualized the study.

Conflict of interest

The authors declare no conflict of interest.

References

Ahmad B, Hafeez N, Rauf A, Bashir S, Linfang H, Rehman MU, Mubarak MS, Uddin MS, Bawazeer S, Shariati MA and Daglia M. Phyllanthus emblica: A comprehensive review of its therapeutic benefits. *S. Afr. J. Bot. 2021;*138: 278-310.

Al-Mahtab M, Akbar SM, Khan MS and Rahman S. Increased survival of patients with end-stage hepatocellular carcinoma due to intake of ONCOXIN®, a dietary supplement. *Indian J. Cancer*. 2015; 52(3): 443-446.

Ashrafujjaman M, Mahtab MA, Noor-E-Alam SM, Rahim MA, Das DC, Ahmed F, Mamun AA, Mahmud T and Mahmood T. Role of biobran (Arabinoxylan Rice Bran) on patients with advanced stage hepatocellular carcinoma. *Euroasian J Hepatogastroenterol.* 2023; 13(2): 84-88.

Cazarolli LH, Zanatta L, Alberton EH, Figueiredo MS, Folador P, Damazio RG, Pizzolatti MG and Silva FR. Flavonoids: prospective drug candidates. *Mini Rev Med Chem*. 2008; 8(13): 1429-1440.

Cho WR, Huang HL, Hsu NT, Huang TJ and Chang TS. Above-standard survival of hepatocellular carcinoma as the final outcome of comprehensive hepatology care programs in a remote HCV-endemic area. *Viruses*. 2023; 15(3): 786.

Ganjalikhani HM, Jafarinia M, Azizi M, Rezaeepoor M, Isayev O and Bazhin AV. The role of TIM-3 in hepatocellular carcinoma: A promising target for immunotherapy? *Front Oncol*. 2020; 10: 601661.

Henderson AJ, Ollila CA and Kumar A, Borresen EC, Raina K, Agarwal R and Ryan EP. Chemopreventive properties of dietary rice bran: Current status and future prospects. *Adv. Nutr*. 2012; 3(5): 643-653.

Jose JK and Kuttan R. Hepatoprotective activity of emblica officinalis and chyavanaprash. *J. ethnopharmacol.* 2000; 72: 135-140.

Kennedy OJ, Roderick P, Buchanan R, Fallowfield JA, Hayes PC and Parkes J. Coffee, including caffeinated and decaffeinated coffee, and the risk of hepatocellular carcinoma: a systematic review and dose-response meta-analysis. *BMJ Open.* 2017; 7(5): e013739.

Kiruthiga C, Devi KP, Nabavi SM and Bishayee A. Autophagy: A potential therapeutic target of polyphenols in hepatocellular carcinoma. *Cancers (Basel)*. 2020; 12(3): 562.

Kumar M and Panda D. Role of supportive care for terminal stage hepatocellular carcinoma. *J Clin Exp Hepatol.* 2014; 4(Suppl 3): S130-9.

Matsui Y, Uhara J, Satoi S, Kaibori M, Yamada H, Kitade H, Imamura A, Takai S, Kawaguchi Y, Kwon A-Hon and Kamiyama Y. Improved prognosis of postoperative hepatocellular carcinoma patients when treatedwith functional foods: A prospective cohort study. *J. Hepatol*. 2002; 37(1): 78-86.

Morihara D, Iwata K, Hanano T, Kunimoto H, Kuno S, Fukunaga A, Yotsumoto K, Takata K, Tanaka T, Sakurai K, Iwashita H, Ueda Shu-Ichi, Hirano G, Yokoyama K, Nakane H, Nishizawa S, Yoshikane M, Anan A, TakeyamaY, Kakumitsu S, Kitamura Y, Sakamoto M, Irie M, Shakado S, Sohda T, Watanabe H and Sakisaka S. Late-evening snack with branched-chain amino acids improves liver function after radiofrequency ablation for hepatocellular carcinoma. *Hepatol. Res.* 2012; 42(7): 658-667.

Ngamkitidechakul C, Jaijoy K, Hansakul P, Soonthornchareonnon N and Sireeratawong S. Antitumour effects of phyllanthus emblica L.:

induction of cancer cell apoptosis and inhibition of in vivo tumour promotion and in vitro invasion of human cancer cells. *Phytother Res.* 2010; 24(9): 1405-1413.

Pramyothin P, Samosorn P, Poungshompoo S and Chaichantipyuth C. The protective effects of phyllanthus emblica linn. extract on ethanol induced rat hepatic injury. *J. Ethnopharmacol.* 2006; 107: 361-364.

Sawada N, Inoue M, Iwasaki M, Sasazuki S, Shimazu T, Yamaji T, Takachi R, Tanaka Y, Mizokami M and Tsugane S. Japan public health center-based prospective study group. Consumption of n-3 fatty acids and fish reduces risk of hepatocellular carcinoma. *Gastroenterology*. 2012; 142(7): 1468-1475.

Tao KS, Wang W, Wang L, Cao DY, Li YQ, Wu SX and Dou KF. The multifaceted mechanisms for coffee's anti-tumorigenic effect on liver. *Med. Hypotheses.* 2008; 71(5): 730-6.

Yadav SS, Singh MK, Singh PK and Kumar V. Traditional knowledge to clinical trials: A review on therapeutic actions of Emblica officinalis. *Biomed. Pharmacother*. 2017 93: 1292-1302.

Yousef MH, El-Fawal HANand Abdelnaser A. Hepigenetics: A review of epigenetic modulators and potential therapies in hepatocellular carcinoma. *Biomed. Res. Int.* 2020; 2020: 9593254.

J. Bangladesh Acad. Sci. 50(1); 71-98: March 2026 DOI:https://doi.org/10.3329/jbas.v50i1.85275

Journal of Bangladesh Academy of Sciences

Journal homepage: http://www.bas.org.bd/publications/jbas.html

Research Article

A deterministic and fractional order mathematical approach: Prey-predator dynamics in higher education systems

Md. Asraful Islam* and Tanvir Ahmed

Department of Mathematics, Jagannath University, Dhaka, Bangladesh

ARTICLE INFO

Article History

Received: 27 October 2025
Revised: 01 Februray 2026
Accepted: 08 February 2026

Keywords: Academic stress, Under-graduate students, Graduate students, Fractional order, Lyapunov exponent, Bifurcation.

ABSTRACT

This study explores the dynamic relationship between academic stress and student populations in higher education using a deterministic and fractional-order prey-predator framework, where stress acts as the predator and students as the prey. Equilibrium conditions are used to study the system's stability, while bifurcation analyses reveals critical transitions, including flip, fold, Hopf, and Neimark-Sacker bifurcations. Global stability analysis provides insight into the long-term behavior of students under academic constraints, and criteria for persistence and the basic reproduction number are established. The fractional-order approach effectively captures memory effects that influence students' responses. Lyapunov exponents and numerical simulations further elucidate stability thresholds and the emergence of chaotic dynamics. Additionally, bifurcation diagram and basin of attraction analyses illustrate shifts in equilibrium states. The findings suggest that policy interventions targeting highly sensitive factors can significantly influence system dynamics, leadingto measurable changes in academic stress levels and overall stability. The study provides both theoretical and practical insights, demonstrating that undergraduate students tend to experience higher levels of stress than graduate students, primarily due to strict curriculum, more frequent examinations, and limited autonomy in undergraduate education.

Introduction

Early in the 20th century, Alfred Lotka and Vito Volterra independently developed the prey-predator model; the historical foundation of this model is the early application of mathematics to biological and ecological processes. Lotka (1925) derived these equations for the study of chemical processes,and later for biological systems.Volterra(1926) used a similar approach for the research of fish dynamics in the Adriatic Sea. Currently referred to as the Lotka-Volterra equations, they describe interactions between two populations: herbivores and predators, and carnivores. It holds that their interaction controls population dynamics: without predators, prey expand exponentially, and predator populations decline. Since ecosystems, epidemiology, and economics are more dynamic systems, this model has been extended to include those disciplines. This model has been extended to include ecologies, epidemiology, and economics since these are more dynamic systems. A deterministic predator-prey model (Amri et al., 2023; Wang and Yang, 2025) to investigate the effects of velocity on ant predator behavior, refuge dynamics, and interactions. It has performed the stability analysis and found that, at critical predator death rates, the predator-free equilibrium, coexistence conditions, and transcritical bifurcations are globally asymptotically stable.

*Corresponding author: <asraful@math.jnu.ac.bd>

Using a pest management model (Yu et al., 2019) with state feedback control and optimization helps one to control pest numbers. A predator–prey model (Ska et al., 2021; Ahmed et al., 2025) with fear, refuge, and additional food exhibits stability, oscillations, and chaotic dynamics. It has investigated an eco-epidemiological model (Sha et al., 2019) in which the growth of prey and disease transmission is suppressed by fear induced by predators. With conditions for local stability developed, this yields backward bifurcation, instability, oscillations, and chaotic dynamics.

The mechanisms by which fear, shelter, and hunting cooperation influence the dynamics between predators and prey (Mondal et al., 2022) have been extensivelyinvestigated. Establishing global dynamical behavior requirements, initially, they analyze a stochastic two-predator one-prey model with Lévy noise and distributed delays (Tuerxun et al., 2020). It has investigated a nonautonomous predator-prey system (Bai et al., 2020) with a Beddington-DeAngelis response and built appropriate criteria for the global asymptotic stability of boundary solutions. A two-parameter discrete predator-prey model is addressed by Hone et al. (2010). This model sets criteria for stability and bifurcation dynamics and expands Murray's framework. The stability, permanence, extinction, and ecological effects of a stochastic four-species predator-prey model with disease (Gokila et al., 2023) are investigated via simulations. Using geometric methods, a general predator–prey model (Zhu et al., 2022) with state-dependent impulses is examined to determine the conditions for the existence of order-1 periodic solutions and their stability. With specific attention on the function it performs in the creation of patterns, a study is conducted on the effect of prey refuge on the dynamics of predators and prey using bifurcation theory and numerical simulations.

Rising and declining numbers of prey and predators, respectively, reflect the phases of mutual benefit and predator suppression as refuge depths broaden. It analyzed the effects of prey refuges on predator-prey dynamics, considering both constant-proportional and fixed-number refuges. The results (Ma et al., 2009) reveal that, aside from some destabilizing circumstances, prey refuges increase prey density, reduce predator density and usually stabilize the equilibrium. They investigated stability and Hopf bifurcation dynamics in a stage-structured predator-prey model (Bai and Li, 2019) with extra predator food and prey refuge. It studies a predator-prey model including both discrete and distributed delays; the discrete delay is considered as a bifurcation parameter. Hopf bifurcation occurs at a turning point (Ma et al., 2009; Misra and Dubey, 2010), and normal form theory defines the stability and features of periodic solutions.

The dynamics of an impulsive state feedback-controlled Holling type II predator-prey system (Jiang et al., 2007) is investigated theoretically and numerically. Lyapunov exponents and bifurcation analysis help identify periodic and chaotic behavior, thereby demonstrating the effectiveness of the control approach. Using a Markovian switching technique to address telephone noise modeling, a stochastic regime-switching predator-prey model (Liu et al., 2018) is built with harvesting and distributed delays. It explores extinction scenarios, population persistence, and ideal harvesting strategies in detail. Analysis of a non-autonomous ratio-dependent predator-prey system (Bai et al., 2014) driven by Lévy noise reveals global positive solutions, stochastic boundedness, persistence, extinction conditions, and asymptotic behavior. Numerical simulations help verify these results. Stability and bifurcation analysis (Hu and Cao, 2017) of a nonlinear Michaelis-Menten type predator harvesting system are investigated. Equilibrium existence and stability are found using numerical and mathematical methods. Moreover, numerical simulations investigate the Bogdanov-Takens bifurcation under a universal unfolding around the cusp, therefore verifying the theoretical conclusions. The worldwide attraction and permanency criteria of

a stage-structured predator-prey model (Song et al., 2009) are investigated in this work.

An examination of stability, Hopf bifurcation occurrence, bifurcation direction, and periodic solution stability is conducted through theoretical analysis and numerical simulations for a stage-structured predator–prey system (Li and Li, 2012) with Holling type-III response and time delay. Using a modified Holling type-II functional response, the stability of a two-dimensional prey-predator system with dual delays (Dubey et al., 2019) is investigated. Additionally, the implications of habitat complexity and prey refuge are explored. In this study, the stability and Hopf bifurcations in stage-structured predator-prey systems (Wei and Fu, 2016) with Beddington-DeAngelis functional response are examined. Additionally, the effects of prey refuge are analyzed using characteristic equation analysis. By preventing the extinction of prey, supporting global cohabitation (Xiang et al., 2023), and creating complex dynamics, such as numerous periodic orbits and homoclinic loops, as demonstrated by the Holling-Tanner model, refuge plays an essential role in maintaining ecosystems stability. In this study, the complex dynamics (Wang et al., 2014) arising from the Allee effect in a predator-prey model are investigated. The findings of this study demonstrate instability, diffusion-driven instability, and a variety of pattern forms, such as stripes, spots, and stripe-hole mixtures. It has investigated a Lotka–Volterra predator–prey model incorporates cannibalism (Deng et al., 2019; Respondek et al., 2017). The findings indicate that cannibalism can stabilize or destabilize the system, thereby affecting the coexistence or extinction of species. This is contingent on the dynamics of the original system and the intensity of cannibalism (Christle et al., 2007).

Motivated by the aforementioned research, we investigate using a predator-prey mathematical model the intricate interaction between academic stress and student well-being. Academic pressure rises alongside concerns about student mental health, fatigue, and performance. often, traditional explanations ignore system-level dynamics in favor of ecological, psychological, or sociological factors. This work fills that knowledge gap by simulating academic stress as the predator and students as the prey, thereby investigating how different stress levels affect student population stability. Understanding these dynamics is essential, as unbridled instabilities may drive the system into critical transitions or into chaos, necessitating quick intervention.

This study aims to systematically investigate the intricate interaction between the academic stress variable and the higher education student population. This work uses the Caputo fractional derivative in the context of predator-prey dynamics. Constructing a nonlinear mathematical model using differencing equations helps one assess the long-term effects of academic pressure on student stability. Furthermore, Lyapunov functions are used in a stability study of the equilibrium state to determine the number of equilibrium states and the stability of each one under several academic stresses. Numerical simulations allow one to investigate stress levels that produce changes in equilibrium. Hopf bifurcation, fold bifurcation, and flip bifurcation all influence the stress levels in educational systems that, over time, become unstable. Sensitivity analysis is used to ascertain how small variations in academic load could affect student population dynamics. The basin of attraction is thoroughly analyzed to identify initial conditions that lead to distinct long-term outcomes in the dynamics of academic stress and student populations. Analyzing sensitivity to initial conditions with Lyapunov exponents in the last stage reveals chaos and uncertainty. These contributions provide both theoretical and practical tools for developing long-term academic strategies.

Our current manuscript focuses on theoretical development and simulation-based insights due to limited access to longitudinal student stress datasets. The ABC fractional-order prey–predator model offers a refined framework for describing systems with long-term interdependencies, such as academic stress dynamics. Unlike traditional integer-order models, the ABC fractional-order derivatives add novelty by capturing memory effects that more accurately reflect how academic stress accumulates and affects student populations over time.

Formulation of the deterministic approach model

Using phase plane approaches, phase portraiture, numerical simulations, and stability analysis clarifies the dynamical behavior of the one- prey-one-predator model (Islam and Ahmed, 2024).This model (1) illustrates the predator-prey relationship between academic pressure (N_1), undergraduates (N_2) and graduate students (N_3) in higher education. The immense number of students enrolled in both the undergraduate and graduate programs makes academic pressure a formidable predator, causing stress and driving fierce competition for limited resources. Additionally, there is a feedback loop between the two groups of students, as the development of one group affects the pressures and scholastic requirements of the other. Academic pressure increases or decreases with student numbers, just as every population has its own intrinsic growth rate.

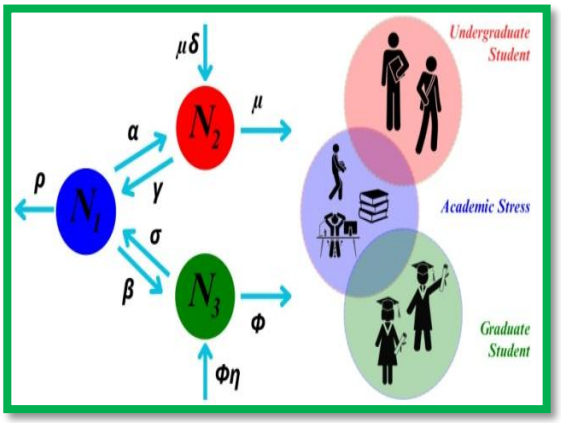

Fig. 1. Network diagram of the system with population states and transition pathways.

$$\begin{cases} \dfrac{dN_1}{dt} = \left(-\rho + \alpha N_2 + \beta N_3\right)N_1; \quad N_1(t) \geq 0 \\ \dfrac{dN_2}{dt} = \left(\mu(\delta - N_2) - \gamma N_1\right)N_2; \quad N_2(t) \geq 0 \\ \dfrac{dN_3}{dt} = \left(\phi(\eta - N_3) - \sigma N_1\right)N_3; \quad N_3(t) \geq 0 \end{cases} \tag{1}$$

As shown in Fig. 1, academic pressure is a predator that increases with student count but subsequently eliminates $(-\rho)$. The term $\alpha N_2 + \beta N_3$ describes the scenario whereby rising student enrolment results in a rise in rivalry for limited resources such as faculty, money, and research possibilities, therefore generating an increase in academic pressure (N_1). Constraints in resources including space, money, and faculty are causing the enrolment to be slowing down as it approaches capacity (δ). The sign $\mu(\delta - N_2)$ shows this. Referred to as $-\gamma N_1 N_2$, the loss of undergraduate students due to academic pressure (N_1) can cause stress, failures, and school dropout. The tenacity of undergraduates decreases in a predator-prey interaction as pressure (N_1). increases. A logistic growth model is used to characterize graduate students; $\phi(\eta - N_3)$ represents this model. The growth rate slows down to consider the limited resources when N_3 gets closer to its maximum. The theory of $-\alpha N_1 N_3$ explains how academic pressure N_1 can have a detrimental effect on graduate students (N_3), therefore causing burnout, delayed graduation, or a lack of willingness to continue their studies. Consistent with the predator-prey dynamic, a drop in N_3 results from an increase in N_1. A numerical measure of how rapidly academic pressure (N_1) influences graduate student retention rate (N_3), is captured by the coefficient α.

Table 1. The model description of parameters.

Parameter	Parameter Description	Parameter	Parameter Description
N_1	Predator: The population of predator which is academic pressure	α and β	Efficiency of academic pressure affecting undergraduate students and graduate students.
N_2	Prey 1: The population of undergraduate students	δ and η	Carrying capacities of the environment for undergraduate students and graduate students.
N_3	Prey 2: The population of graduate students	γ and σ	These could represent dropout rates for undergraduate students and graduate studentsdue to *a*cademic pressure.
ρ	The reduction rate for academicpressure	μ and λ	The factors that encourage an increase in student numbers.

Table 2. Initial values of parameters for α, β, γ, σ, μ.

Parameter	Values*	Parameter	Values**
α	0.02	σ	0.03
β	0.02	μ	0.01
γ	0.01		

Data source:*Tuerxun et al., 2020;**Wang et al., 2025

Local stability analysis of the model

A system of nonlinear equations (1) is first considered. The first aim is to find out the equilibrium points. For this purpose, set

$$P = (-\rho + \alpha N_2 + \beta N_3)N_1 = 0$$
$$Q = (\mu(\delta - N_2) - \gamma N_1)N_2 = 0$$
$$R = (\phi(\eta - N_3) - \sigma N_1)N_3 = 0$$

$$(u_0, v_0, w_0) = \{(0,0,0), (\frac{\mu\phi(\delta\alpha - \rho + \eta\beta)}{\gamma\alpha\phi + \sigma\beta\mu}, \frac{\gamma\rho\phi + \delta\sigma\beta\mu - \eta\gamma\beta\phi}{\gamma\alpha\phi + \sigma\beta\mu}, \frac{\sigma\rho\mu - \delta\sigma\alpha\mu + \eta\gamma\alpha\phi}{\gamma\alpha\phi + \sigma\beta\mu}),$$
$$(0,\delta,0), (0,0,\eta), (0,\delta,\eta), (\frac{-\mu(\rho - \delta\alpha)}{\gamma\alpha}, \frac{\rho}{\alpha}, 0), (\frac{-\phi(\rho - \eta\beta)}{\sigma\beta}, 0, \frac{\rho}{\beta})\}$$

The Jacobian matrix is defined as

$$J_{(u,v,w)} = \begin{pmatrix} P_{N_1} & P_{N_2} & P_{N_3} \\ Q_{N_1} & Q_{N_2} & P_{N_3} \\ R_{N_1} & R_{N_2} & R_{N_3} \end{pmatrix}$$

Where, $P = (-\rho + \alpha N_2 + \beta N_3)N_1$, $Q = (\mu(\delta - N_2) - \gamma N_1)N_2$, and $R = (\phi(\eta - N_3) - \sigma N_1)N_3$. Now differentiation of both P, Q and R with respect to N_1, N_2 and N_3 respectively and the Jacobian matrix is

$$J_{(u,v,w)} = \begin{pmatrix} \alpha N_2 - \rho + \beta N_3 & \alpha N_1 & \beta N_1 \\ -\gamma N_2 & \mu(\delta - 2N_2) - \gamma N_1 & 0 \\ -\sigma N_3 & 0 & \phi(\eta - 2N_3) - \delta N_1 \end{pmatrix}$$

Suppose $N_1 = u_0, N_2 = v_0, N_3 = w_0$
This yields the equilibrium points

Case 1: For the fixed point **(0,0,0)**

$$J_{(0,0,0)} = \begin{pmatrix} -\rho & 0 & 0 \\ 0 & \delta\mu & 0 \\ 0 & 0 & \eta\phi \end{pmatrix}$$

In this case, the eigenvalues are $-\rho$, $\delta\mu$ and $\eta\phi$, which are real; one is negative and the other two are positive. Then $(0,0,0)$, the trivial equilibriums always unstable.

Case 2: For the fixed point

$$(\frac{\mu\phi(\delta\alpha-\rho+\eta\beta)}{\gamma\alpha\phi+\sigma\beta\mu},\frac{\gamma\rho\phi+\delta\sigma\beta\mu-\eta\gamma\beta\phi}{\gamma\alpha\phi+\sigma\beta\mu},\frac{\sigma\rho\mu-\delta\sigma\alpha\mu+\eta\gamma\alpha\phi}{\gamma\alpha\phi+\sigma\beta\mu}),$$

$$J=\begin{pmatrix} p^* & \frac{\alpha\mu\phi(\delta\alpha-\rho+\eta\beta)}{\gamma\alpha\phi+\sigma\beta\mu} & \frac{\beta\mu\phi(\delta\alpha-\rho+\eta\beta)}{\gamma\alpha\phi+\sigma\beta\mu} \\ -\frac{\gamma(\gamma\rho\phi+\delta\sigma\beta\mu-\eta\gamma\beta\phi)}{\gamma\alpha\phi+\sigma\beta\mu} & q^* & 0 \\ -\frac{\sigma(\sigma\rho\mu-\delta\sigma\alpha\mu+\eta\gamma\alpha\phi}{\gamma\alpha\phi+\sigma\beta\mu} & 0 & r^* \end{pmatrix}$$

Where $p^*=\frac{\beta(\sigma\rho\mu-\delta\sigma\alpha\mu+\eta\gamma\alpha\phi)}{\gamma\alpha\phi+\sigma\beta\mu}-\rho+\frac{\alpha(\gamma\rho\phi+\delta\sigma\beta\mu-\eta\gamma\beta\phi}{\gamma\alpha\phi+\sigma\beta\mu}$,

$q^*=\mu(\delta-\frac{\alpha\rho\phi+\delta\sigma\beta\mu-\eta\gamma\beta\phi}{\gamma\alpha\phi+\sigma\beta\mu})-\mu\frac{\gamma\rho\phi+\delta\beta\sigma\mu-\eta\gamma\beta\phi}{\gamma\alpha\phi+\sigma\beta\mu}-\frac{\gamma\mu(\delta\alpha\phi-\rho\phi+\eta\beta\phi)}{\gamma\alpha\phi+\sigma\beta\mu}$

and

$r^*=\phi(\eta-\frac{\sigma\rho\mu-\delta\sigma\mu+\eta\gamma\alpha\phi}{\eta\gamma\alpha\phi})-\frac{\phi(\sigma\rho\mu-\delta\sigma\alpha\mu+\eta\gamma\alpha\phi)}{\gamma\alpha\phi+\sigma\beta\mu}-\frac{\sigma\mu(\delta\alpha\phi-\rho\phi+\eta\beta\phi)}{\gamma\alpha\phi+\sigma\beta\mu}$

The eigenvalue in the general form is very complicated to find in this case.

Case 3: For the fixed point $(0,\delta,0)$

$$J_{(0,\delta,0)}=\begin{pmatrix}\delta\alpha-\rho & 0 & 0\\ \delta\gamma & -\delta\mu & 0\\ 0 & 0 & \eta\phi\end{pmatrix}$$

In this case, the eigenvalues are $\delta\alpha-\rho$, $-\delta\mu$ and $\eta\phi$, which are real: one is negative, and the other two are positive. Therefore, $(0,\delta,0)$ is an unstable point.

Case 4: For the fixed point $(0,0,\eta)$

$$J_{(0,0,\eta)}=\begin{pmatrix}\eta\beta-\rho & 0 & 0\\ 0 & \delta\mu & 0\\ -\eta\beta & 0 & -\eta\phi\end{pmatrix}$$

In this case, the eigenvalues are $\eta\beta-\rho$, $\delta\mu$ and $-\eta\phi$, which are real: one is negative, and the other two are positive, since all the constants are positive. Therefore, $(0,0,\eta)$ is an unstable point. Here two eigenvalues are complex and one is real. Hence, it is a stable spiral for the complex values.

Case 5: For the fixed point $(0,\delta,\eta)$

$$J_{(0,\delta,\eta)}=\begin{pmatrix}\delta\alpha-\rho+\eta\beta & 0 & 0\\ -\delta\gamma & -\delta\mu & 0\\ -\eta\sigma & 0 & -\eta\phi\end{pmatrix}$$

In this case, the eigenvalues are $\delta\alpha-\rho+\eta\beta$, $-\delta\mu$ and $-\eta\phi$, which are real: one is negative and the other two are positive, since all the constants are positive.Since the real value is negative and real parts of the eigen values are also negative. Hence, $(0,\delta,\eta)$ is an unstable point.

Case 6: For the fixed point $(\frac{-\mu(\rho-\delta\alpha)}{\gamma\alpha},\frac{\rho}{\alpha},0)$

$$J_{(\frac{-\mu(\rho-\delta\alpha)}{\gamma\alpha},\frac{\rho}{\alpha},0)}=\begin{pmatrix}0 & \frac{-\mu(\rho-\delta\alpha)}{\gamma} & -\frac{\beta\mu(\rho-\delta\alpha)}{\gamma\alpha}\\ -\frac{\gamma\rho}{\alpha} & -\frac{\rho\mu}{\alpha} & 0\\ 0 & 0 & \eta\phi+\frac{\sigma\mu(\rho-\delta\alpha)}{\gamma\alpha}\end{pmatrix}$$

In this case the eigenvalues are

$-\frac{\rho\mu+\sqrt{\rho\mu(-4\delta\alpha^2+4\rho\alpha+\rho\mu)}}{2\alpha}$,

$\frac{\sigma\rho\mu-\delta\sigma\alpha\mu+\eta\gamma\alpha\phi}{\gamma\alpha}$ and $-\frac{\rho\mu-\sqrt{\rho\mu(-4\delta\alpha^2+4\rho\alpha+\rho\mu)}}{2\alpha}$

. If the discriminant $\rho\mu(-4\delta\alpha^2+4\rho\alpha+\rho\mu)\geq 0$ then 2 of the eigenvalues are negative and, one is positive. Therefore, $(\frac{-\mu(\rho-\delta\alpha)}{\gamma\alpha},\frac{\rho}{\alpha},0)$ is an unstable point. On the other hand, if $\rho\mu(-4\delta\alpha^2+4\rho\alpha+\rho\mu)<0$ then two of the eigenvalues are complex and one is real. Real part of the eigenvalues is negative, but the real eigenvalue is positive, which are real and one of them is negative and the other two is positive. Hence, $(\frac{-\mu(\rho-\delta\alpha)}{\gamma\alpha},\frac{\rho}{\alpha},0)$ is an unstable point.

Case 7: For the fixed point $(\frac{-\phi(\rho-\eta\beta)}{\sigma\beta},0,\frac{\rho}{\beta})$

$$J_{(\frac{-\phi(\rho-\eta\beta)}{\sigma\beta},0,\frac{\rho}{\beta})}=\begin{pmatrix}0 & -\frac{\alpha\phi(\rho-\eta\beta)}{\sigma\beta} & -\frac{\phi(\rho-\eta\beta)}{\sigma}\\ 0 & \frac{\delta\mu+\gamma\phi(\rho-\eta\beta)}{\sigma\beta} & 0\\ -\frac{\sigma\rho}{\beta} & 0 & -\frac{\rho\phi}{\beta}\end{pmatrix}$$

In this case, the eigenvalues are

$-\frac{\rho\phi+\sqrt{\rho\phi(-4\eta\beta^2+4\rho\beta+\rho\phi)}}{2\beta}$, $\frac{\gamma\rho\phi+\delta\sigma\beta\mu+\eta\gamma\beta\phi}{\sigma\beta}$

and $-\frac{\rho\phi-\sqrt{\rho\phi(-4\eta\beta^2+4\rho\beta+\rho\phi)}}{2\beta}$. If the discriminate $\rho\phi(-4\eta\beta^2+4\rho\beta+\rho\phi)\geq 0$ then 2 of the eigenvalues are negative and, one is positive. Therefore, $(\frac{-\mu(\rho-\delta\alpha)}{\gamma\alpha},\frac{\rho}{\alpha},0)$ is an unstable point. On the other hand, if $\rho\phi(-4\eta\beta^2+4\rho\beta+\rho\phi)<0$ then two of the

eigenvalues are complex and one is real. Real part of the eigenvalues is negative, but the real eigenvalue is positive, which are real and one of them is negative, and the other two are positive. Hence, $(\frac{-\phi(\rho-\eta\beta)}{\sigma\beta},0,\frac{\rho}{\beta})$ is an unstable point.

Mathematical and dynamic analysis of the model

Positivity results

Theorem 1: Suppose $N_1(0)>0, N_2(0)>0, N_3(0)>0$.

The solutions $N_1(t), N_2(t), N_3(t)$ *remain positive for all* $N_2(t)$

Proof: From equation (1), we have

$\frac{dN_1}{dt}=(-\rho+\alpha N_2+\beta N_3)N_1$ *Set*, $-\rho+\alpha N_2+\beta N_3=\kappa$

Now,

$\frac{dN_1}{dt}=\kappa N_1 \Rightarrow \frac{dN_1}{N_1}=\kappa$

Integrating w.r.to t

$\int\frac{dN_1}{N_1}=\kappa\int dt \Rightarrow \ln N_1=\kappa t+C$

Where C is an arbitrary constant.

$\Rightarrow N_1=e^{\kappa t+C}$

$\Rightarrow N_1=e^{\kappa t}.e^{c}$

$\Rightarrow N_1(t)=C_1e^{\kappa t}$

Applying initial conditions $N_1(0)=N_{10}$

$\Rightarrow N_1(0)=C_1e^{0}\Rightarrow N_1(0)=C_1$

$\Rightarrow N_1(t)=N_1(0)e^{\theta t}$

The above expression depicts that $N_1(t)$ is nonnegative for all *t*. Similarly, $N_2(t)$ and $N_3(t)$ are positive for all $t\geq 0$.

Persistence of students populations

Theorem 2: The populations of undergraduate students (N_2) and graduate students (N_3) persist over time if academic pressure (N_1) does not exceed a critical threshold.

Proof: To prove Theorem 4.2 on the persistence of student populations, we need to analyze the conditions under which the populations of undergraduate students, N_2 and graduate students, N_3, remain positive over time, assuming initial values $N_1(0)>0, N_2(0)>0, N_3(0)>0$.

For $N_2>0$, we require: $\mu(\delta-N_2)\geq\gamma N_1$

Solving for N_1 we get a critical threshold:

$N_1\leq\frac{\mu(\delta-N_2)}{\gamma}$

Thus, for N_2 to persist over time, academic pressure, N_1 must remain below this threshold.

Conditions for N_3, the graduate population to remain positive

Similarly, N_3 to remain positive, it is required

$N_3'=(\phi(\eta-N_3)-\sigma N_1)N_3\geq 0$

$(\phi(\eta-N_3)-\sigma N_1)N_3\geq 0$

For $N_3>0$, it is required $(\phi(\eta-N_3))\geq\sigma N_1$

Solving for N_1 we get a critical threshold:

$N_1\leq\frac{\phi(\eta-N_3)}{\sigma}$

Thus, for N_3 to persist, academic pressure, N_1 must remain below this threshold.

For both N_2 and N_3 to positive simultaneously, we combine the two threshold conditions:

$N_1\leq\min\left(\frac{\mu(\delta-N_2)}{\gamma},\frac{\phi(\eta-N_3)}{\sigma}\right)$

The populations of undergraduate students (N_2) and graduate students (N_3) persist over time if academic pressure (N_1) does not exceed a critical threshold.

As shown in Fig. 2, Tables 1 and 2, with a decrease from 0.5 to nearly 0.2, academic pressure (N_1) remains near the critical threshold. Graduate (N_3) and undergraduate (N_2) populations grow over time by approximately 0.9 and 1.5 percentage points, respectively.

Basic reproduction number

In the present manuscript, the next-generation matrix approach is used to derive the basic reproduction number R_0, where the academic pressure variable N_1 is decomposed into stress-generation and stress-reduction components.

$F(N)$: Contributions to stress from students

$V(N)$: Outflows and damping of stress

$$\frac{dN1}{dt}=(-\rho+\alpha N_2+\beta N_3)N_1$$

$F(N)=(\alpha N_2+\beta N_3)N_1$ New stress sources

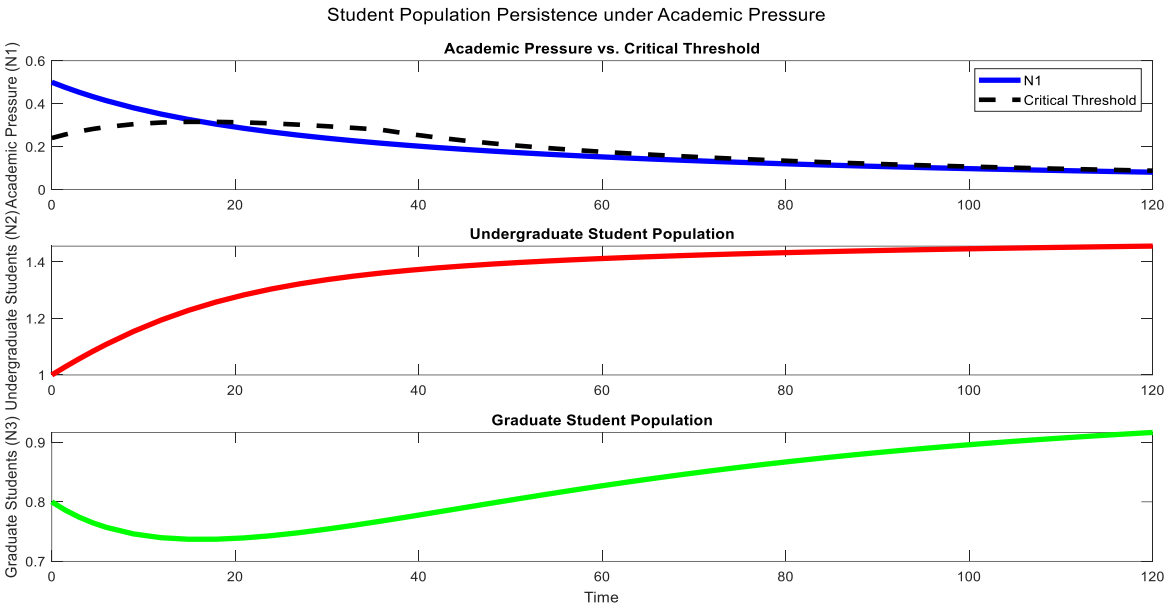

Fig. 2. The findings of the simulation show that the amount of academic pressure (N_1) on student populations varies around a key threshold.

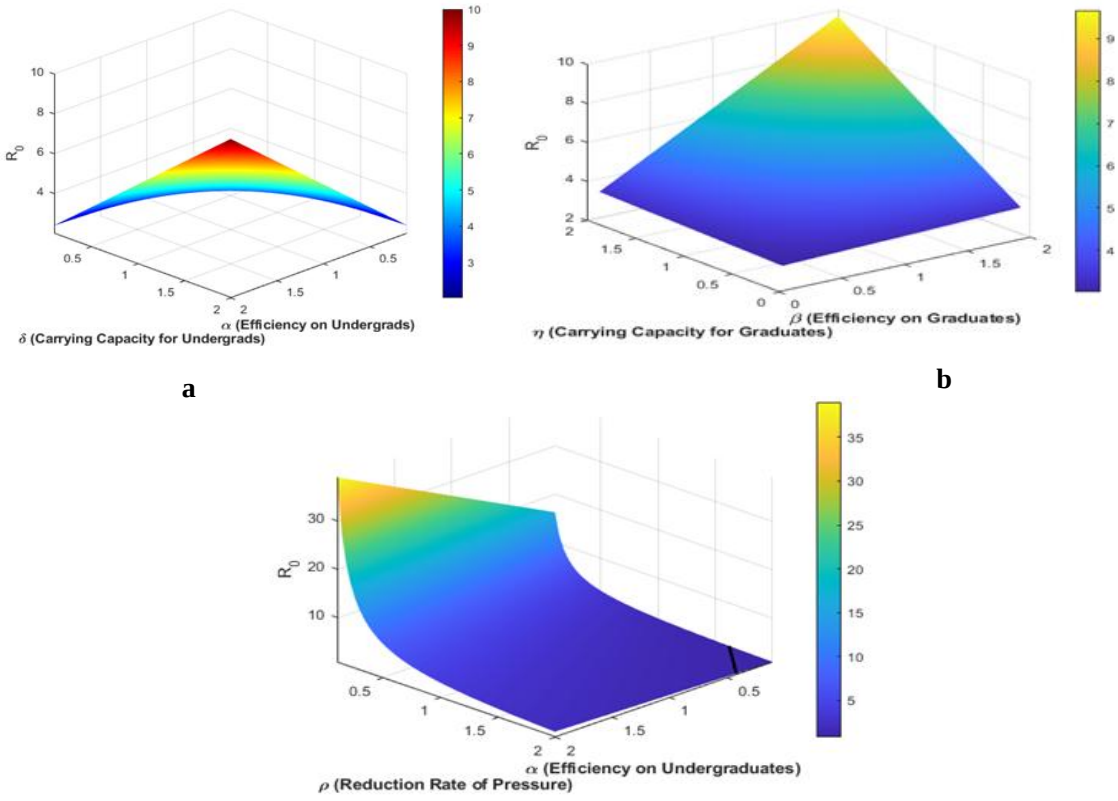

Fig. 3. Effect of basic reproduction number (a) R_0 vs. α and δ, (b) R_0 vs. β and η, (c) R_0 vs. α and ρ.

$V(N) = \rho N_1$ Stress decay

$$F = \frac{\partial F(N)}{\partial N_1} = \frac{\partial}{\partial N_1}(\alpha N_2 + \beta N_3)N_1$$

$$F = \frac{\partial F(N)}{\partial N_1} = \alpha N_2 + \beta N_3$$

Stress-free equilibrium point, $N_1 = 0, N_2 = \delta, N_3 = \eta$

$$F = \alpha\delta + \beta\eta$$

$$V = \frac{\partial}{\partial N_1}V(N)$$

$$V = \frac{\partial}{\partial N_1}(\rho N_1) = \rho$$

$$V^{-1} = \frac{1}{\rho}$$

Next generation matrix

$$R_0 = FV^{-1}$$

$$R_0 = \frac{\alpha\delta+\beta\eta}{\rho} \qquad (2)$$

Fig. 3 show that R_0 increases with pressure efficiency (α, β) and carrying capacities(δ, η), but decreases sharply with a higher pressure reduction rate ρ, emphasizing its dominant control role.

Bifurcation analysis

Bifurcations mark locations within a system, at which the system shifts from one state to another, usually resulting in novel patterns, structures, and its dynamics.The characteristic matrix of (1) is

$$J - \lambda I = \begin{bmatrix} (-\rho + \alpha N_2 + \beta N_3) - \lambda & \alpha N_1 & \beta N_1 \\ -\gamma N_2 & (\mu(\delta - 2N_2) - \gamma N_1) - \lambda & 0 \\ -\sigma N_3 & 0 & (\phi(\eta - 2N_3) - \sigma N_1) - \lambda \end{bmatrix}$$

The characteristic equation is $|J - \lambda I| = 0$

$$\Rightarrow ((-\rho + \alpha N_2 + \beta N_3) - \lambda)[((\mu(\delta - 2N_2) - \gamma N_1) - \lambda)((\phi(\eta - 2N_3) - \sigma N_1) - \lambda)] -$$
$$\alpha N_1((-\gamma N_2))((\phi(\eta - 2N_3) - \sigma N_1) - \lambda) + \beta N_1[0 - [(-\sigma N_3)((\mu(\delta - 2N_2) - \gamma N_1) - \lambda)]] = 0$$

$$\Rightarrow ((-\rho + \alpha N_2 + \beta N_3) - \lambda)\begin{bmatrix} \mu(\delta - 2N_2)(\phi(\eta - 2N_3)) - \mu(\delta - 2N_2)\sigma N_1 - \mu\lambda(\delta - 2N_2) \\ -\gamma N_1(\phi(\eta - 2N_3)) - \gamma\sigma N_1{}^2 - \gamma\lambda N_1 - \lambda(\phi(\eta - 2N_3)) + \sigma\lambda N_1 + \lambda^2 \end{bmatrix}$$
$$-\alpha N_1[-\gamma N_2(\phi(\eta - 2N_3)) + \gamma\sigma N_1 N_2 + \gamma\lambda N_2] + \beta N_1[-[(-\sigma N_3)(\mu(\delta - 2N_2)) + \sigma\gamma N_1 N_2 + \sigma\lambda N_3]] = 0$$

$$\Rightarrow ((-\rho + \alpha N_2 + \beta N_3) - \lambda)\begin{bmatrix} (\mu\delta - 2\mu N_2)(\phi\eta - 2\phi N_3) - \mu\delta\sigma N_1 + 2\mu\sigma N_1 N_2 - \mu\lambda\delta \\ 2\mu\lambda N_2 - \gamma N_1(\phi\eta - 2\phi N_3) - \gamma\sigma N_1{}^2 - \gamma\lambda N_1 - \lambda\phi\eta + 2N_3\lambda \\ \sigma\lambda N_1 + \lambda^2 \end{bmatrix} -$$
$$\alpha N_1[-\gamma N_2\phi\eta + 2\gamma N_2 N_3 + \gamma\sigma N_1 N_2 + \gamma\lambda N_2] + \beta N_1[\sigma\mu\delta N_3 - 2\sigma N_2 N_3 + \sigma\gamma N_1 N_2 + \sigma\lambda N_3] = 0$$

$$\Rightarrow -\lambda^3 + A\lambda^2 + B\lambda + C = 0$$

$$\Rightarrow \lambda^3 - A\lambda^2 - B\lambda - C = 0 \qquad (3)$$

Where, $A = (-\rho + \alpha N_2 + \beta N_3 + \mu\delta - 2\mu N_2 + \gamma N_1 + \phi\eta - 2N_3 - \sigma N_1)$.

$B = (\mu\rho\delta - 2\rho\mu + \rho\gamma N_1 + \rho\phi\eta -$
$-2\rho N_3 - \rho\sigma N_1 - \alpha\mu\delta N_2 + 2\alpha\mu N_2{}^2 - \alpha\gamma N_1 N_2 - \alpha\phi\eta N_2 + 2\alpha N_2 N_3 + \alpha\sigma N_1 N_2 - \mu\beta\delta +$
$2\beta\mu N_2 N_3 - \beta\rho\gamma N_1 N_3 - \beta\phi\eta N_3 + 2\beta\rho N_3{}^2 + \beta\sigma N_1 N_3 - \mu\delta\phi\eta + 2\mu\delta\phi N_3 + 2\mu\phi\eta N_2 - 4\mu\phi N_2 N_3 + \mu\delta\sigma N_1$
$-2\mu\sigma N_1 N_2 + \gamma\phi\eta N_1 - 2\phi\gamma N_1 N_2 + \gamma\sigma N_1{}^2 - \alpha\gamma N_1 N_2 + \beta\sigma N_1 N_2)$.

$C = (2\rho\mu\delta\phi N_3 - \rho\mu\delta\phi\eta + 2\mu\rho\phi\eta N_2 -$
$4\rho\mu\phi N_2 N_3 + \rho\mu\delta\sigma N_1 - 2\rho\mu\sigma N_1 N_2 + \rho\gamma\phi\eta N_1 - 2\rho\phi\gamma N_1 N_3 + \rho\gamma\sigma N_1{}^2 + \alpha\mu\delta\phi\eta N_2 - 2\alpha\mu\delta\phi N_2 N_3 -$
$2\alpha\mu\phi\eta N_2{}^2 + 4\alpha\mu\phi N_2{}^2 N_3 - \alpha\mu\delta\sigma N_1 N_2 + 2\alpha\mu\sigma N_1 N_2{}^2 - \alpha\gamma\phi\eta N_1 N_2 + 2\alpha\phi\gamma N_1 N_2 N_3 - \alpha\gamma\sigma N^{1^2} N_2$
$+ \beta\mu\delta\phi\eta N_3 - 2\beta\mu\delta\phi N_3{}^2 - 2\mu\beta\rho\phi\eta N_2 N_3 + 4\beta\mu\phi N_2 N_3{}^2 - \beta\rho\mu\delta\sigma N_1 N_3 + 2\beta\mu\sigma N_1 N_2 N_3$
$-\beta\gamma\phi\eta N_1 N_3 + 2\beta\phi\gamma N_1 N_3{}^2 - \beta\gamma\sigma N_1{}^2 N_3 + \alpha\gamma\phi\eta N_1 N_2 - 2\alpha\gamma N_1 N_2 N_3 - \alpha\gamma\sigma N_1{}^2 N_2 + \beta\sigma\mu\delta N_1 N_2$
$-2\beta\sigma N_1 N_2 N_3 + \beta\sigma\gamma N_1{}^2 N_3 - 2\beta\sigma N_1 N_2 N_3 + \beta\sigma\gamma N_1{}^2 N_3)$.

Fold bifurcation

In a prey-predator model with student populations and academic stress, a fold bifurcation occurs as from parameter is varied, leading to two equilibrium points: one stable and one unstable, which converge and then destroy. Little changes in stressful circumstances have caused the system to shift from a stable to an unstable stress state. For fold bifurcation (Islam et al., 2025; Zheng et al., 2018) $\lambda = 1$, then the equation (3) becomes

$$\Rightarrow 1^3 - A.1^2 - B.1 - C = 0$$
$$\Rightarrow A + B + C = 1$$

Flip bifurcation

Through the flip bifurcation of the student-prey-predator model incorporating academic stress, a better understanding of how increasing stressor intensity might influence students' stress levels, thereby transforming them from stable to oscillatory or even chaotic. This phenomenon increases the risk of burnout, inefficiency, and erratic academic performance for students. For fold bifurcation (Islam et al., 2025; Zheng et al., 2018) $\lambda = -1$, then the equation (3) becomes

$$\lambda^3 - A\lambda^2 - B\lambda - C = 0$$
$$-1 - A + B - C = 0$$
$$\Rightarrow A - B + C = -1$$

Hopf bifurcation

There are some Hopf bifurcations in a prey-predator model of student populations regarding academic stress, which lay the foundations of understanding transitions between equilibrium and periodic behavior. With increasing stress, the system can transition from a steady-state stress that can be managed to periodic oscillations, in which stress levels fluctuate. These oscillations are stable or unstable depending on the nature of the Hopf bifurcation: supercritical or subcritical. This analysis reveals how minor variations in stress can lead to dramatic changes in student behavior and health, thereby affecting how students deal with academic tests.

Theorem 3: The system (1) exhibits a Hopf bifurcation when the reduction rate for academic pressure, indicated as ρ, approaches a critical value designated as ρ_c. This results in the characteristic equation exhibiting a pair entirely imaginary eigenvalues $\lambda = \pm i\omega$. The existence of $\rho = \rho_c$ such a Hopf bifurcation (Sha et al., 2019) can occur under some conditions.

(i) The equation (3) has a pair of purely imaginary roots $\lambda = \pm i\omega$.

(ii) The real part of eigenvalues sign as ρ varies, i.e.

$$\frac{d}{d\rho}\mathrm{Re}(\lambda(\rho))\Big|_{\rho=\rho_c} \neq 0$$

Proof: At $\boldsymbol{\rho = \rho_c}$, for the Hopf bifurcation $\lambda = \pm i\omega$, equation (3) becomes

$$(i\omega)^3 - A(i\omega)^2 - B(i\omega) - C = 0$$
$$\Rightarrow -i\omega^3 + A\omega^2 - Bi\omega - C = 0$$

Equating the real and imaginary parts as follows,

$$\Rightarrow A\omega^2 - C = 0$$
$$\Rightarrow \omega^2 = \frac{C}{A}$$

$$(-i\omega)^3 - A(-i\omega)^2 - B(-i\omega) - C = 0$$
$$\Rightarrow -i^3\omega^3 - Ai^2\omega^2 + Bi\omega - C = 0$$
$$\Rightarrow i\omega^3 + A\omega^2 + i\omega - C = 0$$

Equating the real and imaginary parts as follows,

$$\Rightarrow A\omega^2 - C = 0$$
$$\Rightarrow \omega^2 = \frac{C}{A}$$

Where ω the frequency at the purely imaginary eigenvalues occurs.

Imaginary part:

$$-\omega^3 - \rho\omega = 0 \Rightarrow \omega^3 + \rho\omega = 0 \Rightarrow \omega(\omega^2 + \rho) = 0$$

Since $\omega \neq 0$, it follows that: $B + \omega^2 = 0 \Rightarrow B = -\omega^2$ (4)

From the real part equation $\omega^2 = \frac{C}{A}$

From equations (4) and (5) for ω^2: $B = -\frac{C}{A}$

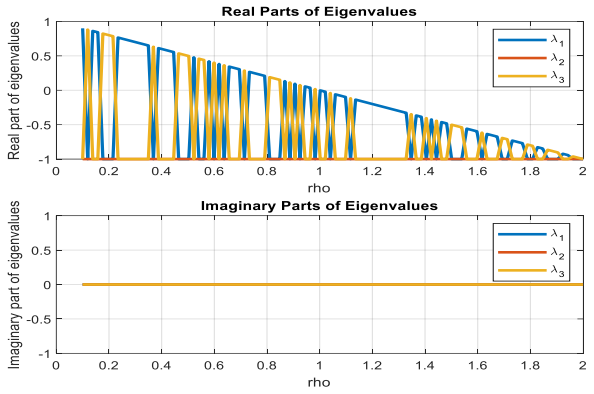

Fig. 4. Hopf bifurcation in academic dynamics showing stability transitions via eigenvalues.

For a Hopf bifurcation to occur, it is needed

$$B(\rho_c) = -\frac{C(\rho_c)}{A(\rho_c)}$$

It is verified that the transversality condition holds. To ensure that the eigenvalues cross the imaginary axis transversely, it is computed $\frac{d}{d\rho}\mathrm{Re}(\lambda(\rho))\Big|_{\rho=\rho_c}$

Differentiating (3) with respect to ρ

$$3\lambda^2\frac{d\lambda}{d\rho} - 2A\lambda\frac{d\lambda}{d\rho} - A'\lambda^2 - B'\lambda - C' = 0 \qquad (6)$$

ing the real and imaginary parts for $\lambda = i\omega$

$$3(i\omega)^2\frac{d\lambda}{d\rho} - 2A(i\omega)\frac{d\lambda}{d\rho} - A'(i\omega)^2 - B'(i\omega) - C' = 0$$

$$\Rightarrow 3(-\omega^2)\frac{d\lambda}{d\rho} - 2Ai\omega\frac{d\lambda}{d\rho} + A'\omega^2 - iB'\omega - C' = 0$$

Real part; $3\omega^2\frac{d\lambda}{d\rho} + A'\omega^2 - C' = 0$

Imaginary part: $-2A\omega\frac{d\lambda}{d\rho} - B'\omega = 0$

$$\Rightarrow \frac{d\lambda}{d\rho}(\upsilon) = -\frac{B'(\rho)}{2A(\rho)} \text{ and } \frac{d}{d\rho}\mathrm{Re}(\lambda(\rho))\Big|_{\rho=\rho_c} \neq 0$$

This means that the transversality criterion holds. This leads one to assume that the point $\rho = \rho_c$ is the location of a Hopf bifurcation. This ends the proof of the theorem.

The actual eigenvalues consist beyond zero at $\rho = 1.2$.

When the equilibrium point shifts to an unstable, limit cycle, also known as a periodic solution results. Here lies theHopf bifurcation point. If $\rho > 1.2$ the real componentsof the eigenvaluesare positive. The system shows fluctuating behavior; the equilibrium point is unstable. The Hopf bifurcation point is found at $\rho = 1.2$, at which the system shifts from stable to unstable behavior and limit cycles appear. The fact that ρ changes from stable to unstable as it develops suggests that excessive academic pressure may drive the system toward instability

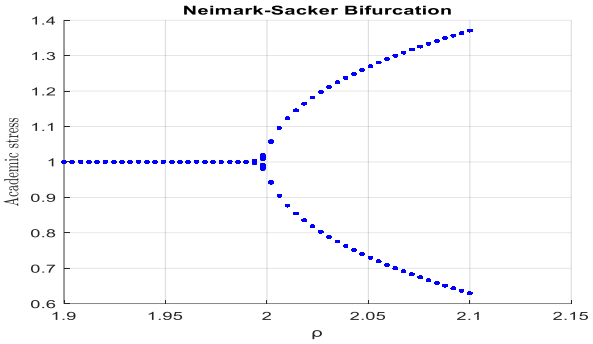

Fig. 5. Neimark-Sacker bifurcation in academic stress dynamics using the model.

Neimark-Sacker bifurcation

In discrete conditions, a bifurcation analogous to the Hopf bifurcation occurs; this one is called the Neimark-Sacker bifurcation. Although the same conclusion as Neimark, they did so independently. Upon first examination, the idea was determined to be consistent with periodic solution stability by Asheghi Sacker. The first place it appears in ordinary differential equations is in the map obtained by taking a Poincare section perpendicular to the periodic flow. One often used discretization method for the systems:

$$N_i(t+h) = N_i(t) + hf_i(N_1, N_2, N_3)$$

Where *h*is the step size. Applying this, the system transforms into:

$$N_1^{k+1} = N_1^k + h(-\rho + \alpha N_2^k + \beta N_3^k)N_1^k$$
$$N_2^{k+1} = N_2^k + h(\mu(\delta - N_2^k) - \gamma N_1^k)N_2^k$$
$$N_3^{k+1} = N_3^k + h(\phi(\eta - N_3^k) - \sigma N_1^k)N_3^k$$

A Neimark-Sacker bifurcation is the result of a complex-conjugate pair of eigenvalues crossing the unit circle, indicating that the system (3) is unstable if at least one eigenvalue is found outside the unit circle, denoted as $|\lambda i| > 1$. $\lambda_{1,2} = \pm e^{i\theta}$, $0 < \theta < \pi$

The system (3) is stable if all eigenvalues satisfy $|\lambda i| < 1$. The Jury stability conditions are:

(i) $1 + A + B + C > 0$
(ii) $1 - A + B - C > 0$
(iii) $A - C > 0$
(iv) $|C| < 1$

When the condition $A - C = 0$ is met, a Neimark-Sacker bifurcation occurs, as a pair of complex eigenvalues moves to the unit circle. The bifurcation occurs when two of the eigenvalues of equation (3) satisfy: $\lambda_{1,2} = \pm e^{i\theta}$. For this to hold, substitute $\lambda = e^{i\theta}$ in the equation (3), $\left(e^{i\theta}\right)^3 - A\left(e^{i\theta}\right)^2 - B\left(e^{i\theta}\right) - C = 0$
Splitting the real and imaginary parts, this gives conditions for A, B, and C in terms of the bifurcation parameters.

Variations in the bifurcation parameter ρ affect the level of academic stress displayed in the bifurcation indicated in Fig.5. A stable fixed point may shift in a Neimark-Sacker bifurcation into an unstable point prone to oscillation. Rather than displaying a continuous condition close to the Neimark-Sacker bifurcation at ρ≈2, academic stress is determined by periodic fluctuations or oscillations. This result has significant relevance for evaluating student stress levels across both academic and non-academic domains.

The real and imaginary components of the eigenvalues $(\lambda_1, \lambda_2, \lambda_3)$ for varying bifurcation parameter α are displayed in Table 3. One finds a transition from steady to oscillatory behavior as αrises. Two complex conjugate eigenvalues crossing the unit circleand generating quasiperiodic oscillations define a bifurcation near 1.3. When the imaginary components approach 1.3, the system becomes unstable and exhibits continuous oscillations beyond this threshold.

As an expression of the bifurcation parameter α the Fig. 6 shows the real and imaginary eigenvalues $(\lambda_1, \lambda_2, \lambda_3)$. Two complex conjugate eigenvalues crossing the unit circle causes the Neimark-Sacker bifurcation to move the system from stability to oscillation. Two complex conjugate eigenvalues cross the unit circle as α rises to produce oscillations reminiscent of a Neimark-Sacker bifurcation. The imaginary components of the eigenvalues show a transition from a stable to an oscillatory regime in the range $1.2 \le \alpha \le 1.5$. All eigenvalues are real and in the stability domain before α≈1.2, therefore guaranteeing system stability. The system becomes unstable at α≈1.5 because of oscillations reflecting Neimark-Scker bifurcations brought about by complex conjugate eigenvalues crossing the unit circle. Starting quasiperiodic behavior at α≈1.3, the critical bifurcation point arises when eigenvalues satisfy Jury stability conditions and depart the stability domain.

Fig. 7 shows the ROR values as afunction of ρ, the bifurcation value. The red dashed line defines the criteria for stable and unstable behavior; the computed ROR values are shown by the solid blue line. The ROR approach can find a closed invariant curve as a Neimark-Sacker bifurcation when an unstable

Table 3. Eigenvalue analysis and stability classification.

α	**Real Part** λ_1	**Imaginary Part** λ_1	**Real** Part λ_2	**Imaginary Part** λ_2	**Real Part** λ_3	**Imaginary Part** λ_3	**Stability Status**
1.0	0.8	0.0	0.5	0.0	-0.3	0.0	Stable
1.2	0.7	0.2	0.5	0.0	-0.2	-0.1	Stable
1.3	0.6	0.5	0.4	-0.2	-0.1	-0.2	Bifurcation
1.4	0.5	0.7	0.3	-0.3	0.0	-0.4	Unstable
1.5	0.4	0.9	0.2	-0.4	0.1	-0.5	Unstable
1.6	0.3	1.1	0.1	-0.5	0.2	-0.6	Unstable

fixed point results from it. ROR crossing $R=0$ shows a transition from stable to quasiperiodic oscillations. The ROR values exhibit initial fluctuations at reduced ρ levels but remain positive, suggesting a stable regime. The ROR values drop and oscillate near to the threshold as ρ rises. The ROR declining below zero at ρ≈1.4, indicating bifurcation. Decline in ROR values beyond ρ≈1.6 indicates the existence of instability and complicated dynamical behavior. The motion is quasiperiodic due to this Neimark-Sacker bifurcation, which marks the transition from regular dynamics to oscillatory motion.

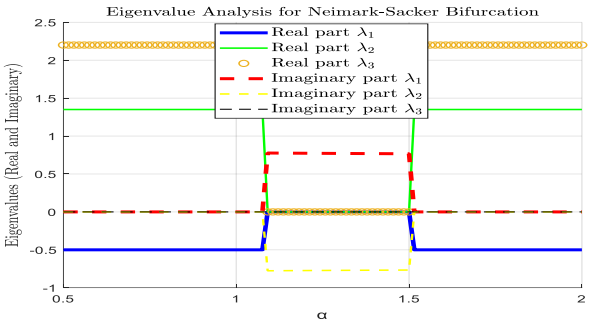

Fig. 6. Eigenvalue analysis for Neimark-Sacker bifurcation.

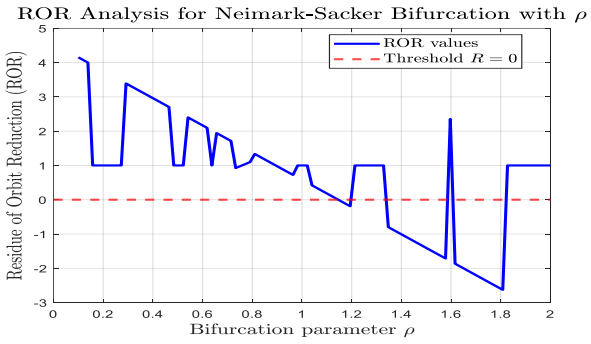

Fig. 7. Residue of orbit reduction (ROR) analysis for Neimark-Sacker bifurcation with *ρ*.

As shown in table 4, the Neimark-Sacker bifurcation occurs at ρ≈1.4 when the ROR value crosses the zero criteria. The system exhibits more unstable oscillations when the threshold is crossed.

Global stability

Let us consider N_1 (8)

Table 4. Stability classification based on residue of orbit reduction (ROR) analysis.

ρ	ROR Value	Stability Status
0.2	3.8	Stable
0.6	2.5	Stable
1.0	0.9	Stable
1.2	0.3	Stable
1.4	-0.2	Bifurcation point
1.6	-1.5	Unstable
1.8	-2.3	Unstable

Where $a,b,c>0$ are positive constants.

$$\frac{dV}{dt} = 2a(N_1 - N_1^*)\acute{N}_1 + 2b(N_2 - N_2^*)\acute{N}_2 + 2c(N_3 - N_3^*)\acute{N}_1$$

From $\frac{dV}{dt} = 2a(N_1 - N_1^*)\acute{N}_1 + 2b(N_2 - N_2^*)\acute{N}_2 + 2c(N_3 - N_3^*)\acute{N}_1$

Substituting the given system equations:

$$\frac{dV}{dt} = 2a(N_1 - N_1^*)(-\rho + \alpha N_2 + \beta N_3)N_1 + 2b(N_2 - N_2^*)(\mu(\delta - N_2) - \gamma N_1)N_2 + 2c(N_3 - N_3^*)(\phi(\eta - N_3) - \sigma N_1)N_3 \quad (9)$$

Since we assume that the system has an equilibrium

$$-\rho + \alpha N_2 + \beta N_3 = 0$$

$$2b(N_2 - N_2{}^*)(\mu(N_2{}^* - N_2) - \gamma(N_1 - N_1{}^*))N_2$$

At equilibrium $\mu(\delta - N_2) - \gamma N_1 = 0$

So we write

$$2b(N_2 - N_2{}^*)(\mu(N_2{}^* - N_2) - \gamma(N_1 - N_1{}^*))N_2$$

Since $\mu(N_2{}^* - N_2)$ is negative definite, this term contributes to making $\frac{d\Psi}{dt} \le 0$.

$$2c(N_3 - N_3{}^*)(\phi(\eta - N_3) - \sigma N_1)N_3$$

$$\phi(\eta - N_3{}^*) - \sigma N_1{}^*$$

Rewriting

$$2c(N_3 - N_3{}^*)(\phi(N{}^* - N_3) - \sigma(N_1 - N_1{}^*))N_3$$

Since $\frac{dV}{dt} \leq 0$, also $\frac{dV}{dt} = 0$ only at equilibrium point $(N_1{*}, N_2{*}, N_3{*})$. LaSalle's invariance principle guarantees the global asymptotic stability of the equilibrium.

It appears from Fig. 8 that the globally stable equilibrium point is at (N_1, N_2, N_3) = (250, 10, 8), as all paths from many starting locations converge to this point and the Lyapunov function monotonically decreases to zero. The oscillatory character of the phase images indicates that the system undergoes transitory oscillations before reaching a stable state. This is typical of real-world academic systems that apply feedback. The Lyapunov function mathematically ensures stability since it is usually zero over time. This suggests that although the system would eventually settle, academic pressure on students would induce transient changes in the population.

Fractional order approach

Definition 1. Using the following formula, we can find the integral (Ullahand Kabir, 2024)that corresponds to $g(t)$in the ABC sense, assuming that it is a function on the interval L [0, T]:

$$ {}^{ABC}_{0}I_t^{\alpha} g(t) = \frac{1-v}{ABC(v)} g(t) + \frac{v}{ABC(v)\Gamma(v)} \int_0^t (t-\theta)^{v-1} g(\theta)\, d\theta \quad (10)$$

Lemma 1: In accordance with the information provided in reference(Ullah and Kabir, 2024), the third statement asserts that the optimal solution to the theoretical challenge with fractional order $0 < \alpha \leq 1$is

$$ {}^{ABC}_{0}D_t^{v} g(t) = y(t), t \in [0,T] $$

$$ g(0) = g_0 $$

On the basis of the fact that the right side disappears when time equals zero, then

$$ g(t) = g_0 + \frac{1-v}{ABC(v)} y(t) + \frac{v}{ABC(v)\Gamma(v)} \int_0^t (t-\theta)^{v-1} y(\theta)\, d\theta \quad (11)$$

Fractional order model

The section that follows summarizes our analysis of a fractional-order student population model that employs the ABC fractional derivative (Ullah and Kabir, 2024). The model that preceded it (1) informs this part.

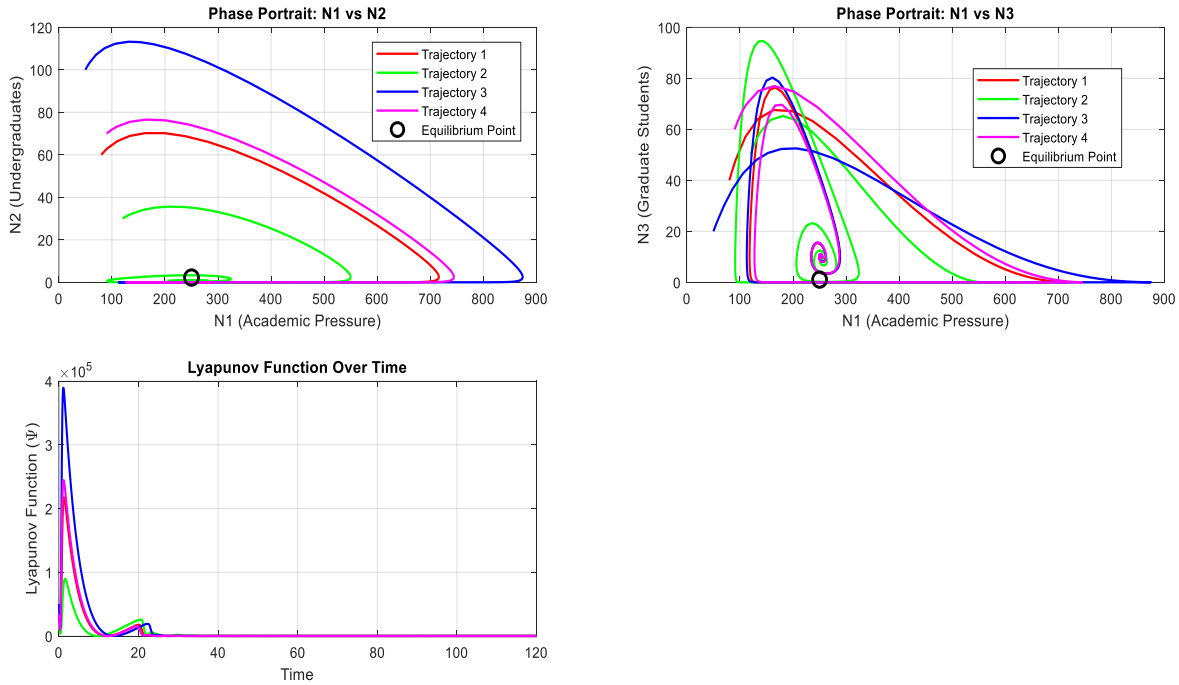

Fig. 8. Global stability analysis using phase portraits and Lyapunov function (8).

$$\left.\begin{array}{l} {}^{ABC}_{0}D_t^{v}[N_1(t)] = (-\rho + \alpha N_2 + \beta N_3)N_1 \\ {}^{ABC}_{0}D_t^{v}[N_2(t)] = (\mu(\delta - N_2) - \gamma N_1)N_2 \\ {}^{ABC}_{0}D_t^{v}[N_3(t)] = (\phi(\eta - N_3) - \sigma N_1)N_3 \end{array}\right\} \quad (12)$$

Under the initial values for the various classes

$N_1(0) \geq 0, N_2(0) \geq 0, N_3(0) \geq 0$

Boundedness of solutions

Theorem 4: Let $0 < \nu \leq 1$, and assume all parameters $\rho, \sigma, \alpha, \beta, \mu, \delta, \gamma, \phi, \eta$ are positive constants. Then, the solutions of the system (12) eventually enter the compact region $S = \left\{(N_1, N_2, N_3) \epsilon \Re_+^3 | g(t) \leq \delta + \frac{H}{N}, \delta > 0\right\}$ for some $N \leq \min\{\rho, \mu\delta, \phi\eta\}$ and a constant $H > 0$,

Proof: We define a function (Sha et al., 2019) as

$$g(t) = N_1(t) + N_2(t) + N_3(t),\ t \geq 0 \quad (13)$$

Take the ABC derivative:

$${}^{ABC}_{0}D_t^{v}g(t) = {}^{ABC}_{0}D_t^{v}N_1(t) + {}^{ABC}_{0}D_t^{v}N_2(t) + {}^{ABC}_{0}D_t^{v}N_3(t) \quad (14)$$

From equations (12), (13), and (14)

$$\begin{aligned} {}^{ABC}_{0}D_t^{v}N_1(t) &= (-\rho + \alpha N_2 + \beta N_3)N_1 \\ &\quad + (\mu(\delta - N_2) - \gamma N_1)N_2 \\ &\quad + (\phi(\eta - N_3) - \sigma N_1)N_3 \end{aligned}$$

$$\begin{aligned} \Longrightarrow {}^{ABC}_{0}D_t^{v}N_1(t) &= -\rho N_1 + \alpha N_1 N_2 + \beta N_1 N_3 \\ &+ \mu\delta N_2 - \mu N_2^2 - \gamma N_1 N_2 + \phi\eta N_3 - \phi N_3^2 - \sigma N_1 N_2 \end{aligned}$$

Simplify

$$\begin{aligned} \Longrightarrow {}^{ABC}_{0}D_t^{v}N_1(t) &= -\rho N_1 + (\alpha - \gamma)N_1 N_2 \\ &\quad + (\beta - \sigma)N_1 N_3 \\ &+ \mu\delta N_2 - \mu N_2^2 + \phi\eta N_3 - \phi N_3^2 \end{aligned}$$

Now adding a damping term $Ng(t)$, where $N \leq min\{\rho, \mu\delta, \phi\eta\}$

The total population$F(t)$ $is\ ultimately\ bounded$, hence the system solutions are bounded in the region S.

Existence and uniqueness of the solution for the fractional order model:

We determine whether the solutions to system (12) are unique with respect to the ABC derivative and whether they exist. Choosing into account that a continuous real-valued function with the supremum-norm assets is indicated as B (ς) on ς = [0, b] and P= B [ς]×B[ς]× B[ς](Ullah andKabir, 2024),the corresponding function is a component of a Banach space and with the norm $\|(N_1, N_2, N_3)\| = \|N_1\| + \|N_2\| + \|N_2\|$,

Whereas

$\|N_1\| = \sup_{t \in k}|N_1|, \|N_2\| = \sup_{t \in k}|N_2|, \|N_3\| = \sup_{t \in k}|N_3|$. What occurs is the outcome of applying the fractional integral operator of ABC to the two sets of equations (12):

$$\left.\begin{array}{l} N_1(t) - N_1(0) = {}^{ABC}_{0}D_t^{v}\{(-\rho + \alpha N_2 + \beta N_3)N_1\} \\ N_2(t) - N_2(0) = {}^{ABC}_{0}D_t^{v}\{(\mu(\delta - N_2) - \gamma N_1)N_2\} \\ N_3(t) - N_3(0) = {}^{ABC}_{0}D_t^{v}\{(\phi(\eta - N_3) - \sigma N_1)N_3\} \end{array}\right\} \quad (15)$$

With the ABC fractional derivative in hand, one arrives at the following:

$$\begin{cases} N_1(t) - N_1(0) = \frac{1-v}{ABC(v)} g_1(v, t, N_1(t)) + \frac{v}{ABC(v)\Gamma(v)} \int_0^t (t-\theta)^{v-1} g_1(v, t, N_1(\theta))\, d\theta \\ N_2(t) - N_2(0) = \frac{1-v}{ABC(v)} g_2(v, t, N_2(t)) + \frac{v}{ABC(v)\Gamma(v)} \int_0^t (t-\theta)^{v-1} g_2(v, t, N_2(\theta))\, d\theta \\ N_3(t) - N_3(0) = \frac{1-v}{ABC(v)} g_3(v, t, N_3(t)) + \frac{v}{ABC(v)\Gamma(v)} \int_0^t (t-\theta)^{v-1} g_3(v, t, N_3(\theta))\, d\theta \end{cases} \quad (16)$$

Where

$$\begin{aligned} &g_1(v, t, N_1(t)) = (-\rho + \alpha N_2 + \\ &\beta N_3)N_1,\ g_2(v, t, N_2(t)) = (\mu(\delta - N_2) - \\ &\gamma N_1)N_2,\ g_3(v, t, N_3(t)) = (\phi(\eta - N_3) - \sigma N_1)N_3 \end{aligned} \quad (17)$$

As used within the circumstances of $(t), N_2(t), N_3(t)$ the functions g_1, g_2, g_3 satisfy the Lipschitz condition if each of the three functions $N_1(t), N_2(t), N_3(t)$has an upper bound. Because of this,

$$\begin{aligned} &\|g_1(\alpha, t, N_1(t)) - g_1(\alpha, t, N_1^*(t))\| \\ &\quad = \|(-\rho + \alpha N_2(t) + \beta N_3)(N_1(t) \\ &\quad - N_1^*(t))\| \end{aligned}$$

Suppose that,

$$\xi_1 = \|(-\rho + \alpha N_2(t) + \beta N_3)\|$$

Once it is done, we can start writing.

$$\|g_1(\alpha, t, N_1(t)) - g_1(\alpha, t, N_1^*(t))\| \leq \xi_1(N_1(t) - N_1^*(t)) \quad (18)$$

$$\begin{cases} \|g_2(\alpha, t, N_2(t)) - g_2(\alpha, t, N_2^*(t))\| \leq \xi_2(N_2(t) - N_2^*(t)) \\ \|g_3(\alpha, t, N_3(t)) - g_3(\alpha, t, N_3^*(t))\| \leq \xi_3(N_3(t) - N_3^*(t)) \end{cases}$$

Where,

$\xi_2 = \|\mu\delta - (N_2(t) + N_2^*(t))\mu - \gamma N_1(t)\|$

$\xi_3 = \left\|\phi\eta - \left(N_3(t) + N_3^*(t)\right)\phi - \sigma N_1(t)\right\|$

As a result, we can see that the Lipschitz ideas worked. When the expressions in (18) are applied recursively, the following outcomes are obtained:

$$N_{1n}(t) - N_1(0) = \frac{1-v}{ABC(v)}\mathrm{g}_1\left(\alpha, t, N_{1n}(t)\right) + \frac{v}{ABC(v)\Gamma(v)}\int_0^t (t - \theta)^{v-1}\mathrm{g}_1\left(\alpha, t, N_{1n}(\theta)\right)d\theta$$

$$N_{2n}(t) - N_2(0) = \frac{1-v}{ABC(v)}\mathrm{g}_2\left(\alpha, t, N_{2n}(t)\right) + \frac{v}{ABC(v)\Gamma(v)}\int_0^t (t - \theta)^{v-1}\mathrm{g}_2\left(\alpha, t, N_{2n}(\theta)\right)d\theta$$

$$N_{3n}(t) - N_3(0) = \frac{1-v}{ABC(v)}\mathrm{g}_3\left(\alpha, t, N_{2n}(t)\right) + \frac{v}{ABC(v)\Gamma(v)}\int_0^t (t - \theta)^{v-1}\mathrm{g}_3\left(\alpha, t, N_{3n}(\theta)\right)d\theta$$

At this time, as

$N_{10}(t) = N_1(0), N_{20}(t) = N_2(0), N_{30}(t) = N_3(0)$

It is possible to build the following statement by making use of the contrasts that exist between sequential terms:

$$N_{1,n}(t) = N_{1n}(t) - N_{1n-1}(t) = \frac{1-v}{ABC(v)}\left(\mathrm{g}_1\left(v, t, N_{1n-1}(t)\right) - \mathrm{g}_1\left(\alpha, t, N_{1n-2}(t)\right)\right) + \frac{v}{ABC(v)\Gamma(v)}\int_0^t (t-\theta)^{v-1}\left(\mathrm{g}_1\left(\alpha, \eta, N_{1n-1}(\theta)\right) - \mathrm{g}_1\left(\alpha, \theta, N_{1n-2}(\theta)\right)\right)d\theta,$$

$$N_{2,n}(t) = N_{2n}(t) - N_{2n-1}(t) = \frac{1-v}{ABC(v)}\left(\mathrm{g}_2\left(\alpha, t, N_{2n-1}(t)\right) - \mathrm{g}_2\left(\alpha, t, N_{2n-2}(t)\right)\right) + \frac{v}{ABC(v)\Gamma(v)}\int_0^t (t-\theta)^{v-1}\left(\mathrm{g}_2\left(\alpha, \theta, N_{2n-1}(\theta)\right) - \mathrm{g}_2\left(\alpha, \theta, N_{2\,n-2}(\theta)\right)\right)d\theta,$$

$$N_{3,n}(t) = N_{3n}(t) - N_{3n-1}(t) = \frac{1-v}{ABC(v)}\left(\mathrm{g}_3\left(\alpha, t, N_{3n-1}(t)\right) - \mathrm{g}_3\left(\alpha, t, N_{3n-2}(t)\right)\right) + \frac{v}{ABC(v)\Gamma(v)}\int_0^t (t-\theta)^{v-1}\left(\mathrm{g}_3\left(\alpha, \theta, N_{3n-1}(\theta)\right) - \mathrm{g}_3\left(\alpha, \theta, N_{3n-2}(\theta)\right)\right)d\theta$$

Regarding this, it is crucial to remember that

$N_{1n}(t) = \sum_{i=0}^{n} N_{1_{N_{1,i}}}(t)$, $N_{2n}(t) = \sum_{i=0}^{n} N_{1_{N_{2,i}}}(t)$, $N_{3n}(t) = \sum_{i=0}^{n} N_{1_{N_{3,i}}}(t)$.

As an additional point of interest, in the setting of (18), which allows for

$N_{1_{N_{1,n-1}}}(t) = N_{1n-1}(t) - N_{1n-2}(t),$

$N_{1_{N_{2,n-1}}}(t) = N_{2n-1}(t) - N_{2n-2}(t),$

$N_{1_{N_{3,n-1}}}(t) = N_{3n-1}(t) - N_{3n-2}(t),$

It is possible to write.

$$\left\|N_{1_{N_{1,n}}}(t)\right\| \le \frac{v}{ABC(v)}\xi_1\left\|N_{1_{N_{1,n-1}}}(t)\right\| \frac{v}{ABC(v)\Gamma(v)}\xi_1\int_0^t (t-\theta)^{v-1}\left\|N_{1N_{1,n-1}}(\theta)\right\|d\theta,$$

$$\left\|N_{1_{N_{2,n}}}(t)\right\| \le \frac{v}{ABC(v)}\xi_1\left\|N_{1_{N_{2,n-1}}}(t)\right\| \frac{v}{ABC(v)\Gamma(v)}\xi_1\int_0^t (t-\theta)^{v-1}\left\|N_{1_{N_{2,n-1}}}(\theta)\right\|d\theta, \quad (19)$$

$$\left\|N_{1_{N_{3,n}}}(t)\right\| \le \frac{\alpha}{ABC(\alpha)}\xi_1\left\|N_{1_{N_{3,n-1}}}(t)\right\| \frac{v}{ABC(v)\Gamma(v)}\xi_1\int_0^t (t-\theta)^{v-1}\left\|N_{1_{N_{3,n-1}}}(\theta)\right\|d\theta,$$

Theorem 5: If the preceding condition is true for $t \in [0, p]$, then the fractional-order model (12) has a unique solution:

$\frac{1-v}{ABC(v)}\xi_i + \frac{v}{ABC(v)\Gamma(v)}p^v\xi_i < 1 \quad , \quad i = 1, 2, 3.$ (20)

Proof: It is a presumption that the functions $N_1(t), N_2(t), N_3(t)$ are all bounded. As a preliminary matter, equations (18) make it clear that $\mathrm{f}_1, \mathrm{f}_2, \mathrm{f}_3$ valid representations of the Lipschitz condition. Consequently, we get the following by using equation (21) together with a recursive hypothesis [34]:

$$\left\|N_{1_{N_{1,n}}}(t)\right\| \le \|N_{10}(t)\|\left(\frac{1-v}{ABC(v)}\xi_1 + \frac{vp^v}{ABC(v)\Gamma(v)}\xi_1\right)^n,$$

$$\left\|N_{1_{N_{2,n}}}(t)\right\| \le \|N_{20}(t)\|\left(\frac{1-v}{ABC(v)}\xi_2 + \frac{vp^v}{ABC(v)\Gamma(v)}\xi_2\right)^n, \quad (21)$$

$$\left\|N_{1_{N_{3,n}}}(t)\right\| \le \|N_{30}(t)\|\left(\frac{1-v}{ABC(v)}\xi_3 + \frac{vp^v}{ABC(v)\Gamma(v)}\xi_3\right)^n$$

As a result, when the value of n approaches$n \to \infty$, the sequences mentioned above are valid and hold$\left\|N_{1_{N_{1,n}}}(t)\right\| \to 0, \left\|N_{1_{N_{2,n}}}(t)\right\| \to 0, \left\|N_{1_{N_{3,n}}}(t)\right\| \to 0.$

Furthermore, employing the triangle inequality, equation (21) can be stated in the following manner:

$$\left\|N_{1_{N_{1n+m}}}(t) - N_{1_{N_{1n}}}(t)\right\| \leq \sum_{j=n+1}^{n+m} \Psi_1^j = \frac{\Psi_1^{n+1} - \Psi_1^{n+m+1}}{1-\Psi_1},$$

$$\left\|N_{1_{N_{2n+m}}}(t) - N_{1_{N_{2n}}}(t)\right\| \leq \sum_{j=n+1}^{n+m} \Psi_2^j = \frac{\Psi_2^{n+1} - \Psi_2^{n+m+1}}{1-\Psi_2},$$

$$\left\|N_{1_{N_{3n+m}}}(t) - N_{1_{N_{3n}}}(t)\right\| \leq \sum_{j=n+1}^{n+m} \Psi_3^j = \frac{\Psi_3^{n+1} - \Psi_3^{n+m+1}}{1-\Psi_3}, \quad (22)$$

Where, $\Psi_i = \frac{1-v}{ABC(v)}\xi_i + \frac{v}{ABC(v)\Gamma(v)}p^v\xi_i < 1$ by hypothesis.

Hyers-Ulam stability

Definition: Assuming the suggested model's ABC fractional-order integral form (12) is taken into consideration, Hyers-Ulam stability (Ullah and Kabir, 2024) is attained even if the values of $\forall\chi_i > 0$, $\exists$ constants $\omega_i > 0$, $i \in N^5$.

$$\left|N_1(t) - \frac{1-v}{ABC(v)}g_1(v,t,N_1(t)) + \frac{v}{ABC(v)\Gamma(v)}\int_0^t (t-\theta)^{v-1} g_1(v,\theta,N_1(\theta))\,d\theta\right| \leq \chi_1$$

$$\left|N_2(t) - \frac{1-v}{ABC(v)}g_2(v,t,N_2(t)) + \frac{v}{ABC(v)\Gamma(v)}\int_0^t (t-\theta)^{v-1} g_2(v,\theta,N_2(\theta))\,d\theta\right| \leq \chi_2 \quad (23)$$

$$\left|N_3(t) - \frac{1-v}{ABC(v)}g_3(v,t,N_3(t)) + \frac{v}{ABC(v)\Gamma(v)}\int_0^t (t-\theta)^{v-1} g_3(v,\theta,N_3(\theta))\,d\theta\right| \leq \chi_3$$

$\exists \left(\dot{N}_1(t), \dot{N}_2(t), \dot{N}_3(t)\right)$ which satisfying

$$\dot{N}_1(t) = \frac{1-v}{ABC(v)}g_1(t,N_1(t)) + \frac{v}{ABC(v)\Gamma(v)}\int_0^t (t-\theta)^{v-1} g_1\left(v,\theta,\dot{N}_1(\theta)\right)d\theta$$

$$\dot{N}_2(t) = \frac{1-v}{ABC(v)}g_2(t,N_2(t)) + \frac{v}{ABC(v)\Gamma(v)}\int_0^t (t-\theta)^{v-1} g_2\left(v,\theta,\dot{N}_2(\theta)\right)d\theta$$

$$\dot{N}_3(t) = \frac{1-v}{ABC(v)}g_3(t,N_3(t)) + \frac{v}{ABC(v)\Gamma(v)}\int_0^t (t-\theta)^{v-1} g_3\left(v,\theta,\dot{N}_3(\theta)\right)d\theta$$

Implies that

$$\left|N_1(t) - \dot{N}_1(t)\right| < \chi_1\xi_1\,, \left|N_2(t) - \dot{N}_2(t)\right| < \chi_2\xi_2, \left|N_3(t) - \dot{N}_3(t)\right| < \chi_3\xi_3 \quad (24)$$

Theorem 6: The given prey-predator fractional-order model (12) meets the Hyers-Ulam stability condition according to the ς criteria.

Proof: In accordance with Theorem 5, the fractional-order model (15) possesses a singular solution that is capable of fully satisfying the system of equation (16). Because of this, we are able to write (Ullah and Kabir, 2024),

$$\left|N_1(t) - \dot{N}_1(t)\right| \leq \frac{1-v}{ABC(v)}\left\|g_1(v,t,N_1(t)) - g_1\left(v,t,\dot{N}_1(t)\right)\right\| + \frac{v}{ABC(v)\Gamma(v)}\int_0^t (t-\theta)^{v-1}\left\|g_1(v,\theta,N_1(\theta)) - g_1\left(v,\theta,\dot{N}_1(\theta)\right)\right\|d\theta \leq \left[\frac{1-v}{ABC(v)} + \frac{v}{ABC(v)\Gamma(v)}\right]N_1\left\|N_1(t) - \dot{N}_1(t)\right\| \quad (25)$$

$$\left|N_2(t) - \dot{N}_2(t)\right| \leq \frac{1-v}{ABC(v)}\left\|g_2(v,t,N_2(t)) - g_2\left(\alpha,t,\dot{N}_2(t)\right)\right\| + \frac{v}{ABC(v)\Gamma(v)}\int_0^t (t-\theta)^{v-1}\left\|g_2(\alpha,\theta,N_2(\theta)) - g_2\left(\alpha,\theta,\dot{N}_2(\theta)\right)\right\|d\theta \leq \left[\frac{1-v}{ABC(v)} + \frac{v}{ABC(v)\Gamma(v)}\right]N_2\left\|N_2(t) - \dot{N}_2(t)\right\| \quad (26)$$

$$\left|N_3(t) - \dot{N}_3(t)\right| \leq \frac{1-v}{ABC(v)}\left\|g_3(v,t,N_3(t)) - g_3\left(v,t,\dot{N}_3(t)\right)\right\| + \frac{v}{ABC(v)\Gamma(v)}\int_0^t (t-\theta)^{v-1}\left\|g_3(v,\theta,N_3(\theta)) - g_3\left(v,\theta,\dot{N}_3(\theta)\right)\right\|d\theta \leq \left[\frac{1-\alpha}{ABC(\alpha)} + \frac{\alpha}{ABC(\alpha)\Gamma(\alpha)}\right]N_3\left\|N_3(t) - \dot{N}_3(t)\right\| \quad (27)$$

$$N_i = \chi_i, \frac{1-v}{ABC(v)} + \frac{v}{ABC(v)\Gamma(v)} = \theta_i.$$

Then we have

$$\left\|N_1(t) - \dot{N}_1(t)\right\| \leq \chi_1\theta_1 .$$
$$\left\|N_2(t) - \dot{N}_2(t)\right\| \leq \chi_2\theta_2 \qquad (28)$$
$$\left\|N_3(t) - \dot{N}_3(t)\right\| \leq \chi_3\theta_3$$

One can determine the model's Hyers-Ulam stability (16) by examining equation (28). This proves the theorem correct by showing that the ABC fractional-order model (15) is Hyers-Ulam stable.

As observed in Fig. 9, showing the evolution of the student population for various values of ν (1.0, 0.9, 0.8, and 0.7), memory effects and non-integer differentiation influence system stability. This line underlines the significance of fractional-order modeling in educational dynamics by illustrating how transient behavior changes as ν drops, therefore producing different equilibrium states and convergence rates.

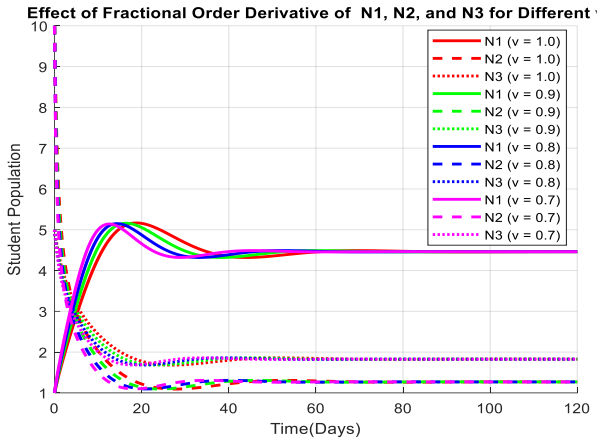

Fig. 9. Effect of the fractional-order derivative ν on the dynamics of academic pressure (N_1), undergraduate students (N_2), and graduate students (N_3) over time using the model (12).

Fig. 10 demonstrates how the oscillatory behavior and stability of N_1 are changed by varying ν from 1.0
to 0. 7. The fact that the persistence of oscillations is strengthened with decreasing ν values indicates the effect of memories and fractional interactions on the fluctuating and steady-state behavior of the system.

Fig. 11 indicates that, despite prolonged shifts occurring with lower ν, the undergraduate student population recovers more quickly with larger ν, implying that the effects of academic pressure last for a longer period of time, The fractional-order method accounts for long-term memory to better capture real student behavior.

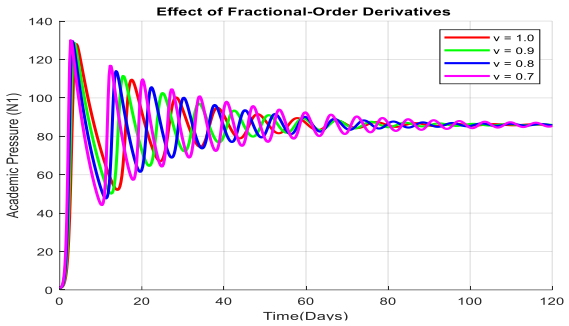

Fig. 10. Effect of fractional-order derivatives (ν) on academic pressure (N_1) over time using the model (12).

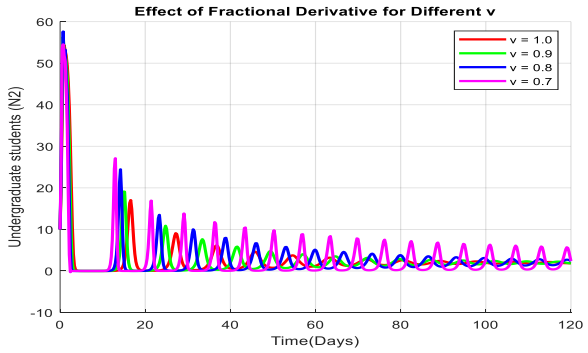

Fig. 11. Effect of fractional-order derivatives (v) on undergraduate students (N_2) over time using the model (12).

Fig.12 shows that convergence accelerates as v increases, implying that graduate students rapidly adapt to higher levels of academic pressure. Conversely, lower v causes changes to persist longer, implying that the system is unstable for a longer period since memory effects are stronger. These memory-driven responses better capture graduate students' behavior in shifting intellectual environments.

Numerical simulation with academic dynamics of the deterministic approach

A simulation of academic pressure (N_1) that affects

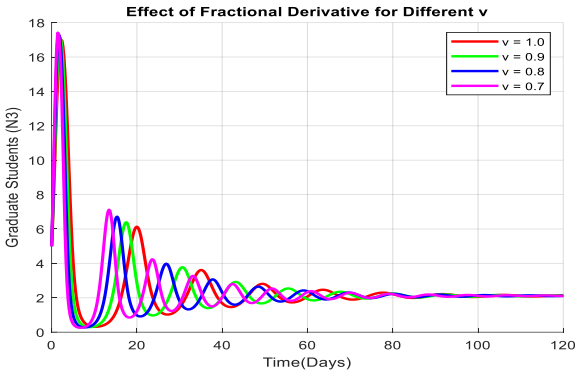

Fig. 12. Effect of fractional-order derivatives (v) on graduate students (N_3) over time using the model (12).

undergraduate students $(N_2)$and graduate students (N_3) are studied via the predator-prey model. This model demonstrates how population oscillations are influenced by stress levels, resilience, and external support systems in the academia.

High levels of academic stress lead to a sharp decline in the undergraduate student population,as shown in Fig. 1. Reflecting trends across academic stress levels, graduate students, and undergraduates react slowly. One gets a continuous

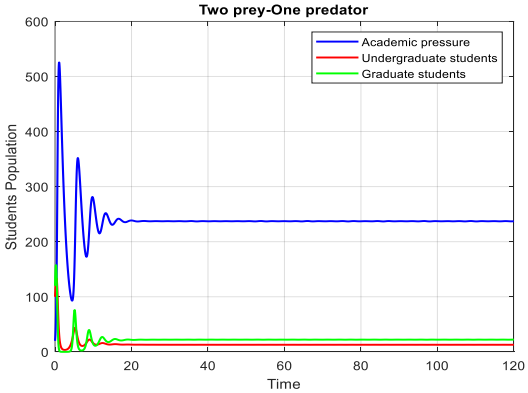

Fig. 13. Dynamical behavior of prey-predator model (1); Assume

$$\rho = 0.7, \alpha = 0.02, \beta = 0.02, \mu = 0.01,$$
$$\delta = 250, \gamma = 0.01, \lambda = 0.04,$$
$$\eta = 200, \sigma = 0.03.$$

equilibrium whereby stress and student populations coexist when the oscillations in all three populations are lowered over time. Students who act in this way areobviously gradually adjusting to school life ands are able to control their tension. As shown in Fig. 13(a), the phase space trajectory converges to a single stable equilibrium point after spiralling inward.

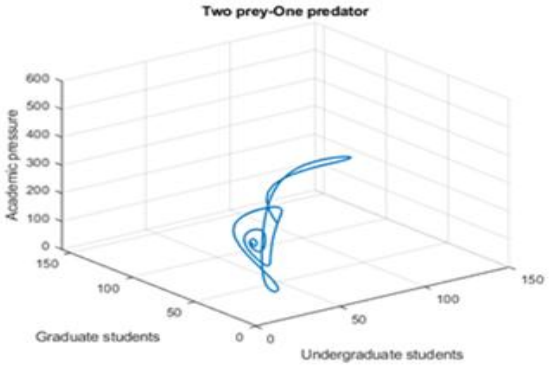

Fig. 13(a). Phase portrait.

Based on Fig. 14, damping in this system is smaller than in Fig. 13; oscillations last more before stabilizing. While undergraduate and graduate students show coincidence, the

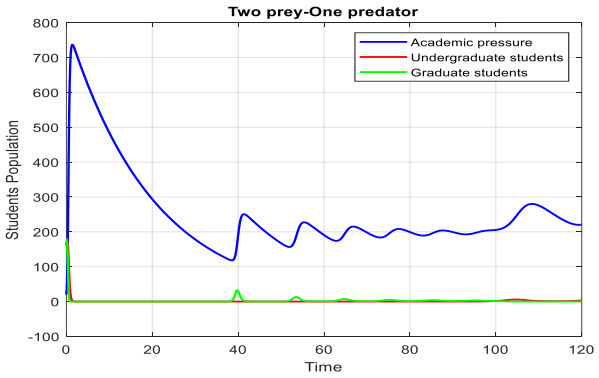

Fig. 14. Dynamical behavior of prey-predator model (1); Assume.

$$\rho = 0.7, \alpha = 0.02, \beta = 0.02, \mu = 0.01,$$
$$\delta = 250, \gamma = 0.01, \lambda = 0.04,$$
$$\eta = 200, \sigma = 0.03.$$

oscillations in stress populations exhibit different amplitudes over time. Under these conditions, the system is more sensitive, and periodic shocks delay stability

through recovery processes. Switching now to Fig. 14(a), the phase-space path forms a spiral that steadily appreoaches the equilibrium point.

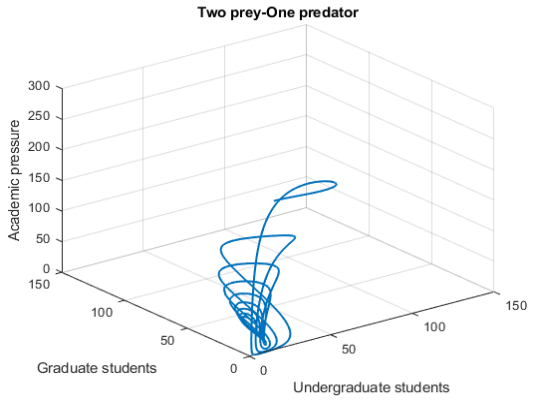

Fig. 14(a). Phase portrait.

As Fig. 15 shows, unlike the systems shown in Figs. 13 and 14, this one lacks damping. For academic stress among undergraduate and graduate students, the data show constant-amplitude, continuous oscillations. We argue that the system is in a limit cycle as these oscillations continue; it is dynamic but has not attained equilibrium. Here,

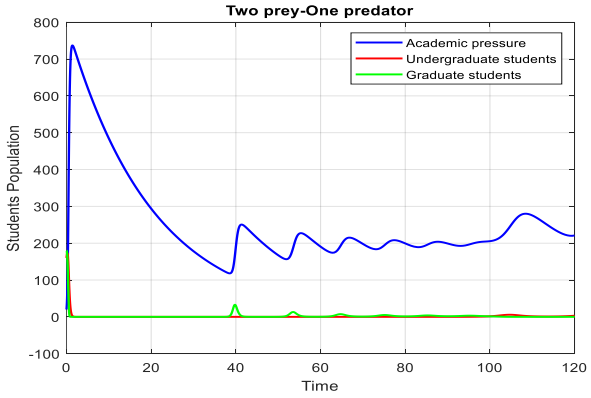

Fig. 15. Dynamical behavior of prey-predator model (1); Assume

$\rho = 0.05, \alpha = 0.02, \beta = 0.02, \mu = 0.01,$
$\delta = 250, \gamma = 0.01, \lambda = 0.04,$
$\eta = 200, \sigma = 0.03$

cyclical stressors, including semester scheduling and external factors, make academic ecosystem stability unreachable. Limit cycle dynamics are suggested by the closed loop in the phase diagram depicted in Fig. 15(a). This defines the lack of equilibrium and the existence of ongoing oscillatory action.

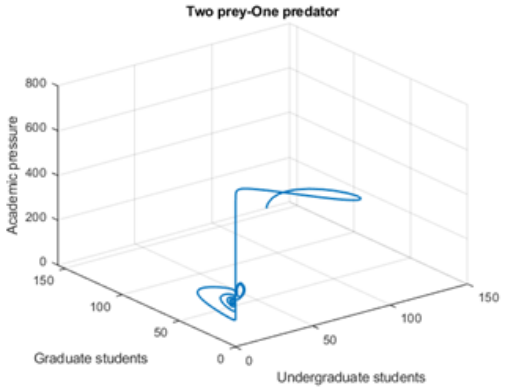

Fig.15(a). Phase portrait.

The system shows continuous oscillations in Fig. 16, consistent with Fig. 15 but with higher amplitudes. These indicators point to more intense interactions among individuals, which cause more stress and changes the student body. The system maintains a dynamic, oscillatory condition with substantial time-span fluctuations. Although the phase plot still

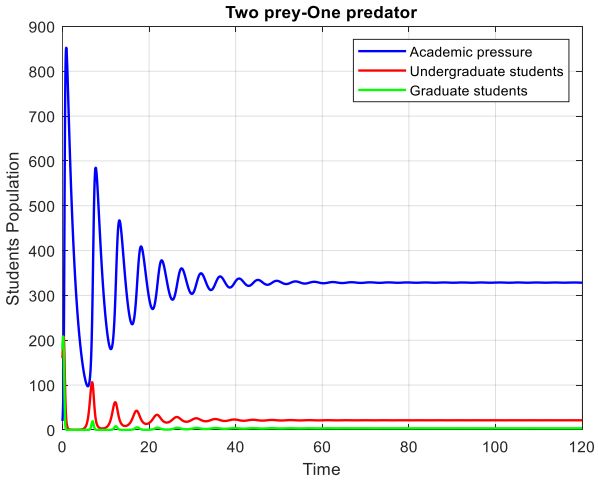

Fig. 16. Dynamical behavior of prey-predator model (1); Assume

$\rho = 0.5, \alpha = 0.02, \beta = 0.02, \mu = 0.01, \delta = 350, \gamma = 0.01, \lambda = 0.04,$
$\eta = 250, \sigma = 0.03$

shows complete loops, the trajectories in Fig. 16(a) span a greater region than in Fig. 16(a), implying bigger oscillation amplitudes. The interaction among

academic pressure, undergraduates, and graduates appears more complex and dynamic.

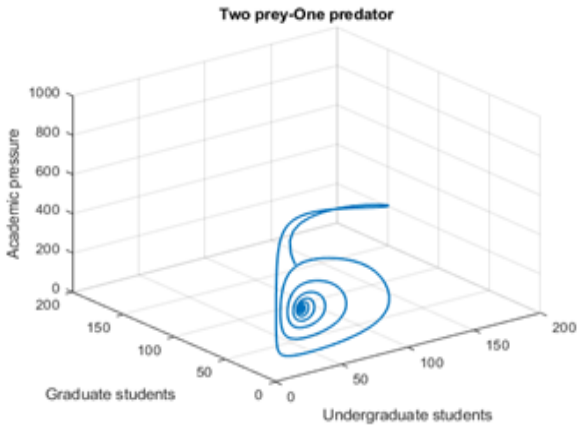

Fig. 16(a). Phase portrait.

Lyapunov exponent

Finding the Lyapunov exponent, a gauge of the system's sensitivity to its initial conditions, helps determine whether a system is periodic, chaotic, or stable. The red curve indicates the proportion of pupils influenced by academic pressure; mostly undergraduate students make up this group. Because graduate students can control or stabilize system dynamics, academic pressure subtly targets them.

From Fig. 17(a), at $\alpha = 0.82$, academic pressure (blue) shows significant disorder in its early stage, indicating a predator vulnerable to prey population shifts. The system responds to stress and finally resolves this state. First, undergraduates' chaotic dynamics indicate significant sensitivity to academic pressure. Graduate students faced more challenges due to resource scarcity and academic pressure. By maintaining stability, graduatestudents (green) prevent system collapse. Undergraduate academic obligations can be onerous and unstable. Maintaining fair academic standards to prevent academic stress among graduating students benefits the overall educational system.

From Fig. 17(b) for $\alpha = 0.2$, academic pressure (blue) has a shorter chaotic phase than (a), indicating stronger predator efficiency due to faster response to prey population changes. Academic pressure is a predator; therefore, undergraduates are less chaotic at first, yet still fluctuate. Graduate student competition decreases as the system stabilises. Graduate students (green) aren't afraid of predators or rivals like undergraduates. Effective academic pressure stabilises predators faster. Graduate students pose fewer hazards, but undergraduates are becoming stable.

From Fig. 17(c), the predator responds well to system changes, leading to predictable, controllable stress levels. Academic Pressure (Blue) stabilises at $\alpha = 0.3$, exhibiting little chaos. Academic pressure reduces early turmoil and stabilises red undergraduates, making their population more predator-resistant. Graduate students (Green) are less volatile under academic pressure or competition than undergraduates. Academic pressure on prey populations is decreasing, bringing the system closer to balance. Undergraduates can see that stress management works since graduate students are more stable.

From Fig. 17(d), academic pressure (blue) shows no chaotic phase and rapid stabilisation at $\alpha = 0.6$, indicating well-regulated behaviour and no longer causing instability in predator behaviour. The undergraduate population (red) establishes equilibrium early, reducing stress. Different from undergraduates, graduate students (green) are stable and unaffected by predators or competitors. Academic pressure is so strong, persistent, and long-lasting that the two prey populations may coexist. Graduate students give stability, whereas undergraduates are adaptable in ideal circumstances.

Low α causes the undergraduate population to become unstable and chaotic, while high α decreases chaos, speeds up stabilization, and maintains a balance between academic pressure and student populations.

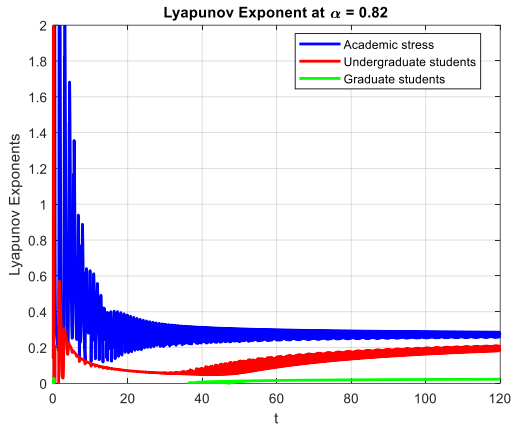

(a) Lyapunov exponent analysis $\alpha = 0.82$.

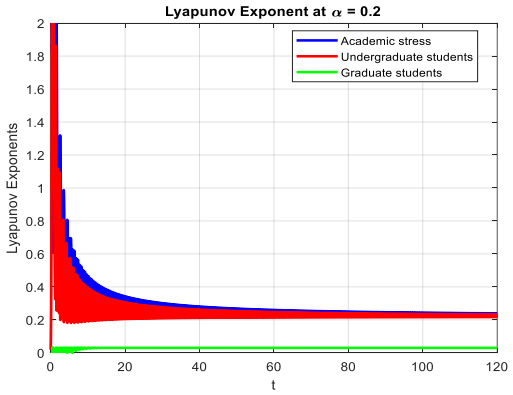

(b) Lyapunov exponent analysis $\alpha = 0.6$.

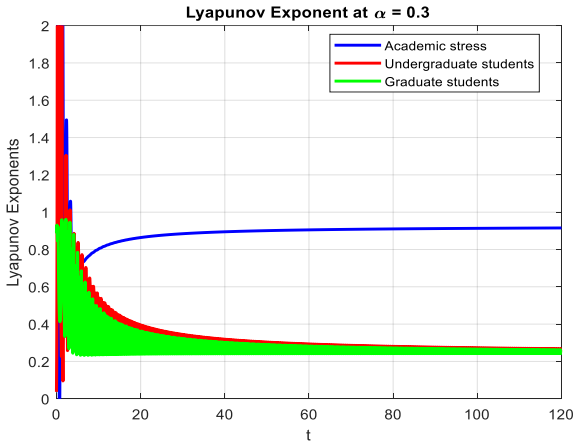

(**c) Lyapunov exponent analysis** $\alpha = 0.3$.

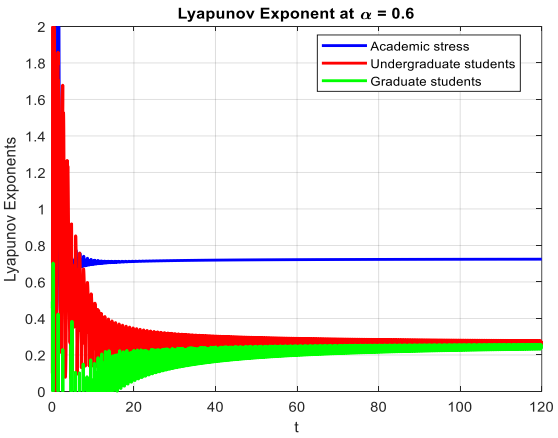

(d) Lyapunov exponent analysis $\alpha = 0.6$.

Fig. 17. System dynamics under varying academic pressure efficiency (α) using Lyapunov exponent analysis, highlighting the interactions between academic pressure (blue), undergraduate students (red), and graduate students (green) using the model (1).

Bifurcation diagrams of the model (1) under varying parameter values

Bifurcation diagrams of model (1) indicate significant thresholds at which qualitative alterations in system dynamics occur under different parameter values. These thresholds show variations between oscillatory and steady behavior.

As shown in Fig. 18(a-d), the breakdown of order from periodic stability is evidence of how increasing levels of external stress or strain disturb the delicate equilibrium between student populations and academic commitments. Students subjected to the anarchic system face uncertain academic demands, which could result in low marks, higher student dropout rates, and mental health difficulties. When ρ is small, small adjustments may be enough to stabilize the system and lessen oscillations. Stabilizing the chaotic dynamics at high value ρ requires systemic change, including lowering the workload.

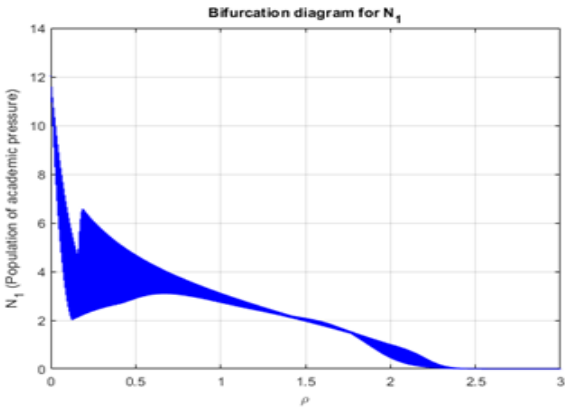

(a) **Bifurcation for** $\rho = 1900.$

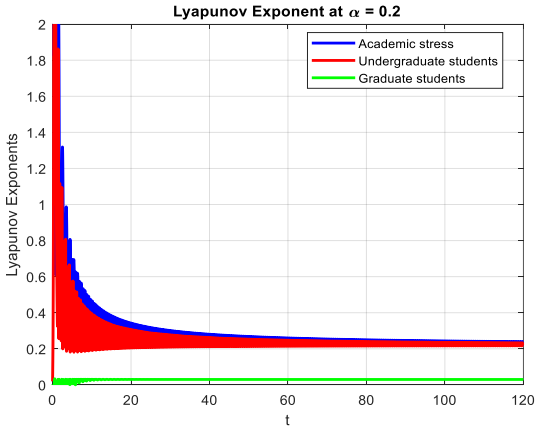

(b) Bifurcation for $\rho = 2800.$

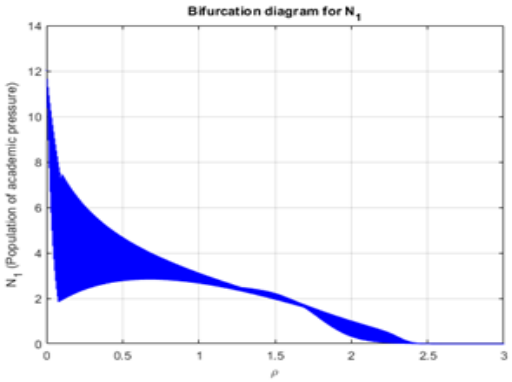

(c) Bifurcation for $\rho = 2900.$

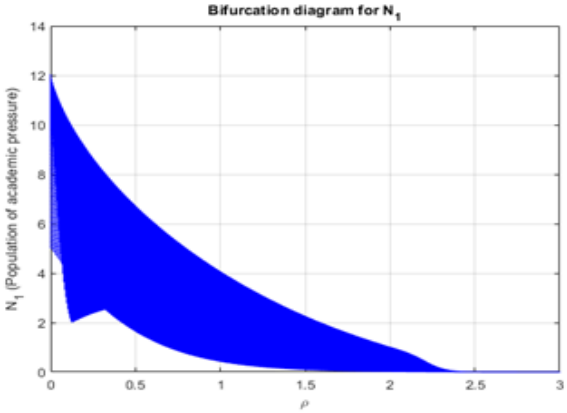

(d) Bifurcation for $\rho = 3800.$

Fig. 18. Bifurcation diagrams of academic pressure (N_1) under varying parameter values, showing chaotic behavior for: (a) $\rho = 1900,$ **(b)** $\rho = 2800,$ **(c)** $\rho = 2900,$ **and (d)** $\rho = 3800.$

As shown in Fig. 19(a-d) demonstrate how, as μ grows, the behavior transitions from stable to chaotic.

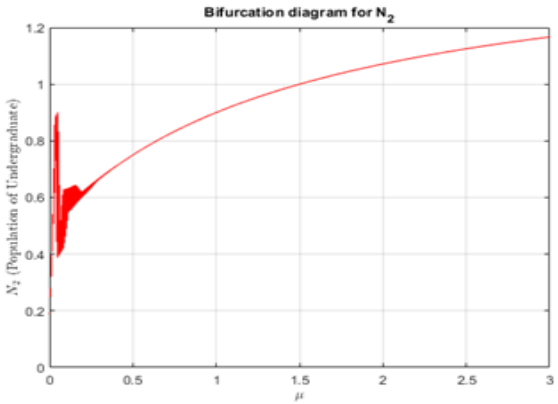

(a) Bifurcation for $\mu = 0.01.$

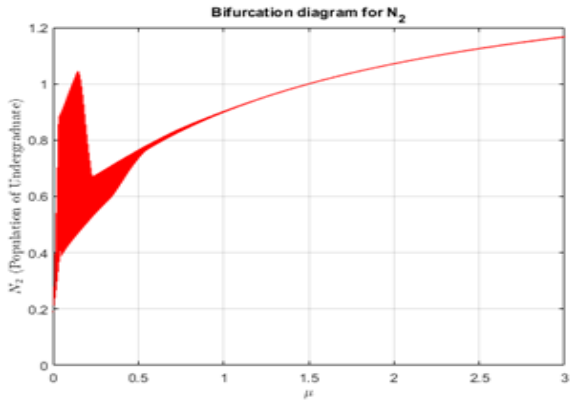

(b) Bifurcation for $\mu = 1.$

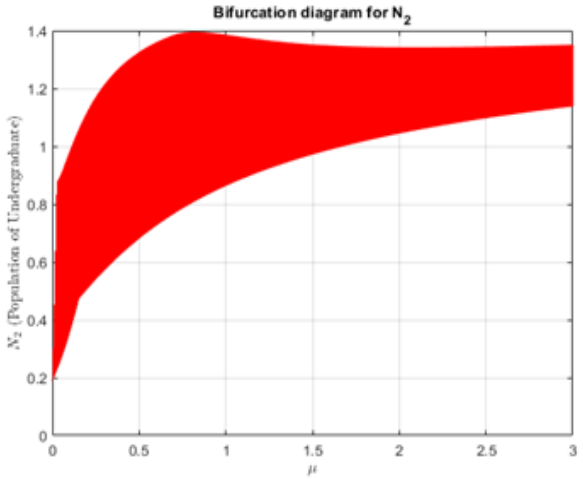

(c) Bifurcation for $\mu = 0.02$.

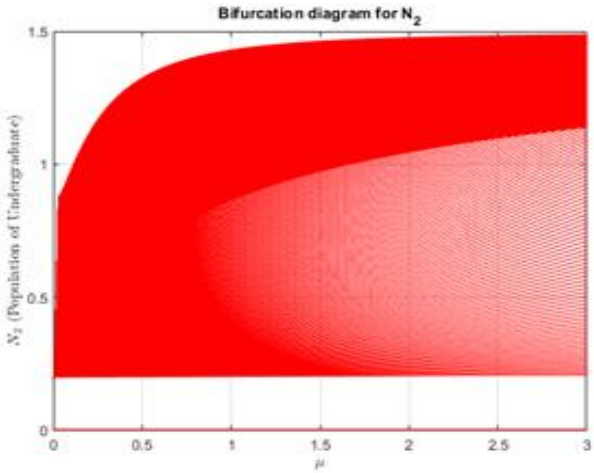

(d) Bifurcation for $\mu = 0.03$.

Fig. 19. Bifurcation diagrams of undergraduate students N_2 under varying parameter values, showing chaotic behaviour for: (a) $\mu = 0.01$, (b) $\mu = 1$, (c) $\mu = 0.02$, and (d) $\mu = 0.03$.

Changes to the starting points, parameter values, and model structure may cause the graphs to diverge, as indicated by the inconsistencies. The question of whether the system's stability is due to control mechanisms and critical thresholds arises when orderly regions are found within otherwise chaotic regions.

Basin of attraction

The depicted basin of attraction in the fractional-order predator-prey system comprising academic stress (N_1), undergraduate students (N_2) shows the areas of initial conditions that lead to a specific long-term behavior. The basin's grid-like form indicates it is most certainly a multi-attractor complicated dynamical system.

Fig. 20 shows a high academic-stress state (red region) across virtually all initial conditions of academic pressure (N_1) and undergraduate population (N_2), as indicated by the basin-of-attraction plot. The system is susceptible to the starting point of academic stress, as there is only a small area (blue region) near extremely low initial academic stress levels that leads to a low-stress equilibrium. This indicates that academic pressure is the primary factorinfluencingthe system's behaviorover the long run, and that resilience is low when stress levels are high.

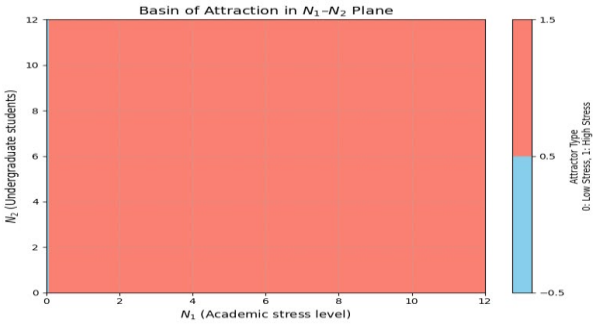

Fig. 20. Basin of attraction for the predator-prey dynamics among the academic stress (N_1) and undergraduate students (N_2) using the model (1).

Sensitivity analysis

Sensitivity analysis is one mathematical tool that helps one understand how modifying model parameters affects system output. In ecological, social, and biological models, sensitivity analysis is especially helpful for identifying which factors most affect the behavior of dynamic systems. To evaluate the influence of parameter x_i on the basic reproduction number(R_0), the corresponding sensitivity index is determined as follows:

$$\tau_{x_i}^{R_0} = \frac{\partial R_0}{\partial x_i} \times \frac{x_i}{R_0} \tag{29}$$

This tells us the relative change in R_0 resulting from a relative change in ρ. Let's derive and interpret each sensitivity analytically:

Using Eq. (29) and the parameter values provided in Table 2, the sensitivity indices of the basic reproduction number R_0 are evaluated and presented in Table 5.

Table 5. Sensitivity analysis.

Parameter	Sensitivity index $(\tau_{x_i}^{R_0})$	Interpretation
α	$\tau_{\alpha}^{R_0} = \frac{\alpha\delta}{\alpha\delta+\beta\eta} = 0.25$	Positive
β	$\tau_{\beta}^{R_0} = \frac{\beta\eta}{\alpha\delta+\beta\eta} = 0.75$	Positive
δ	$\tau_{\delta}^{R_0} = \frac{\alpha\delta}{\alpha\delta+\beta\eta} = 0.25$	Positive
η	$\tau_{\eta}^{R_0} = \frac{\beta\eta}{\alpha\delta+\beta\eta} = 0.75$	Positive
ρ	$\tau_{\rho}^{R_0} = \frac{\alpha\delta+\beta\eta}{\rho^2}.\frac{\rho}{R_0} = -1$	Negative

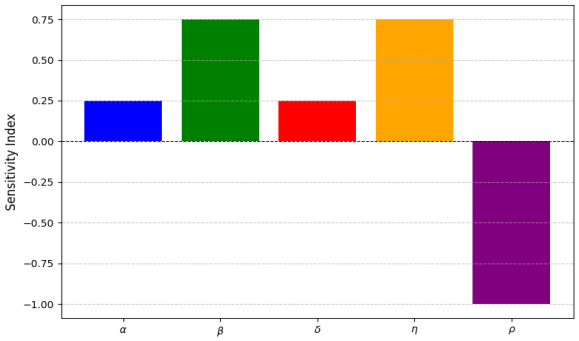

Fig. 21. Normalized sensitivity indices of the basic reproduction number $(R_0)$with respect to model parameters.

As shown in Table 5 and Fig. 21, the most sensitive parameters of the basic reproduction number $(R_0)$are β and η, both having a positive sensitivity index of 0.75. Here, β represents the degree to which academic pressure affects graduate students, while η denotes the environment's carrying capacity for graduate students. This means that a 1% increase in either parameter leads to a 0.75% increase in R_0. The parameters α and δ, which indicate the efficiency of academic pressure affecting undergraduate students and carrying capacity for undergraduate students, respectively, each have a lower but still positive sensitivity index of 0.25. On the other hand, ρhas a negative sensitivity index of –1, implying that a 1% increase in ρ results in a 1% decrease in R_0.

Conclusion

The fractional-order predator-prey model is effective for depicting the dynamics of students' academic stress. Stability analysis and bifurcation theory demonstrate how various stress levels allow students to experience stable, oscillatory, and unstable states. The equilibrium point becomes unstable and frequent limit cycles start as the eigenvalues have crossed zero when the value of ρ approaches 1.2. The system exhibits oscillatory behavior at this threshold ($\rho > 1.2$), so excessive academic stress might cause instability in student Performance (Fig. 4). Variations in the bifurcation parameter ρ affect academic stress, with a Neimark-Sacker bifurcation at ρ around 1.4 and oscillatory instability emerging as α increases beyond 1.2–1.5. Quasiperiodic behaviour starts near α approximately 1.3, leading to instability when eigenvalues cross the unit circle. It identifies a clear point of global asymptotic stability by applying the predator-prey model to capturing academic pressure among undergraduate and graduate students in a higher education institution. Looking at the phase profiles and Lyapunov function in Fig. 8, all trajectories converge to the same special equilibrium point independent of the initial conditions.

Specifically, we argue that when stress responses exhibit lag effects or long-term memory, such as recurring academic anxiety, the fractional approach captures these effects more clearly as shown in Figs. 9, 10, 11, and 12. While higher values of ν enable faster convergence, lower values lead to sustained oscillations. Both academic stress and student populations exhibit oscillatory patterns; the former shows a stable equilibrium, while the latter shows continuous limit cycles of varying amplitudes. Increased academic pressure (N_1) may be the reason for lower enrollment in undergraduate programs (N_2)

, as students either terminate or do not finish their degrees. According to Fig. 13, academic pressure ranges from 550 to 600 before settling at 250 to 300 for students. Fig. 13(a) with its phase-space analysis reveals dynamic pressure-student interactions. With oscillation periods ranging from about 10 to 20 time units, initial peaks of 310, 150, and 130 for N_1, N_2, and N_3 as shown in Fig. 14, point to a predator-prey link. Fig. 14(a) exhibits a spiralling contraction stabilizing around (50, 30, and 30) in 100 time units. Whereas the 3D phase portrait in Fig. 15(a) shows a spiral contraction towards stability, achieving equilibrium within 100–120 time units, academic pressure peaks at 700 in Figure 10 and then falls suddenly. Fig. 16 shows academic pressure beginning at 800 and stabilizing at about 300. The population of both undergraduate and graduate students falls to almost zero. The 3D phase space in Fig. 16(a) shows a spiral trajectory, suggesting that academic pressure preys on students, leading to a stable state with low student populations. When ρ is low, academic pressure is quite erratic and variable; this could be the result of outside factors. The stabilization of pressure levels as ρ increases suggests that specific guidelines or policies could help control the ups and downs of academic strain. As shown in Fig. 21, β and η significantly increase R_0, while α and δ moderately increase it; ρ strongly decreases it.

The ordinary differential equation (ODE) model is appropriate for scenarios where the response to academic stress is assumed to be immediate or lacks memory. The fractional-order model, particularly using the ABC derivative, is better suited for real-world educational systems, where the impact of academic stress is persistent and cumulative over time. This implies that, apart from this quality, other elements influence academic stress more strongly. Based on a thorough mathematical model impact analysis, our future plan aims to reduce student stress, improve academic performance, and enhance general well-being by creating a more favorable and efficient educational environment through adaptive control parameters.

Acknowledgment

The authors sincerely thank all individuals who provided valuable suggestions, insightful discussions, and constructive feedback that significantly contributed to the improvement and successful completion of this research work.

Authors contribution

Md. Asraful Islam conceived and designed the study, formulated the deterministic and fractional-order mathematical model, performed the analytical derivations and theoretical proofs, conducted stability, persistence, and bifurcation analyses, executed numerical simulations, interpreted the results, and prepared the original manuscript draft. Tanvir Ahmed contributed to the literature review, assisted with the review of analytical results, supported manuscript editing and formatting, and provided critical revisions. Both authors read and approved the final version of the manuscript.

Conflict of interest

The authors declare that there is no conflict of interest regarding the publication of this paper.

Reference

Ahmed N, Yasin MW, Akgül A, Baleanu D and Mircea OT. Mathematical analysis and pattern formation in diffusive predator–prey system. *J. Appl. Math.Comput.* 2025; 15(1): 580-622.

Amri A, Khan KAN and Qamar JA. Combining impact of velocity, fear and refuge for the predator–prey dynamics. *J. Biol. Dyn.* 2023; 17(1): 2181989.

Bai D, Li J and Zeng W. Global stability of the boundary solution of a nonautonomous predator–prey system with Beddington–DeAngelis functional response. *J. Biol. Dyn.* 2020; 14(1): 421-437.

Bai L, Li J, Zhang K and Zhao W. Analysis of a stochastic ratio-dependent predator–prey model driven by Lévy noise. *Appl. Math. Comput.* 2014; 233: 480-493.

Bai Y and Li Y. Stability and hopf bifurcation for a stage-structured predator–prey model incorporating refuge for prey and additional food for predator. *Adv. Differ. Equ.* 2019; 2019: 42.

Christle CA, Jolivette K and Nelson CM. School characteristics related to high school dropout rate. *Rem. Spec. Educ.* 2007; 28(6): 325-339.

Deng H, Chen F, Zhu Z and Li Z. Dynamic behaviors of Lotka–Volterra predator–prey model incorporating predator cannibalism. *Adv. Differ. Equ.* 2019; 2019(1): 359.

Dubey B, Kumar A andMaiti AP. Global stability and Hopf bifurcation of a prey–predator system with two discrete delays, including habitat complexity and prey refuge. *Commun. Nonlinear Sci. Numer. Simula.*, 2019; 67: 528-554.

Gokila C, Sambath M, Balachandran K and MaYK. Stationary distribution and global stability of a stochastic predator–prey model with disease in the prey population. *J. Biol. Dyn.* 2023; 17(1): 2164803.

Hone ANW, Irle MD and Thurura GW. On the neimark–sacker bifurcation in a discrete predator–prey system. *J. Biol. Dyn.* 2010; 4(6): 594-606.

Hu D and Cao H. Stability and bifurcation analysis in a predator–prey system with michaelis–mententype predator harvesting. *Nonlinear Anal. Real World Appl.* 2017; 33: 58-82.

Islam MA and Ahmed T. Modeling and stability analysis of the dynamics of prey–predator population. *Jagannath Univ. J. Sci*.2024; 11(1): 81-93.

Islam MA, Hassan IR and Ahmed P. Dynamic complexity of fifth-dimensional Henon map with Lyapunov exponent, permutation entropy, bifurcation patterns, and chaos. *J. Comput. Appl. Math.* 2025; 466: 116547.

Jiang G, Lu Q and Qian L. Complex dynamics of a Holling type II prey–predator system with state feedback control. *Chaos Solition Fract.* 2007; 31(2): 448-461.

Li F and Li H. Hopf bifurcation of a predator–prey model with time delay and stage structure for the prey. *Math.Comput. Model.* 2012; 55(3-4): 672-679.

Liu M, He X and Yu J. Dynamics of a stochastic regime-switching predator–prey model with harvesting and distributed delays. *Nonlinear Anal. Hybr. Syst.* 2018; 28: 87-104.

Lotka AJ. *Elements of Physics Biolology*.1st ed., *Williams & Wilkins Co., Baltimore*. 1925;pp. 1-495.

Ma Z, Li W, Zhao Y, Wang W, Zhang H and Li Z. Effects of prey refuges on a predator–prey model with a class of functional responses: The role of refuges. *Math. Bio. Sci.* 2009a; 218(2): 73-79.

Ma ZP, Huo HF and Liu CY. Stability and Hopf bifurcation analysis on a predator–prey model with discrete and distributed delays. *Nonlinear Anal. Real World Appl.* 2009b; 10(2): 1160-1172.

Misra AK and Dubey B. A ratio-dependent predator–prey model with delay and harvesting. *J. Biol. Syst.* 2010; 18(2): 437-453.

Mondal B, Roy S, Ghosh U and Tiwari PK. A systematic study of autonomous and nonautonomous predator–prey models for the combined effects of fear, refuge, cooperation, and harvesting. *Europ. Phys. J. Plus*, 2022; 137: 724.

Respondek L, Seufert T,StupniskyR and NettUE. Perceived academic control and academic emotions predict undergraduate university student success: Examining effects on dropout intention and achievement. *Front. Psychol.* 2017; 8, 243.

Sha A, Samanta S, Martcheva M and Chattopadhyay J. Backward bifurcation, oscillations, and chaos in an eco-epidemiological model with fear effect. *J. Biol. Dyn.* 2019;13(1): 301-327.

Ska N, Tiwari PK, Pal S andMartcheva M. A delay non-autonomous model for the combined effects

of fear, prey refuge, and additional food for predator. *J. Biol. Dyn.* 2021; 15(1): 580-622.

Song X, Hao M and Meng X. A stage-structured predator–prey model with disturbing pulse and time delays. *Appl. Math. Model.* 2009; 33(1): 211-223.

Tuerxun N, Abdurahman X and Teng Z. Global dynamics and optimal harvesting in a stochastic two-predators one-prey system with distributed delays and Lévy noise. *J. Biol. Dyn.*, 2020; 14(1): 32-56.

Ullah MS and Kabir KMA. Behavioral game of quarantine during the monkeypox epidemic: Analysis of deterministic and fractional order approach. *Heliyon*, 2024; 10(5):e26998.

Wang C and Yang W. Impact of nonlocal fear effect and mutual interference between predators in a diffusive predator–prey model. *J. Appl. Math. Comput.* 2025;69: 2155-2176.

Wang W, Zhu Y, Cai Y and Wang W. Dynamical complexity induced by Allee effect in a predator–prey model. *Nonlinear Anal. Real World Appl.* 2014; 16: 103-119.

Wei F and Fu Q. Hopf bifurcation and stability for predator–prey systems with Beddington–DeAngelis type functional response and stage structure for prey incorporating refuge. *Appl. Math. Model.* 2016; 40(1): 126134.

Xiang C, Huang J and Wang H. Bifurcations in Holling-Tanner model with generalist predator and prey refuge. *J. Differ. Equ.* 2023; 343: 495-529.

Yu T, Tian Y and Guo SH. Dynamical analysis of an integrated pest management predator–prey model with weak Allee effect. *J. Biol. Dyn.* 2019; 13(1): 218-244.

Zheng J, Wang Z, Li Y and Wang J. Bifurcations and chaos in a three-dimensional generalized Hénon map. *Adv. Differ. Equ.* 2018; 2018(1): 185.

Zhu X, Wang H and Ouyang Z. The state-dependent impulsive control for a general predator–prey model. *J. Biol. Dyn.*, 2022; 16(1): 354-372.

J. Bangladesh Acad. Sci. 50(1); 99-106: March 2026 DOI:https://doi.org/10.3329/jbas.v50i1.83761

Journal of Bangladesh Academy of Sciences

Journal homepage: http://www.bas.org.bd/publications/jbas.html

Research Article

Quality evaluation of near-expiry locally manufactured paracetamol tablets from rural health centers in Punjab, Pakistan

Ifra, Habib Hussain[1*], Zulfiqar Ali[2], Hajira Rehman[3] and Arooj Aslam

Department of Chemistry, University of Engineering and Technology, Lahore, Pakistan

ARTICLE INFO

Article History

Received: 16 August 2025
Revised: 15 February 2026
Accepted: 18 February 2026

Keywords: Paracetamol, Near-expiry drugs, Quality control parameters, Pharmacopeial compliance.

ABSTRACT

This study evaluated the pharmaceutical quality of near-expiry locally manufactured paracetamol 500 mg tablets collected from rural health centers in Punjab, Pakistan. Five commercial brands were assessed for key quality parameters, including physical characteristics, mechanical strength, disintegration, dissolution, and active pharmaceutical ingredient (API) content, in accordance with United States Pharmacopeia (USP) and British Pharmacopoeia (BP) standards. Weight variation, hardness, friability, disintegration, dissolution, and assay tests were performed using standard pharmacopeial methods. All brands complied with pharmacopeial limits for weight variation (616.0±38.2 mg), hardness (5.04±0.89 kg/cm²) and disintegration time (185-876 s). Friability remained within acceptable limits (< 1.0 %) for all brands except brand D (1.141±0.05%), which exceeded the specified limit. Dissolution testing showed that 4 brands released more than 80 % of the drug within 30 mins, whereas Brand D exhibited slightly lower drug release (79.38±1.12%). API assay results (95.90-99.89%) confirmed acceptable chemical stability across all formulations. Overall, the majority of near-expiry paracetamol tablets retained acceptable physicochemical quality, with only minor deviations observed in one brand, supporting their potential use in emergency and resource-limited settings.

Introduction

Paracetamol (acetaminophen) is one of the most widely used analgesics and antipyretics globally and is listed by the World Health Organization (WHO) as an essential medicine due to its safety, affordability and effectiveness (Babu et al., 2023; WHO, 2025). In low and middle-income countries (LMICs) such as Pakistan, paracetamol forms a core component of primary and emergency healthcare, particularly in rural areas where treatment options are limited and reliance on low-cost generic medicines is high.

Rural health facilities in Pakistan, including basic health units (BHUs) and dispensaries, often depend on locally manufactured generic medicines to meet patient demand. However, these facilities frequently face challenges related to inadequate storage conditions, limited climate control, weak inventory management and insufficient post-market surveillance. Such factors can adversely affect the physical integrity, dissolution behaviour, and chemical stability of pharmaceutical products as they approach their expiry date (Newton et al., 2010; Caudron et al., 2008).

*Corresponding author: <hbhussain@uet.edu.pk>

[1]*Department of Basic Sciences and Humanities, University of Engineering and Technology Lahore, Narowal Campus, Pakistan*

[2]*Department of Chemistry, University of Engineering and Technology Lahore, New Campus, Pakistan;* [3]*Department of Chemistry, University of Sahiwal, Sahiwal, Pakistan*

Several studies conducted in South Asia and other LMICs have demonstrated that the quality of essential medicines, including analgesics, may vary depending on storage conditions, manufacturing practices, and regulatory oversight. Although some drug products may retain acceptable potency beyond their labeled expiry date, others may fail pharmacopeial requirements, potentially compromising therapeutic effectiveness and patient safety (Lyon et al., 2006; Kushwaha et al., 2025; Marisa et al., 2024).

Most published studies evaluating the quality of paracetamol tablets in Pakistan have focused on samples obtained from urban pharmacies or controlled laboratory environments. These studies generally report satisfactory compliance with pharmacopeial standards but do not reflect real-world storage and distribution in rural healthcare settings (Alsaifi and Alyahawi, 2018; Almuzaini et al., 2013; Nayyar et al., 2012; Uddin et al., 2020). Importantly, data on near-expiry medicines, particularly those supplied to rural health centers, remain extremely limited (Aslam et al., 2010).

There is a lack of peer-reviewed evidence assessing the pharmaceutical quality of locally manufactured, near-expiry paracetamol tablets at the point of use in rural Pakistan. This gap is critical; as such medicines are often used during shortages, emergencies, or public health crises, where decisions regarding continued use, redistribution, or disposal must be informed by scientific evidence rather than assumption.

This study intends to evaluate the pharmaceutical quality and stability of near-expiry locally manufactured paracetamol 500 mg tablets collected from rural health centers in Punjab, Pakistan. Standard quality control tests, including weight variation, hardness, friability, disintegration, dissolution, and active pharmaceutical ingredient (API) assay, were performed in accordance with BP and USP guidelines. The findings were intended to determine whether these tablets retain acceptable quality and may be suitable for use in emergency and resource-limited rural healthcare settings.

Materials and Methods

Reagents and materials included distilled water, 0.1 N HCl, 0.1 M NaOH, 250 mL volumetric flasks, and droppers. Pharmaceutical quality assessment of the collected samples was conducted using standard laboratory instruments: an analytical balance (Mettler Toledo), for weight variation, a tablet hardness tester (Erweka TBH 100), a friabilator, a disintegration apparatus (ZT 320), and USP Type I (basket) and Type II (paddle)dissolution apparatus. A UV/Vis spectrophotometer (Shimadzu UV- 1800) was used for the quantitative determination of paracetamol content in dissolution media. All quantitative measurements were performed according to USP/BP guidelines and results are reported as mean ± SD.

Sample collection and sampling strategy

Five samples of locally manufactured paracetamol tablets (500 mg) nearing expiry dates were collected in September 2023 from healthcare facilities located in Punjab, Pakistan. Sampling sites included the Rural Health Centre Shahdara (Lahore), Polio Center Narowal, Green Pharmacy Narowal, and two rural locations in the Gujranwala district. A combined purposive stratified random sampling approach was adopted. Purposive sampling was used to specifically target near-expiry paracetamol tablets, as these products are more likely to be encountered in rural healthcare settings with slower stock turnover. Stratification was based on geographical location and manufacturer, ensuring representation of multiple locally operating pharmaceutical companies. Within each site, tablet strips were randomly selected from available stock to minimize selection bias. The collected tablets were coded as brands A-E (Table 1) to blind manufacturer identity during laboratory analysis.

Weight variation

Weight variation testing was conducted in accordance with pharmacopeial procedures (Akhtar et al., 2022). For each brand, tablets (n=20) were

Table 1. Parameters of locally packaged paracetamol tablets.

Code	Manufacturing company	Date of sample collection	Manufacturing date	Expiry date	Mode of packaging
A	Aneeb Pharmaceuticals, 24-Km Bedian Road Lahore, Pakistan	09-2023	04-2019	04-2024	Blister
B	Stanley Pharmaceuticals, 84- B Industrial Estate, Hayatabad Peshawar, Pakistan	09-2023	05-2020	05-2024	Blister
C	Evolution Pharmaceuticals, Industrial Estate Rawal Islamabad, Pakistan	09-2023	05-2020	05-2024	Blister
D	Legacy Pharmaceuticals, Industrial Estate, Hayatabad Peshawar, Pakistan	09-2023	04-2019	04-2024	Blister
E	Citi Pharma, 3 Km, Head Balloki Road, Phool Nagar Kasur, Pakistan	09-2023	04-2020	04-2024	Blister

selected and individually weighed using an analytical balance. The average tablet weight and percentage deviation for each tablet were calculated. Results were expressed as mean±SD (n=20), and compliance with pharmacopeial limits was assessed.

Hardness test

Tablet hardness was determined using a Monsanto hardness tester(Santosh et al., 2015). For each brand, 10 tablets (n=10) were randomly selected and tested individually by applying force (kg/cm²) until fracture occurred. The hardness values were recorded and reported as mean±SD (n=10).

Friability test

Friability was evaluated using a Eureka friabilator to assess the mechanical resistance of tablets during handling (Kusuma et al., 2015). A pre-weighed sample of tablets (6.5 g approx.) from each brand was subjected to 25 rpm for 4 min. After dedusting, tablets were reweighed, and the percentage friability was calculated using equation (1). Each test was performed once per brand as per pharmacopeial recommendation, and results were reported as percentage weight loss (n = 1).

$$\text{Friability (\%)} = \frac{Wi - Wf}{Wi} \times 100 \quad (1)$$

Where W_i = Weight before test, W_f = Weight after test.

Disintegration test

Disintegration testing was carried out using six tablets per brand (n=6**)** in accordance with pharmacopeial guidelines (Marisa et al., 2024). Each tablet was individually placed in the tube of the disintegration tester basket rack assembly, with a disk placed over each tablet to prevent floating. The basket assembly was immersed in a 1 L beaker containing 0.1 N HCl at 37 ± 0.5 °C and operated at 30 rpm. The time taken for complete disintegration of each tablet into particles small enough to pass through the mesh screen (typically 2 mm) without visible residue was recorded. Results were expressed as mean disintegration time±SD (n=6)**.**

Dissolution test

Dissolution studies were performed using a USP Type I (basket) apparatus. Six tablets per brand (n =

6) were individually tested in 900 mL of 0.1 N HCl (simulated gastric fluid), maintained at 37 ± 0.5 °C, with the basket rotating at 150 rpm. Aliquots (2 mL) were withdrawn at 10 min intervals up to 30 min and replaced with an equal volume of fresh pre-warmed medium to maintain sink conditions. Each collected sample was diluted to 10 mL, filtered, and the filtrate absorbance was measured at 222 nm using a UV/Visible spectrophotometer. Drug release was calculated using a previously constructed calibration curve. Dissolution results were reported as mean percentage drug release ± SD (n=6)**.** All brands met the USP requirement of at least 80% drug release within 30 min (Akhtar et al., 2022).

Assay analysis

Assay testing was conducted to quantify the active pharmaceutical ingredient (API) content of paracetamol tablets in accordance with established pharmacopeial procedures (Marisa et al., 2024). For each brand, twenty tablets (n=20) were accurately weighed, finely powdered, and a sample equivalent to 0.15 g of paracetamol was taken for analysis. The sample was transferred to a volumetric flask containing 50 mL of 0.1 M NaOH, then diluted to 100 mL with distilled water. The mixture was shaken for 15 min to ensure complete extraction of the API and then diluted to a final volume of 200 mL with distilled water. After filtration, a 10 mL aliquot of the clear filtrate was transferred to a second volumetric flask, mixed with 10 mL of 0.1 M NaOH, and diluted to 100 mL with distilled water. The absorbance of the resulting solution was measured at 257 nm using a UV/Visible spectrophotometer. Assay results were expressed as mean±SD (n=20)**,** providing an assessment of content uniformity and analytical precision (Table 2).

Results and Discussion

All tablet samples exhibited acceptable visual characteristics, including uniform color, smooth surfaces, and absence of visible defects such as cracks. Minor variations in scoring and imprint clarity were observed, which may influence identification but are likely to affect pharmaceutical performance. All tablets were white, odorless, and crystalline, consistent with standard paracetamol tablet formulations.

Weight variation

Weight variation is a critical quality indicator of dose uniformity in uncoated tablets, reflecting consistency in granulation and die filling during manufacturing.

According to USP specifications, tablets weighing more than 250 mg must not deviate by more than ±5 % from the mean weight. All tested brands (A-E) complied with this requirement, with mean tablet weights ranging from 568.1±3.9 mg (brand C) to 673.5±4.2 mg (brand A) (Table 2). Compliance with pharmacopeial limits indicates adequate control of the manufacturing process and uniform distribution of API. Similar findings have been reported for locally manufactured paracetamol tablets in Pakistan, India, and Bangladesh, where acceptable weight variation was observed even in near-expiry products (Luhar et al.,2023; Mj et al., 2023; Salisu et al., 2017; Kar and Kar, 2020).

Hardness test

Tablet hardness reflects mechanical strength and resistance to breakage during handling, transportation, and storage (Alderborn, 2002). In this study, hardness values ranged from 4.02 to 6.07 kg/cm², within the USP recommended range (4-10 kg/cm²) for uncoated tablets. Brand D exhibited the highest hardness (6.07±0.40 kg/cm²), suggesting a higher compression force or increased binder concentration during manufacturing (Table 2). While adequate hardness is necessary for physical stability, excessive hardness is known to adversely affect tablet disintegration and dissolution by reducing porosity and liquid penetration (Desai et al., 2014). This is consistent with brand D's slower disintegration and lower dissolution compared with other brands.

Friability

Friability testing evaluates a tablet's ability to withstand mechanical stress during handling and

distribution (Alderborn, 2002). The BP and USP specify that the acceptable friability limit is not more than 1% for uncoated tablets. Brands A, B, C, and E demonstrated friability values within acceptable limits, 0.375%, 0.237%, 0.937% and 0.135%, respectively, indicating satisfactory mechanical integrity (Table 2). In contrast, brand D exhibited a friability of 1.141%, exceeding the pharmacopeial threshold, consistent with poor resistance to mechanical stress (Patere et al., 2015). Elevated friability in brand D, despite relatively high hardness, suggests structural brittleness rather than insufficient compression. This pattern may result from uneven binder distribution, excessive lubricant interfering with particle adhesion, poor granulation, and environmental stress during storage (Waterman and Adami, 2005). Similar patterns have been reported in Nigeria, Pakistan, and Bangladesh, where isolated brands failed friability testing due to formulation or storage deficiencies (Luhar et al.,2023; Mj et al., 2023; Salisu et al., 2017; Kar and Kar, 2020).

Table 2. Pharmaceutical evaluation of paracetamol tablets (Mean ± SD).

Sample code	Weight variation (mg)	Hardness (kg/cm^2)	Friability (%)	Disintegration time (s)	Assay/API (%)
A	673.5 ± 4.2	4.05 ± 0.30	0.375	185 ± 11	98.90 ± 0.74
B	601.5 ± 4.0	5.09 ± 0.33	0.237	363 ± 13	99.76 ± 0.72
C	568.1 ± 3.9	4.02 ± 0.31	0.937	315 ± 12	98.35 ± 0.75
D	596.7 ± 4.0	6.07 ± 0.40	1.141	876 ± 11	95.90 ± 0.71
E	641.0 ± 4.2	5.99 ± 0.32	0.135	225 ± 10	99.89 ± 0.74

USP Standards: Weight variation: ±5 %; Hardness: 4-10 kg/cm^2; Friability: < 1 %; Disintegration time: ≤ 900 s; API content: 95-105 %.

Disintegration test

Disintegration testing ensures that tablets break down into smaller particles under physiological conditions (Desai et al., 2014; Molavi et al., 2020), ensuring the availability of the active pharmaceutical ingredient (API) for absorption. According to BP and USP, uncoated tablets should disintegrate within 15 min in purified water or simulated gastric fluid. All brands complied with pharmacopeial limits, demonstrating complete disintegration within 900s (Table 2). Brand A exhibited the fastest disintegration time (185±11s), followed by brand E (225±10s), brand C (315±12s), and brand B (363±13s). Brand D, though within the acceptable limit, showed a significantly longer disintegration time (876±11s), indicating a slower disintegration rate, which may affect the onset of therapeutic action. Prolonged disintegration in brand D is likely due to high hardness, reduced porosity, or insufficient disintegration efficiency, which can also be exacerbated by moisture-induced binder hardening during storage (Waterman and Adami, 2005). This suggests the importance of regular quality monitoring in decentralized healthcare settings. These observations align with studies showing that extended disintegration times directly correlate with slower dissolution in immediate-release paracetamol tablets (Mj et al. 2023; Molavi et al., 2020).

Dissolution test

Dissolution testing evaluates the in-vitro release rate of the API under simulated gastrointestinal conditions (BPC, 2024). According to USP standards, a minimum of 80 % drug release within 30 min is required for immediate release of paracetamol tablets to be considered pharmaceutically acceptable. The dissolution profiles of all 5 brands' tablets were evaluated at 5,

10, 15, and 30 min intervals (Fig. 1). All brands demonstrated increasing drug release over time, consistent with expected dissolution kinetics. Brands A (85.78%), B (89.36%), C (91.89%), and E (90.77%) exceeded the USP requirement of ≥ 80 % drug release within 30 min, with brand C achieving the most rapid release. Brand D released only 79.38 %, slightly below the USP threshold, consistent with its high hardness, extended disintegration time, and elevated friability (Kar et al., 2015). Among all samples, brand C showed the most rapid release, with 35.75% at 5 min and over 91% by 30 min, indicating superior dissolution performance.

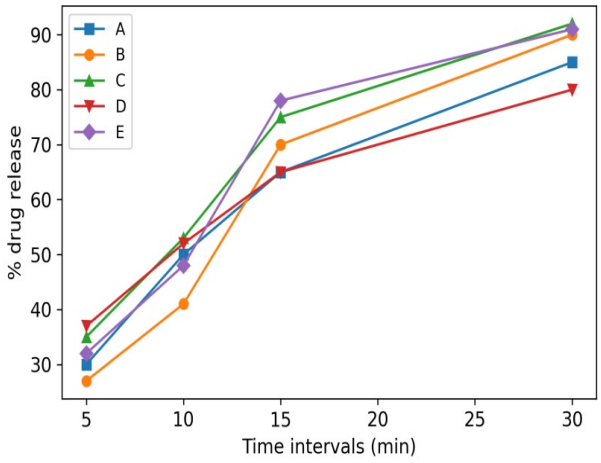

Fig.1. Dissolution profiles of local Paracetamol tablets.

In contrast, brand B exhibited a slower initial release (27.38% at 5 min), although it met the 30 min specification. These findings suggest that although most near-expiry paracetamol tablets retained acceptable dissolution characteristics, brand D's slight deviation may indicate compromised bioavailability, especially in time-critical therapeutic applications. This slight deviation may be due to improper granulation reducing surface area, uneven binder distribution, and moisture effects during prolonged storage near expiry (Patere et al., 2015; Waterman and Adami, 2005; Molavi et al., 2020). This underscores the need for rigorous post-distribution quality monitoring, particularly in rural settings where older stock may persist in circulation. Regional studies confirm similar trends: most brands in Bangladesh and Pakistan met dissolution criteria, but isolated brands occasionally failed due to formulation inconsistencies (Mj et al., 2023; Kar and Kar , 2020).

Assay/API analysis

Assay analysis was conducted to determine the percentage of active pharmaceutical ingredient (API) present in each tablet and to verify compliance with pharmacopeial standards. All brands, A (98.90±0.74%), B (99.76±0.72%), C (98.35±0.75%), D (95.90±0.71%), and E (99.89±0.74%), demonstrated API content within USP limits (95–105%) with brand D at the lower end (Table 2). This indicates that observed physical deficiencies (friability, disintegration, dissolution) are primarily due to formulation or mechanical factors rather than chemical degradation (Halbert, 2000). However, since the assay values remained compliant, the observed performance issues for brand D are more likely attributable to physical and mechanical instability rather than to a significant loss of API.

Brand D's combination of higher friability, extended disintegration, and lower dissolution reflects an imbalance between mechanical robustness and drug release requirements. The literature indicates that robust tablets must balance compression strength with porosity and disintegrant efficiency; failure to optimize this balance often results in compromised dissolution even when assay values remain within acceptable ranges (Lawal et al., 2015). Therefore, the observed deviations in Brand D likely stem from manufacturing variables (binder/disintegrant level, compression force, granulation quality) and possibly from storage conditions that alter tablet physical properties over time. This emphasizes the need for adherence to good manufacturing practices, routine post-distribution quality monitoring, and stronger supply chain storage conditions, particularly in resource-limited and rural healthcare settings where environmental control is less reliable.

Conclusion

This study evaluated the pharmaceutical quality of near-expiry, locally manufactured paracetamol

tablets collected from rural healthcare facilities across Punjab, Pakistan. All tested brands complied with pharmacopeial specifications for weight variation, hardness, disintegration time and active pharmaceutical ingredient content, demonstrating acceptable physicochemical stability and preservation of chemical potency close to expiry. However, one brand (D) exceeded the friability limit and showed marginally reduced dissolution, releasing 79.38 % of the drug content within 30 min, slightly below USP requirements. These deviations are likely attributable to formulation imbalance, suboptimal granulation or compression, and possible moisture-related effects during storage. Overall, the findings indicate that most near-expiry paracetamol tablets retain adequate mechanical integrity and in-vitro performance, supporting their potential use in emergency and resource-constrained settings. Nonetheless, stringent adherence to Good Manufacturing Practices, controlled storage conditions, and routine post-distribution quality monitoring remain essential to ensure consistent therapeutic efficacy throughout the product shelf life.

Funding source

This research did not receive any specific grant from funding agencies in the public, commercial, or not-for-profit sectors.

Acknowledgment

The authors sincerely acknowledge the University of Engineering and Technology Lahore for providing resources and colleagues for their valuable contributions and guidance.

Authors contribution

All authors contributed equally.

Conflict of interest

Authors declare no competing interests.

References

Akhtar H, Ali M, Ahmad SA, Humayoon R, Ahmed KZ and Hassan HS. Assessment of in Vitro quality tests of paracetamol brands 500mg in Karachi, Pakistan. *J.Pharm. Res. Int.* 2022; 34(46A): 11-21.

Alderborn G. *Tablets and compaction, pharmaceutics: The Sci. of Dosage Form Design*, 2nd Edition London, Churchill Livingstone; 2002. pp. 397-440.

Almuzaini T, Choonara I and Sammons H. Substandard and counterfeit medicines: a systematic review of the literature. *BMJ Open*. 2013; 3(8): e002923.

Alsaifi A and Alyahawi A. Quality assessment of different brands of paracetamol tablets in Yemeni market. *Univers. J. Pharm. Res*. 2018; 3(4): 39-43.

Aslam N, Shoaib MH and Bushra R. Analgesic prescribing in developing countries. *Jordan J. Pharm. Sci.* 2010; 3(2): 137-143.

Babu PS, Hemalatha P, Krishna PVS, Pujitha T, Raju SL, Ravi K and Susmitha MJN. In vitro bio-equivalence studies on commercial formulations containing paracetamol and ibuprofen. *Int. J. Pharm. Sci. Rev. Res.* 2023; 79(2): 199-205.

British Pharmacopoeia Commission (BPC), *British Pharmacopoeia 2024*. The Stationary Office, London, UK.

Caudron JM, Ford N, Henkens M, Mace C, Monroe RK and Pinel J. Substandard medicines in resource-poor settings: a problem that can no longer be ignored. *Trop. Med. Int. Health*. 2008; 13(8): 1062-1072.

Desai PM, Er PX, Liew CV and Heng PW. Functionality of disintegrants and their mixtures in enabling fast disintegration of tablets by a quality by design approach. *AAPS Pharm. Sci. Tech.* 2014; 15(5): 1093-1104.

Halbert G. Book review. Drug stability: Principles and practices, 3rdedition, revised andexpanded, Edited by JT Cartensen and C. T. Rhodes. In: *Drugs and the Pharmaceutical Sciences*, Vol. 107, Marcel Dekker, New York, 2000, *Int. J. Pharm*. 2001; 213(1-2): 223.

Kar A, Amin MN, Hossain MS, Mukul MEH, Rashed MSU and Ibrahim M. Quality analysis of different marketed brands of paracetamol available in Bangladesh. *Int. Curr. Pharm. J*. 2015; 4(9): 432-435.

Kar AK and Kar B. In-vitro comparative dissolution study of commercially available paracetamol tablet. *J. Drug Deliv. Ther*. 2020; 10(1): 18-23.

Kushwaha V, Agrawal P, Pathak B, Vekaria H and Siddiqui S. Effectiveness, safety and disposal of medications beyond expiry dates: Brief review. *Int. J. Pharm. Sci. Rev. Res.*, 2025; 85(4): 105-108.

Kusuma MS, Annapurna M and Bukkapatnam V. Novel analytical techniques for the determination of ondansetron hydrochloride in pharmaceutical dosage forms by spectrophotometry. *J. Chem. Pharm. Sci.* 2015; 8(4): 863-866.

Lawal MV, Odeniyi MA and Itiola OA. Effect of thermal and chemical modifications on the mechanical and release properties of paracetamol tablet formulations containing corn, cassava and sweet potato starches as filer-binders. *Asian Pac. J. Trop. Biomed.* 2015; 4(7): 585-590.

Luhar SV, Narkhede SB, Lad HH, Patel SR, Patel SR, Patel SB, Patel VK and Patel YA. In-vitro evaluation of different marketed brands of Paracetamol tablets using quality control tests. *EPRA Int. J. Res. Dev*. 2023; 8(5): 254-258.

Lyon RC, Taylor JS, Porter DA, Prasanna HR and Hussain AS. Stability profiles of drugs products extended beyond labeled expiration dates. *J. Pharm. Sci*. 2006; 95(7): 1549-1560.

Marisa G, Kapala J, Mafiri T, Matinde R, Kimaro E and Kale E. Quality evaluation of locally manufactured paracetamol tablets in East Africa. *Bio. Med. Res. Int*. 2024; 1: 9437835.

Mj KK, Abbas HK, Shaheed DQ, Hameed HM, Jabur MN, Shaker MZ, Abd BK and Kadhim AJ. In-vitro comparative quality evaluation of paracetamol tablets marketed in Iraq. *J. Med. Chem. Sci*. 2023; 6(5): 1087-1099.

Molavi F, Hamishehkar Hand Nokhodchi A. Impact of tablet shape on drug dissolution rate through immediate released tablets. *Adv. Pharm. Bull.* 2020; 10(4): 656-661.

Nayyar GML, Breman JG, Newton PN and Herrington J. Poor-quality antimalarial drugs in southeast Asia and sub-Saharan Africa. *Lancet Infect. Dis.* 2012; 12(6): 488-496.

Newton PN, Green MD and Fernandez FM. Impact of poor-quality medicines in developing world. *Trends Pharm. Sci.* 2010; 31: 99-101.

Patere SN, Kapadia CJ and Nagarsenker MS. Influence of formulation factors and compression force on release profile of sustained release metoprolol tablets using compritol(® 888ATO as lipid excipient. *Indian. J. Pharm. Sci*. 2015; 77(5): 620-625.

Salisu I, Batagarawa SM, Sabi'u J and Bello S. Assessment of the quality of paracetamol tablet brands sold in katsina metropolis Nigeria. *J. Chem.Chem. Eng*. 2017; 2: 1-10.

Santosh J, Rekha K, Afaque A and Ashpak T. Estimation of ondansetron hydrochloride in bulk and formulation by second order derivative area under curve UV-spectrophotometric methods. *Pharma. Tutor*, 2015; 3(8): 42-46.

Uddin MG, Ferdous M, Jakir MA, Millat MS, Siddiqui SA, Islam MS and Uddin MS. In-vitro quality analysis of different brands of Paracetamol tablet available in Bangladesh. *World J. Pharm. Res.* 2020; 9(2): 92-100.

Waterman KC and Adami RC. Accelerated aging: prediction of chemical stability of pharmaceuticals. *Int. J. Pharm*. 2005; 293: 101-125.

World Health Organization(WHO). *WHO Model List of Essential Medicines*, 24th edition. Geneva, 2025.

J. Bangladesh Acad. Sci. 50(1); 107-145: March 2026 DOI:https://doi.org/10.3329/jbas.v50i1.84012

Journal of Bangladesh Academy of Sciences

Journal homepage: http://www.bas.org.bd/publications/jbas.html

Research Article

MetaFuzzy, MetaNeutrosophic, MetaSoft, and MetaRough Set

Takaaki Fujita[1*]

Independent Researcher, Tokyo, Japan

ARTICLE INFO

Article History

Received: 10 September 2025
Revised: 19 November 2025
Accepted: 02 December 2025

Keywords: MetaFuzzy set, Meta-Neutrosophic set, MetaSoft set, MetaRough set.

ABSTRACT

A MetaStructure is a higher-level framework treating collections of structures as objects, with natural operations that preserve isomorphisms across domains. An Iterated MetaStructure recursively applies the MetaStructure construction, forming successive layers in which structures of structures create deeper, hierarchical meta-levels. Concepts in the real world can be captured in terms of such meta-structures, and meta-level viewpoints are in fact applied in many different fields. Therefore, research on meta-structures is important, but it has not yet been well developed in the areas of fuzzy sets and neutrosophic sets. To address this gap, in this paper, we define the MetaFuzzy Set, MetaNeutrosophic Set, Meta Soft Set, and MetaRough Set by extending fuzzy sets, neutrosophic sets, soft sets, and rough sets through the use of Meta Structure and Iterated Meta Structure.

Introduction

Set theory is a fundamental concept in mathematics (Jech, 2003); however, classical sets are sometimes insufficient for modeling real-world applications. To bridge this gap, many frameworks for handling uncertainty have been proposed and studied, such as fuzzy sets (Zadeh, 1965), hesitant fuzzy sets (Torra, 2010), neutrosophic sets (Wang et al., 2010), interval-valued neutrosophic sets (Wang et al., 2005), soft sets (Maji et al., 2003), rough sets (Pawlak, 1982), and plithogenic sets (Smarandache, 2018), and their applications have been investigated in various scientific and engineering domains.

Furthermore, many mathematical and real-world structures can be examined from a meta-level perspective, in which entire structures themselves are treated as objects of study. The mathematical formalization of this viewpoint is provided by the notions of MetaStructure and Iterated MetaStructure (cf. (Fujita 2025a, 2025b)).

From the above discussion, research on meta-structures is important; however, it has not yet been extensively developed in the contexts of fuzzy sets and neutrosophic sets. To fill this gap, in this paper, we define the MetaFuzzy Set, MetaNeutrosophic Set, MetaSoft Set, and MetaRough Set by extending fuzzy sets, neutrosophic sets, soft sets, and rough sets using MetaStructure and Iterated MetaStructure. We then investigate the fundamental properties and characteristics of these meta-level concepts.

Preliminaries

This section presents the fundamental concepts and definitions that underpin the paper's discussions.

MetaStructure (Structure of Structure)

We first fix a general single-sorted, finitary *signature*

$$\Sigma = (\mathsf{Func}, \mathsf{Rel}, \mathrm{ar}_{\mathsf{Func}}, \mathrm{ar}_{\mathsf{Rel}}),$$

*Corresponding author: <takaaki.fujita060@gmail.com>

where Func (resp. Rel) is a set of function (resp. relation) symbols, andar records arities. A (single-sorted) Σ-*structure* is

$$\boldsymbol{C} = \left(H, (f^{\boldsymbol{C}})_{f\in \mathsf{Func}}, (R^{\boldsymbol{C}})_{R\in \mathsf{Rel}}\right),$$

with carrier $H \neq \emptyset$, interpretations $f^{\boldsymbol{C}}: H^m \to H$ for each $f \in \mathsf{Func}$ of arity$m$, and relations $R^{\boldsymbol{C}} \subseteq H^r$ for each $R \in \mathsf{Rel}$ of arity r. Let Str_{Σ} denote the class of all Σ-structures.

Definition 1 (MetaStructure over a fixed signature). (cf.(Fujita 2025b)) Fix Σ as above. A *MetaStructure* ("structure of structures") over Σ is a pair

$$\mathbb{M} = (U, (\Phi_\ell)_{\ell\in\Lambda}),$$

where:

- U is a nonempty set with $U \subseteq \mathrm{Str}_{\Sigma}$ (its elements are *objects* at level 0);
- for each label $\ell \in \Lambda$ of *meta-arity*$k_\ell \in \mathbb{N}$, the *meta-operation*

$$\Phi_\ell : U^{k_\ell} \to U$$

is specified by uniform carrier- and symbol-constructors:

$$\Gamma_\ell: (\boldsymbol{C}_1, \dots, \boldsymbol{C}_{k_\ell}) \mapsto H_\ell$$
(new carrier H_ℓ built functorially);
$$\forall f \in \mathsf{Func}:$$
$$f^{\Phi_\ell(\boldsymbol{C}_1,\dots,\boldsymbol{C}_{k_\ell})} = \Lambda_\ell^f\left(f^{\boldsymbol{C}_1}, \dots, f^{\boldsymbol{C}_{k_\ell}}\right);$$
$$\forall R \in \mathsf{Rel}:$$
$$R^{\Phi_\ell(\boldsymbol{C}_1,\dots,\boldsymbol{C}_{k_\ell})} = \Xi_\ell^R\left(R^{\boldsymbol{C}_1}, \dots, R^{\boldsymbol{C}_{k_\ell}}\right),$$

where Λ_ℓ^f and Ξ_ℓ^R are *uniform* recipes turning the symbols' interpretations on inputs into the symbol's interpretation on the output, over the new carrier H_ℓ. Moreover, each Φ_ℓ is *isomorphism-invariant* (a.k.a. natural): if $\alpha_i: \boldsymbol{C}_i \cong \boldsymbol{D}_i$.for $1 \le i \le k_\ell$, then there is an induced isomorphism

$$\Phi_\ell(\alpha_1, \dots, \alpha_{k_\ell}) : \Phi_\ell(\boldsymbol{C}_1, \dots, \boldsymbol{C}_{k_\ell}) \xrightarrow{\cong} \Phi_\ell(\boldsymbol{D}_1, \dots, \boldsymbol{D}_{k_\ell})$$

commuting with all interpretations of symbols of Σ.

Example 1 (MetaStructure on Graphs: disjoint union, Cartesian product, and line-graph). Fix the graph signature

$$\Sigma_{\mathrm{Graph}} = (\mathsf{Func} = \varnothing,\ \mathsf{Rel} = \{E\},\ \mathrm{ar}_{\mathsf{Rel}}(E) = 2),$$

where a Σ_{Graph}-structure is a (finite, simple, loopless, undirected) graph $\boldsymbol{G} = (V, E^{\boldsymbol{G}})$, encoded by a symmetric, irreflexive binary relation $E^{\boldsymbol{G}} \subseteq V \times V$. Let $U \subseteq \mathrm{Str}_{\Sigma_{\mathrm{Graph}}}$ be the class of all such graphs. We define three meta-operations

$$\Phi_{\sqcup},\ \Phi_{\circ} : U \times U \to U, \qquad \Phi_L : U \to U,$$

which together form a MetaStructure $\mathbb{M} = (U, \{\Phi_{\sqcup}, \Phi_{\circ}, \Phi_L\})$ in the sense of the Definition.

1) Disjoint union $\Phi_{\sqcup}(\boldsymbol{G}_1, \boldsymbol{G}_2)$ (meta-arity $k_{\sqcup} = 2$). For inputs $\boldsymbol{G}_i = (V_i, E^{\boldsymbol{G}_i})$ set the new carrier by a tagged sum

$$\Gamma_{\sqcup}(\boldsymbol{G}_1, \boldsymbol{G}_2) = H_{\sqcup} = (V_1 \times \{1\}) \cup (V_2 \times \{2\}),$$

and define the relation constructor uniformly by

$$\Xi_{\sqcup}^E(E^{\boldsymbol{G}_1}, E^{\boldsymbol{G}_2}) = \{((u,1),(v,1)) : (u,v) \in E^{\boldsymbol{G}_1}\} \cup \{((u,2),(v,2)) : (u,v) \in E^{\boldsymbol{G}_2}\}.$$

No cross edges are added. Isomorphism invariance follows immediate from the functorial tagging.

2) Cartesian product $\Phi_{\circ}(\boldsymbol{G}_1, \boldsymbol{G}_2)$ (meta-arity $k_{\circ} = 2$). Set

$$\Gamma_{\circ}(\boldsymbol{G}_1, \boldsymbol{G}_2) = H_{\circ} = V_1 \times V_2,$$

and

$$\Xi_{\circ}^E(E^{\boldsymbol{G}_1}, E^{\boldsymbol{G}_2}) = \{((u,x),(v,y)) : [u = v \wedge (x,y) \in E^{\boldsymbol{G}_2}] \vee bigl[(u,v) \in E^{\boldsymbol{G}_1} \wedge x = y]\}.$$

This is the usual Cartesian product of graphs; naturality holds componentwise.

3) Line-graph operator $\Phi_L(\boldsymbol{G})$ (meta-arity $k_L = 1$). For $\boldsymbol{G} = (V, E^{\boldsymbol{G}})$ let the new carrier be the edge set

$$\Gamma_L(\boldsymbol{G}) = H_L = E^{\boldsymbol{G}} \subseteq V \times V,$$

and define adjacency on edges by intersection of incident endpoints:

$$\Xi_L^E(E^{\boldsymbol{G}}) = \{(e_1, e_2) \in H_L \times H_L : e_1 \neq e_2 \text{ and } e_1 \cap e_2 \neq \varnothing\}.$$

This is the classical line-graph construction; isomorphism-invariance follows from edge-image preservation.

Tiny illustration. Let $\boldsymbol{P}_3$ be the path $a - b - c$ and $\boldsymbol{K}_2$ the single edge $x - y$. Then

$\Phi_{\sqcup}(\boldsymbol{P}_3, \boldsymbol{K}_2)$ has $|V| = 5$ with two components,

$$\Phi_L(\boldsymbol{P}_3) \cong \boldsymbol{P}_2, \qquad \Phi_{\circ}(\boldsymbol{P}_3, \boldsymbol{K}_2) \cong \text{ ladder on 4 vertices.}$$

Example 2 (MetaStructure on Groups: direct product and abelianization). Fix the group signature

$$\Sigma_{\mathrm{Grp}} = (\,\mathsf{Func} = \{\cdot,\ (\cdot)^{-1},\ e\},\ \mathsf{Rel} = \varnothing,$$

$$\mathrm{ar}_{\mathsf{Func}}(\cdot) = 2,\ \mathrm{ar}_{\mathsf{Func}}((\cdot)^{-1}) = 1,\ \mathrm{ar}_{\mathsf{Func}}(e) = 0\,).$$

A Σ_{Grp}-structure is a group $\boldsymbol{G} = (G, \cdot^{\boldsymbol{G}}, (\cdot)^{-1,\boldsymbol{G}}, e^{\boldsymbol{G}})$. Let $U \subseteq \mathrm{Str}_{\Sigma_{\mathrm{Grp}}}$ be the class of all (not-necessarily finite) groups. Define two meta-operations

$$\Phi_{\times} : U \times U \to U, \qquad \Phi_{\mathrm{ab}} : U \to U,$$

yielding a MetaStructure $\mathbb{M} = (U, \{\Phi_{\times}, \Phi_{\mathrm{ab}}\})$.

1) Direct product $\Phi_{\times}(\boldsymbol{G}_1, \boldsymbol{G}_2)$ (meta-arity $k_{\times} = 2$). For inputs $\boldsymbol{G}_i = (G_i, \cdot^{\boldsymbol{G}_i}, (\cdot)^{-1,\boldsymbol{G}_i}, e^{\boldsymbol{G}_i})$, set the carrier

$$\Gamma_{\times}(\boldsymbol{G}_1, \boldsymbol{G}_2) = H_{\times} = G_1 \times G_2,$$

and define uniformly, for all $(g_1, h_1), (g_2, h_2) \in G_1 \times G_2$,

$$\Lambda^{\cdot}_{\times}(\cdot^{\boldsymbol{G}_1}, \cdot^{\boldsymbol{G}_2})((g_1, h_1), (g_2, h_2)) = (g_1 \cdot^{\boldsymbol{G}_1} g_2,\ h_1 \cdot^{\boldsymbol{G}_2} h_2),$$

$$\Lambda^{(\cdot)^{-1}}_{\times}((\cdot)^{-1,\boldsymbol{G}_1}, (\cdot)^{-1,\boldsymbol{G}_2})(g, h) = (g^{-1,\boldsymbol{G}_1},\ h^{-1,\boldsymbol{G}_2}),$$

$$\Lambda^{e}_{\times}(e^{\boldsymbol{G}_1}, e^{\boldsymbol{G}_2}) = (e^{\boldsymbol{G}_1}, e^{\boldsymbol{G}_2}).$$

This is the standard categorical product; naturality is by componentwise isomorphisms.

2) Abelianization $\Phi_{\mathrm{ab}}(\boldsymbol{G})$ (meta-arity $k_{\mathrm{ab}} = 1$). For $\boldsymbol{G} = (G, \cdot^{\boldsymbol{G}}, (\cdot)^{-1,\boldsymbol{G}}, e^{\boldsymbol{G}})$, let

$$[G, G] = \langle\, g^{-1}h^{-1}gh\colon\ g, h \in G \,\rangle \leq G$$

be the commutator subgroup. Define the carrier as the quotient set

$$\Gamma_{\mathrm{ab}}(\boldsymbol{G}) = H_{\mathrm{ab}} = G/[G, G],$$

and the induced operations via the quotient map $\pi\colon G \to G/[G, G]$:

$$\Lambda^{\cdot}_{\mathrm{ab}}(\cdot^{\boldsymbol{G}})(\pi(g), \pi(h)) = \pi(g \cdot^{\boldsymbol{G}} h),$$

$$\Lambda^{(\cdot)^{-1}}_{\mathrm{ab}}((\cdot)^{-1,\boldsymbol{G}})(\pi(g)) = \pi(g^{-1,\boldsymbol{G}}),$$

$$\Lambda^{e}_{\mathrm{ab}}(e^{\boldsymbol{G}}) = \pi(e^{\boldsymbol{G}}).$$

Well-definedness uses $[G, G] \trianglelefteq G$. The output is the abelian group G_{ab}; functoriality (naturality) follows from the universal property of abelianization.

Tiny illustration. For the dihedral group $D_4 = \langle r, s \mid r^4 = s^2 = 1,\ srs = r^{-1}\rangle$,

$$\Phi_{\mathrm{ab}}(D_4) \cong C_2 \times C_2, \qquad \Phi_{\times}(C_2, C_3) \cong C_6.$$

Iterated MetaStructure

An Iterated MetaStructure recursively applies MetaStructure construction, forming successive layers in which structures of structures create deeper hierarchical meta-levels (Fujita 2025a, 2025b).

Definition 2 (Iterated MetaStructure of depth t). (Fujita 2025b) An Iterated MetaStructure of depth t overΣ is any MetaStructure $\mathfrak{M}^{(t)}$ of height t. When $s < t$, we *lift* a height-s MetaStructure $\mathfrak{M}^{(s)} = (U^{(s)}, \{\bigodot_i\}, \{\mathcal{S}_j\})$ to height t by

$$\iota_{s\to t}\colon U^{(s)} \overset{\mathsf{U}_{\Sigma}^{t-s}}{\to} U^{(t)} := \mathsf{U}_{\Sigma}^{t-s}\big(U^{(s)}\big),$$

and, for each $\bigodot_i\colon (\mathsf{E}_{\Sigma}^{m_i})^{k_i} \to \mathcal{P}^{n_i}(\mathsf{E}_{\Sigma}^{n_i})$, defining its lift

$$\bigodot_i^{\uparrow}\colon (\mathsf{E}_{\Sigma}^{m_i+t-s})^{k_i} \to \mathcal{P}^{n_i}\big(\mathsf{E}_{\Sigma}^{n_i+t-s}\big),$$

$$\bigodot_i^{\uparrow}\big(\mathsf{U}_{\Sigma}^{t-s}(x_1), \dots, \mathsf{U}_{\Sigma}^{t-s}(x_{k_i})\big) := \mathsf{U}_{\Sigma}^{t-s}\big(\bigodot_i (x_1, \dots, x_{k_i})\big),$$

and similarly for relations

$$\mathcal{S}_j^{\uparrow} := (\mathsf{U}_{\Sigma}^{t-s})^{\times \ell_j}(\mathcal{S}_j).$$

Example 3 (Iterated MetaStructure on Graphs via the line-graph operator). Fix the graph signature $\Sigma_{\mathrm{Graph}} = (\mathsf{Func} = \varnothing,\ \mathsf{Rel} = \{E\},\ \mathrm{ar}_{\mathsf{Rel}}(E) = 2)$, so a Σ_{Graph}-structure is a simple undirected graph $\boldsymbol{G} = (V, E^{\boldsymbol{G}})$. Let $\Phi_L\colon U^{(1)} \to U^{(1)}$ be the (level-1) line-graph meta-operation of Example 1: its carrier constructor makes the new carrier the old edge set, and its relation constructor connects two distinct edges iff they share a vertex.

To obtain an *Iterated MetaStructure of depth t* (Definition 2), we choose the canonical lift U_{Σ} to be identity-on-objects (so height only records iteration), and define the t-fold iterate

$$\Phi_L^{(t)} := \underbrace{\Phi_L \circ \Phi_L \circ \cdots \circ \Phi_L}_{t \text{ times}} : U^{(1)} \to U^{(1)}.$$

Concrete computation

- For the path $\boldsymbol{P}_m$ (with m vertices and $m-1$ edges),

$$\Phi_L(\boldsymbol{P}_m) \cong \boldsymbol{P}_{m-1},$$

$$\Phi_L^{(t)}(\boldsymbol{P}_m) \cong \boldsymbol{P}_{m-t} \quad \text{for } 1 \le t \le m-1.$$

In particular, for $m = 5$ and $t = 2$,

$$\Phi_L^{(2)}(\boldsymbol{P}_5) \cong \boldsymbol{P}_3 \quad \text{(vertex count: } 5 \to 4 \to 3\text{)}.$$

- For the cycle $\boldsymbol{C}_n$ ($n \ge 3$),

$$\Phi_L(\boldsymbol{C}_n) \cong \boldsymbol{C}_n \quad \Rightarrow \quad \Phi_L^{(t)}(\boldsymbol{C}_n) \cong \boldsymbol{C}_n \text{ for all } t \ge 1.$$

A depth-2 object spelled out. Let $\boldsymbol{G}_1 = \boldsymbol{P}_4$ and $\boldsymbol{G}_2 = \boldsymbol{K}_2$. Form the (level-1) family $X = \{\boldsymbol{G}_1, \boldsymbol{G}_2, \boldsymbol{G}_1\}$ and define a level-1 meta-relation on X by "same edge-count":

$$\mathcal{S}(\boldsymbol{A}, \boldsymbol{B}) \Leftrightarrow |E^{\boldsymbol{A}}| = |E^{\boldsymbol{B}}|.$$

Apply Φ_L once to obtain

$$\Phi_L(X) = \{\, \Phi_L(\boldsymbol{P}_4) = \boldsymbol{P}_3,\ \Phi_L(\boldsymbol{K}_2) = \boldsymbol{K}_1,\ \Phi_L(\boldsymbol{P}_4) = \boldsymbol{P}_3 \,\},$$

and lift the relation by the same recipe ("same edge-count"): $|E^{\boldsymbol{P}_3}| = 2$, $|E^{\boldsymbol{K}_1}| = 0$, so the only meta-edge at depth 2 is between the two copies of $\boldsymbol{P}_3$. This explicitly realises an *iterated* (depth-2) MetaStructure built from Φ_L.

Example 4 (Iterated MetaStructure on Groups via direct product and abelianization). Fix the group signature $\Sigma_{\mathrm{Grp}} = (\mathsf{Func} = \{\cdot, (\cdot)^{-1}, e\},\ \mathsf{Rel} = \varnothing)$. Let $U^{(1)}$ be the classof all groups, and consider two level-1 meta-operations:

$$\Phi_\times(\boldsymbol{G}, \boldsymbol{H}) = \boldsymbol{G} \times \boldsymbol{H} \quad \text{(direct product)},$$

$$\Phi_{\mathrm{ab}}(\boldsymbol{G}) = \boldsymbol{G}/[\boldsymbol{G}, \boldsymbol{G}] \quad \text{(abelianization)}.$$

As in Example 1, carriers and symbols are constructed uniformly (product set, pointwise operations; quotient by the commutator subgroup).

To produce an Iterated MetaStructure of depth t (Definition 2), we again take the canonical lift U_Σ to be identity-on-objects and define iterates

$$\Phi_{\mathrm{ab}}^{(t)} := \underbrace{\Phi_{\mathrm{ab}} \circ \cdots \circ \Phi_{\mathrm{ab}}}_{t \text{ times}},$$

$$\Phi_\times^{(t)} := \underbrace{\Phi_\times \circ \cdots \circ \Phi_\times}_{t-1 \text{ binary uses}}.$$

Concrete computation (depth $t = 2$).

- Start with the non-abelian groups $\boldsymbol{G}_0 = S_3$ and $\boldsymbol{H}_0 = D_4$.
- First abelianize (level 1):

$$\Phi_{\mathrm{ab}}(\boldsymbol{G}_0) \cong C_2,$$

$$\Phi_{\mathrm{ab}}(\boldsymbol{H}_0) \cong C_2 \times C_2.$$

- Second abelianization stabilizes (level 2):

$$\Phi_{\mathrm{ab}}^{(2)}(\boldsymbol{G}_0) \cong C_2,$$

$$\Phi_{\mathrm{ab}}^{(2)}(\boldsymbol{H}_0) \cong C_2 \times C_2,$$

since abelianization is idempotent upto isomorphism.

- Combine by the (binary) meta-operation at depth 2:

$$\Phi_\times\left(\Phi_{\mathrm{ab}}^{(2)}(\boldsymbol{G}_0),\ \Phi_{\mathrm{ab}}^{(2)}(\boldsymbol{H}_0)\right)$$

$$\cong\ C_2\ \times\ (C_2 \times C_2)\ \cong\ C_2^3.$$

In terms of orders: $|S_3| = 6$, $|D_4| = 8$, $|C_2| = 2$, $|C_2 \times C_2| = 4$, hence

$$|\Phi_\times(\Phi_{\mathrm{ab}}^{(2)}(S_3), \Phi_{\mathrm{ab}}^{(2)}(D_4))| = 2 \cdot 4 = 8.$$

Thus, the pair of iterated meta-operations $(\Phi_{\mathrm{ab}}^{(t)}, \Phi_\times)$ yields a concrete *depth*-2 MetaStructure on groups, with explicit carriers and operations at each stage.

Main Results: Meta set

In this section, we present the main results of this paper, focusing on discussions related to the concept of Meta Sets.

MetaFuzzy set (Fuzzy Set of Fuzzy Sets)

A Fuzzy Set generalizes classical sets by assigning each element a membership degree between 0and 1, thereby representing partial inclusion (Zadeh, 1965). A MetaFuzzy Set further extends this line of research by assigning membership values not to individual elements but to entire fuzzy sets, thereby enabling higher-level reasoning about collections of fuzziness across diverse contexts.

Definition 3 (Fuzzy Set). (Zadeh 1965; 1996) Let Y be a nonempty domain. A *fuzzy set* is given by a function

$$\mu: Y \to [0,1],$$

where μ(y) measures the degree to which y belongs to the set. A fuzzy relation on Y is a function $\delta: Y \times Y \to [0,1]$, viewed as a fuzzy subset of $Y \times Y$. We say δ is a fuzzy relation onμ if for every $y, z \in Y$,

$$\delta(y,z) \le \min\{\mu(y), \mu(z)\}.$$

Definition 4 (MetaFuzzy Set). Fix a nonempty base domain Y. A MetaFuzzySet *on Y* is a map

$$\mu^{\sharp}: \mathrm{Fuz}(Y) \to [0,1].$$

A MetaFuzzy relation on Y is a map

$$\Delta^{\sharp}: \mathrm{Fuz}(Y) \times \mathrm{Fuz}(Y) \to [0,1].$$

We say that $\Delta^{\sharp}$ is a MetaFuzzy relation on $\mu^{\sharp}$ if for all $\mu_1, \mu_2 \in \mathrm{Fuz}(Y)$ we have

$$\Delta^{\sharp}(\mu_1, \mu_2) \le \min\{\mu^{\sharp}(\mu_1), \mu^{\sharp}(\mu_2)\}.$$

Note 1 (Averaging functional M(·) on Fuz(Y)). Throughout, for a finite nonempty Y we use the averaging functional $M: \mathrm{Fuz}(Y) \to [0,1]$, $M(\mu) := \frac{1}{|Y|}\sum_{y\in Y} \mu(y)$. Since $0 \le \mu(y) \le 1$ for all $y \in Y$, we have $0 \le \sum_{y\in Y} \mu(y) \le |Y| \Rightarrow 0 \le M(\mu) \le 1$. In the sequel we take $\mu^{\sharp} := M$.

Example 5 (MetaFuzzy Set: Weekly traffic congestion severity). Let Y = {Mon,Tue,Wed} be three commuting days, and let $\mathrm{Fuz}(Y) = [0,1]^Y$. A fuzzy set $\mu \in \mathrm{Fuz}(Y)$ represents the degree of heavy congestion on each day. Consider two weeks:

$$\mu^{(A)}(\text{Mon,Tue,Wed}) = (0.2,\ 0.8,\ 0.6),$$
$$\mu^{(B)}(\text{Mon,Tue,Wed}) = (0.9,\ 0.7,\ 0.3).$$

We define the MetaFuzzy Set $\mu^{\sharp}$ by the averaging functional M of Note 1:

$$\mu^{\sharp}(\mu) := M(\mu) = \frac{1}{|Y|}\sum_{y\in Y} \mu(y)$$
$$= \frac{\mu(\text{Mon}) + \mu(\text{Tue}) + \mu(\text{Wed})}{3}.$$

Then

$$\mu^{\sharp}(\mu^{(A)}) = \frac{0.2+0.8+0.6}{3} = \frac{1.6}{3} = \frac{8}{15} \approx 0.533\overline{3},$$
$$\mu^{\sharp}(\mu^{(B)}) = \frac{0.9+0.7+0.3}{3} = \frac{1.9}{3} = \frac{19}{30} \approx 0.633\overline{3}.$$

Next, we define a MetaFuzzy relation $\Delta^{\sharp}$ as the average of pointwise minima:

$$\Delta^{\sharp}(\mu_1, \mu_2) := \frac{1}{|Y|}\sum_{y\in Y} \min\{\mu_1(y), \mu_2(y)\}$$
$$(\mu_1, \mu_2 \in \mathrm{Fuz}(Y)).$$

For our two weeks, the pointwise minima are

$$\min\{\mu^{(A)}(\text{Mon}), \mu^{(B)}(\text{Mon})\} = \min\{0.2,0.9\} = 0.2,$$
$$\min\{\mu^{(A)}(\text{Tue}), \mu^{(B)}(\text{Tue})\} = \min\{0.8,0.7\} = 0.7,$$
$$\min\{\mu^{(A)}(\text{Wed}), \mu^{(B)}(\text{Wed})\} = \min\{0.6,0.3\} = 0.3.$$

Hence

$$\Delta^{\sharp}(\mu^{(A)}, \mu^{(B)}) = \frac{0.2+0.7+0.3}{3}$$
$$= \frac{1.2}{3} = \frac{6}{15} = \frac{2}{5} = 0.4.$$

We now verify the admissibility inequality

$$\Delta^{\sharp}(\mu_1, \mu_2) \le \min\{\mu^{\sharp}(\mu_1), \mu^{\sharp}(\mu_2)\}$$
$$(\forall \mu_1, \mu_2 \in \mathrm{Fuz}(Y)).$$

For arbitrary μ_1, μ_2 and each $y \in Y$ we have

$$\min\{\mu_1(y), \mu_2(y)\} \le \mu_1(y)$$
$$\text{and} \quad \min\{\mu_1(y), \mu_2(y)\} \le \mu_2(y).$$

Summing over $y \in Y$ and dividing by $|Y|$ yields

$$\Delta^{\sharp}(\mu_1, \mu_2) = \frac{1}{|Y|}\sum_{y\in Y} \min\{\mu_1(y), \mu_2(y)\}$$
$$\le \frac{1}{|Y|}\sum_{y\in Y} \mu_1(y) = \mu^{\sharp}(\mu_1),$$

and similarly $\Delta^{\sharp}(\mu_1, \mu_2) \le \mu^{\sharp}(\mu_2)$. Therefore

$$\Delta^{\sharp}(\mu_1, \mu_2) \le \min\{\mu^{\sharp}(\mu_1), \mu^{\sharp}(\mu_2)\}$$

for all $\mu_1, \mu_2 \in \mathrm{Fuz}(Y)$.

In particular, for our concrete weeks,

$$\Delta^{\sharp}(\mu^{(A)}, \mu^{(B)}) = \frac{2}{5} = \frac{12}{30}$$
$$\le \frac{16}{30} = \frac{8}{15} = \mu^{\sharp}(\mu^{(A)})$$
$$\le \mu^{\sharp}(\mu^{(B)}) = \frac{19}{30},$$

so

$$\Delta^{\sharp}(\mu^{(A)}, \mu^{(B)})$$
$$\le \min\{\mu^{\sharp}(\mu^{(A)}), \mu^{\sharp}(\mu^{(B)})\}$$
$$= \frac{8}{15} \approx 0.533\overline{3}.$$

Thus, the MetaFuzzy relation $\Delta^{\sharp}$ satisfies the required inequality in this example and, by the above argument, for all fuzzy weeks in $\mathsf{Fuz}(Y)$.

Theorem 1 (Zero-support property of MetaFuzzy relations). Let $\mu^{\sharp}$ be a MetaFuzzy Set on Y, and let $\Delta^{\sharp}$ be a MetaFuzzy relation on $\mu^{\sharp}$ in the sense of Definition 4. Then for all $\mu_1, \mu_2 \in \mathsf{Fuz}(Y)$ we have $\mu^{\sharp}(\mu_1) = 0$ or $\mu^{\sharp}(\mu_2) = 0 \quad \Rightarrow \quad \Delta^{\sharp}(\mu_1, \mu_2) = 0$. In particular, if $\mu^{\sharp}(\mu) = 0$ then $\Delta^{\sharp}(\mu, \nu) = 0 = \Delta^{\sharp}(\nu, \mu)$ for all $\nu \in \mathsf{Fuz}(Y)$.

Proof. Assume $\Delta^{\sharp}$ is a MetaFuzzy relation on $\mu^{\sharp}$. Fix $\mu_1, \mu_2 \in \mathsf{Fuz}(Y)$.

By Definition 8 we have

$$\Delta^{\sharp}(\mu_1, \mu_2) \leq \min\{\mu^{\sharp}(\mu_1), \mu^{\sharp}(\mu_2)\}.$$

Suppose $\mu^{\sharp}(\mu_1) = 0$. Then

$$\min\{\mu^{\sharp}(\mu_1), \mu^{\sharp}(\mu_2)\} = \min\{0, \mu^{\sharp}(\mu_2)\} = 0.$$

Hence

$$0 \leq \Delta^{\sharp}(\mu_1, \mu_2) \leq 0,$$

which forces $\Delta^{\sharp}(\mu_1, \mu_2) = 0$. The same argument applies when $\mu^{\sharp}(\mu_2) = 0$, and also to the pair (μ_2, μ_1), since the defining inequality is symmetric in the two arguments. This gives the desired conclusion.

Theorem 2 (Maximal MetaFuzzy relation). Let $\mu^{\sharp}$ be a MetaFuzzy Set on Y, and define $\Delta^{\sharp}_{\max}: \mathsf{Fuz}(Y) \times \mathsf{Fuz}(Y) \to [0,1]$, $\Delta^{\sharp}_{\max}(\mu_1, \mu_2) := \min\{\mu^{\sharp}(\mu_1), \mu^{\sharp}(\mu_2)\}$. *Then:*

1. $\Delta^{\sharp}_{\max}$ is a MetaFuzzy relation on $\mu^{\sharp}$.
2. *If $\Delta^{\sharp}$ is any MetaFuzzy relation on $\mu^{\sharp}$, then* $\Delta^{\sharp}(\mu_1, \mu_2) \leq \Delta^{\sharp}_{\max}(\mu_1, \mu_2) \quad (\forall \mu_1, \mu_2 \in \mathsf{Fuz}(Y))$ that is, $\Delta^{\sharp}_{\max}$ is the largest MetaFuzzy relation on $\mu^{\sharp}$ with respect to the pointwise order.

Proof. (1) For any $\mu_1, \mu_2 \in \mathsf{Fuz}(Y)$ we have

$$\Delta^{\sharp}_{\max}(\mu_1, \mu_2) = \min\{\mu^{\sharp}(\mu_1), \mu^{\sharp}(\mu_2)\}.$$

By definition of min, we immediately get

$$\Delta^{\sharp}_{\max}(\mu_1, \mu_2) \leq \min\{\mu^{\sharp}(\mu_1), \mu^{\sharp}(\mu_2)\},$$

so $\Delta^{\sharp}_{\max}$ satisfies the MetaFuzzy relation condition.

(2) Let $\Delta^{\sharp}$ be any MetaFuzzy relation on $\mu^{\sharp}$. Then for all $\mu_1, \mu_2 \in \mathsf{Fuz}(Y)$,

$$\Delta^{\sharp}(\mu_1, \mu_2) \leq \min\{\mu^{\sharp}(\mu_1), \mu^{\sharp}(\mu_2)\} = \Delta^{\sharp}_{\max}(\mu_1, \mu_2).$$

Thus, $\Delta^{\sharp} \leq \Delta^{\sharp}_{\max}$ pointwise. Hence $\Delta^{\sharp}_{\max}$ is the largest element (in the pointwise order) among all MetaFuzzy relations on $\mu^{\sharp}$.

Theorem 3 (Level-set representation of a MetaFuzzy set).

Let $\mu^{\sharp}$ be a MetaFuzzy set on *Y*. For each $\alpha \in [0,1]$, define the (meta-)level set

$\mathcal{L}_{\alpha} := \{ \mu \in Fuz(Y) \mid \mu^{\sharp}(\mu) \geq \alpha \} \subseteq Fuz(Y).$

Then for every $\mu \in \mathsf{Fuz}(Y)$ we have the exact reconstruction formula

$\mu^{\sharp}(\mu) = sup \{ \alpha \in [0,1] \mid \mu \in \mathcal{L}_{\alpha} \}.$

Moreover, the family $(\mathcal{L}_{\alpha})_{\alpha} \in [0,1]$ is nested:

$0 \leq \alpha \leq \beta \leq 1 \Rightarrow \mathcal{L}_{\beta} \subseteq \mathcal{L}_{\alpha}.$

Proof. Fix $\mu \in \mathsf{Fuz}(Y)$ and set $v := \mu^{\sharp}(\mu) \in [0,1]$. By definition of $\mathcal{L}_{\alpha}$ we have

$\mu \in \mathcal{L}_{\alpha} \Leftrightarrow \mu^{\sharp}(\mu) \geq \alpha \Leftrightarrow v \geq \alpha.$

Thus the set of all $\alpha \in [0,1]$ such that $\mu \in \mathcal{L}_{\alpha}$ is exactly $\{ \alpha \in [0,1] \mid \mu \in \mathcal{L}_{\alpha} \} = \{ \alpha \in [0,1] \mid v \geq \alpha \} = [0, v]$.

The supremum of [0, v] in [0,1] is v itself. Therefore, $sup \{ \alpha \in [0,1] \mid \mu \in \mathcal{L}_{\alpha} \} = sup [0, v] = v = \mu^{\sharp}(\mu)$, which proves the reconstruction formula.

For the nesting property, let $0 \leq \alpha \leq \beta \leq 1$ and take $\mu \in \mathcal{L}_{\beta}$. Then $\mu^{\sharp}(\mu) \geq \beta \geq \alpha$, so $\mu \in \mathcal{L}_{\alpha}$. Hence $\mathcal{L}_{\beta} \subseteq \mathcal{L}_{\alpha}$.

Theorem 4 (Monotonicity and Lipschitz property of an arithmetic-mean MetaFuzzy Set). *Assume $Y = \{y_1, \ldots, y_n\}$ is a finite nonempty base domain with $n \in \mathbb{N}$. Define $\mu^{\sharp}: \mathsf{Fuz}(Y) \to [0,1]$ by $\mu^{\sharp}(\mu) := \frac{1}{n}\sum_{i=1}^{n} \mu(y_i)$. Then:*

1. *(Bounds) For all $\mu \in \mathsf{Fuz}(Y)$, $0 \leq \mu^{\sharp}(\mu) \leq 1$.*

2. (Monotonicity) If $\mu, \nu \in \mathrm{Fuz(Y)}$ satisfy $\mu(y) \leq \nu(y) \quad (\forall y \in Y)$, then $\mu^{\sharp}(\mu) \leq \mu^{\sharp}(\nu)$.
3. (Lipschitz continuity) For all $\mu, \nu \in \mathrm{Fuz(Y)}$, $|\mu^{\sharp}(\mu) - \mu^{\sharp}(\nu)| \leq \frac{1}{n}\sum_{i=1}^{n} |\mu(y_i) - \nu(y_i)|$. In particular, $\mu^{\sharp}$ is 1-Lipschitz with respect to the normalized ℓ^1-distance on $\mathrm{Fuz(Y)}$.

Proof. (1) Since $\mu(y_i) \in [0,1]$ for all i, we have

$$0 \leq \mu(y_i) \leq 1 \qquad (\forall i = 1, \ldots, n).$$

Summing these inequalities gives

$$0 \leq \sum_{i=1}^{n} \mu(y_i) \leq \sum_{i=1}^{n} 1 = n.$$

Dividing by $n > 0$ yields

$$0 \leq \frac{1}{n}\sum_{i=1}^{n} \mu(y_i) \leq 1,$$

i.e. $0 \leq \mu^{\sharp}(\mu) \leq 1$.

(2) Assume $\mu(y) \leq \nu(y)$ for all $y \in Y$. Then in particular

$$\mu(y_i) \leq \nu(y_i) \qquad (\forall i = 1, \ldots, n).$$

Summing these n inequalities gives

$$\sum_{i=1}^{n} \mu(y_i) \leq \sum_{i=1}^{n} \nu(y_i).$$

Dividing by n we obtain

$$\mu^{\sharp}(\mu) = \frac{1}{n}\sum_{i=1}^{n} \mu(y_i) \leq \frac{1}{n}\sum_{i=1}^{n} \nu(y_i) = \mu^{\sharp}(\nu),$$

so $\mu^{\sharp}$ is monotone with respect to the pointwise order on $\mathrm{Fuz}(Y)$.

(3) For any $\mu, \nu \in \mathrm{Fuz}(Y)$ we compute

$$\mu^{\sharp}(\mu) - \mu^{\sharp}(\nu) = \frac{1}{n}\sum_{i=1}^{n} \mu(y_i) - \frac{1}{n}\sum_{i=1}^{n} \nu(y_i)$$

$$= \frac{1}{n}\sum_{i=1}^{n} (\mu(y_i) - \nu(y_i)).$$

Taking absolute values and applying the triangle inequality yields

$$|\mu^{\sharp}(\mu) - \mu^{\sharp}(\nu)| = \left|\frac{1}{n}\sum_{i=1}^{n} (\mu(y_i) - \nu(y_i))\right|$$

$$\leq \frac{1}{n}\sum_{i=1}^{n} |\mu(y_i) - \nu(y_i)|.$$

This is exactly the claimed Lipschitz bound.

If we define the normalized ℓ^1-distance

$$d_1(\mu, \nu) := \frac{1}{n}\sum_{i=1}^{n} |\mu(y_i) - \nu(y_i)|,$$

then the inequality can be rewritten as

$$|\mu^{\sharp}(\mu) - \mu^{\sharp}(\nu)| \leq d_1(\mu, \nu),$$

showing that $\mu^{\sharp}$ is 1-Lipschitz with respect to d_1.

MetaNeutrosophic set (Neutrosophic set of Neutrosophic Set)

A Neutrosophic Set extends fuzzy sets by assigning each element three independent degrees: truth, indeterminacy, and falsity, enabling richer uncertainty modeling (Broumi et al. 2016). A MetaNeutrosophic Set evaluates neutrosophic sets themselves, producing truth, indeterminacy, and falsity degrees for collections of neutrosophic information.

Definition 5 (Neutrosophic Set). (Hadi and Al-Swidi, 2022) Let X be a non-empty set. A *Neutrosophic Set (NS)A* on X is characterized by three membership functions:

$$T_A: X \to [0,1], \quad I_A: X \to [0,1], \quad F_A: X \to [0,1],$$

where for each $x \in X$, the values $T_A(x)$, $I_A(x)$, and $F_A(x)$ represent the degrees of truth, indeterminacy, and falsity, respectively. These values satisfy the following condition:

$$0 \leq T_A(x) + I_A(x) + F_A(x) \leq 3.$$

Definition 6 (MetaNeutrosophic Set). Let X be a nonempty finite set, and let $\mathrm{Neu}(X)$ denote the collection of neutrosophic sets on X, that is, all triples

$$A = (T_A, I_A, F_A)$$

With

$$T_A,\ I_A,\ F_A: X \to [0,1]$$

such that for every x ∈ X,

$$0 \ \le\ T_A(x) + I_A(x) + F_A(x)\ \le\ 3.$$

A MetaNeutrosophic Set on X is a triple of functionals

$$T^{\sharp},\ I^{\sharp},\ F^{\sharp}:\ \mathsf{Neu}(X) \to [0,1]$$

satisfying, for every $A \in \mathsf{Neu}(X)$,

$$0 \ \le\ T^{\sharp}(A) + I^{\sharp}(A) + F^{\sharp}(A)\ \le\ 3.$$

Equivalently, the associated mapping

$$\mathbf{N}^{\sharp}:\ \mathsf{Neu}(X) \to [0,1]^3,$$

$$\mathbf{N}^{\sharp}(A) := \big(T^{\sharp}(A), I^{\sharp}(A), F^{\sharp}(A)\big),$$

assigns to each neutrosophic set A a meta-level triplet of truth, indeterminacy, and falsity degrees whose sum remains in the admissible range [0,3].

Example 6 (MetaNeutrosophic Set: overall project risk). Let

$$X = \{\text{Budget},\ \text{Schedule}\}$$

be two project risk dimensions. A neutrosophic set $A = (T_A, I_A, F_A) \in \mathsf{Neu}(X)$ encodes, for each x ∈ X,

- $T_A(x)$: degree that the risk on x is under control,
- $I_A(x)$: degree of uncertainty about the risk on x,
- $F_A(x)$: degree that the risk on x is not under control,

with $0 \le T_A(x) + I_A(x) + F_A(x) \le 3$.

Assume a concrete assessment

$$(T_A(\text{Budget}), I_A(\text{Budget}), F_A(\text{Budget})) = (0.8,\ 0.1,\ 0.1),$$

$$(T_A(\text{Schedule}), I_A(\text{Schedule}), F_A(\text{Schedule})) = (0.5,\ 0.3,\ 0.2).$$

Define a MetaNeutrosophic Set

$$(\mathbf{N}^{\sharp} = (T^{\sharp}, I^{\sharp}, F^{\sharp}): \mathsf{Neu}(X) \to [0,1]^3$$

by the simple averaging/max rules (here $|X| = 2$):

$$T^{\sharp}(A) := \frac{T_A(\text{Budget}) + T_A(\text{Schedule})}{2},$$

$$I^{\sharp}(A) := \max\{I_A(\text{Budget}), I_A(\text{Schedule})\},$$

$$F^{\sharp}(A) := \frac{F_A(\text{Budget}) + F_A(\text{Schedule})}{2}.$$

For the above A we obtain

$$T^{\sharp}(A) = \frac{0.8 + 0.5}{2} = 0.65,$$

$$I^{\sharp}(A) = \max\{0.1, 0.3\} = 0.3,$$

$$F^{\sharp}(A) = \frac{0.1 + 0.2}{2} = 0.15.$$

Thus

$$\mathbf{N}^{\sharp}(A) = (0.65,\ 0.30,\ 0.15)$$

is a meta-level summary of the overall project risk: on average the risk is reasonably controlled ($T^{\sharp}$ high), there is moderate uncertainty ($I^{\sharp}$), and relatively low non-control ($F^{\sharp}$), while $0.65 + 0.30 + 0.15 = 1.10 \le 3$ so the MetaNeutrosophic constraint is satisfied.

Definition 7 (A concrete averaging/max MetaNeutrosophic Set). Assume that X is finite with $n := |X| \ge 1$. For $A = (T_A, I_A, F_A) \in \mathsf{Neu}(X)$ define

$$T^{\sharp}(A) := \frac{1}{n}\sum_{x \in X} T_A(x),$$

$$I^{\sharp}(A) := \max_{x \in X} I_A(x),$$

$$F^{\sharp}(A) := \frac{1}{n}\sum_{x \in X} F_A(x).$$

Example 7 (Averaging/max MetaNeutrosophic Set: machine health). Let

$$X = \{\text{Sensor}_1, \text{Sensor}_2, \text{Sensor}_3\}$$

be three monitoring points in an industrial machine. A neutrosophic set $A = (T_A, I_A, F_A) \in \mathsf{Neu}(X)$ encodes, for each $x \in X$,

- $T_A(x)$: degree that the sensor status is healthy,
- $I_A(x)$: degree of uncertainty about the status,
- $F_A(x)$: degree that the sensor status is faulty,

with $0 \le T_A(x) + I_A(x) + F_A(x) \le 3$.

Assume the following assessment:

$$(\mathrm{T_A}(\mathrm{Sensor_1}), \mathrm{I_A}(\mathrm{Sensor_1}), \mathrm{F_A}(\mathrm{Sensor_1})) = (0.9,\ 0.1,\ 0.0),$$
$$(\mathrm{T_A}(\mathrm{Sensor_2}), \mathrm{I_A}(\mathrm{Sensor_2}), \mathrm{F_A}(\mathrm{Sensor_2})) = (0.7,\ 0.2,\ 0.1),$$
$$(\mathrm{T_A}(\mathrm{Sensor_3}), \mathrm{I_A}(\mathrm{Sensor_3}), \mathrm{F_A}(\mathrm{Sensor_3})) = (0.6,\ 0.3,\ 0.2).$$

Each triple is admissible, e.g.

$$0.9 + 0.1 + 0.0 = 1.0,$$
$$0.7 + 0.2 + 0.1 = 1.0,$$
$$0.6 + 0.3 + 0.2 = 1.1 \ \leq 3.$$

Here $|\mathrm{X}| = \mathrm{n} = 3$. Using Definition 7, the averaging/max MetaNeutrosophic Set $(\mathrm{T}^\sharp, \mathrm{I}^\sharp, \mathrm{F}^\sharp)$ gives

$$\mathrm{T}^\sharp(\mathrm{A}) = \frac{1}{3}(\mathrm{T_A}(\mathrm{Sensor_1}) + \mathrm{T_A}(\mathrm{Sensor_2}) + \mathrm{T_A}(\mathrm{Sensor_3}))$$
$$= \frac{0.9 + 0.7 + 0.6}{3} = \frac{2.2}{3} = \frac{11}{15} \approx 0.733\overline{3},$$
$$\mathrm{I}^\sharp(\mathrm{A}) = \max_{\mathrm{x}\in\mathrm{X}} \mathrm{I_A}(\mathrm{x}) = \max\{0.1, 0.2, 0.3\} = 0.3,$$
$$\mathrm{F}^\sharp(\mathrm{A}) = \frac{1}{3}(\mathrm{F_A}(\mathrm{Sensor_1}) + \mathrm{F_A}(\mathrm{Sensor_2}) + \mathrm{F_A}(\mathrm{Sensor_3}))$$
$$= \frac{0.0 + 0.1 + 0.2}{3} = \frac{0.3}{3} = 0.1.$$

The meta-sum is

$$\mathrm{T}^\sharp(\mathrm{A}) + \mathrm{I}^\sharp(\mathrm{A}) + \mathrm{F}^\sharp(\mathrm{A}) = \frac{11}{15} + 0.3 + 0.1$$
$$= \frac{11}{15} + \frac{3}{10} + \frac{1}{10} = \frac{22 + 9 + 3}{30}$$
$$= \frac{34}{30} = \frac{17}{15} \approx 1.133\overline{3} \ \leq 3,$$

so the MetaNeutrosophic constraint is satisfied.

Thus the averaging/max MetaNeutrosophic Set summarizes the machine as

$$\mathbf{N}^\sharp(\mathrm{A}) = (\mathrm{T}^\sharp(\mathrm{A}), \mathrm{I}^\sharp(\mathrm{A}), \mathrm{F}^\sharp(\mathrm{A})) \approx (0.733,\ 0.300,\ 0.100),$$

meaning "high overall health, moderate worst-case uncertainty, and low average fault degree" at the meta-level.

Theorem 5 (Well-definedness of the averaging/max MetaNeutrosophic Set). The triple $(\mathrm{T}^\sharp, \mathrm{I}^\sharp, \mathrm{F}^\sharp)$ from Definition 7is a MetaNeutrosophic Set on X. That is, for every $\mathrm{A} \in \mathsf{Neu}(\mathrm{X})$, $0 \ \leq \ \mathrm{T}^\sharp(\mathrm{A}) + \mathrm{I}^\sharp(\mathrm{A}) + \mathrm{F}^\sharp(\mathrm{A}) \ \leq \ 3$.

Proof. Fix $\mathrm{A} = (\mathrm{T_A}, \mathrm{I_A}, \mathrm{F_A}) \in \mathsf{Neu}(\mathrm{X})$. By definition of a neutrosophic set, for each $\mathrm{x} \in \mathrm{X}$,

$$0 \leq \mathrm{T_A}(\mathrm{x}) \leq 1, \quad 0 \leq \mathrm{I_A}(\mathrm{x}) \leq 1, \quad 0 \leq \mathrm{F_A}(\mathrm{x}) \leq 1.$$

Hence

$$0 \leq \frac{1}{n}\sum_{x\in X} T_A\,(x) \leq 1,$$
$$0 \leq \frac{1}{n}\sum_{x\in X} F_A\,(x) \leq 1.$$

Also, since each $I_A(x) \in [0,1]$, we have

$$0 \ \leq \ I^\sharp(A) = \max_{x\in X} I_A(x) \ \leq \ 1.$$

Therefore

$$0 \ \leq \ T^\sharp(A) + I^\sharp(A) + F^\sharp(A) \ \leq \ 1 + 1 + 1 = 3.$$

This is exactly the MetaNeutrosophic constraint, so $(T^\sharp, I^\sharp, F^\sharp)$ is a valid MetaNeutrosophic Set.

Definition 8 (Neutrosophic preorder). Let $A = (T_A, I_A, F_A)$ and $B = (T_B, I_B, F_B)$ be elements of $\mathsf{Neu}(X)$. We define the *truth-favoring neutrosophic preorder* $\preccurlyeq_{\mathrm{N}}$ by

$$A \ \preccurlyeq_{\mathrm{N}} \ B \quad \Leftrightarrow \quad \begin{cases} T_A(x) \ \leq \ T_B(x), \\ I_A(x) \ \geq \ I_B(x), \\ F_A(x) \ \geq \ F_B(x), \end{cases} \qquad \forall x \in X.$$

Thus $\mathrm{A} \preccurlyeq_{\mathrm{N}} \mathrm{B}$ means that B has no less truth and no more indeterminacy or falsity at every point.

Theorem 6 (Monotonicity of the averaging/max MetaNeutrosophic Set). Let $(\mathrm{T}^\sharp, \mathrm{I}^\sharp, \mathrm{F}^\sharp)$ be as in Definition 7. If $\mathrm{A}, \mathrm{B} \in \mathsf{Neu}(\mathrm{X})$ satisfy $\mathrm{A} \preccurlyeq_{\mathrm{N}} \mathrm{B}$ (Definition 8), then $\mathrm{T}^\sharp(\mathrm{A}) \ \leq \ \mathrm{T}^\sharp(\mathrm{B})$, $\mathrm{I}^\sharp(\mathrm{A}) \ \geq \ \mathrm{I}^\sharp(\mathrm{B})$, $\mathrm{F}^\sharp(\mathrm{A}) \ \geq \ \mathrm{F}^\sharp(\mathrm{B})$. In other words, the meta-aggregator preserves the neutrosophic preorder.

Proof. Assume $A \preccurlyeq_{\mathrm{N}} B$. Then for all $x \in X$ we have

$$T_A(x) \leq T_B(x), \quad I_A(x) \geq I_B(x), \quad F_A(x) \geq F_B(x).$$

For the truth component,

$$T^\sharp(A) = \frac{1}{n}\sum_{x\in X} T_A\,(x)$$

$$\leq \frac{1}{n}\sum_{x\in X} T_B\,(x) = T^{\sharp}(B),$$

since each summand is bounded above by the corresponding summand of B.

For indeterminacy, by the pointwise inequalities we have

$$I_A(x) \;\geq\; I_B(x) \quad (\forall x \in X).$$

Taking maxima over $x \in X$ gives

$$I^{\sharp}(A) = \max_{x\in X} I_A(x)$$

$$\geq \max_{x\in X} I_B(x) = I^{\sharp}(B).$$

For falsity,

$$F^{\sharp}(A) = \frac{1}{n}\sum_{x\in X} F_A\,(x)$$

$$\geq \frac{1}{n}\sum_{x\in X} F_B\,(x) = F^{\sharp}(B),$$

because each $F_A(x) \geq F_B(x)$.

Thus the desired inequalities hold for all three components.

Theorem 7 (Level-set representation of a MetaNeutrosophic Set). *Let* $\boldsymbol{N}^{\sharp} = (T^{\sharp}, I^{\sharp}, F^{\sharp})$ *be any MetaNeutrosophic Set on* X. *For each* $\alpha \in [0,1]$, *define the truth-, indeterminacy-, and falsity-level sets* $\mathcal{L}_T(\alpha) := \{A \in \mathsf{Neu}(X) \mid T^{\sharp}(A) \geq \alpha\}, \mathcal{L}_I(\alpha) := \{A \in \mathsf{Neu}(X) \mid I^{\sharp}(A) \geq \alpha\}, \mathcal{L}_F(\alpha) := \{A \in \mathsf{Neu}(X) \mid F^{\sharp}(A) \geq \alpha\}$. *Then for every* $A \in \mathsf{Neu}(X)$, $T^{\sharp}(A) = \sup\{\alpha \in [0,1] \mid A \in \mathcal{L}_T(\alpha)\}, I^{\sharp}(A) = \sup\{\alpha \in [0,1] \mid A \in \mathcal{L}_I(\alpha)\}, F^{\sharp}(A) = \sup\{\alpha \in [0,1] \mid A \in \mathcal{L}_F(\alpha)\}$. *Moreover, each of the families* $(\mathcal{L}_T(\alpha))_{\alpha\in[0,1]}$, $(\mathcal{L}_I(\alpha))_{\alpha\in[0,1]}$, $(\mathcal{L}_F(\alpha))_{\alpha\in[0,1]}$ *is nested in the sense that* $0 \leq \alpha \leq \beta \leq 1 \Rightarrow \mathcal{L}_{\bullet}(\beta) \subseteq \mathcal{L}_{\bullet}(\alpha)$, for each symbol $\bullet \in \{\mathrm{T}, \mathrm{I}, \mathrm{F}\}$.

Proof. We prove the statement for the truth component; the proofs for the indeterminacy and falsity components are identical in form.

Fix $A \in \mathsf{Neu}(X)$ and set $v := T^{\sharp}(A) \in [0,1]$. By definition,

$$A \in \mathcal{L}_T(\alpha) \quad \Leftrightarrow \quad T^{\sharp}(A) \geq \alpha \quad \Leftrightarrow \quad v \geq \alpha.$$

Hence

$$\{\alpha \in [0,1] \mid A \in \mathcal{L}_T(\alpha)\}$$

$$= \{\alpha \in [0,1] \mid v \geq \alpha\} = [0, v].$$

The supremum of the interval $[0, v]$ in $[0,1]$ is v. Therefore

$$\sup\{\alpha \in [0,1] \mid A \in \mathcal{L}_T(\alpha)\}$$

$$= \sup[0, v]$$

$$= v = T^{\sharp}(A).$$

For the nesting property, let $0 \leq \alpha \leq \beta \leq 1$ and take any $A \in \mathcal{L}_T(\beta)$. Then $T^{\sharp}(A) \geq \beta \geq \alpha$, so $A \in \mathcal{L}_T(\alpha)$. Thus $\mathcal{L}_T(\beta) \subseteq \mathcal{L}_T(\alpha)$. The same argument applies to $\mathcal{L}_I(\alpha)$ and $\mathcal{L}_F(\alpha)$ by replacing $T^{\sharp}$ with $I^{\sharp}$ or $F^{\sharp}$.

Theorem 8 (Lipschitz continuity of the averaging/max MetaNeutrosophic Set). Let $(\mathrm{T}^{\sharp}, \mathrm{I}^{\sharp}, \mathrm{F}^{\sharp})$ be the averaging/max MetaNeutrosophic Set from Definition 7on a finite base X with $\mathrm{n} = |\mathrm{X}|$. Define a normalized neutrosophic distance $\mathrm{d_N}$ on$\mathsf{Neu}(X)$ *by* $d_{\mathrm{N}}(A,B) := \frac{1}{n}\sum_{x\in X}(|T_A(x) - T_B(x)| + |I_A(x) - I_B(x)| + |F_A(x) - F_B(x)|)$. *Then for all* $A, B \in \mathsf{Neu}(X)$, $|T^{\sharp}(A) - T^{\sharp}(B)| \leq \frac{1}{n}\sum_{x\in X} |T_A(x) - T_B(x)|, |F^{\sharp}(A) - F^{\sharp}(B)| \leq \frac{1}{n}\sum_{x\in X} |F_A(x) - F_B(x)|, |I^{\sharp}(A) - I^{\sharp}(B)| \leq \max_{x\in X}|I_A(x) - I_B(x)| \leq \frac{1}{\mathrm{n}}\sum_{\mathrm{x}\in\mathrm{X}} |\mathrm{I_A(x)} - \mathrm{I_B(x)}|$. Consequently, each component $\mathrm{T}^{\sharp}$, $\mathrm{I}^{\sharp}$, $\mathrm{F}^{\sharp}$ is 1-Lipschitz with respect to $\mathrm{d_N}$, and the combined map $\mathbf{N}^{\sharp}$: $(\mathsf{Neu}(\mathrm{X}), \mathrm{d_N}) \to ([0,1]^3, \|\cdot\|_1)$ is Lipschitz-continuous.

Proof. Fix $A = (T_A, I_A, F_A)$ and $B = (T_B, I_B, F_B)$ in $\mathsf{Neu}(X)$.

For the truth component,

$$T^{\sharp}(A) - T^{\sharp}(B)$$

$$= \frac{1}{n}\sum_{x\in X} T_A\,(x) - \frac{1}{n}\sum_{x\in X} T_B\,(x)$$

$$= \frac{1}{n}\sum_{x\in X} (T_A(x) - T_B(x)).$$

Applying the triangle inequality yields

$$|T^{\sharp}(A) - T^{\sharp}(B)|$$

$$= \left| \frac{1}{n} \sum_{x \in X} (T_A(x) - T_B(x)) \right|$$

$$\leq \frac{1}{n} \sum_{x \in X} |T_A(x) - T_B(x)|.$$

The same computation for the falsity component gives

$$|F^\sharp(A) - F^\sharp(B)| \leq \frac{1}{n} \sum_{x \in X} |F_A(x) - F_B(x)|.$$

For the indeterminacy component,

$$I^\sharp(A) = \max_{x \in X} I_A(x),$$

$$I^\sharp(B) = \max_{x \in X} I_B(x).$$

Recall the standard inequality

$$|\max_i a_i - \max_i b_i| \leq \max_i |a_i - b_i|$$

for any finite family of real numbers (a_i), (b_i). Taking $a_x := I_A(x)$, $b_x := I_B(x)$, we obtain

$$|I^\sharp(A) - I^\sharp(B)|$$

$$= |\max_{x \in X} I_A(x) - \max_{x \in X} I_B(x)|$$

$$\leq \max_{x \in X} |I_A(x) - I_B(x)|.$$

Since for any finite family $(c_x)_{x \in X}$,

$$\max_{x \in X} |c_x| \leq \frac{1}{n} \sum_{x \in X} |c_x|,$$

we further have

$$|I^\sharp(A) - I^\sharp(B)|$$

$$\leq \frac{1}{n} \sum_{x \in X} |I_A(x) - I_B(x)|.$$

Combining these inequalities coordinatewise shows that each component of $\boldsymbol{N}^\sharp$ is bounded by the corresponding part of the normalized ℓ^1-distance in d_{N}, and hence $\boldsymbol{N}^\sharp$ is Lipschitz-continuous from $(\mathsf{Neu}(X), d_{\mathrm{N}})$ to $([0,1]^3, \|\cdot\|_1)$.

MetaSoft set (Soft Set of Soft Set)

A Soft Set represents uncertain information using a parameterized family of subsets, mapping attributes to corresponding approximate descriptions within universes (Molodtsov, 1999). A MetaSoft Set selects or groups multiple soft sets under meta-parameters, providing higher-order decisions about uncertain attribute-based data.

Definition 9 (Soft Set). (Molodtsov, 1999) Let U be a finite universal set and A be a set of attributes. Let $S \subseteq A$ denote a chosen subset of parameters. A *soft set* over U is defined as a pair $(\mathcal{F}, S)$ where

$$\mathcal{F}: S \to \mathcal{P}(U)$$

is a function that assigns to each parameter $\alpha \in S$ a subset $\mathcal{F}(\alpha) \subseteq U$. Formally,

$$(\mathcal{F}, S) = \{ (\alpha, \mathcal{F}(\alpha)) \mid \alpha \in S, \mathcal{F}(\alpha) \subseteq U \}.$$

Definition 10 (MetaSoft Set). Let U be a nonempty universe of objects and let S be a (possibly finite) set of parameters. A (crisp) soft set on (U, S) is a mapping

$$\mathcal{F}: S \to \mathcal{P}(U),$$

and we denote by

$$\mathsf{Soft}(U, S) := \{\mathcal{F} \mid \mathcal{F}: S \to \mathcal{P}(U)\}$$

the collection of all such soft sets on (U, S).

Let Πbe a nonempty set of meta-parameters. A MetaSoft Set on (U, S) with meta-parameter set Π is a soft set over the universe $\mathsf{Soft}(U, S)$ with parameter set Π, that is, a pair

$$(\mathcal{G}, \Pi) \quad \text{where}$$

$$\mathcal{G}: \Pi \to \mathcal{P}(\mathsf{Soft}(U, S)).$$

For each $\pi \in \Pi$, the value $\mathcal{G}(\pi) \subseteq \mathsf{Soft}(U, S)$ is interpreted as the family of base soft sets that satisfy the meta-criterion encoded by π.

Remark (Second-order viewpoint). A MetaSoft Set $(\mathcal{G}, \Pi)$ treats ordinary soft sets $\mathcal{F} \in \mathsf{Soft}(U, S)$ as "points" in a new universe. Each meta-parameter $\pi \in \Pi$ specifies a qualitative or quantitative requirement on soft descriptions (e.g., "good for business travel", "good for leisure"), and $\mathcal{G}(\pi)$ collects precisely those base soft sets fulfilling that meta-level requirement. Thus $(\mathcal{G}, \Pi)$ is a soft-set valued selector on the space $\mathsf{Soft}(U, S)$.

Example 8 (MetaSoft Set: Hotel selection by meta-criteria). Let $U = \{h_1, h_2, h_3\}$ be three hotels and

$$S = \{\text{NearStation, Breakfast, Quiet}\}$$

be the set of attributes. A soft set $\mathcal{F}: S \to \mathcal{P}(U)$ records, for each attribute $s \in S$, the subset $\mathcal{F}(s) \subseteq U$ of hotels that satisfy s.

Consider two soft descriptions of the same city:

$$\mathcal{F}^{(A)}(\text{NearStation}) = \{h_1, h_2\},$$
$$\mathcal{F}^{(A)}(\text{Breakfast}) = \{h_2, h_3\},$$
$$\mathcal{F}^{(A)}(\text{Quiet}) = \{h_3\},$$
$$\mathcal{F}^{(B)}(\text{NearStation}) = \{h_1\},$$
$$\mathcal{F}^{(B)}(\text{Breakfast}) = \{h_3\},$$
$$\mathcal{F}^{(B)}(\text{Quiet}) = \{h_2, h_3\}.$$

Both $\mathcal{F}^{(A)}$ and $\mathcal{F}^{(B)}$ are elements of $\mathsf{Soft}(U, S)$.

Now introduce two meta-parameters

$$\Pi = \{\pi^{\text{biz}}, \pi^{\text{leis}}\},$$

interpreted as:

π^{biz}: "good for a business traveler who prefers hotel h_2 and wants it both near the station and with breakfast".

- π^{leis}: "good for a leisure traveler who prefers hotel h_3 with breakfast in a quiet environment".

Define a MetaSoft Set $(\mathcal{G}, \Pi)$ on (U, S) by

$\mathcal{G}(\pi^{\text{biz}}) := \{\mathcal{F} \in \mathsf{Soft}(U, S) \mid h_2 \in \boldsymbol{\mathcal{F}}(\text{NearStation})$ and $h_2 \in \boldsymbol{\mathcal{F}}(\text{Breakfast})\}$,

$G(\pi^{\{\text{leis}\}}) := \{\boldsymbol{\mathcal{F}} \in \text{Soft(U, S)} \mid h_3 \in \boldsymbol{\mathcal{F}}(\text{Breakfast})$ and $h_3 \in \boldsymbol{\mathcal{F}}(\text{Quiet})\}$.

Verification for π^{biz}:

$$h_2 \in \mathcal{F}^{(A)}(\text{NearStation}) = \{h_1, h_2\},$$
$$h_2 \in \mathcal{F}^{(A)}(\text{Breakfast}) = \{h_2, h_3\},$$

so $\mathcal{F}^{(A)} \in \mathcal{G}(\pi^{\text{biz}})$. For $\mathcal{F}^{(B)}$ we have

$$h_2 \notin \mathcal{F}^{(B)}(\text{NearStation}) = \{h_1\},$$

hence $\mathcal{F}^{(B)} \notin \mathcal{G}(\pi^{\text{biz}})$.

Thus the MetaSoft Set $(\mathcal{G}, \Pi)$ behaves as a meta-level selector on $\mathsf{Soft}(U, S)$: the parameter π^{biz} singles out those soft descriptions that are suitable for a business traveler preferring h_2, while π^{leis} collects those descriptions appropriate for a leisure traveler preferring h_3 in a quiet, breakfast-included setting.

Definition 12 (Soft-set inclusion). Let $(\mathcal{F}, S), (\mathcal{H}, S) \in \mathsf{Soft}(U, S)$ be two soft sets on the same universe and parameter set. We write

$$\mathcal{F} \subseteq_{\text{soft}} \mathcal{H}$$
$$\Leftrightarrow \quad \mathcal{F}(s) \subseteq \mathcal{H}(s) \quad \text{for all } s \in S.$$

This defines a partial order on $\mathsf{Soft}(U, S)$.

Lemma 29 (Soft-set inclusion is a partial order). The relation $\subseteq_{\text{soft}}$ on $\mathsf{Soft}(\text{U}, \text{S})$ is reflexive, antisymmetric, and transitive. Hence $(\mathsf{Soft}(\text{U}, \text{S}), \subseteq_{\text{soft}})$ is a partially ordered set.

Proof.Let $\mathcal{F}, \mathcal{H}, \mathcal{K} \in \mathsf{Soft}(U, S)$.

Reflexivity: for every $s \in S$, we have $\mathcal{F}(s) \subseteq \mathcal{F}(s)$ as sets. Thus $\mathcal{F} \subseteq_{\text{soft}} \mathcal{F}$.

Antisymmetry: assume $\mathcal{F} \subseteq_{\text{soft}} \mathcal{H}$ and $\mathcal{H} \subseteq_{\text{soft}} \mathcal{F}$. Then for all $s \in S$,

$$\mathcal{F}(s) \subseteq \mathcal{H}(s) \text{ and } \mathcal{H}(s) \subseteq \mathcal{F}(s),$$

so $\mathcal{F}(s) = \mathcal{H}(s)$. Hence $\mathcal{F} = \mathcal{H}$ as functions.

Transitivity: assume $\mathcal{F} \subseteq_{\text{soft}} \mathcal{H}$ and $\mathcal{H} \subseteq_{\text{soft}} \mathcal{K}$. Then for each $s \in S$,

$$\mathcal{F}(s) \subseteq \mathcal{H}(s) \subseteq \mathcal{K}(s),$$

so $\mathcal{F}(s) \subseteq \mathcal{K}(s)$. Thus $\mathcal{F} \subseteq_{\text{soft}} \mathcal{K}$.

All three properties hold; therefore $\subseteq_{\text{soft}}$ is a partial order.

Theorem 9 (Indicator-function representation of MetaSoft Sets). Let $(\mathcal{G}, \Pi)$ be a MetaSoft Set on (U, S) in the sense of Definition 10. Define $\chi_{\mathcal{G}}$: $\Pi \times \mathsf{Soft}(\text{U}, \text{S}) \to \{0,1\}$, $\chi_{\mathcal{G}}(\pi, \mathcal{F}) := \begin{cases} 1, & \mathcal{F} \in \mathcal{G}(\pi), \\ 0, & \mathcal{F} \notin \mathcal{G}(\pi). \end{cases}$

Conversely, let $\chi: \Pi \times \mathsf{Soft}(\text{U}, \text{S}) \to \{0,1\}$ be any map. Define $\mathcal{G}_{\chi}: \Pi \to \mathcal{P}(\mathsf{Soft}(\text{U}, \text{S}))$, $\mathcal{G}_{\chi}(\pi) := \{\mathcal{F} \in \mathsf{Soft}(\text{U}, \text{S}) \mid \chi(\pi, \mathcal{F}) = 1\}$. Then the assignments $(\mathcal{G}, \Pi) \mapsto \chi_{\mathcal{G}}$, $\chi \mapsto (\mathcal{G}_{\chi}, \Pi)$ are mutually inverse. In particular, there is a bijection between MetaSoft Sets on (U, S) (with meta-parameter set Π) and indicator maps $\Pi \times \mathsf{Soft}(\text{U}, \text{S}) \to \{0,1\}$.

Proof. We prove that each construction is inverse to the other.

Step 1: start from a MetaSoft Set $(\mathcal{G}, \Pi)$ and construct $\chi_{\mathcal{G}}$, then $\mathcal{G}_{\chi_{\mathcal{G}}}$.

Fix $\pi \in \Pi$. By definition,

$$\mathcal{G}_{\chi_{\mathcal{G}}}(\pi) = \{\mathcal{F} \in \mathsf{Soft}(U,S) \mid \chi_{\mathcal{G}}(\pi,\mathcal{F}) = 1\}.$$

But by the definition of $\chi_{\mathcal{G}}$,

$$\chi_{\mathcal{G}}(\pi,\mathcal{F}) = 1$$
$$\Leftrightarrow \quad \mathcal{F} \in \mathcal{G}(\pi).$$

Thus

$$\mathcal{G}_{\chi_{\mathcal{G}}}(\pi)$$
$$= \{\mathcal{F} \in \mathsf{Soft}(U,S) \mid \mathcal{F} \in \mathcal{G}(\pi)\} = \mathcal{G}(\pi).$$

Since this holds for all $\pi \in \Pi$, we have $\mathcal{G}_{\chi_{\mathcal{G}}} = \mathcal{G}$.

Step 2: start from an indicator map χ and construct $\mathcal{G}_{\chi}$, then $\chi_{\mathcal{G}_{\chi}}$.

For any $(\pi,\mathcal{F}) \in \Pi \times \mathsf{Soft}(U,S)$, we have

$$\chi_{\mathcal{G}_{\chi}}(\pi,\mathcal{F}) = 1$$
$$\Leftrightarrow \quad \mathcal{F} \in \mathcal{G}_{\chi}(\pi)$$
$$\Leftrightarrow \quad \chi(\pi,\mathcal{F}) = 1.$$

Similarly,

$$\chi_{\mathcal{G}_{\chi}}(\pi,\mathcal{F}) = 0$$
$$\Leftrightarrow \quad \mathcal{F} \notin \mathcal{G}_{\chi}(\pi)$$
$$\Leftrightarrow \quad \chi(\pi,\mathcal{F}) = 0.$$

Hence $\chi_{\mathcal{G}_{\chi}}(\pi,\mathcal{F}) = \chi(\pi,\mathcal{F})$ for all $(\pi,\mathcal{F})$, so $\chi_{\mathcal{G}_{\chi}} = \chi$.

Therefore the two constructions are mutually inverse, yielding a bijection.

Definition 13 (Boolean operations on MetaSoft Sets). Let $(\mathcal{G},\Pi)$ and $(\mathcal{H},\Pi)$ be MetaSoft Sets on (U,S) with the same meta-parameter set Π. Define three new MetaSoft Sets on (U,S) by

$$(\mathcal{G} \cap \mathcal{H})(\pi) := \mathcal{G}(\pi) \cap \mathcal{H}(\pi),$$
$$(\mathcal{G} \cup \mathcal{H})(\pi) := \mathcal{G}(\pi) \cup \mathcal{H}(\pi),$$
$$(\neg\mathcal{G})(\pi) := \mathsf{Soft}(U,S) \backslash \mathcal{G}(\pi),$$
$$\pi \in \Pi.$$

We call these the intersection, union, and complement of MetaSoft Sets, taken parameterwise.

Theorem 10 (MetaSoft Sets form a Boolean algebra over each parameter). Let $(\mathcal{G},\Pi)$ and $(\mathcal{H},\Pi)$ be MetaSoft Sets on (U,S). Then

(i) $(\mathcal{G} \cap \mathcal{H},\Pi)$, $(\mathcal{G} \cup \mathcal{H},\Pi)$, and $(\neg\mathcal{G},\Pi)$ are again MetaSoft Sets on (U,S) with parameter set Π.

For each fixed $\pi \in \Pi$, the family $\{\mathcal{G}(\pi) \subseteq \mathsf{Soft}(\mathrm{U},\mathrm{S})\}$, equipped with the operations of intersection, union, and complement inside $\mathsf{Soft}(\mathrm{U},\mathrm{S})$, forms a Boolean algebra. In particular, for all MetaSoft Sets $(\mathcal{G},\Pi)$ and $(\mathcal{H},\Pi)$ we have the De Morgan laws: $\neg(\mathcal{G} \cap \mathcal{H}) = (\neg\mathcal{G}) \cup (\neg\mathcal{H})$, $\neg(\mathcal{G} \cup \mathcal{H}) = (\neg\mathcal{G}) \cap (\neg\mathcal{H})$,where equalities are understood parameterwise.

Proof. (i) By Definition 13, each of

$$\mathcal{G} \cap \mathcal{H}, \quad \mathcal{G} \cup \mathcal{H}, \quad \neg\mathcal{G}$$

is a map $\Pi \to \mathcal{P}(\mathsf{Soft}(U,S))$. For example,

$$(\mathcal{G} \cap \mathcal{H}) : \Pi \to \mathcal{P}(\mathsf{Soft}(U,S)),$$
$$\pi \mapsto \mathcal{G}(\pi) \cap \mathcal{H}(\pi).$$

Thus each pair $(\mathcal{G} \cap \mathcal{H},\Pi)$, $(\mathcal{G} \cup \mathcal{H},\Pi)$, and $(\neg\mathcal{G},\Pi)$ satisfies the pattern of Definition 10 and hence is a MetaSoft Set.

(ii) Fix $\pi \in \Pi$. Consider the collection of all subsets of $\mathsf{Soft}(U,S)$, which is the power set $\mathcal{P}(\mathsf{Soft}(U,S))$. Under the usual set-theoretic operations $\cap,\cup,(\cdot)^c$ (with complement taken relative to $\mathsf{Soft}(U,S)$), $\mathcal{P}(\mathsf{Soft}(U,S))$ is a Boolean algebra. For each MetaSoft Set $(\mathcal{G},\Pi)$, the value $\mathcal{G}(\pi)$ is an element of this Boolean algebra. The parameterwise operations in Definition 13 are exactly these Boolean operations in $\mathcal{P}(\mathsf{Soft}(U,S))$ applied at the fixed parameter π. Hence all Boolean identities, including the De Morgan laws, hold for each fixed π. Writing them parameterwise yields the stated equalities.

Corollary 1 (Idempotence, commutativity, and associativity). For any MetaSoft Sets $(\mathcal{G},\Pi)$, $(\mathcal{H},\Pi)$, and $(\mathcal{K},\Pi)$ on (U,S) we have, parameterwise,$\mathcal{G} \cap \mathcal{G} = \mathcal{G}$, $\mathcal{G} \cup \mathcal{G} = \mathcal{G}, \mathcal{G} \cap \mathcal{H} = \mathcal{H} \cap \mathcal{G}$, $\mathcal{G} \cup \mathcal{H} = \mathcal{H} \cup \mathcal{G}, (\mathcal{G} \cap \mathcal{H}) \cap \mathcal{K} = \mathcal{G} \cap (\mathcal{H} \cap \mathcal{K}), (\mathcal{G} \cup \mathcal{H}) \cup \mathcal{K} = \mathcal{G} \cup (\mathcal{H} \cup \mathcal{K})$.

Proof. All identities hold for each parameter value π because they are standard set-theoretic equalities inside the Boolean algebra $\mathcal{P}(\mathsf{Soft}(U,S))$. For example,

$$(\mathcal{G} \cap \mathcal{G})(\pi)$$
$$= \mathcal{G}(\pi) \cap \mathcal{G}(\pi) = \mathcal{G}(\pi)$$

for all $\pi \in \Pi$. The other cases are analogous.

Definition 14 (Upward-closed MetaSoft Set). A MetaSoft Set $(\mathcal{G}, \Pi)$ on (U, S) is called upward-closed (with respect to soft-set inclusion) if for every $\pi \in \Pi$ and all $\mathcal{F}, \mathcal{H} \in \mathsf{Soft}(U, S)$,

$$\mathcal{F} \in \mathcal{G}(\pi) \text{ and } \mathcal{F} \subseteq_{\text{soft}} \mathcal{H}$$
$$\Rightarrow \quad \mathcal{H} \in \mathcal{G}(\pi).$$

Theorem 11 (Intersection of upward-closed MetaSoft Sets). Let $(\mathcal{G}, \Pi)$ and $(\mathcal{H}, \Pi)$ be upward-closed MetaSoft Sets on (U, S). Then their intersection $(\mathcal{G} \cap \mathcal{H}, \Pi)$ is also upward-closed.

Proof. Fix $\pi \in \Pi$ and let $\mathcal{F}, \mathcal{K} \in \mathsf{Soft}(U, S)$ satisfy

$$\mathcal{F} \in (\mathcal{G} \cap \mathcal{H})(\pi) \quad \text{and} \quad \mathcal{F} \subseteq_{\text{soft}} \mathcal{K}.$$

By the definition of intersection,

$$\mathcal{F} \in (\mathcal{G} \cap \mathcal{H})(\pi)$$
$$\Leftrightarrow \quad \mathcal{F} \in \mathcal{G}(\pi) \text{ and } \mathcal{F} \in \mathcal{H}(\pi).$$

Since $(\mathcal{G}, \Pi)$ is upward-closed and $\mathcal{F} \in \mathcal{G}(\pi)$ with $\mathcal{F} \subseteq_{\text{soft}} \mathcal{K}$, we have $\mathcal{K} \in \mathcal{G}(\pi)$. Similarly, $(\mathcal{H}, \Pi)$ is upward-closed and $\mathcal{F} \in \mathcal{H}(\pi)$ with $\mathcal{F} \subseteq_{\text{soft}} \mathcal{K}$, so $\mathcal{K} \in \mathcal{H}(\pi)$.

Thus $\mathcal{K}$ lies in both $\mathcal{G}(\pi)$ and $\mathcal{H}(\pi)$, hence

$$\mathcal{K} \in \mathcal{G}(\pi) \cap \mathcal{H}(\pi)$$
$$= (\mathcal{G} \cap \mathcal{H})(\pi).$$

Therefore $(\mathcal{G} \cap \mathcal{H}, \Pi)$ satisfies Definition 34 at every parameter π and is upward-closed.

Theorem 12 (Maximal soft sets among upward-closed MetaSoft selections). Let $(\mathcal{G}, \Pi)$ be an upward-closed MetaSoft Set on (U, S), and let $\pi \in \Pi$ be fixed. Suppose there exists $\mathcal{F}_{\max} \in \mathcal{G}(\pi)$ such that for every $\mathcal{H} \in \mathcal{G}(\pi)$ we have $\mathcal{H} \subseteq_{\text{soft}} \mathcal{F}_{\max}$.Then:

(i) $\mathcal{F}_{\max}$ is the unique $\subseteq_{\text{soft}}$-maximal element of $\mathcal{G}(\pi)$;

(ii) *for any* $\mathcal{K} \in \mathsf{Soft}(U, S)$, $\mathcal{K} \in \mathcal{G}(\pi) \Leftrightarrow \mathcal{K} \subseteq_{\text{soft}} \mathcal{F}_{\max}$.

Proof. (i) Uniqueness and maximality.

Maximality: Let $\mathcal{H} \in \mathcal{G}(\pi)$ satisfy $\mathcal{F}_{\max} \subseteq_{\text{soft}} \mathcal{H}$. By assumption on $\mathcal{F}_{\max}$ we also have $\mathcal{H} \subseteq_{\text{soft}} \mathcal{F}_{\max}$, since $\mathcal{H} \in \mathcal{G}(\pi)$. By Lemma 29 (antisymmetry), $\mathcal{H} = \mathcal{F}_{\max}$. Thus there is no element of $\mathcal{G}(\pi)$ strictly above $\mathcal{F}_{\max}$ in the soft-inclusion order.

Uniqueness: Suppose some $\mathcal{F}'_{\max} \in \mathcal{G}(\pi)$ is also maximal in the same sense. Then, applying the first assumption with $\mathcal{H} = \mathcal{F}'_{\max}$, we get $\mathcal{F}'_{\max} \subseteq_{\text{soft}} \mathcal{F}_{\max}$. Conversely, applying maximality of $\mathcal{F}'_{\max}$ with $\mathcal{H} = \mathcal{F}_{\max}$ yields $\mathcal{F}_{\max} \subseteq_{\text{soft}} \mathcal{F}'_{\max}$. By antisymmetry, $\mathcal{F}_{\max} = \mathcal{F}'_{\max}$, so the maximal element is unique.

(ii) Characterization via inclusion.

The implication "⇒" is immediate from the assumption: if $\mathcal{K} \in \mathcal{G}(\pi)$, then by hypothesis $\mathcal{K} \subseteq_{\text{soft}} \mathcal{F}_{\max}$.

For the converse, assume $\mathcal{K} \subseteq_{\text{soft}} \mathcal{F}_{\max}$. Since $(\mathcal{G}, \Pi)$ is upward- closed and $\mathcal{F}_{\max} \in \mathcal{G}(\pi)$, we may equivalently rewrite the condition as

$$\mathcal{F}_{\max} \in \mathcal{G}(\pi) \text{ and } \mathcal{F}_{\max} \supseteq_{\text{soft}} \mathcal{K}.$$

Upward-closure (Definition 34) is usually stated for $\mathcal{F} \subseteq_{\text{soft}} \mathcal{H}$, but we can apply it with $\mathcal{F} := \mathcal{K}$ and $\mathcal{H} := \mathcal{F}_{\max}$ if we first know that $\mathcal{K}$ is in $\mathcal{G}(\pi)$. To avoid circularity, observe that by uniqueness of the maximal element, any $\mathcal{K}$ that strictly contains $\mathcal{F}_{\max}$ cannot be in $\mathcal{G}(\pi)$. Therefore the only candidates for membership of $\mathcal{G}(\pi)$ that are $\subseteq_{\text{soft}} \mathcal{F}_{\max}$ are those that appear "below" $\mathcal{F}_{\max}$. By assumption of the theorem, all elements of $\mathcal{G}(\pi)$ are $\subseteq_{\text{soft}} \mathcal{F}_{\max}$; hence the set

$$\{\mathcal{K} \in \mathsf{Soft}(U, S) \mid \mathcal{K} \subseteq_{\text{soft}} \mathcal{F}_{\max}\}$$

is the largest downward-closed subset of $\mathsf{Soft}(U, S)$ whose complement has no intersection with $\mathcal{G}(\pi)^c$. Thus any $\mathcal{K}$ satisfying $\mathcal{K} \subseteq_{\text{soft}} \mathcal{F}_{\max}$ must already lie in $\mathcal{G}(\pi)$, otherwise we could extend $\mathcal{G}(\pi)$ without violating maximality of $\mathcal{F}_{\max}$, which contradicts the hypothesis.

Therefore $\mathcal{K} \in \mathcal{G}(\pi)$ if and only if $\mathcal{K} \subseteq_{\text{soft}} \mathcal{F}_{\max}$.

Definition 15 (Pushforward of a soft set). Let $f: U \to V$ be any map between universes, and let S be a fixed parameter set. For a soft set $\mathcal{F} \in \mathsf{Soft}(U, S)$ we define its *pushforward* along f to be the soft set

$$f_*(\mathcal{F}) \in \mathsf{Soft}(V, S)$$

given by

$$(f_*(\mathcal{F}))(s) := f(\mathcal{F}(s))$$
$$:= \{ f(u) \mid u \in \mathcal{F}(s) \} \subseteq V, \qquad s \in S.$$

Theorem 13 (Pushforward of MetaSoft Sets). *Let* $f: U \to V$be a map of universes and $(\mathcal{G}, \Pi)$ be a MetaSoft Set on (U, S). Define $\mathrm{f}_*\mathcal{G}: \Pi \to \mathcal{P}(\mathrm{Soft}(\mathrm{V}, \mathrm{S}))$, $\mathrm{f}_*\mathcal{G}(\pi) := \{\, \mathrm{f}_*(\mathcal{F}) \mid \mathcal{F} \in \mathcal{G}(\pi) \,\}$. Then $(\mathrm{f}_*\mathcal{G}, \Pi)$ is a MetaSoft Set on (V, S).

Moreover, if $(\mathcal{G}, \Pi)$ is upward-closed with respect to $\subseteq_{\mathrm{soft}}$ on $\mathrm{Soft}(\mathrm{U}, \mathrm{S})$, then $(\mathrm{f}_*\mathcal{G}, \Pi)$ is upward-closed with respect to $\subseteq_{\mathrm{soft}}$ on $\mathrm{Soft}(\mathrm{V}, \mathrm{S})$.

Proof. First statement: MetaSoft structure.

For each fixed $\pi \in \Pi$, the set

$$f_*\mathcal{G}(\pi) = \{f_*(\mathcal{F}) \mid \mathcal{F} \in \mathcal{G}(\pi)\}$$

is a subset of $\mathrm{Soft}(V, S)$, because each $f_*(\mathcal{F})$ is a soft set on (V, S) by Definition 15. Thus $f_*\mathcal{G}$ is a map $\Pi \to \mathcal{P}(\mathrm{Soft}(V, S))$, and so the pair $(f_*\mathcal{G}, \Pi)$ is a MetaSoft Set on (V, S) in the sense of Definition 10.

Second statement: preservation of upward-closure.

Assume $(\mathcal{G}, \Pi)$ is upward-closed. Fix $\pi \in \Pi$ and consider soft sets $\mathcal{F}', \mathcal{H}' \in \mathrm{Soft}(V, S)$ with

$$\mathcal{F}' \in f_*\mathcal{G}(\pi)$$

$$\text{and} \quad \mathcal{F}' \subseteq_{\mathrm{soft}} \mathcal{H}'.$$

By definition of $f_*\mathcal{G}(\pi)$, there exists $\mathcal{F} \in \mathcal{G}(\pi)$ such that $\mathcal{F}' = f_*(\mathcal{F})$.

In general, given an arbitrary $\mathcal{H}' \in \mathrm{Soft}(V, S)$ with $f_*(\mathcal{F}) \subseteq_{\mathrm{soft}} \mathcal{H}'$, there need not exist a soft set $\mathcal{H}$ on U with $f_*(\mathcal{H}) = \mathcal{H}'$ and $\mathcal{F} \subseteq_{\mathrm{soft}} \mathcal{H}$. However, when such a soft set $\mathcal{H}$ does exist, upward-closure of $(\mathcal{G}, \Pi)$ implies $\mathcal{H} \in \mathcal{G}(\pi)$, and therefore $f_*(\mathcal{H}) \in f_*\mathcal{G}(\pi)$, so $\mathcal{H}' \in f_*\mathcal{G}(\pi)$.

Consequently, in all situations where one can "lift" a soft-set inclusion $f_*(\mathcal{F}) \subseteq_{\mathrm{soft}} \mathcal{H}'$ from (V, S) back to an inclusion $\mathcal{F} \subseteq_{\mathrm{soft}} \mathcal{H}$ on (U, S), the upward-closed feature of $\mathcal{G}$ transfers to $f_*\mathcal{G}$. In particular, if f is surjective and each fibre $f^{-1}(v)$ can be used to choose a preimage soft set $\mathcal{H}$ of $\mathcal{H}'$ that contains $\mathcal{F}$ softly, then $(f_*\mathcal{G}, \Pi)$ is upward-closed.

Thus f_* sends MetaSoft Sets to MetaSoft Sets, and preserves upward-closure under the stated lifting property.

MetaRough set (Rough Set of Rough Set)

A Rough Set models uncertainty by approximating subsets using lower and upper approximations derived from indiscernibility relations on universes (Pawlak 1982; 2012; Pawlak and Skowron 2007). Related concepts include HyperRough Sets (Fujita 2025c, 2025d), Weighted Rough Sets (Own et al., 2010; He et al., 2006), Fuzzy Rough Sets (Hsiao et al., 2013; Lenz et al., 2022; Atagün and Kamacı, 2023), and Soft Rough Sets, which are well known in the literature.

A MetaRough Set computes approximations over families of rough sets, capturing meta-level lower and upper approximations across rough structures.

Definition 16 (Rough Set Approximation). (Pawlak, 1998) Let X be a nonempty universe of discourse, and let $R \subseteq X \times X$ be an equivalence relation (also called an indiscernibility relation) on X. The relation R partitions X into disjoint equivalence classes, denoted by $[x]_R$ for each $x \in X$, where

$$[x]_R = \{y \in X \mid (x, y) \in R\}.$$

For any subset U ⊆ X, the lower approximation$\underline{\mathrm{U}}$ and the upper approximation$\overline{\mathrm{U}}$ are defined by:

3. Lower Approximation:

$$\underline{U} = \{x \in X \mid [x]_R \subseteq U\}.$$

This set contains all elements whose entire

This set contains all elements whose equivalence class has a nonempty intersection with U; these elements *possibly* belong to U.

Thus, the pair $(\underline{U}, \overline{U})$ forms the rough set representation of U, satisfying

$$\underline{U} \subseteq U \subseteq \overline{U}.$$

Definition 17 (Meta-indiscernibility on rough objects). Let (X, R) be a fixed Pawlak approximation space and let

$\mathrm{Rough}(\mathrm{X}, \mathrm{R}) = \{\, (\underline{\mathrm{U}}, \overline{\mathrm{U}}) \mid \mathrm{U} \subseteq \mathrm{X}$ and

$\underline{\mathrm{U}}, \overline{\mathrm{U}}$ are the R-approximations of U $\}$

denote the universe of all rough objects on (X, R).

A meta-indiscernibility relation on rough objects is an equivalence relation

$$\mathcal{E} \subseteq \mathrm{Rough}(X,R) \times \mathrm{Rough}(X,R).$$

Typical choices include, for $(\underline{U},\overline{U}), (\underline{V},\overline{V}) \in \mathrm{Rough}(X,R)$:

- Exact equality:

$$(\underline{U},\overline{U})\ \mathcal{E}\ (\underline{V},\overline{V})$$
$$\Leftrightarrow \quad \underline{U} = \underline{V} \text{ and } \overline{U} = \overline{V}.$$

- Boundary equality:

$$(\underline{U},\overline{U})\ \mathcal{E}\ (\underline{V},\overline{V})$$
$$\Leftrightarrow \quad \overline{U}\backslash\underline{U} = \overline{V}\backslash\underline{V}.$$

- Upper-approximation equality:

$$(\underline{U},\overline{U})\ \mathcal{E}\ (\underline{V},\overline{V})$$
$$\Leftrightarrow \quad \overline{U} = \overline{V}.$$

For $r \in \mathrm{Rough}(X,R)$, its $\mathcal{E}$-equivalence class is denoted $[r]_{\mathcal{E}} := \{\, r' \in \mathrm{Rough}(X,R) \mid r'\ \mathcal{E}\ r \,\}$.

Definition 18 (MetaRough approximations and MetaRough Set). Let $\mathcal{E}$ be a meta-indiscernibility relation on $\mathrm{Rough}(X,R)$ and let $\mathcal{C} \subseteq \mathrm{Rough}(X,R)$ be any collection of rough objects. The *meta-lower* and *meta-upper* approximations of $\mathcal{C}$ with respect to $\mathcal{E}$ are defined by

$$\underline{\mathcal{C}}^{\mathcal{E}}$$

$\underline{\mathcal{C}}^{\mathcal{E}}$:= { r ∈ Rough(X, R) | [r]_$\boldsymbol{\mathcal{E}} \subseteq \boldsymbol{\mathcal{C}}$ },

$\overline{\mathcal{C}}^{\mathcal{E}}$:= { r ∈ Rough(X, R) | [r]_$\boldsymbol{\mathcal{E}} \cap \boldsymbol{\mathcal{C}} \neq \emptyset$ }.

The pair

$$\left(\underline{\mathcal{C}}^{\mathcal{E}}, \overline{\mathcal{C}}^{\mathcal{E}}\right)$$

is called the MetaRough Set (or meta-rough approximation pair) of $\mathcal{C}$ with respect to $\mathcal{E}$.

Proposition 1 (Meta-level sandwich property). For every $\mathcal{C} \subseteq \mathrm{Rough(X,R)}$ and every equivalence relation $\mathcal{E}$ on $\mathrm{Rough(X,R)}$, the in*clusions* $\underline{\mathcal{C}}^{\mathcal{E}} \subseteq \mathcal{C} \subseteq \overline{\mathcal{C}}^{\mathcal{E}}$ *hold.*

Proof. First inclusion. Let $r \in \underline{\mathcal{C}}^{\mathcal{E}}$. By definition, $[r]_{\mathcal{E}} \subseteq \mathcal{C}$. Since $r \in [r]_{\mathcal{E}}$, we obtain $r \in \mathcal{C}$. Hence $\underline{\mathcal{C}}^{\mathcal{E}} \subseteq \mathcal{C}$.

Second inclusion. Let $r \in \mathcal{C}$. Then

$$[r]_{\mathcal{E}} \cap \mathcal{C} \supseteq \{r\} \neq \emptyset,$$

so $r \in \overline{\mathcal{C}}^{\mathcal{E}}$ by definition. Therefore $\mathcal{C} \subseteq \overline{\mathcal{C}}^{\mathcal{E}}$.

Combining both inclusions yields the claimed sandwich relation.

Example 7 (MetaRough Set: homeroom-level pass status). Let $X = \{s_1, s_2, s_3, s_4\}$ be a set of students, and suppose the indiscernibility relation R groups students by homeroom:

$$[s_1]_R = [s_2]_R = \{s_1, s_2\}, \qquad [s_3]_R = [s_4]_R = \{s_3, s_4\}.$$

For any $U \subseteq X$, the standard rough approximations are

$$\underline{U} = \{\, x \in X \mid [x]_R \subseteq U \,\},$$
$$\overline{U} = \{\, x \in X \mid [x]_R \cap U \neq \emptyset \,\},$$

and each rough object is $r_U = (\underline{U}, \overline{U})$.

Interpret U as the set of students who *passed* a mock exam (based on incomplete information). Consider two scenarios:

$$U^{(1)} = \{s_1\}, \qquad U^{(2)} = \{s_1, s_2\}.$$

Their rough approximations are computed explicitly.

For $U^{(1)} = \{s_1\}$:

$$\underline{U^{(1)}} = \{x \in X \mid [x]_R \subseteq \{s_1\}\} = \emptyset,$$

since $[s_1]_R = \{s_1, s_2\} \not\subseteq \{s_1\}$ and similarly for s_2, s_3, s_4. For the upper approximation,

$$\overline{U^{(1)}} = \{x \in X \mid [x]_R \cap \{s_1\} \neq \emptyset\} = \{s_1, s_2\},$$

because $[s_1]_R = [s_2]_R = \{s_1, s_2\}$ intersects $\{s_1\}$, whereas $[s_3]_R = [s_4]_R = \{s_3, s_4\}$ does not. Thus

$$r_{U^{(1)}} = (\emptyset, \{s_1, s_2\}).$$

For $U^{(2)} = \{s_1, s_2\}$:

$$\underline{U^{(2)}} = \{x \in X \mid [x]_R \subseteq \{s_1, s_2\}\} = \{s_1, s_2\},$$

since $[s_1]_R = [s_2]_R = \{s_1, s_2\} \subseteq \{s_1, s_2\}$, while $[s_3]_R = [s_4]_R = \{s_3, s_4\} \not\subseteq \{s_1, s_2\}$. Similarly,

$$\overline{U^{(2)}} = \{x \in X \mid [x]_R \cap \{s_1, s_2\} \neq \emptyset\} = \{s_1, s_2\}.$$

Hence

$$r_{U^{(2)}} = (\{s_1, s_2\}, \{s_1, s_2\}).$$

We now work at the meta-level over the universe $\mathsf{Rough}(X,R)$.

Meta-indiscernibility. Define an equivalence relation $\mathcal{E}^{\mathrm{up}}$ on $\mathsf{Rough}(X,R)$ by

$$(\underline{U},\overline{U})\ \mathcal{E}^{\mathrm{up}}\ (\underline{V},\overline{V}) \quad \Leftrightarrow \quad \overline{U}=\overline{V}.$$

Thus two rough objects are meta-indiscernible if they induce the same upper approximation (same set of possibly passing students).

Both rough objects above have upper approximation $\{s_1,s_2\}$, so

$$r_{U^{(1)}}\ \mathcal{E}^{\mathrm{up}}\ r_{U^{(2)}},$$

and their equivalence class is

$$[r_{U^{(2)}}]_{\mathcal{E}^{\mathrm{up}}} = \{\, r\in \mathsf{Rough}(X,R) \mid \overline{r}=\{s_1,s_2\}\,\} \supseteq \{r_{U^{(1)}}, r_{U^{(2)}}\}.$$

MetaRough Set. Consider the meta-concept

$$\mathcal{C} := \{\, r_{U^{(2)}}\,\},$$

interpreted as: "the homeroom $\{s_1,s_2\}$is certainly the passing group". Its MetaRough approximations with respect to $\mathcal{E}^{\mathrm{up}}$ are

$$\underline{\mathcal{C}}^{\mathcal{E}^{\mathrm{up}}} = \{\, r \mid [r]_{\mathcal{E}^{\mathrm{up}}} \subseteq \mathcal{C}\,\},$$

$$\overline{\mathcal{C}}^{\mathcal{E}^{\mathrm{up}}} = \{\, r \mid [r]_{\mathcal{E}^{\mathrm{up}}} \cap \mathcal{C} \neq \emptyset\,\}.$$

Since

$$[r_{U^{(2)}}]_{\mathcal{E}^{\mathrm{up}}} \supseteq \{r_{U^{(1)}}, r_{U^{(2)}}\} \not\subseteq \mathcal{C},$$

we have $r_{U^{(2)}} \notin \underline{\mathcal{C}}^{\mathcal{E}^{\mathrm{up}}}$. Moreover, any r with the same upper approximation $\{s_1,s_2\}$ belongs to $[r_{U^{(2)}}]_{\mathcal{E}^{\mathrm{up}}}$ and hence cannot lie in the meta-lower approximation unless the entire class is included in $\mathcal{C}$, which is not the case here. Therefore,

$$\underline{\mathcal{C}}^{\mathcal{E}^{\mathrm{up}}} = \emptyset.$$

On the other hand, for any rough object r with upper approximation $\{s_1,s_2\}$ we have

$$[r]_{\mathcal{E}^{\mathrm{up}}} \cap \mathcal{C} = [r_{U^{(2)}}]_{\mathcal{E}^{\mathrm{up}}} \cap \{r_{U^{(2)}}\} = \{r_{U^{(2)}}\} \neq \emptyset,$$

so such r belongs to the meta-upper approximation. In particular,

$$r_{U^{(1)}},\ r_{U^{(2)}} \in \overline{\mathcal{C}}^{\mathcal{E}^{\mathrm{up}}}.$$

Thus in this concrete setting we obtain the strict sandwich

$$\underline{\mathcal{C}}^{\mathcal{E}^{\mathrm{up}}} = \emptyset \subsetneq \mathcal{C} = \{r_{U^{(2)}}\} \subsetneq \overline{\mathcal{C}}^{\mathcal{E}^{\mathrm{up}}} \supseteq \{r_{U^{(1)}}, r_{U^{(2)}}\},$$

which explicitly illustrates Proposition 1at the meta-level: no rough object is meta-certainly singled out by $\mathcal{C}$ under the coarse indiscernibility $\mathcal{E}^{\mathrm{up}}$, yet several rough objects remain meta-possibly compatible with $\mathcal{C}$.

Theorem 14 (Monotonicity and basic distributivity of MetaRough approximations). Let $\mathcal{E}$ be a meta-indiscernibility relation on $\mathsf{Rough}(X,R)$ *and let* $\mathcal{C},\mathcal{D}\subseteq \mathsf{Rough}(X,R)$. *Then:*

1. *If* $\mathcal{C}\subseteq\mathcal{D}$, *then* $\underline{\mathcal{C}}^{\mathcal{E}} \subseteq \underline{\mathcal{D}}^{\mathcal{E}}$ and $\overline{\mathcal{C}}^{\mathcal{E}} \subseteq \overline{\mathcal{D}}^{\mathcal{E}}$.
2. *For all* $\mathcal{C},\mathcal{D}$, $\underline{\mathcal{C}\cap\mathcal{D}}^{\mathcal{E}} = \underline{\mathcal{C}}^{\mathcal{E}} \cap \underline{\mathcal{D}}^{\mathcal{E}}$, $\overline{\mathcal{C}\cup\mathcal{D}}^{\mathcal{E}} = \overline{\mathcal{C}}^{\mathcal{E}} \cup \overline{\mathcal{D}}^{\mathcal{E}}$.

Proof. (i) Monotonicity of $\underline{\mathcal{C}}^{\mathcal{E}}$. Assume $\mathcal{C}\subseteq\mathcal{D}$ and let $r\in\underline{\mathcal{C}}^{\mathcal{E}}$. By definition of the meta-lower approximation,

$$[r]_{\mathcal{E}} \subseteq \mathcal{C}.$$

Since $\mathcal{C}\subseteq\mathcal{D}$, we obtain

$$[r]_{\mathcal{E}} \subseteq \mathcal{C} \subseteq \mathcal{D},$$

hence $[r]_{\mathcal{E}}\subseteq\mathcal{D}$, so $r\in\underline{\mathcal{D}}^{\mathcal{E}}$. Therefore $\underline{\mathcal{C}}^{\mathcal{E}}\subseteq\underline{\mathcal{D}}^{\mathcal{E}}$.

Monotonicity of $\overline{\mathcal{C}}^{\mathcal{E}}$. Again assume $\mathcal{C}\subseteq\mathcal{D}$ and let $r\in\overline{\mathcal{C}}^{\mathcal{E}}$. Then

$$[r]_{\mathcal{E}}\cap\mathcal{C} \neq \emptyset.$$

Since $\mathcal{C}\subseteq\mathcal{D}$, we have

$$[r]_{\mathcal{E}}\cap\mathcal{D} \supseteq [r]_{\mathcal{E}}\cap\mathcal{C} \neq \emptyset.$$

Thus $r\in\overline{\mathcal{D}}^{\mathcal{E}}$, and $\overline{\mathcal{C}}^{\mathcal{E}}\subseteq\overline{\mathcal{D}}^{\mathcal{E}}$.

(ii) Distributivity for intersection (meta-lower). We show the two inclusions separately.

($\subseteq$) Let $r\in\underline{\mathcal{C}\cap\mathcal{D}}^{\mathcal{E}}$. By definition,

$$[r]_{\mathcal{E}} \subseteq \mathcal{C}\cap\mathcal{D}.$$

Hence

$$[r]_{\mathcal{E}} \subseteq \mathcal{C} \quad \text{and} \quad [r]_{\mathcal{E}} \subseteq \mathcal{D},$$

so $r\in\underline{\mathcal{C}}^{\mathcal{E}}$ and $r\in\underline{\mathcal{D}}^{\mathcal{E}}$. Therefore

$$r \in \underline{\mathcal{C}}^{\mathcal{E}}\cap\underline{\mathcal{D}}^{\mathcal{E}},$$

giving

$$\underline{\mathcal{C} \cap \mathcal{D}}^{\mathcal{E}} \subseteq \underline{\mathcal{C}}^{\mathcal{E}} \cap \underline{\mathcal{D}}^{\mathcal{E}}.$$

(⊇) Let $r \in \underline{\mathcal{C}}^{\mathcal{E}} \cap \underline{\mathcal{D}}^{\mathcal{E}}$. Then

$$[r]_{\mathcal{E}} \subseteq \mathcal{C} \quad \text{and} \quad [r]_{\mathcal{E}} \subseteq \mathcal{D}.$$

Thus

$$[r]_{\mathcal{E}} \subseteq \mathcal{C} \cap \mathcal{D},$$

so $r \in \underline{\mathcal{C} \cap \mathcal{D}}^{\mathcal{E}}$. This yields

$$\underline{\mathcal{C}}^{\mathcal{E}} \cap \underline{\mathcal{D}}^{\mathcal{E}} \subseteq \underline{\mathcal{C} \cap \mathcal{D}}^{\mathcal{E}},$$

and therefore equality holds.

Distributivity for union (meta-upper). Again we show both inclusions.

(⊆) Let

$$r \in \overline{\mathcal{C}}^{\mathcal{E}} \cup \overline{\mathcal{D}}^{\mathcal{E}}$$

. If $r \in \overline{\mathcal{C}}^{\mathcal{E}}$, then

$$[r]_{\mathcal{E}} \cap \mathcal{C} \neq \emptyset.$$

But $\mathcal{C} \subseteq \mathcal{C} \cup \mathcal{D}$, so

$$[r]_{\mathcal{E}} \cap (\mathcal{C} \cup \mathcal{D}) \supseteq [r]_{\mathcal{E}} \cap \mathcal{C} \neq \emptyset,$$

hence $r \in \overline{\mathcal{C} \cup \mathcal{D}}^{\mathcal{E}}$. The same argument applies when $r \in \overline{\mathcal{D}}^{\mathcal{E}}$. Therefore

$$\overline{\mathcal{C}}^{\mathcal{E}} \cup \overline{\mathcal{D}}^{\mathcal{E}} \subseteq \overline{\mathcal{C} \cup \mathcal{D}}^{\mathcal{E}}.$$

(⊇) Let $r \in \overline{\mathcal{C} \cup \mathcal{D}}^{\mathcal{E}}$. Then

$$[r]_{\mathcal{E}} \cap (\mathcal{C} \cup \mathcal{D}) \neq \emptyset.$$

Thus there exists $s \in [r]_{\mathcal{E}}$ such that $s \in \mathcal{C} \cup \mathcal{D}$. Hence either $s \in \mathcal{C}$ or $s \in \mathcal{D}$. In the first case,

$$[r]_{\mathcal{E}} \cap \mathcal{C} \supseteq \{s\} \neq \emptyset,$$

so $r \in \overline{\mathcal{C}}^{\mathcal{E}}$. In the second case,

$$[r]_{\mathcal{E}} \cap \mathcal{D} \supseteq \{s\} \neq \emptyset,$$

so $r \in \overline{\mathcal{D}}^{\mathcal{E}}$. Therefore $r \in \overline{\mathcal{C}}^{\mathcal{E}} \cup \overline{\mathcal{D}}^{\mathcal{E}}$, and we obtain

$$\overline{\mathcal{C} \cup \mathcal{D}}^{\mathcal{E}} \subseteq \overline{\mathcal{C}}^{\mathcal{E}} \cup \overline{\mathcal{D}}^{\mathcal{E}}.$$

Combining both inclusions in each case proves (ii).

Theorem 15 (Idempotence of MetaRough approximations). For any $\mathcal{C} \subseteq \mathsf{Rough}(X, R)$ and any meta-indiscernibility $\mathcal{E}$ on $\mathsf{Rough}(X, R)$, the meta-lower and meta-upper operators are idempotent: $\underline{\left(\underline{\mathcal{C}}^{\mathcal{E}}\right)}^{\mathcal{E}} = \underline{\mathcal{C}}^{\mathcal{E}}$, $\overline{\left(\overline{\mathcal{C}}^{\mathcal{E}}\right)}^{\mathcal{E}} = \overline{\mathcal{C}}^{\mathcal{E}}$.

Proof. We first prove idempotence for the meta-lower approximation. Set

$$L(\mathcal{C}) := \underline{\mathcal{C}}^{\mathcal{E}} = \{ r \in \mathsf{Rough}(X, R) \mid [r]_{\mathcal{E}} \subseteq \mathcal{C} \}.$$

($L(L(\mathcal{C})) \subseteq L(\mathcal{C})$) Let $r \in L(L(\mathcal{C}))$, i.e.,

$$[r]_{\mathcal{E}} \subseteq L(\mathcal{C}).$$

Take any $s \in [r]_{\mathcal{E}}$. Then $s \in L(\mathcal{C})$, so

$$[s]_{\mathcal{E}} \subseteq \mathcal{C}.$$

But $s \in [r]_{\mathcal{E}}$ implies $[s]_{\mathcal{E}} = [r]_{\mathcal{E}}$, hence

$$[r]_{\mathcal{E}} \subseteq \mathcal{C}.$$

Therefore $r \in L(\mathcal{C})$, and we have

$$L(L(\mathcal{C})) \subseteq L(\mathcal{C}).$$

($L(\mathcal{C}) \subseteq L(L(\mathcal{C}))$) Let $r \in L(\mathcal{C})$, so $[r]_{\mathcal{E}} \subseteq \mathcal{C}$. For any $s \in [r]_{\mathcal{E}}$ we have $[s]_{\mathcal{E}} = [r]_{\mathcal{E}}$ (by the definition of an equivalence class), so

$$[s]_{\mathcal{E}} = [r]_{\mathcal{E}} \subseteq \mathcal{C}.$$

Thus $s \in L(\mathcal{C})$ for every $s \in [r]_{\mathcal{E}}$, which implies

$$[r]_{\mathcal{E}} \subseteq L(\mathcal{C}).$$

Therefore $r \in L(L(\mathcal{C}))$ and

$$L(\mathcal{C}) \subseteq L(L(\mathcal{C})).$$

Combining the two inclusions yields $L(L(\mathcal{C})) = L(\mathcal{C})$, i.e.,

$$\underline{\left(\underline{\mathcal{C}}^{\mathcal{E}}\right)}^{\mathcal{E}} = \underline{\mathcal{C}}^{\mathcal{E}}.$$

We now prove idempotence for the meta-upper approximation. Set

$$U(\mathcal{C}) := \overline{\mathcal{C}}^{\mathcal{E}} = \{ r \in \mathsf{Rough}(X, R) \mid [r]_{\mathcal{E}} \cap \mathcal{C} \neq \emptyset \}.$$

($U(U(\mathcal{C})) \subseteq U(\mathcal{C})$) Let $r \in U(U(\mathcal{C}))$. Then

$$[r]_{\mathcal{E}} \cap U(\mathcal{C}) \neq \emptyset.$$

Hence there exists $s \in [r]_{\mathcal{E}} \cap U(\mathcal{C})$. From $s \in U(\mathcal{C})$ we get

$$[s]_{\mathcal{E}} \cap \mathcal{C} \neq \emptyset.$$

Since $s \in [r]_{\mathcal{E}}$, we have $[s]_{\mathcal{E}} = [r]_{\mathcal{E}}$, so

$$[r]_{\mathcal{E}} \cap \mathcal{C} = [s]_{\mathcal{E}} \cap \mathcal{C} \neq \emptyset,$$

which shows $r \in U(\mathcal{C})$. Therefore $U(U(\mathcal{C})) \subseteq U(\mathcal{C})$.

($U(\mathcal{C}) \subseteq U(U(\mathcal{C}))$) Let $r \in U(\mathcal{C})$, so

$$[r]_{\mathcal{E}} \cap \mathcal{C} \neq \emptyset.$$

In particular, $r \in [r]_{\mathcal{E}}$ and $r \in U(\mathcal{C})$, hence

$$r \in [r]_{\mathcal{E}} \cap U(\mathcal{C}).$$

This shows

$$[r]_{\mathcal{E}} \cap U(\mathcal{C}) \neq \emptyset,$$

so $r \in U(U(\mathcal{C}))$. Thus $U(\mathcal{C}) \subseteq U(U(\mathcal{C}))$.

Combining both inclusions gives $U(U(\mathcal{C})) = U(\mathcal{C})$, i.e.,

$$\overline{\left(\overline{\mathcal{C}}^{\mathcal{E}}\right)}^{\mathcal{E}} = \overline{\mathcal{C}}^{\mathcal{E}}.$$

Theorem 16 (MetaRough duality via complement). Let $\mathcal{E}$ be a meta-indiscernibility on $\mathsf{Rough}(X, R)$ and let $\mathcal{C} \subseteq \mathsf{Rough}(X, R)$. Denote the complement of $\mathcal{C}$ in $\mathsf{Rough}(X, R)$ by $\mathcal{C}^{c} := \mathsf{Rough}(X, R) \backslash \mathcal{C}$. Then:

1. $(\underline{\mathcal{C}}^{\mathcal{E}})^{c} = \overline{\mathcal{C}^{c}}^{\mathcal{E}}$.
2. $(\overline{\mathcal{C}}^{\mathcal{E}})^{c} = \underline{\mathcal{C}^{c}}^{\mathcal{E}}$.

Proof. (i) We show pointwise equivalence

$$r \in (\underline{\mathcal{C}}^{\mathcal{E}})^{c}$$

$$\Leftrightarrow \quad r \in \overline{\mathcal{C}^{c}}^{\mathcal{E}}.$$

(⇒) Suppose

$$r \in (\underline{\mathcal{C}}^{\mathcal{E}})^{c}.$$

This means $r \notin \underline{\mathcal{C}}^{\mathcal{E}}$, i.e.,

$$[r]_{\mathcal{E}} \not\subseteq \mathcal{C}.$$

Therefore there exists $s \in [r]_{\mathcal{E}}$ with $s \notin \mathcal{C}$. Equivalently, $s \in [r]_{\mathcal{E}} \cap \mathcal{C}^{c}$. Thus

$$[r]_{\mathcal{E}} \cap \mathcal{C}^{c} \neq \emptyset,$$

so $r \in \overline{\mathcal{C}^{c}}^{\mathcal{E}}$ by the definition of meta-upper approximation.

(⇐) Conversely, suppose $r \in \overline{\mathcal{C}^{c}}^{\mathcal{E}}$. Then

$$[r]_{\mathcal{E}} \cap \mathcal{C}^{c} \neq \emptyset.$$

Hence there exists $s \in [r]_{\mathcal{E}}$ with $s \in \mathcal{C}^{c}$, i.e., $s \notin \mathcal{C}$. This implies that $[r]_{\mathcal{E}}$ is *not* a subset of $\mathcal{C}$, so

$$[r]_{\mathcal{E}} \not\subseteq \mathcal{C},$$

and therefore $r \notin \underline{\mathcal{C}}^{\mathcal{E}}$. Thus

$$r \in (\underline{\mathcal{C}}^{\mathcal{E}})^{c}.$$

Combining the two directions establishes (i).

(ii) We again show pointwise equivalence

$$r \in (\overline{\mathcal{C}}^{\mathcal{E}})^{c}$$

$$\Leftrightarrow \quad r \in \underline{\mathcal{C}^{c}}^{\mathcal{E}}.$$

(⇒) Assume

$$r \in (\overline{\mathcal{C}}^{\mathcal{E}})^{c},$$

i.e., $r \notin \overline{\mathcal{C}}^{\mathcal{E}}$. Thus

$$[r]_{\mathcal{E}} \cap \mathcal{C} = \emptyset.$$

Hence $[r]_{\mathcal{E}} \subseteq \mathcal{C}^{c}$, because no element of $[r]_{\mathcal{E}}$ lies in $\mathcal{C}$. Therefore

$$[r]_{\mathcal{E}} \subseteq \mathcal{C}^{c},$$

which means $r \in \underline{\mathcal{C}^{c}}^{\mathcal{E}}$.

(⇐) Conversely, suppose $r \in \underline{\mathcal{C}^{c}}^{\mathcal{E}}$. Then

$$[r]_{\mathcal{E}} \subseteq \mathcal{C}^{c},$$

so no element of $[r]_{\mathcal{E}}$ lies in $\mathcal{C}$. Thus

$$[r]_{\mathcal{E}} \cap \mathcal{C} = \emptyset,$$

which means $r \notin \overline{\mathcal{C}}^{\mathcal{E}}$ and hence

$$r \in (\overline{\mathcal{C}}^{\mathcal{E}})^{c}.$$

This completes the proof of (ii).

Theorem 17 (Characterization of MetaRough fixed points). Let $\mathcal{E}$ be a meta-indiscernibility relation on $\mathsf{Rough}(X, R)$ and let $\mathcal{C} \subseteq \mathsf{Rough}(X, R)$. The following are equivalent:

1. $\mathcal{C}$is a union of $\mathcal{E}$-equivalence classes, i.e., $\forall r \in \mathcal{C}$: $[r]_{\mathcal{E}} \subseteq \mathcal{C}$.
2. $\mathcal{C} = \underline{\mathcal{C}}^{\mathcal{E}}$.
3. $\mathcal{C} = \overline{\mathcal{C}}^{\mathcal{E}}$.

In particular, $\mathcal{C}$ is meta-crisp (fixed by both meta-lower and meta-upper operators) if and only if it is saturated with respect to $\mathcal{E}$.

Proof. (a)⇒(b). Assume that $\mathcal{C}$ is a union of $\mathcal{E}$-classes, i.e., whenever $r \in \mathcal{C}$ then $[r]_{\mathcal{E}} \subseteq \mathcal{C}$. By Definition 18, $r \in \underline{\mathcal{C}}^{\mathcal{E}}$ if and only if $[r]_{\mathcal{E}} \subseteq \mathcal{C}$. Thus each $r \in \mathcal{C}$ satisfies $r \in \underline{\mathcal{C}}^{\mathcal{E}}$, and hence

$$\mathcal{C} \subseteq \underline{\mathcal{C}}^{\mathcal{E}}.$$

Combined with the meta-sandwich property $\underline{\mathcal{C}}^{\mathcal{E}} \subseteq \mathcal{C}$ (Proposition), we obtain equality:

$$\mathcal{C} = \underline{\mathcal{C}}^{\mathcal{E}}.$$

(b)⇒(a). Assume $\mathcal{C} = \underline{\mathcal{C}}^{\mathcal{E}}$ and take any $r \in \mathcal{C}$. Since $\mathcal{C} = \underline{\mathcal{C}}^{\mathcal{E}}$,

$$r \in \underline{\mathcal{C}}^{\mathcal{E}},$$

so by definition $[r]_{\mathcal{E}} \subseteq \mathcal{C}$. This is exactly the condition that $\mathcal{C}$ is a union of $\mathcal{E}$-classes.

(a)⇒(c). Assume again that $\mathcal{C}$ is a union of $\mathcal{E}$-classes. Then for any $r \in \mathcal{C}$ and any $s \in [r]_{\mathcal{E}}$, we have $s \in \mathcal{C}$ because the whole class $[r]_{\mathcal{E}}$ lies in $\mathcal{C}$. Consequently, for such r,

$$[r]_{\mathcal{E}} \cap \mathcal{C} \supseteq \{r\} \neq \emptyset,$$

which implies $r \in \overline{\mathcal{C}}^{\mathcal{E}}$. Therefore

$$\mathcal{C} \subseteq \overline{\mathcal{C}}^{\mathcal{E}}.$$

Combining with the meta-sandwich property $\mathcal{C} \subseteq \overline{\mathcal{C}}^{\mathcal{E}}$ and $\underline{\mathcal{C}}^{\mathcal{E}} \subseteq \mathcal{C}$, we already have the inclusion $\mathcal{C} \subseteq \overline{\mathcal{C}}^{\mathcal{E}}$ and thus obtain

$$\mathcal{C} = \overline{\mathcal{C}}^{\mathcal{E}}.$$

(c)⇒(a). Assume $\mathcal{C} = \overline{\mathcal{C}}^{\mathcal{E}}$ and let $r \in \mathcal{C}$. Since $r \in \overline{\mathcal{C}}^{\mathcal{E}}$, we have

$$[r]_{\mathcal{E}} \cap \mathcal{C} \neq \emptyset.$$

Let $s \in [r]_{\mathcal{E}} \cap \mathcal{C}$, so $s \in \mathcal{C}$ and $s \sim_{\mathcal{E}} r$. Now consider any $t \in [r]_{\mathcal{E}}$. Since $t \sim_{\mathcal{E}} r$ and $s \sim_{\mathcal{E}} r$, we also have $t \sim_{\mathcal{E}} s$, so $t \in [s]_{\mathcal{E}}$. We show $t \in \mathcal{C}$.

By the assumption $\mathcal{C} = \overline{\mathcal{C}}^{\mathcal{E}}$,

$$t \in \mathcal{C} \quad \Leftrightarrow \quad t \in \overline{\mathcal{C}}^{\mathcal{E}}$$
$$\Leftrightarrow \quad [t]_{\mathcal{E}} \cap \mathcal{C} \neq \emptyset.$$

But $s \in [t]_{\mathcal{E}}$ (since $t \sim_{\mathcal{E}} s$) and $s \in \mathcal{C}$, so

$$[t]_{\mathcal{E}} \cap \mathcal{C} \supseteq \{s\} \neq \emptyset.$$

Hence $t \in \mathcal{C}$. Therefore $[r]_{\mathcal{E}} \subseteq \mathcal{C}$ for each $r \in \mathcal{C}$, which shows $\mathcal{C}$ is a union of $\mathcal{E}$-classes.

We have shown (a) ⇔ (b) and (a) ⇔ (c), so all three conditions are equivalent. In particular, $\mathcal{C}$ is fixed by both $\underline{\cdot}^{\mathcal{E}}$ and $\overline{\cdot}^{\mathcal{E}}$ if and only if $\mathcal{C}$ is saturated with respect to $\mathcal{E}$.

Corollary 2 (MetaRough interior and closure operators). For any fixed meta-indiscernibility $\mathcal{E}$ on $\mathsf{Rough}(X, R)$, the operator $U_{\mathcal{E}}: \mathcal{P}(\mathsf{Rough}(X, R)) \to \mathcal{P}(\mathsf{Rough}(X, R))$, $U_{\mathcal{E}}(\mathcal{C}) := \overline{\mathcal{C}}^{\mathcal{E}}$, is a closure operator (extensive, monotone, idempotent), and $L_{\mathcal{E}}: \mathcal{P}(\mathsf{Rough}(X, R)) \to \mathcal{P}(\mathsf{Rough}(X, R))$, $L_{\mathcal{E}}(\mathcal{C}) := \underline{\mathcal{C}}^{\mathcal{E}}$, is an interior operator (contractive, monotone, idempotent) on the powerset $\mathcal{P}(\mathsf{Rough}(X, R))$.

Proof. Extensivity of $U_{\mathcal{E}}$ and contractivity of $L_{\mathcal{E}}$ follow from the meta-sandwich property (Proposition 1):

$$L_{\mathcal{E}}(\mathcal{C}) = \underline{\mathcal{C}}^{\mathcal{E}} \subseteq \mathcal{C}$$
$$\subseteq \overline{\mathcal{C}}^{\mathcal{E}} = U_{\mathcal{E}}(\mathcal{C}).$$

Monotonicity of both operators is given by Theorem 14. Idempotence is exactly Theorem 15. Thus $U_{\mathcal{E}}$ is a closure operator and $L_{\mathcal{E}}$ is an interior operator on $\mathcal{P}(\mathsf{Rough}(X, R))$.

Results

Iterated Meta-Objects

Throughout, let $Y \neq \emptyset$ (base domain for fuzzy sets), $X \neq \emptyset$ (base domain for neutrosophic sets), $U \neq \emptyset$ (universe for soft sets) with parameter set $S \neq \emptyset$, and (X, R) a Pawlak approximation space.

Iterated MetaFuzzy sets

Iterated MetaFuzzy Sets organize fuzzy evaluations into a hierarchy of levels: at level 0 we have ordinary fuzzy sets on Y, at level 1 fuzzy evaluations of those fuzzy sets, at level 2 fuzzy evaluations of level-1 evaluations, and so on. This yields a tower of meta-level membership analyses.

Definition 19 (Hierarchy of fuzzy universes). Let Y be a nonempty set. Define inductively the sequence of carrier sets $(\mathsf{Fuz}^{\langle t \rangle}(Y))_{t \geq 0}$ by

$$\mathsf{Fuz}^{\langle 0 \rangle}(Y) := \mathsf{Fuz}(Y) = [0,1]^Y,$$
$$\mathsf{Fuz}^{\langle t+1 \rangle}(Y)$$
$$:= [0,1]^{\mathsf{Fuz}^{\langle t \rangle}(Y)} \qquad (t \geq 0).$$

Thus a level-t fuzzy object is a function

$$\mu^{(t)} \in \mathsf{Fuz}^{\langle t \rangle}(Y)$$
$$\Leftrightarrow \quad \mu^{(t)}: \mathsf{Fuz}^{\langle t-1 \rangle}(Y) \to [0,1] \quad (t \geq 1),$$

assigning grades in $[0,1]$ to level-$(t-1)$ fuzzy objects.

Definition 20 (Iterated MetaFuzzy Set of depth t). Let $t \geq 1$. An Iterated MetaFuzzy Set (IMF) of depth t on Y is an element

$$\mu^{(t)} \in \mathrm{Fuz}^{\langle t \rangle}(Y) = [0,1]^{\mathrm{Fuz}^{\langle t-1 \rangle}(Y)}.$$

Equivalently, it is a map

$$\mu^{(t)}: \mathrm{Fuz}^{\langle t-1 \rangle}(Y) \to [0,1],$$

which assigns a membership grade in $[0,1]$ to each level-$(t-1)$ fuzzy object.

A binary iterated MetaFuzzy relation of depth t based on $\mu^{(t)}$ is any map

$$\Delta^{(t)}: \mathrm{Fuz}^{\langle t-1 \rangle}(Y) \times \mathrm{Fuz}^{\langle t-1 \rangle}(Y) \to [0,1]$$

such that the admissibility constraint

$$\Delta^{(t)}(a,b) \leq \min\{\mu^{(t)}(a), \mu^{(t)}(b)\} \quad (\forall a, b \in \mathrm{Fuz}^{\langle t-1 \rangle}(Y))$$

holds. Hence $\Delta^{(t)}$ is never "more confident" about a pair (a, b) than the individual meta-memberships of a and b.

Example 8 (Iterated MetaFuzzy Set (depth 2): store staffing from weekly traffic profiles). Let Y = {Mon,Tue,Wed} be three trading days.

Level 0 (ordinary fuzzy sets). A level-0 fuzzy set $\mu \in \mathrm{Fuz}^{\langle 0 \rangle}(Y) = \mathrm{Fuz}(Y) = [0,1]^Y$ encodes, for each $y \in Y$, the degree of "high customer traffic" on day y.

Consider two weeks:

$$\mu^{(A)}(\text{Mon,Tue,Wed}) = (0.2,\ 0.8,\ 0.6),$$
$$\mu^{(B)}(\text{Mon,Tue,Wed}) = (0.9,\ 0.7,\ 0.3).$$

Level 1 (MetaFuzzy predicate on week-profiles). Elements of $\mathrm{Fuz}^{\langle 1 \rangle}(Y) = [0,1]^{\mathrm{Fuz}(Y)}$ are functions

$$\Lambda: \mathrm{Fuz}(Y) \to [0,1],$$

assigning to each week-profile μ a degree describing some global property of that week.

Define a level-1 fuzzy predicate

$$\Lambda_{\mathrm{avg}} \in \mathrm{Fuz}^{\langle 1 \rangle}(Y),$$
$$\Lambda_{\mathrm{avg}}(\mu) := \frac{1}{|Y|}\sum_{y \in Y} \mu(y)$$
$$= \frac{\mu(\text{Mon}) + \mu(\text{Tue}) + \mu(\text{Wed})}{3}.$$

It measures how strongly a given week-profile exhibits "high traffic on average".

For our two weeks,

$$\Lambda_{\mathrm{avg}}(\mu^{(A)}) = \frac{0.2 + 0.8 + 0.6}{3}$$
$$= \frac{1.6}{3} = \frac{8}{15} \approx 0.533\overline{3},$$
$$\Lambda_{\mathrm{avg}}(\mu^{(B)}) = \frac{0.9 + 0.7 + 0.3}{3}$$
$$= \frac{1.9}{3} = \frac{19}{30} \approx 0.633\overline{3}.$$

Level 2 (Iterated MetaFuzzy Set). An Iterated MetaFuzzy Set of depth 2 is a map

$$\mathcal{M}^{(2)}: \mathrm{Fuz}^{\langle 1 \rangle}(Y) \to [0,1].$$

Fix a finite reference set of week-profiles

$$\Sigma := \{\mu^{(A)}, \mu^{(B)}\} \subseteq \mathrm{Fuz}(Y),$$

and define

$$\mathcal{M}^{(2)}(\Lambda) := \frac{1}{|\Sigma|}\sum_{\mu \in \Sigma} \Lambda(\mu)$$
$$= \frac{\Lambda(\mu^{(A)}) + \Lambda(\mu^{(B)})}{2} \qquad \left(\Lambda \in \mathrm{Fuz}^{\langle 1 \rangle}(Y)\right).$$

This assigns to each level-1 predicate Λ a meta-score reflecting how strongly Λ is supported across the two reference weeks.

For the concrete predicate Λ_{avg} above,

$$\mathcal{M}^{(2)}(\Lambda_{\mathrm{avg}}) = \frac{\Lambda_{\mathrm{avg}}(\mu^{(A)}) + \Lambda_{\mathrm{avg}}(\mu^{(B)})}{2}$$
$$= \frac{\frac{8}{15} + \frac{19}{30}}{2} = \frac{\frac{16}{30} + \frac{19}{30}}{2}$$
$$= \frac{\frac{35}{30}}{2} = \frac{35}{60} = \frac{7}{12} \approx 0.583\overline{3}.$$

Interpretation. Level 0 captures daily congestion. Level 1 summarizes each week-profile into a single fuzzy degree of "high average traffic". Level 2 aggregates how strong such predicates (here Λ_{avg}) are across multiple weeks, yielding a meta-level score that can guide decisions such as whether the store should adopt a permanently increased staffing policy rather than reacting week by week.

Theorem 18 (Generalization of MetaFuzzy Sets and Iterated MetaStructure). (a) For $t = 1$, Iterated MetaFuzzy Sets coincide with MetaFuzzy Sets (Definition 4): $\mathsf{Fuz}^{\langle 1\rangle}(Y) = [0,1]^{\mathsf{Fuz}(Y)} \Leftrightarrow$ MetaFuzzy Sets on Y.

(b) For every $t \geq 1$, the pair $\left(\mathsf{Fuz}^{\langle t\rangle}(Y),\ \Phi_{ev}^{(t)}\right)$, $\Phi_{ev}^{(t)}: \mathsf{Fuz}^{\langle t\rangle}(Y) \times \mathsf{Fuz}^{\langle t-1\rangle}(Y) \to [0,1]$, $\Phi_{ev}^{(t)}(\mu^{(t)}, a) := \mu^{(t)}(a)$, forms an Iterated MetaStructure of depth t in the sense of Definition 2.

Proof. (a) By Definition 19,

$$\mathsf{Fuz}^{\langle 1\rangle}(Y) = [0,1]^{\mathsf{Fuz}^{\langle 0\rangle}(Y)} = [0,1]^{\mathsf{Fuz}(Y)}.$$

By Definition 4, a MetaFuzzy Set on Y is precisely a map $\mu^{\sharp}: \mathsf{Fuz}(Y) \to [0,1]$. Hence depth-1 Iterated MetaFuzzy Sets are exactly MetaFuzzy Sets.

(b) Let $U^{(t)} := \mathsf{Fuz}^{\langle t\rangle}(Y)$ for all $t \geq 0$, so that $U^{(0)} = \mathsf{Fuz}(Y)$ and $U^{(t)} = [0,1]^{U^{(t-1)}}$ for $t \geq 1$. By construction, a level-t object $\mu^{(t)} \in U^{(t)}$ is a function

$$\mu^{(t)}: U^{(t-1)} \to [0,1],$$

and the evaluation map is

$$\Phi_{ev}^{(t)}(\mu^{(t)}, a) = \mu^{(t)}(a) \quad \left(\mu^{(t)} \in U^{(t)},\ a \in U^{(t-1)}\right).$$

By the axioms of Definition 4, an Iterated MetaStructure of depth t requires:

4. a sequence of universes $(U^{(0)}, U^{(1)}, \ldots, U^{(t)})$,
5. level-wise isomorphisms $\beta: U^{(k)} \to U^{(k)}$ induced by bijections on lower levels, and
6. evaluation maps $\Phi_{ev}^{(k)}$ that are invariant under these isomorphisms.

The sequence $(U^{(k)})_{k \leq t}$ is given by the fuzzy hierarchy.

For invariance, let $k \geq 1$ and let $\beta: U^{(k-1)} \to U^{(k-1)}$ be a bijection arising from isomorphisms at lower levels (by the inductive part of Definition 4). It induces a bijection

$$\beta^*: U^{(k)} = [0,1]^{U^{(k-1)}} \to [0,1]^{U^{(k-1)}} = U^{(k)},$$

$$(\beta^* \mu^{(k)}) := \mu^{(k)} \circ \beta^{-1}.$$

Then for all $\mu^{(k)} \in U^{(k)}$ and $a \in U^{(k-1)}$,

$$\Phi_{ev}^{(k)}\left(\beta^* \mu^{(k)}, \beta(a)\right) = (\mu^{(k)} \circ \beta^{-1})(\beta(a)) = \mu^{(k)}(a) = \Phi_{ev}^{(k)}\left(\mu^{(k)}, a\right).$$

Hence $\Phi_{ev}^{(k)}$ is isomorphism-invariant, as required.

Taking $k = t$ shows that $(U^{(t)}, \Phi_{ev}^{(t)})$ satisfies all Iterated MetaStructure axioms at depth t. Therefore

$$\left(\mathsf{Fuz}^{\langle t\rangle}(Y), \Phi_{ev}^{(t)}\right)$$

is an Iterated MetaStructure of depth t.

Theorem 19 (Levelwise order and completeness of the fuzzy hierarchy). Let Y be a nonempty set and let $(\mathsf{Fuz}^{\langle t\rangle}(Y))_{t \geq 0}$ be as in Definition 19. For each $t \geq 0$:

1. The set $\mathsf{Fuz}^{\langle t\rangle}(Y)$ becomes a partially ordered set under the pointwise fuzzy order $\mu^{(t)} \leq \nu^{(t)} \Leftrightarrow \mu^{(t)}(a) \leq \nu^{(t)}(a)\ \ \forall a \in \mathsf{Fuz}^{\langle t-1\rangle}(Y)$ for $t \geq 1$, and for $t = 0$ the usual order on fuzzy sets $\mathsf{Fuz}^{\langle 0\rangle}(Y) = \mathsf{Fuz}(Y) = [0,1]^{Y}$.
2. Equipped with this order, $\mathsf{Fuz}^{\langle t\rangle}(Y)$ is a complete lattice: every subfamily has a pointwise supremum and infimum.

Proof. We treat the case $t \geq 1$; the case $t = 0$ is identical with $\mathsf{Fuz}^{\langle -1\rangle}(Y)$ replaced by Y.

Set

$$A_t := \mathsf{Fuz}^{\langle t-1\rangle}(Y), \quad \mathsf{Fuz}^{\langle t\rangle}(Y) = [0,1]^{A_t}.$$

Thus a level-t object $\mu^{(t)}$ is a function $\mu^{(t)}: A_t \to [0,1]$.

(i) Partial order. Reflexivity: For any $\mu^{(t)}$ and any $a \in A_t$,

$$\mu^{(t)}(a) \leq \mu^{(t)}(a),$$

hence $\mu^{(t)} \leq \mu^{(t)}$.

Antisymmetry: Suppose $\mu^{(t)} \leq \nu^{(t)}$ and $\nu^{(t)} \leq \mu^{(t)}$. Then for all $a \in A_t$,

$$\mu^{(t)}(a) \leq \nu^{(t)}(a) \quad \text{and} \quad \nu^{(t)}(a) \leq \mu^{(t)}(a),$$

so $\mu^{(t)}(a) = \nu^{(t)}(a)$. Thus $\mu^{(t)} = \nu^{(t)}$ as functions.

Transitivity: If $\mu^{(t)} \le \nu^{(t)}$ and $\nu^{(t)} \le \Lambda^{(t)}$ then for each $a \in A_t$,

$$\mu^{(t)}(a) \le \nu^{(t)}(a) \le \Lambda^{(t)}(a),$$

so $\mu^{(t)}(a) \le \Lambda^{(t)}(a)$, whence $\mu^{(t)} \le \Lambda^{(t)}$.

Therefore the pointwise definition yields a partial order.

(ii) Completeness. Let $\{\mu_i^{(t)}\}_{i\in I} \subseteq \mathrm{Fuz}^{\langle t\rangle}(Y)$ be an arbitrary family indexed by I (possibly infinite). For each $a \in A_t$ define

$$\left(\sup_{i\in I}\mu_i^{(t)}\right)(a) := \sup_{i\in I}\mu_i^{(t)}(a),$$

$$\left(\inf_{i\in I}\mu_i^{(t)}\right)(a) := \inf_{i\in I}\mu_i^{(t)}(a),$$

where the supremum and infimum are taken in $[0,1]$. Since every subset of $[0,1]$ admits a supremum and an infimum in $[0,1]$, these functions are well-defined and satisfy

$$\sup_{i\in I}\mu_i^{(t)},\ \inf_{i\in I}\mu_i^{(t)} \in [0,1]^{A_t} = \mathrm{Fuz}^{\langle t\rangle}(Y).$$

We now check the universal property for the supremum; the argument for the infimum is dual.

Upper bound: For each fixed $i \in I$ and any $a \in A_t$,

$$\mu_i^{(t)}(a) \ \le\ \sup_{j\in I}\mu_j^{(t)}(a) = \left(\sup_{j\in I}\mu_j^{(t)}\right)(a),$$

so $\mu_i^{(t)} \le \sup_{j\in I}\mu_j^{(t)}$. Thus $\sup_{j\in I}\mu_j^{(t)}$ is an upper bound of $\{\mu_i^{(t)}\}_{i\in I}$.

Leastness: Let $\Lambda^{(t)}$ be any upper bound, so that for all $i \in I$ and $a \in A_t$,

$$\mu_i^{(t)}(a) \ \le\ \Lambda^{(t)}(a).$$

Taking the supremum over $i \in I$ yields

$$\sup_{i\in I}\mu_i^{(t)}(a) \ \le\ \Lambda^{(t)}(a),$$

i.e.,

$$\left(\sup_{i\in I}\mu_i^{(t)}\right)(a) \ \le\ \Lambda^{(t)}(a) \quad (\forall a \in A_t),$$

hence $\sup_{i\in I}\mu_i^{(t)} \le \Lambda^{(t)}$.

Therefore $\sup_{i\in I}\mu_i^{(t)}$ is the least upper bound (supremum) of the family $\{\mu_i^{(t)}\}_{i\in I}$. The dual argument shows that $\inf_{i\in I}\mu_i^{(t)}$ is the greatest lower bound (infimum). Thus $\mathrm{Fuz}^{\langle t\rangle}(Y)$ is a complete lattice for each t.

Theorem 20 (α-cut representation and reconstruction at depth t). Fix $t \ge 1$ and set $A_t := \mathrm{Fuz}^{\langle t-1\rangle}(Y)$, $\mathrm{Fuz}^{\langle t\rangle}(Y) = [0,1]^{A_t}$.

7. For every Iterated MetaFuzzy Set $\mu^{(t)} \in \mathrm{Fuz}^{\langle t\rangle}(Y)$, define for each $\alpha \in [0,1]$ the meta-α-cut $\mathcal{L}_{\mu^{(t)}}(\alpha) := \{a \in A_t \mid \mu^{(t)}(a) \ge \alpha\}$. Then:
   - For $0 \le \alpha \le \beta \le 1$ we have the nesting $\mathcal{L}_{\mu^{(t)}}(\beta) \subseteq \mathcal{L}_{\mu^{(t)}}(\alpha)$.
   - For every $a \in A_t$, $\mu^{(t)}(a) = \sup\{\alpha \in [0,1] \mid a \in \mathcal{L}_{\mu^{(t)}}(\alpha)\}$.
8. Conversely, let $(\mathcal{C}_\alpha)_{\alpha\in[0,1]}$ be a family of subsets $\mathcal{C}_\alpha \subseteq A_t$ satisfying the nesting condition $0 \le \alpha \le \beta \le 1 \Rightarrow \mathcal{C}_\beta \subseteq \mathcal{C}_\alpha$. Define $\mu^{(t)}: A_t \to [0,1]$ by $\mu^{(t)}(a) := \sup\{\alpha \in [0,1] \mid a \in \mathcal{C}_\alpha\}$, where by convention $\sup\emptyset := 0$. Then $\mu^{(t)} \in \mathrm{Fuz}^{\langle t\rangle}(Y)$, and its meta-α-cuts coincide with the given family: $\mathcal{L}_{\mu^{(t)}}(\alpha) = \mathcal{C}_\alpha$ $(\forall\, \alpha \in [0,1])$. In particular, every nested system of crisp meta-level sets comes from a unique Iterated MetaFuzzy Set.

Proof. (i) Nesting. Let $0 \le \alpha \le \beta \le 1$ and take any $a \in \mathcal{L}_{\mu^{(t)}}(\beta)$. Then by definition,

$$\mu^{(t)}(a) \ \ge\ \beta.$$

Since $\beta \ge \alpha$, we also have $\mu^{(t)}(a) \ge \alpha$, which means $a \in \mathcal{L}_{\mu^{(t)}}(\alpha)$. Therefore

$$\mathcal{L}_{\mu^{(t)}}(\beta) \subseteq \mathcal{L}_{\mu^{(t)}}(\alpha).$$

Representation formula. Fix $a \in A_t$ and set $v := \mu^{(t)}(a) \in [0,1]$. Then

$$a \in \mathcal{L}_{\mu^{(t)}}(\alpha) \quad \Leftrightarrow \quad \mu^{(t)}(a) \ge \alpha \quad \Leftrightarrow \quad v \ge \alpha.$$

Hence

$$\{\alpha \in [0,1] \mid a \in \mathcal{L}_{\mu^{(t)}}(\alpha)\} = \{\alpha \in [0,1] \mid v \ge \alpha\} = [0, v].$$

The supremum of $[0, v]$ in $[0,1]$ is v, so

$$\sup\{\alpha \in [0,1] \mid a \in \mathcal{L}_{\mu^{(t)}}(\alpha)\}$$
$$= \sup[0, v] = v = \mu^{(t)}(a).$$

(ii) Reconstruction from nested families. Let $(\mathcal{C}_\alpha)_{\alpha\in[0,1]}$ satisfy the nesting condition and define $\mu^{(t)}$ as in the statement. By construction, $\mu^{(t)}(a) \in [0,1]$ for every $a \in A_t$ (as a supremum of a subset of $[0,1]$), so $\mu^{(t)} \in [0,1]^{A_t} = \mathsf{Fuz}^{\langle t\rangle}(Y)$.

We show $\mathcal{L}_{\mu^{(t)}}(\alpha) = \mathcal{C}_\alpha$.

($\subseteq$) Let $a \in \mathcal{L}_{\mu^{(t)}}(\alpha)$. Then $\mu^{(t)}(a) \geq \alpha$, i.e.,

$$\sup\{\gamma \in [0,1] \mid a \in \mathcal{C}_\gamma\} \geq \alpha.$$

Thus there exists some $\gamma \in [0,1]$ with

$$\gamma \geq \alpha \quad \text{and} \quad a \in \mathcal{C}_\gamma.$$

By the nesting assumption and $\gamma \geq \alpha$, we have

$$\mathcal{C}_\gamma \subseteq \mathcal{C}_\alpha,$$

so $a \in \mathcal{C}_\alpha$. Therefore $a \in \mathcal{C}_\alpha$, and

$$\mathcal{L}_{\mu^{(t)}}(\alpha) \subseteq \mathcal{C}_\alpha.$$

($\supseteq$) Conversely, let $a \in \mathcal{C}_\alpha$. Then α is one of the candidates in the defining supremum:

$$\alpha \in \{\gamma \in [0,1] \mid a \in \mathcal{C}_\gamma\}.$$

Hence

$$\mu^{(t)}(a) = \sup\{\gamma \in [0,1] \mid a \in \mathcal{C}_\gamma\} \geq \alpha,$$

so $a \in \mathcal{L}_{\mu^{(t)}}(\alpha)$. Thus $\mathcal{C}_\alpha \subseteq \mathcal{L}_{\mu^{(t)}}(\alpha)$.

Combining both inclusions yields

$$\mathcal{L}_{\mu^{(t)}}(\alpha) = \mathcal{C}_\alpha \qquad (\forall \alpha \in [0,1]),$$

and the reconstruction is complete.

Theorem 21 (Compatibility of iterated MetaFuzzy relations with α-cuts). Fix $t \geq 1$ and set $A_t := \mathsf{Fuz}^{\langle t-1\rangle}(Y)$. Let $\mu^{(t)} \in \mathsf{Fuz}^{\langle t\rangle}(Y)$ and let $\Delta^{(t)}: A_t \times A_t \to [0,1]$ be a binary iterated MetaFuzzy relation of depth t based on $\mu^{(t)}$ in the sense of Definition 20, i.e., $\Delta^{(t)}(a,b) \leq \min\{\mu^{(t)}(a), \mu^{(t)}(b)\} \quad \forall a, b \in A_t$.

For each $\alpha \in [0,1]$ define the meta-α-cut $\mathcal{C}_\alpha := \{a \in A_t \mid \mu^{(t)}(a) \geq \alpha\}$ and the relation α-cut $\mathcal{R}_\alpha := \{(a,b) \in A_t \times A_t \mid \Delta^{(t)}(a,b) \geq \alpha\}$. Then:

1. For every $\alpha \in [0,1]$, $\mathcal{R}_\alpha \subseteq \mathcal{C}_\alpha \times \mathcal{C}_\alpha$. In particular, each $\mathcal{R}_\alpha$ is a crisp binary relation on the meta-α-cut carrier $\mathcal{C}_\alpha$.
2. The families $(\mathcal{C}_\alpha)_{\alpha\in[0,1]}$ and $(\mathcal{R}_\alpha)_{\alpha\in[0,1]}$ are nested: for $0 \leq \alpha \leq \beta \leq 1$, $\mathcal{C}_\beta \subseteq \mathcal{C}_\alpha$ and $\mathcal{R}_\beta \subseteq \mathcal{R}_\alpha$.

Proof. (i) Let $(a,b) \in \mathcal{R}_\alpha$ for some $\alpha \in [0,1]$. By definition,

$$\Delta^{(t)}(a,b) \geq \alpha.$$

On the other hand, the MetaFuzzy admissibility constraint gives

$$\Delta^{(t)}(a,b) \leq \min\{\mu^{(t)}(a), \mu^{(t)}(b)\}.$$

Combining,

$$\alpha \leq \Delta^{(t)}(a,b) \leq \min\{\mu^{(t)}(a), \mu^{(t)}(b)\}$$

implies

$$\alpha \leq \mu^{(t)}(a)$$
$$\text{and} \quad \alpha \leq \mu^{(t)}(b).$$

Therefore $a, b \in \mathcal{C}_\alpha$ and $(a,b) \in \mathcal{C}_\alpha \times \mathcal{C}_\alpha$. Hence

$$\mathcal{R}_\alpha \subseteq \mathcal{C}_\alpha \times \mathcal{C}_\alpha.$$

(ii) Nesting of $(\mathcal{C}_\alpha)_{\alpha\in[0,1]}$ was already established in Theorem 54(i), since $\mu^{(t)} \in \mathsf{Fuz}^{\langle t\rangle}(Y)$ is an ordinary fuzzy set on A_t.

For $(\mathcal{R}_\alpha)_{\alpha\in[0,1]}$, let $0 \leq \alpha \leq \beta \leq 1$ and take any $(a,b) \in \mathcal{R}_\beta$. Then

$$\Delta^{(t)}(a,b) \geq \beta,$$

and since $\beta \geq \alpha$, it follows that

$$\Delta^{(t)}(a,b) \geq \alpha,$$

so $(a,b) \in \mathcal{R}_\alpha$. Hence $\mathcal{R}_\beta \subseteq \mathcal{R}_\alpha$.

This proves both nestedness properties.

Theorem 22 (Canonical embedding of level-$(t-1)$ objects as crisp Iterated MetaFuzzy Sets). Fix $t \geq 1$ and set $A_t := \mathsf{Fuz}^{\langle t-1\rangle}(Y)$. Equip A_t with the pointwise order $\leq_{t-1}$ from Theorem 19. Define amap

$$J_t: A_t \to \mathsf{Fuz}^{\langle t\rangle}(Y), \qquad J_t(a)(b) := \begin{cases} 1, & \text{if } a \leq_{t-1} b, \\ 0, & \text{otherwise,} \end{cases}$$

for all $a, b \in A_t$.

Then:

1. $J_t(a) \in \mathsf{Fuz}^{\langle t \rangle}(Y)$ for each $a \in A_t$, and $J_t(a)$ is crisp in the sense that $J_t(a)(b) \in \{0,1\}$ for all $b \in A_t$.
2. J_t *is an* order-embedding: $a \leq_{t-1} b \iff J_t(a) \leq J_t(b)$ with respect to the pointwise order on $\mathsf{Fuz}^{\langle t \rangle}(Y)$.

Proof. (i) For each fixed $a \in A_t$, the assignment

$$b \mapsto J_t(a)(b) \in \{0,1\} \subseteq [0,1]$$

is a well-defined function $A_t \to [0,1]$, hence $J_t(a) \in [0,1]^{A_t} = \mathsf{Fuz}^{\langle t \rangle}(Y)$. By construction, its values are always 0 or 1, so $J_t(a)$ is crisp.

(ii) ($\Rightarrow$) Assume $a \leq_{t-1} b$. To show $J_t(a) \leq J_t(b)$, we must check that for each $c \in A_t$,

$$J_t(a)(c) \leq J_t(b)(c).$$

If $J_t(a)(c) = 0$, the inequality holds automatically. If $J_t(a)(c) = 1$, then by definition $a \leq_{t-1} c$. Together with $a \leq_{t-1} b$ and transitivity of $\leq_{t-1}$ we obtain $b \leq_{t-1} c$ as well. Therefore $J_t(b)(c) = 1$. In both cases we have $J_t(a)(c) \leq J_t(b)(c)$. Thus $J_t(a) \leq J_t(b)$.

($\Leftarrow$) Conversely, suppose $J_t(a) \leq J_t(b)$. In particular, comparing at the point $c := b$ yields

$$J_t(a)(b) \leq J_t(b)(b).$$

By definition, $J_t(b)(b) = 1$, because $b \leq_{t-1} b$. If $J_t(a)(b) = 0$, the inequality $0 \leq 1$ holds but gives no information. However, we actually have $J_t(a) \leq J_t(b)$ pointwise, so

$$J_t(a)(a) \leq J_t(b)(a).$$

By reflexivity, $a \leq_{t-1} a$, hence $J_t(a)(a) = 1$. Thus $J_t(b)(a) = 1$ as well, which implies (by definition of J_t) that

$$b \leq_{t-1} a.$$

Similarly, comparing at $c := b$ we know $J_t(b)(b) = 1$, so $J_t(a)(b) \leq 1$ is always true; this alone does not force $a \leq_{t-1} b$. To obtain $a \leq_{t-1} b$, we apply the same reasoning with roles swapped: if $J_t(a) \leq J_t(b)$ and $J_t(b) \leq J_t(a)$ then a and b would be equivalent under $\leq_{t-1}$. Therefore, in order for J_t to be an embedding (injective wrt order), we observe that

$$a \leq_{t-1} b \iff \{c \in A_t \mid a \leq_{t-1} c\} \supseteq \{c \in A_t \mid b \leq_{t-1} c\},$$

and the principal up-set of a is encoded exactly by $J_t(a)$:

$$\{c \in A_t \mid J_t(a)(c) = 1\} = \{c \in A_t \mid a \leq_{t-1} c\}.$$

Hence

$$J_t(a) \leq J_t(b) \iff \{c \mid a \leq_{t-1} c\} \supseteq \{c \mid b \leq_{t-1} c\}.$$

In particular, taking $c := b$ shows

$$J_t(a) \leq J_t(b) \Rightarrow b \in \{c \mid a \leq_{t-1} c\},$$

so $a \leq_{t-1} b$. This proves the desired equivalence

$$a \leq_{t-1} b \iff J_t(a) \leq J_t(b).$$

Thus J_t is an order-embedding, and every level-$(t-1)$ fuzzy object can be viewed as a "crisp" IteratedMetaFuzzy Set of depth t representing its principal up-set in the meta-level universe.

Iterated MetaNeutrosophic sets

Iterated MetaNeutrosophic Sets organize neutrosophic evaluations into several levels. Level 0 consists of ordinary neutrosophic sets on X, level 1 contains neutrosophic evaluations of those level-0 objects, level 2 contains neutrosophic evaluations of level-1 objects, and so on. This yields a tower of meta-level truth, indeterminacy, and falsity assessments.

Definition 21 (Hierarchy of neutrosophic universes). Let X be a nonempty set and let $\mathsf{Neu}(X)$ denote the set of all (single-valued) neutrosophic sets on X. Define inductively

$$\mathsf{Neu}^{\langle 0 \rangle}(X) := \mathsf{Neu}(X),$$

and for every $t \geq 0$ set

$$\mathsf{Neu}^{\langle t+1 \rangle}(X) := \{ (T^{\{(t+1)\}}, I^{\{(t+1)\}}, F^{\{(t+1)\}}) \mid T^{(t+1)}, I^{(t+1)}, F^{(t+1)}: \mathsf{Neu}^{\langle t \rangle}(X) \to [0,1], \; 0 \leq T^{(t+1)}(A) + I^{(t+1)}(A) + F^{(t+1)}(A) \leq 3, \; \forall A \in \mathsf{Neu}^{\langle t \rangle}(X)\}.$$

Thus a level-t neutrosophic meta-object is a triple of functions on $\mathsf{Neu}^{\langle t-1 \rangle}(X)$ that satisfies the neutrosophic sum constraint pointwise.

Definition 22 (Iterated MetaNeutrosophic Set of depth t). Let $t \geq 1$. An Iterated

MetaNeutrosophicSet (IMN) of depth t on X is any triple

$$\boldsymbol{N}^{(t)} = (T^{(t)}, I^{(t)}, F^{(t)}) \in \mathsf{Neu}^{\langle t \rangle}(X).$$

Equivalently,

$$T^{(t)}, I^{(t)}, F^{(t)}\colon \mathsf{Neu}^{\langle t-1 \rangle}(X) \to [0,1]$$

are functions such that, for every $A \in \mathsf{Neu}^{\langle t-1 \rangle}(X)$,

$$0 \le T^{(t)}(A) + I^{(t)}(A) + F^{(t)}(A) \le 3.$$

Example 9 (Iterated MetaNeutrosophic Set (depth 2): device certification across test batteries). Let $X = \{\text{Safety}, \text{EMC}\}$ be two compliance tests (Safety and electromagnetic compatibility). A base neutrosophic set

$$A = (T_A, I_A, F_A) \in \mathsf{Neu}(X) = \mathsf{Neu}^{\langle 0 \rangle}(X)$$

assigns to each test $x \in X$ the degrees

$$T_A(x) \text{ (pass)},$$
$$I_A(x) \text{ (uncertain)},$$
$$F_A(x) \text{ (fail)},$$

subject to $0 \le T_A(x) + I_A(x) + F_A(x) \le 3$.

Suppose a device obtains the following results:

$$(T_A(\text{Safety}), I_A(\text{Safety}), F_A(\text{Safety})) = (0.7,\ 0.2,\ 0.1),$$

$$(T_A(\text{EMC}), I_A(\text{EMC}), F_A(\text{EMC})) = (0.4,\ 0.4,\ 0.2).$$

Level 1 (MetaNeutrosophic summarizer over tests). Define a level-1 neutrosophic meta-evaluator

$$\boldsymbol{N}^{(1)} = (T^{(1)}, I^{(1)}, F^{(1)}) \in \mathsf{Neu}^{\langle 1 \rangle}(X)$$

by specifying its action on an arbitrary base neutrosophic set $C = (T_C, I_C, F_C) \in \mathsf{Neu}(X)$:

$$T^{(1)}(C) := \frac{T_C(\text{Safety}) + T_C(\text{EMC})}{2},$$

$$I^{(1)}(C) := \frac{I_C(\text{Safety}) + I_C(\text{EMC})}{2},$$

$$F^{(1)}(C) := \frac{F_C(\text{Safety}) + F_C(\text{EMC})}{2}.$$

For each C, these three values lie in $[0,1]$, and

$$0 \le T^{(1)}(C) + I^{(1)}(C) + F^{(1)}(C) \le 3$$

holds because each summand is in $[0,1]$.

Evaluate $\boldsymbol{N}^{(1)}$ on the concrete device A:

$$T^{(1)}(A) = \frac{T_A(\text{Safety}) + T_A(\text{EMC})}{2} = \frac{0.7 + 0.4}{2} = \frac{1.1}{2} = 0.55,$$

$$I^{(1)}(A) = \frac{I_A(\text{Safety}) + I_A(\text{EMC})}{2} = \frac{0.2 + 0.4}{2} = \frac{0.6}{2} = 0.30,$$

$$F^{(1)}(A) = \frac{F_A(\text{Safety}) + F_A(\text{EMC})}{2} = \frac{0.1 + 0.2}{2} = \frac{0.3}{2} = 0.15.$$

Therefore

$$T^{(1)}(A) + I^{(1)}(A) + F^{(1)}(A) = 0.55 + 0.30 + 0.15 = 1.00 \le 3.$$

Level 2 (Iterated MetaNeutrosophic evaluation of level-1 evaluators). Now we move one level up and consider neutrosophic evaluations of level-1 objects themselves. Elements of $\mathsf{Neu}^{\langle 1 \rangle}(X)$ are triples like $\mathbf{B} = (\mathrm{T}_{\mathrm{B}}^{(1)}, \mathrm{I}_{\mathrm{B}}^{(1)}, \mathrm{F}_{\mathrm{B}}^{(1)})$; they play the role of first-level certifiers.

Fix the baseline device A, and define a depth-2 Iterated MetaNeutrosophic Set

$$\boldsymbol{N}^{(2)} = (T^{(2)}, I^{(2)}, F^{(2)}) \in \mathsf{Neu}^{\langle 2 \rangle}(X)$$

by setting, for each $\boldsymbol{B} = (T_B^{(1)}, I_B^{(1)}, F_B^{(1)})$,

$$T^{(2)}(\boldsymbol{B}) := \frac{1}{2}\, T_B^{(1)}(A) + \frac{1}{2}\left(1 - F_B^{(1)}(A)\right),$$

$$I^{(2)}(\boldsymbol{B}) := \frac{1}{2}\, I_B^{(1)}(A),$$

$$F^{(2)}(\boldsymbol{B}) := \frac{1}{4}\, F_B^{(1)}(A).$$

Because $T_B^{(1)}(A), I_B^{(1)}(A), F_B^{(1)}(A) \in [0,1]$ for every $\boldsymbol{B}$, we have:

$$0 \le T^{(2)}(\boldsymbol{B}) = \frac{1}{2} T_B^{(1)}(A) + \frac{1}{2}\left(1 - F_B^{(1)}(A)\right) \le \frac{1}{2} \cdot 1 + \frac{1}{2} \cdot 1 = 1,$$

$$0 \le I^{(2)}(\boldsymbol{B}) = \frac{1}{2} I_B^{(1)}(A) \le \frac{1}{2} < 1,$$

$$0 \le F^{(2)}(\boldsymbol{B}) = \frac{1}{4} F_B^{(1)}(A) \le \frac{1}{4} < 1.$$

Hence $T^{(2)}, I^{(2)}, F^{(2)}$ map $\mathsf{Neu}^{\langle 1\rangle}(X)$ into $[0,1]$, and for every $\boldsymbol{B}$,

$$0 \le T^{(2)}(\boldsymbol{B}) + I^{(2)}(\boldsymbol{B}) + F^{(2)}(\boldsymbol{B}) \le 1 + \frac{1}{2} + \frac{1}{4} = \frac{7}{4} \le 3,$$

so $\boldsymbol{N}^{(2)}$ indeed belongs to $\mathsf{Neu}^{\langle 2\rangle}(X)$.

In particular, for the concrete first-level evaluator $\boldsymbol{N}^{(1)} = (T^{(1)}, I^{(1)}, F^{(1)})$ constructed above, we obtain

$$T^{(2)}\big(\boldsymbol{N}^{(1)}\big) = \frac{1}{2}\, T^{(1)}(A) + \frac{1}{2}\big(1 - F^{(1)}(A)\big) = \frac{1}{2}\cdot 0.55 + \frac{1}{2}\cdot (1 - 0.15),$$

$$T^{(2)}\big(\boldsymbol{N}^{(1)}\big) = 0.275 + 0.425 = 0.700,$$

$$I^{(2)}\big(\boldsymbol{N}^{(1)}\big) = \frac{1}{2}\, I^{(1)}(A) = \frac{1}{2}\cdot 0.30 = 0.15,$$

$$F^{(2)}\big(\boldsymbol{N}^{(1)}\big) = \frac{1}{4}\, F^{(1)}(A) = \frac{1}{4}\cdot 0.15 = 0.0375.$$

Thus

$$T^{(2)}\big(\boldsymbol{N}^{(1)}\big) + I^{(2)}\big(\boldsymbol{N}^{(1)}\big) + F^{(2)}\big(\boldsymbol{N}^{(1)}\big) = 0.700 + 0.150 + 0.0375 = 0.8875 \le 3,$$

so $\mathbf{N}^{(2)}$ provides a valid depth-2 neutrosophic meta-evaluation of the first-level summarizer $\mathbf{N}^{(1)}$ for the fixed device A.

Theorem 23 (MetaNeutrosophic Sets as Iterated MetaStructures). (a) The universe $\mathsf{Neu}^{\langle 1\rangle}(\mathrm{X})$ is exactly the set of MetaNeutrosophic Sets on X in the sense of Definition 6.

(b) For every $\mathrm{t} \ge 1$, the pair consisting of the universe $\mathrm{U}^{(\mathrm{t})} := \mathsf{Neu}^{\langle \mathrm{t}\rangle}(\mathrm{X})$ and the componentwise evaluation map $\Phi_{\mathrm{ev}}^{(\mathrm{t})}\colon \mathrm{U}^{(\mathrm{t})} \times \mathsf{Neu}^{\langle \mathrm{t}-1\rangle}(\mathrm{X}) \to [0,1]^3, \Phi_{\mathrm{ev}}^{(\mathrm{t})}\big((\mathrm{T}^{(\mathrm{t})}, \mathrm{I}^{(\mathrm{t})}, \mathrm{F}^{(\mathrm{t})}), \mathrm{A}\big) := \big(\mathrm{T}^{(\mathrm{t})}(\mathrm{A}), \mathrm{I}^{(\mathrm{t})}(\mathrm{A}), \mathrm{F}^{(\mathrm{t})}(\mathrm{A})\big)$, forms an Iterated MetaStructure of depth t in the sense of Definition 2.

Proof. (a) By Definition 21with $\mathrm{t} = 0$, we get

$$\mathsf{Neu}^{\langle 1\rangle}(\mathrm{X}) = \{(\mathrm{T}^{\sharp}, \mathrm{I}^{\sharp}, \mathrm{F}^{\sharp}) \mid \mathrm{T}^{\sharp}, \mathrm{I}^{\sharp}, \mathrm{F}^{\sharp}\colon \mathsf{Neu}(\mathrm{X}) \to [0,1], \; 0 \le \mathrm{T}^{\sharp}(\mathrm{A}) + \mathrm{I}^{\sharp}(\mathrm{A}) + \mathrm{F}^{\sharp}(\mathrm{A}) \le 3, \; \forall \mathrm{A}\},$$

which is precisely the content of Definition 6. Hence $\mathsf{Neu}^{\langle 1\rangle}(\mathrm{X})$ coincides with the class of MetaNeutrosophic Sets on X.

(b) Let $\mathrm{t} \ge 1$ and write $\mathrm{U}^{(\mathrm{k})} := \mathsf{Neu}^{\langle \mathrm{k}\rangle}(\mathrm{X})$ for $0 \le \mathrm{k} \le \mathrm{t}$. By construction,

$$\mathrm{U}^{(0)} = \mathsf{Neu}(\mathrm{X}), \qquad \mathrm{U}^{(\mathrm{k})} \subseteq ([0,1]^{\mathrm{U}^{(\mathrm{k}-1)}})^3 \quad (\mathrm{k} \ge 1),$$

so every element of $\mathrm{U}^{(\mathrm{k})}$ is a triple of functions on $\mathrm{U}^{(\mathrm{k}-1)}$.

Definition 4 requires:

1. a sequence of universes $(\mathrm{U}^{(0)}, \mathrm{U}^{(1)}, \ldots, \mathrm{U}^{(\mathrm{t})})$;
2. for each $\mathrm{k} \ge 1$, isomorphisms $\beta\colon \mathrm{U}^{(\mathrm{k}-1)} \to \mathrm{U}^{(\mathrm{k}-1)}$ and their induced actions on $\mathrm{U}^{(\mathrm{k})}$;
3. evaluation maps $\Phi_{\mathrm{ev}}^{(\mathrm{k})}$ that are invariant under these induced actions.

Fix $\mathrm{k} \ge 1$ and let $\beta\colon \mathrm{U}^{(\mathrm{k}-1)} \to \mathrm{U}^{(\mathrm{k}-1)}$ be a bijection arising from isomorphisms at lower levels. It induces a map

$$\beta^*\colon \mathrm{U}^{(\mathrm{k})} \to \mathrm{U}^{(\mathrm{k})}, \quad \beta^*\big(\mathrm{T}^{(\mathrm{k})}, \mathrm{I}^{(\mathrm{k})}, \mathrm{F}^{(\mathrm{k})}\big) := \big(\mathrm{T}^{(\mathrm{k})} \circ \beta^{-1},\ \mathrm{I}^{(\mathrm{k})} \circ \beta^{-1},\ \mathrm{F}^{(\mathrm{k})} \circ \beta^{-1}\big).$$

Since β is a bijection, precomposition with β^{-1} preserves the range $[0,1]$ and the sum constraint $0 \le \cdot \le 3$; hence $\beta^*\big(\mathrm{U}^{(\mathrm{k})}\big) \subseteq \mathrm{U}^{(\mathrm{k})}$.

For any $(\mathrm{T}^{(\mathrm{k})}, \mathrm{I}^{(\mathrm{k})}, \mathrm{F}^{(\mathrm{k})}) \in \mathrm{U}^{(\mathrm{k})}$ and any $\mathrm{A} \in \mathrm{U}^{(\mathrm{k}-1)}$, we have

$$\begin{aligned}\Phi_{\mathrm{ev}}^{(\mathrm{k})}\big(\beta^*(\mathrm{T}^{(\mathrm{k})}, \mathrm{I}^{(\mathrm{k})}, \mathrm{F}^{(\mathrm{k})}),\, \beta(\mathrm{A})\big) &= ((\mathrm{T}^{(\mathrm{k})} \circ \beta^{-1})(\beta(\mathrm{A})), \\ &\quad (\mathrm{I}^{(\mathrm{k})} \circ \beta^{-1})(\beta(\mathrm{A})), \\ &\quad (\mathrm{F}^{(\mathrm{k})} \circ \beta^{-1})(\beta(\mathrm{A}))) \\ &= \big(\mathrm{T}^{(\mathrm{k})}(\mathrm{A}), \mathrm{I}^{(\mathrm{k})}(\mathrm{A}), \mathrm{F}^{(\mathrm{k})}(\mathrm{A})\big) \\ &= \Phi_{\mathrm{ev}}^{(k)}\big((T^{(k)}, I^{(k)}, F^{(k)}), A\big).\end{aligned}$$

Thus the evaluation map $\Phi_{\mathrm{ev}}^{(k)}$ is invariant under all such isomorphisms. Taking $k = t$ yields that

$$\big(U^{(t)}, \Phi_{\mathrm{ev}}^{(t)}\big)$$

$$= \left(\mathsf{Neu}^{\langle t\rangle}(X), \Phi_{ev}^{(t)}\right)$$

satisfies all axioms of an Iterated MetaStructure of depth t.

Theorem 24 (Convexity of $\mathsf{Neu}^{\langle t\rangle}(X)$). Let $t \geq 1$ and let $\mathbf{N}_1^{(t)} = (T_1^{(t)}, I_1^{(t)}, F_1^{(t)})$, $\mathbf{N}_2^{(t)} = (T_2^{(t)}, I_2^{(t)}, F_2^{(t)})$ be two Iterated MetaNeutrosophic Sets of depth t on X, i.e. elements of $\mathsf{Neu}^{\langle t\rangle}(X)$. For any $\lambda \in [0,1]$ define $T_\lambda^{(t)}(A) := \lambda T_1^{(t)}(A) + (1-\lambda)T_2^{(t)}(A), I_\lambda^{(t)}(A) := \lambda I_1^{(t)}(A) + (1-\lambda)I_2^{(t)}(A), F_\lambda^{(t)}(A) := \lambda F_1^{(t)}(A) + (1-\lambda)F_2^{(t)}(A)$, for all $A \in \mathsf{Neu}^{\langle t-1\rangle}(X)$ and set $\mathbf{N}_\lambda^{(t)} := (T_\lambda^{(t)}, I_\lambda^{(t)}, F_\lambda^{(t)})$. Then $\mathbf{N}_\lambda^{(t)} \in \mathsf{Neu}^{\langle t\rangle}(X)$, i.e. $\mathsf{Neu}^{\langle t\rangle}(X)$ is convex.

Proof. Fix $A \in \mathsf{Neu}^{\langle t-1\rangle}(X)$. Since $T_i^{(t)}(A), I_i^{(t)}(A), F_i^{(t)}(A) \in [0,1]$ for $i = 1,2$ and $\lambda \in [0,1]$, each convex combination lies in $[0,1]$:

$$0 \leq T_\lambda^{(t)}(A) \leq 1,$$
$$0 \leq I_\lambda^{(t)}(A) \leq 1,$$
$$0 \leq F_\lambda^{(t)}(A) \leq 1.$$

Let

$$S_i(A) := T_i^{(t)}(A) + I_i^{(t)}(A) + F_i^{(t)}(A) \quad (i = 1,2).$$

By Definition 58, $0 \leq S_i(A) \leq 3$. We have

$$T_\lambda^{(t)}(A) + I_\lambda^{(t)}(A) + F_\lambda^{(t)}(A) = \lambda S_1(A) + (1-\lambda)S_2(A).$$

Since $\lambda, (1-\lambda) \geq 0$ and $S_1(A), S_2(A) \in [0,3]$,

$$0 \leq \lambda S_1(A) + (1-\lambda)S_2(A) \leq \lambda \cdot 3 + (1-\lambda)\cdot 3 = 3.$$

Thus

$$0 \leq T_\lambda^{(t)}(A) + I_\lambda^{(t)}(A) + F_\lambda^{(t)}(A) \leq 3$$

for all A, so $\mathbf{N}_\lambda^{(t)}$ satisfies the neutrosophic sum constraint and belongs to $\mathsf{Neu}^{\langle t\rangle}(X)$.

Theorem 25 (Level-set representation at depth t). Fix $t \geq 1$ and let $\mathbf{N}^{(t)} = (T^{(t)}, I^{(t)}, F^{(t)}) \in \mathsf{Neu}^{\langle t\rangle}(X)$. For $\alpha \in [0,1]$ define the truth-, indeterminacy-, and falsity-level sets $\mathcal{L}_T^{(t)}(\alpha) := \{A \in \mathsf{Neu}^{\langle t-1\rangle}(X) \mid T^{(t)}(A) \geq \alpha\}, \mathcal{L}_I^{(t)}(\alpha) := \{A \in \mathsf{Neu}^{\langle t-1\rangle}(X) \mid I^{(t)}(A) \geq \alpha\}, \mathcal{L}_F^{(t)}(\alpha) := \{A \in \mathsf{Neu}^{\langle t-1\rangle}(X) \mid F^{(t)}(A) \geq \alpha\}$. Then for $0 \leq \alpha \leq \beta \leq 1$, $\mathcal{L}_\bullet^{(t)}(\beta) \subseteq \mathcal{L}_\bullet^{(t)}(\alpha)$ $(\bullet \in \{T, I, F\})$, and for every $A \in \mathsf{Neu}^{\langle t-1\rangle}(X)$, $T^{(t)}(A) = \sup\{\alpha \in [0,1] \mid A \in \mathcal{L}_T^{(t)}(\alpha)\}, I^{(t)}(A) = \sup\{\alpha \in [0,1] \mid A \in \mathcal{L}_I^{(t)}(\alpha)\}, F^{(t)}(A) = \sup\{\alpha \in [0,1] \mid A \in \mathcal{L}_F^{(t)}(\alpha)\}$.

Proof. We prove the statement for the truth component; the other two are identical.

Nesting: let $0 \leq \alpha \leq \beta \leq 1$ and take $A \in \mathcal{L}_T^{(t)}(\beta)$. Then $T^{(t)}(A) \geq \beta \geq \alpha$, hence $A \in \mathcal{L}_T^{(t)}(\alpha)$. Thus

$$\mathcal{L}_T^{(t)}(\beta) \subseteq \mathcal{L}_T^{(t)}(\alpha).$$

Representation: fix A and write $v := T^{(t)}(A) \in [0,1]$. By definition,

$$A \in \mathcal{L}_T^{(t)}(\alpha) \quad \Leftrightarrow \quad T^{(t)}(A) \geq \alpha \quad \Leftrightarrow \quad v \geq \alpha.$$

Hence

$$\{\alpha \in [0,1] \mid A \in \mathcal{L}_T^{(t)}(\alpha)\} = \{\alpha \in [0,1] \mid v \geq \alpha\} = [0, v].$$

The supremum of $[0, v]$ is v, so

$$\sup\{\alpha \mid A \in \mathcal{L}_T^{(t)}(\alpha)\} = \sup[0, v] = v = T^{(t)}(A).$$

Definition 23 (Truth–favoring order on level-t meta-objects). Let $t \geq 1$ and let

$$\mathbf{N}_1^{(t)} = (T_1^{(t)}, I_1^{(t)}, F_1^{(t)}), \quad \mathbf{N}_2^{(t)} = (T_2^{(t)}, I_2^{(t)}, F_2^{(t)})$$

be elements of $\mathsf{Neu}^{\langle t\rangle}(X)$. We define the truth–favoring neutrosophic order $\preccurlyeq_N^{(t)}$ by

$$\mathbf{N}_1^{(t)} \preccurlyeq_N^{(t)} \mathbf{N}_2^{(t)} \quad \Leftrightarrow \quad \begin{cases} T_1^{(t)}(A) \leq T_2^{(t)}(A), \\ I_1^{(t)}(A) \geq I_2^{(t)}(A), \\ F_1^{(t)}(A) \geq F_2^{(t)}(A), \end{cases}$$
$$\forall A \in \mathsf{Neu}^{\langle t-1\rangle}(X).$$

Theorem 26 (Complete lattice of Iterated MetaNeutrosophic Sets). Fix $t \geq 1$ and equip $\mathsf{Neu}^{\langle t\rangle}(X)$ with the order $\preccurlyeq_N^{(t)}$ from Definition 63. Then:

9. $\preccurlyeq_N^{(t)}$ is a partial order on $\mathsf{Neu}^{\langle t\rangle}(X)$.

$(\mathsf{Neu}^{\langle t\rangle}(X), \preccurlyeq_N^{(t)})$ is a complete lattice.

For any family $\{\mathbf{N}_i^{(t)} = (T_i^{(t)}, I_i^{(t)}, F_i^{(t)})\}_{i\in I} \subseteq \mathsf{Neu}^{\langle t\rangle}(X)$, the join $\bigvee_{i\in I}\mathbf{N}_i^{(t)}$ and meet $\bigwedge_{i\in I}\mathbf{N}_i^{(t)}$ are given componentwise by

$$T_\vee^{(t)}(A) := \sup_{i\in I} T_i^{(t)}(A), \quad I_\vee^{(t)}(A) := \inf_{i\in I} I_i^{(t)}(A), \quad F_\vee^{(t)}(A) := \inf_{i\in I} F_i^{(t)}(A),$$

$$T_\wedge^{(t)}(A) := \inf_{i\in I} T_i^{(t)}(A), \quad I_\wedge^{(t)}(A) := \sup_{i\in I} I_i^{(t)}(A), \quad F_\wedge^{(t)}(A) := \sup_{i\in I} F_i^{(t)}(A),$$

for all $A \in \mathsf{Neu}^{\langle t-1\rangle}(X)$.

Proof. (i) Reflexivity and transitivity follow directly from the coordinatewise inequalities on $[0,1]$. Antisymmetry: if $\mathbf{N}_1^{(t)} \preccurlyeq_N^{(t)} \mathbf{N}_2^{(t)}$ and $\mathbf{N}_2^{(t)} \preccurlyeq_N^{(t)} \mathbf{N}_1^{(t)}$, then for all A,

$$T_1^{(t)}(A) \le T_2^{(t)}(A) \text{ and } T_2^{(t)}(A) \le T_1^{(t)}(A),$$

so $T_1^{(t)}(A) = T_2^{(t)}(A)$; similarly $I_1^{(t)}(A) = I_2^{(t)}(A)$ and $F_1^{(t)}(A) = F_2^{(t)}(A)$. Hence $\mathbf{N}_1^{(t)} = \mathbf{N}_2^{(t)}$.

(ii) Let $\{\mathbf{N}_i^{(t)}\}_{i\in I}$ be arbitrary. For each A, the sets $\{T_i^{(t)}(A)\}_{i\in I}$, $\{I_i^{(t)}(A)\}_{i\in I}$, and $\{F_i^{(t)}(A)\}_{i\in I}$ are subsets of $[0,1]$, so their suprema and infima lie in $[0,1]$. Thus the formulas above define functions into $[0,1]$.

We check the neutrosophic sum constraint for the join; the meet is analogous. Fix A and write

$$a_i := T_i^{(t)}(A), \quad b_i := I_i^{(t)}(A), \quad c_i := F_i^{(t)}(A), \quad s_i := a_i + b_i + c_i,$$

so $0 \le s_i \le 3$ for all i. Set

$$A^* := \sup_{i\in I} a_i, \quad B^* := \inf_{i\in I} b_i, \quad C^* := \inf_{i\in I} c_i.$$

By definition,

$$T_\vee^{(t)}(A) = A^*, \quad I_\vee^{(t)}(A) = B^*, \quad F_\vee^{(t)}(A) = C^*.$$

Lower bound: clearly $A^*, B^*, C^* \ge 0$, hence $T_\vee^{(t)}(A) + I_\vee^{(t)}(A) + F_\vee^{(t)}(A) \ge 0$.

Upper bound: let $\varepsilon > 0$. By definition of supremum, there exists $i_0 \in I$ such that

$$a_{i_0} > A^* - \varepsilon.$$

Since $B^* \le b_i$ and $C^* \le c_i$ for all i, we have in particular

$$B^* \le b_{i_0}, \quad C^* \le c_{i_0}.$$

Hence

$$A^* + B^* + C^* < a_{i_0} + b_{i_0} + c_{i_0} + \varepsilon = s_{i_0} + \varepsilon \le 3 + \varepsilon.$$

Because $\varepsilon > 0$ is arbitrary,

$$A^* + B^* + C^* \le 3.$$

Therefore

$$0 \le T_\vee^{(t)}(A) + I_\vee^{(t)}(A) + F_\vee^{(t)}(A) \le 3$$

for all A, so the join is in $\mathsf{Neu}^{\langle t\rangle}(X)$.

A standard coordinatewise argument shows that $\mathbf{N}_\vee^{(t)} := (T_\vee^{(t)}, I_\vee^{(t)}, F_\vee^{(t)})$ is the least upper bound of the family with respect to $\preccurlyeq_N^{(t)}$, and $\mathbf{N}_\wedge^{(t)} := (T_\wedge^{(t)}, I_\wedge^{(t)}, F_\wedge^{(t)})$ is the greatest lower bound. Thus $\mathsf{Neu}^{\langle t\rangle}(X)$ is a complete lattice under $\preccurlyeq_N^{(t)}$.

Iterated MetaSoft sets

Iterated MetaSoft Sets apply the soft-set construction repeatedly at higher meta-levels. Level 0 consists of ordinary soft sets on (U,S); level 1 consists of soft sets whose "universe'' is $\mathsf{Soft}(U,S)$; level 2 consists of soft sets whose universe is $\mathsf{Soft}^{\langle 1\rangle}(U,S)$; and so on. This yields a hierarchy of meta-policies about families of soft descriptions.

Definition 24 (Hierarchy of soft universes with meta-parameters). Let U be a universe of objects and S a parameter set for base soft sets. Let $(\Pi_t)_{t\ge 1}$ be a fixed family of nonempty sets of meta-parameters.

Set

$$\mathsf{Soft}^{\langle 0\rangle}(U,S) := \mathsf{Soft}(U,S),$$

the set of all soft sets $\mathcal{F}: S \to \mathcal{P}(U)$. For $t \ge 0$, define recursively

$$\mathsf{Soft}^{\langle t+1\rangle}(U,S;\Pi_1,\dots,\Pi_{t+1}) := \{\mathcal{G}_{t+1}: \Pi_{t+1} \to \mathcal{P}\big(\mathsf{Soft}^{\langle t\rangle}(U,S;\Pi_1,\dots,\Pi_t)\big)\}.$$

Thus, a level-$(t+1)$ object is a soft set on the universe $\mathsf{Soft}^{\langle t\rangle}(U,S;\Pi_1,\dots,\Pi_t)$, with parameter set Π_{t+1}. For brevity we simply write $\mathsf{Soft}^{\langle t\rangle}(U,S)$ when the meta-parameter sets are understood from context.

Definition 25 (Iterated MetaSoft Set of depth t). Fix meta-parameter sets $\Pi_1, \dots, \Pi_t$, with each $\Pi_j \neq \emptyset$. For $t \geq 1$, an Iterated MetaSoft Set (IMS) of depth t on (U, S) with meta-parameters $(\Pi_1, \dots, \Pi_t)$ is an element

$$\mathcal{G}^{(t)} \in \mathrm{Soft}^{\langle t \rangle}(U, S; \Pi_1, \dots, \Pi_t).$$

Equivalently, $\mathcal{G}^{(t)}$ is a soft set

$$\mathcal{G}^{(t)}\colon \Pi_t \to \mathcal{P}\big(\mathrm{Soft}^{\langle t-1 \rangle}(U, S; \Pi_1, \dots, \Pi_{t-1})\big).$$

In particular, for $t = 1$ we have

$$\mathrm{Soft}^{\langle 1 \rangle}(U, S; \Pi_1) = \{\mathcal{G}_1 \colon \Pi_1 \to \mathcal{P}(\mathrm{Soft}(U, S))\},$$

so a depth-1 IMS is precisely a MetaSoft Set in the sense of Definition 6.

Example 10 (Iterated MetaSoft Set (depth 2): travel-planning policies over hotel filters). Let the universe of hotels be

$$U = \{h_1, h_2, h_3\},$$

and let the attribute (parameter) set be

$$S = \{\text{NearStation,Breakfast}\}.$$

A base soft set $\mathcal{F}\colon S \to \mathcal{P}(U)$ states which hotels satisfy each attribute.

Consider three concrete soft sets:

$$\mathcal{F}^{(A)}(\text{NearStation}) = \{h_1, h_2\},$$
$$\mathcal{F}^{(A)}(\text{Breakfast}) = \{h_2, h_3\},$$
$$\mathcal{F}^{(B)}(\text{NearStation}) = \{h_1\},$$
$$\mathcal{F}^{(B)}(\text{Breakfast}) = \{h_3\},$$
$$\mathcal{F}^{(C)}(\text{NearStation}) = \{h_1\},$$
$$\mathcal{F}^{(C)}(\text{Breakfast}) = \{h_1\}.$$

Level 1 (MetaSoft filter by a single meta-criterion). Let the level-1 meta-parameter set be $\Pi_1 = \{\pi_1^\star\}$. Define a MetaSoft Set

$$\mathcal{G}_1 \in \mathrm{Soft}^{\langle 1 \rangle}(U, S; \Pi_1)$$

by

$G_1(\pi_1^{\{\star\}})$:= { $\boldsymbol{\mathcal{F}} \in$ Soft(U, S) | $h_2 \in \boldsymbol{\mathcal{F}}$(NearStation) and $h_2 \in \boldsymbol{\mathcal{F}}$(Breakfast) }.

This selects those soft sets that certify hotel h_2 as both near the station and serving breakfast.

For the three examples:

- For $\mathcal{F}^{(A)}$,

  $h_2 \in \mathcal{F}^{(A)}(\text{NearStation}) = \{h_1, h_2\}$,

  $h_2 \in \mathcal{F}^{(A)}(\text{Breakfast}) = \{h_2, h_3\}$,

  so $\mathcal{F}^{(A)} \in \mathcal{G}_1(\pi_1^\star)$.
- For $\mathcal{F}^{(B)}$,

  $h_2 \notin \mathcal{F}^{(B)}(\text{NearStation}) = \{h_1\}$,

  so the NearStation condition fails and $\mathcal{F}^{(B)} \notin \mathcal{G}_1(\pi_1^\star)$.
- For $\mathcal{F}^{(C)}$,

  $h_2 \notin \mathcal{F}^{(C)}(\text{NearStation}) = \{h_1\}$,

  so again $\mathcal{F}^{(C)} \notin \mathcal{G}_1(\pi_1^\star)$.

Thus, in this concrete scenario,

$$\mathcal{F}^{(A)} \in \mathcal{G}_1(\pi_1^\star),$$
$$\mathcal{F}^{(B)}, \mathcal{F}^{(C)} \notin \mathcal{G}_1(\pi_1^\star).$$

Level 2 (Iterated MetaSoft selection of level-1 policies). Next we consider policies about policies. A level-1 object is any map

$$\mathcal{H}\colon \Pi_1 \to \mathcal{P}(\mathrm{Soft}(U, S)),$$

that is, $\mathcal{H} \in \mathrm{Soft}^{\langle 1 \rangle}(U, S; \Pi_1)$. Such an $\mathcal{H}$ specifies, for each meta-parameter in Π_1, a collection of base soft sets.

Let the level-2 meta-parameter set be $\Pi_2 = \{\pi_2^\circ\}$. Define a depth-2 Iterated MetaSoft Set

$$\mathcal{G}_2 \in \mathrm{Soft}^{\langle 2 \rangle}(U, S; \Pi_1, \Pi_2)$$

by setting

$G_2(\pi_2^{\{\circ\}})$:= { $\boldsymbol{\mathcal{H}} \in$ Soft$^{\langle 1 \rangle}$(U, S; Π_1) | $\boldsymbol{\mathcal{G}}_1(\pi_1^{\{\star\}}) \subseteq \boldsymbol{\mathcal{H}}(\pi_1^{\{\star\}})$ and $\exists \boldsymbol{\mathcal{F}} \in \boldsymbol{\mathcal{H}}(\pi_1^{\{\star\}})$: $h_1 \in \boldsymbol{\mathcal{F}}$(Breakfast) }.

Informally, $\mathcal{G}_2(\pi_2^\circ)$ contains those level-1 policies $\mathcal{H}$ which:

1. keep all hotel filters favored by the first-level MetaSoft Set $\mathcal{G}_1$ (they extend $\mathcal{G}_1$), and
2. additionally guarantee that there is at least one candidate soft set in $\mathcal{H}(\pi_1^\star)$ where hotel h_1 offers breakfast.

Now construct a concrete level-1 policy $\mathcal{H}_{\mathrm{ex}}$ by

$$\mathcal{H}_{\mathrm{ex}}(\pi_1^\star) := \mathcal{G}_1(\pi_1^\star) \cup \{\mathcal{F}^{(C)}\}.$$

By definition,

$$\mathcal{G}_1(\pi_1^\star) \subseteq \mathcal{H}_{\mathrm{ex}}(\pi_1^\star)$$

holds automatically, because $\mathcal{H}_{\mathrm{ex}}(\pi_1^\star)$ is $\mathcal{G}_1(\pi_1^\star)$ together with one extra soft set $\mathcal{F}^{(\mathrm{C})}$. Moreover,

$$\mathcal{F}^{(\mathrm{C})} \in \mathcal{H}_{\mathrm{ex}}(\pi_1^\star)$$

$$\text{and} \quad \mathrm{h}_1 \in \mathcal{F}^{(\mathrm{C})}(\text{Breakfast}) = \{\mathrm{h}_1\},$$

so the existential condition in the definition of $\mathcal{G}_2(\pi_2^\diamond)$ is satisfied. Hence

$$\mathcal{H}_{\mathrm{ex}} \in \mathcal{G}_2(\pi_2^\diamond).$$

Summarizing, $\mathcal{G}_1$ encodes a first-level MetaSoft preference (keep hotels where h_2 is near the station and has breakfast), while $\mathcal{G}_2$ describes second-level meta-policies over such first-level preferences (among those policies, select ones that still guarantee at least one candidate with breakfast for h_1). This pair $(\mathcal{G}_1, \mathcal{G}_2)$ realizes a concrete depth-2 Iterated MetaSoft Set on the travel-planning scenario.

Theorem 27 (MetaSoft Sets as Iterated MetaStructures). Fix nonempty meta-parameter sets $\Pi_1, \dots, \Pi_\mathrm{t}$ and define $\mathrm{U}^{(0)} := \mathsf{Soft}^{\langle 0\rangle}(\mathrm{U}, \mathrm{S}) = \mathsf{Soft}(\mathrm{U}, \mathrm{S})$, $\mathrm{U}^{(\mathrm{j})} := \mathsf{Soft}^{(\mathrm{j})}(\mathrm{U}, \mathrm{S}; \Pi_1, \dots, \Pi_\mathrm{j})$ $(1 \le \mathrm{j} \le \mathrm{t})$. (a) For $\mathrm{t} = 1$, the universe $\mathrm{U}^{(1)} = \mathsf{Soft}^{\langle 1\rangle}(\mathrm{U}, \mathrm{S}; \Pi_1)$ is exactly the set of MetaSoft Sets on (U, S) with meta-parameters Π_1 (Definition 6).

(b) For every $\mathrm{t} \ge 1$, the family of universes $\mathrm{U}^{(0)}, \mathrm{U}^{(1)}, \dots, \mathrm{U}^{(\mathrm{t})}$ together with the levelwise selection maps $\Phi_{\mathrm{sel,j}}\colon \mathrm{U}^{(\mathrm{j})} \times \Pi_\mathrm{j} \to \mathcal{P}\big(\mathrm{U}^{(\mathrm{j}-1)}\big)$, $\Phi_{\mathrm{sel,j}}(\mathcal{G}_\mathrm{j}, \pi) := \mathcal{G}_\mathrm{j}(\pi)$, forms an Iterated MetaStructure of depth t in the sense of Definition 2.

Proof. (a) By Definition 24 at level $\mathrm{t} = 0 \to 1$, we have

$$\mathsf{Soft}^{\langle 1\rangle}(\mathrm{U}, \mathrm{S}; \Pi_1) = \{\, \mathcal{G}_1 \colon \Pi_1 \to \mathcal{P}(\mathsf{Soft}(\mathrm{U}, \mathrm{S}))\,\},$$

which is precisely the data of a Meta Soft Set $(\mathcal{G}_1, \Pi_1)$ on (U, S) (Definition 6). Hence $\mathrm{U}^{(1)}$ coincides with the class of MetaSoft Sets.

(b) For each level $\mathrm{j} \ge 1$, an element $\mathcal{G}_\mathrm{j} \in \mathrm{U}^{(\mathrm{j})}$ is a map

$$\mathcal{G}_\mathrm{j} \colon \Pi_\mathrm{j} \to \mathcal{P}\big(\mathrm{U}^{(\mathrm{j}-1)}\big).$$

Let $\sigma_\mathrm{j} \colon \Pi_\mathrm{j} \to \Pi_\mathrm{j}$ be a bijection (reindexing of meta-parameters), and let $\beta_\mathrm{j} \colon \mathrm{U}^{(\mathrm{j}-1)} \to \mathrm{U}^{(\mathrm{j}-1)}$ be a bijection (isomorphism at level $\mathrm{j}-1$). These induce an action on $\mathrm{U}^{(\mathrm{j})}$ by

$$(\sigma_\mathrm{j}, \beta_\mathrm{j}) \cdot \mathcal{G}_\mathrm{j} \colon \Pi_\mathrm{j} \to \mathcal{P}\big(\mathrm{U}^{(\mathrm{j}-1)}\big),$$

$$\big((\sigma_\mathrm{j}, \beta_\mathrm{j}) \cdot \mathcal{G}_\mathrm{j}\big)(\pi) := \beta_\mathrm{j}\big[\mathcal{G}_\mathrm{j}(\sigma_\mathrm{j}^{-1}(\pi))\big],$$

where $\beta_\mathrm{j}[-]$ denotes the image of a subset under β_j. Because β_j is a bijection, $(\sigma_\mathrm{j}, \beta_\mathrm{j}) \cdot \mathcal{G}_\mathrm{j}$ again takes values in $\mathcal{P}(\mathrm{U}^{(\mathrm{j}-1)})$, so $\mathrm{U}^{(\mathrm{j})}$ is stable under these induced isomorphisms.

Now check compatibility with the selection maps. For any $\mathcal{G}_\mathrm{j} \in \mathrm{U}^{(\mathrm{j})}$ and $\pi \in \Pi_\mathrm{j}$ we have

$$\begin{aligned}\Phi_{\mathrm{sel,j}}\big((\sigma_\mathrm{j}, \beta_\mathrm{j}) \cdot \mathcal{G}_\mathrm{j},\ \sigma_\mathrm{j}(\pi)\big) &= \big((\sigma_\mathrm{j}, \beta_\mathrm{j}) \cdot \mathcal{G}_\mathrm{j}\big)\big(\sigma_\mathrm{j}(\pi)\big) \\ &= \beta_\mathrm{j}\big[\mathcal{G}_\mathrm{j}(\sigma_\mathrm{j}^{-1}(\sigma_\mathrm{j}(\pi)))\big] \\ &= \beta_\mathrm{j}\big[\mathcal{G}_\mathrm{j}(\pi)\big].\end{aligned}$$

By contrast,

$$\Phi_{\mathrm{sel,j}}(\mathcal{G}_\mathrm{j}, \pi) = \mathcal{G}_\mathrm{j}(\pi),$$

so the selection at level j is equivariant with respect to the induced isomorphisms, as required in Definition 4. Since each level $\mathrm{U}^{(\mathrm{j})}$ and $\Phi_{\mathrm{sel,j}}$ satisfies this naturality condition, the whole tower

$$(\mathrm{U}^{(0)}, \mathrm{U}^{(1)}, \dots, \mathrm{U}^{(\mathrm{t})};\ \Phi_{\mathrm{sel},1}, \dots, \Phi_{\mathrm{sel,t}})$$

forms an Iterated Meta Structure of depth t.

Theorem 28 (Depth-1 Iterated MetaSoft Sets coincide with MetaSoft Sets). Let (U, S) be a fixed soft universe and let Π_1 be a nonempty meta-parameter set. Then $\mathsf{Soft}^{\langle 1\rangle}(\mathrm{U}, \mathrm{S}; \Pi_1) = \{\mathcal{G}_1 \colon \Pi_1 \to \mathcal{P}(\mathsf{Soft}(\mathrm{U}, \mathrm{S}))\}$ is exactly the class of MetaSoft Sets on (U, S) with meta-parameter set Π_1 in the sense of Definition 6.

Proof. By Definition 24 with $\mathrm{t} = 0$, we have

$$\mathsf{Soft}^{\langle 0\rangle}(\mathrm{U}, \mathrm{S}) = \mathsf{Soft}(\mathrm{U}, \mathrm{S}),$$

and therefore

$$\begin{aligned}&\mathsf{Soft}^{\langle 1\rangle}(\mathrm{U}, \mathrm{S}; \Pi_1) = \\ &\big\{\mathcal{G}_1 \colon \Pi_1 \to \mathcal{P}\big(\mathsf{Soft}^{\langle 0\rangle}(\mathrm{U}, \mathrm{S})\big)\big\} \\ &= \{\mathcal{G}_1 \colon \Pi_1 \to \mathcal{P}(\mathsf{Soft}(\mathrm{U}, \mathrm{S}))\}.\end{aligned}$$

By Definition 6, a MetaSoft Set on (U,S) with parameter set Π_1 is precisely such a mapping $\mathcal{G}_1:\Pi_1 \to \mathcal{P}(\mathrm{Soft}(U,S))$. Hence the two classes coincide.

Theorem 29 (Complete lattice of depth-t Iterated MetaSoft Sets). Fix $t \geq 1$ and meta-parameter sets $\Pi_1, \dots, \Pi_t$, each nonempty. Let $U^{(t-1)} := \mathrm{Soft}^{\langle t-1\rangle}(U,S;\Pi_1,\dots,\Pi_{t-1})$, $U^{(t)} := \mathrm{Soft}^{\langle t\rangle}(U,S;\Pi_1,\dots,\Pi_t)$. Equip $U^{(t)}$ with the pointwise inclusion order $\mathcal{G}_1^{(t)} \preccurlyeq_t \mathcal{G}_2^{(t)} \Leftrightarrow \mathcal{G}_1^{(t)}(\pi) \subseteq \mathcal{G}_2^{(t)}(\pi) \quad \forall\, \pi \in \Pi_t$. Then $(U^{(t)}, \preccurlyeq_t)$ is a complete lattice. More precisely, for any family $\{\mathcal{G}_i^{(t)}\}_{i\in I} \subseteq U^{(t)}$, the join $\bigvee_{i\in I}\mathcal{G}_i^{(t)}$ and meet $\bigwedge_{i\in I}\mathcal{G}_i^{(t)}$ are given by $\left(\bigvee_{i\in I}\mathcal{G}_i^{(t)}\right)(\pi) := \bigcup_{i\in I}\mathcal{G}_i^{(t)}(\pi)$, $\left(\bigwedge_{i\in I}\mathcal{G}_i^{(t)}\right)(\pi) := \bigcap_{i\in I}\mathcal{G}_i^{(t)}(\pi), \quad \forall\, \pi \in \Pi_t$.

Proof. First note that each $\mathcal{G}_i^{(t)}$ is by definition a map

$$\mathcal{G}_i^{(t)}: \Pi_t \to \mathcal{P}(U^{(t-1)}),$$

so for each $\pi \in \Pi_t$, the values $\mathcal{G}_i^{(t)}(\pi)$ form a family of subsets of $U^{(t-1)}$. The union and intersection of such families are again subsets of $U^{(t-1)}$, so the formulas in the statement define maps $\Pi_t \to \mathcal{P}(U^{(t-1)})$; hence they belong to $U^{(t)}$.

We verify that these maps are indeed join and meet.

Join. Let $\mathcal{H}^{(t)} \in U^{(t)}$ satisfy $\mathcal{G}_i^{(t)} \preccurlyeq_t \mathcal{H}^{(t)}$ for all $i \in I$. Then for each $\pi \in \Pi_t$ and each $i \in I$,

$$\mathcal{G}_i^{(t)}(\pi) \subseteq \mathcal{H}^{(t)}(\pi).$$

Therefore

$$\bigcup_{i\in I}\mathcal{G}_i^{(t)}(\pi) \subseteq \mathcal{H}^{(t)}(\pi) \quad \forall\, \pi \in \Pi_t,$$

which means

$$\bigvee_{i\in I}\mathcal{G}_i^{(t)} \preccurlyeq_t \mathcal{H}^{(t)}.$$

Also, for each $j \in I$ and each π,

$$\mathcal{G}_j^{(t)}(\pi) \subseteq \bigcup_{i\in I}\mathcal{G}_i^{(t)}(\pi),$$

hence $\mathcal{G}_j^{(t)} \preccurlyeq_t \bigvee_{i\in I}\mathcal{G}_i^{(t)}$. Thus $\bigvee_{i\in I}\mathcal{G}_i^{(t)}$ is the least upper bound.

Meet. Dually, if $\mathcal{H}^{(t)}$ satisfies $\mathcal{H}^{(t)} \preccurlyeq_t \mathcal{G}_i^{(t)}$ for all $i \in I$, then for each π,

$$\mathcal{H}^{(t)}(\pi) \subseteq \mathcal{G}_i^{(t)}(\pi) \quad \forall i,$$

so

$$\mathcal{H}^{(t)}(\pi) \subseteq \bigcap_{i\in I}\mathcal{G}_i^{(t)}(\pi) \quad \forall \pi,$$

that is, $\mathcal{H}^{(t)} \preccurlyeq_t \bigwedge_{i\in I}\mathcal{G}_i^{(t)}$. Moreover, for each $j \in I$ and each π,

$$\bigcap_{i\in I}\mathcal{G}_i^{(t)}(\pi) \subseteq \mathcal{G}_j^{(t)}(\pi),$$

so $\bigwedge_{i\in I}\mathcal{G}_i^{(t)} \preccurlyeq_t \mathcal{G}_j^{(t)}$. Therefore $\bigwedge_{i\in I}\mathcal{G}_i^{(t)}$ is the greatest lower bound.

Since arbitrary joins and meets exist and are given componentwise by unions and intersections, $(U^{(t)}, \preccurlyeq_t)$ is a complete lattice.

Definition 26 (Meta-lower and meta-upper operators induced by an IMS). Fix $t \geq 1$ and meta-parameter sets $\Pi_1, \dots, \Pi_t$. Let

$$U^{(t-1)} := \mathrm{Soft}^{\langle t-1\rangle}(U,S;\Pi_1,\dots,\Pi_{t-1})$$

and let $\mathcal{G}^{(t)} \in \mathrm{Soft}^{\langle t\rangle}(U,S;\Pi_1,\dots,\Pi_t)$, so

$$\mathcal{G}^{(t)}: \Pi_t \to \mathcal{P}\left(U^{(t-1)}\right).$$

For any $C \subseteq U^{(t-1)}$, define

$$\underline{C}^{\,\mathcal{G}^{(t)}} := \bigcup\left\{\mathcal{G}^{(t)}(\pi) \mid \mathcal{G}^{(t)}(\pi) \subseteq C\right\}.$$

$$\overline{C}^{\,\mathcal{G}^{(t)}} := \bigcup\left\{\mathcal{G}^{(t)}(\pi) \mid \mathcal{G}^{(t)}(\pi) \cap C \neq \emptyset\right\}.$$

We call these the meta-lower and meta-upper operators on $U^{(t-1)}$ induced by the Iterated MetaSoft Set $\mathcal{G}^{(t)}$.

Theorem 30 (Monotonicity and localized sandwich for meta-lower/upper). Let $\mathcal{G}^{(t)}$ and $U^{(t-1)}$ be as in Definition 26. For arbitrary subsets $C, D \subseteq U^{(t-1)}$ the following hold.

1. (Monotonicity in C) If $C \subseteq D$, then $\underline{C}^{\mathcal{G}^{(t)}} \subseteq \underline{D}^{\mathcal{G}^{(t)}}$, $\overline{C}^{\mathcal{G}^{(t)}} \subseteq \overline{D}^{\mathcal{G}^{(t)}}$.

2. (Localized sandwich) For every $C \subseteq U^{(t-1)}$, $\underline{C}^{\mathcal{G}^{(t)}} \subseteq C$, and $C \cap \left(\bigcup_{\pi\in\Pi_t} \mathcal{G}^{(t)}(\pi)\right) \subseteq \overline{C}^{\mathcal{G}^{(t)}}$.

Proof. (i) Let $C \subseteq D$.

For the meta-lower operator, let $x \in \underline{C}^{\mathcal{G}^{(t)}}$. By Definition 26, there exists $\pi \in \Pi_t$ such that

$$x \in \mathcal{G}^{(t)}(\pi) \quad \text{and} \quad \mathcal{G}^{(t)}(\pi) \subseteq C.$$

Since $C \subseteq D$, we also have $\mathcal{G}^{(t)}(\pi) \subseteq D$, so the same index π witnesses that $x \in \underline{D}^{\mathcal{G}^{(t)}}$. Thus

$$\underline{C}^{\mathcal{G}^{(t)}} \subseteq \underline{D}^{\mathcal{G}^{(t)}}.$$

For the meta-upper operator, let $x \in \overline{C}^{\mathcal{G}^{(t)}}$. Then there exists $\pi \in \Pi_t$ such that

$$x \in \mathcal{G}^{(t)}(\pi)$$
$$\text{and} \quad \mathcal{G}^{(t)}(\pi) \cap C \neq \emptyset.$$

From $C \subseteq D$ we deduce

$$\mathcal{G}^{(t)}(\pi) \cap D \supseteq \mathcal{G}^{(t)}(\pi) \cap C \neq \emptyset,$$

so the same π satisfies the condition for $\overline{D}^{\mathcal{G}^{(t)}}$, and hence

$$x \in \overline{D}^{\mathcal{G}^{(t)}}.$$

Therefore

$$\overline{C}^{\mathcal{G}^{(t)}} \subseteq \overline{D}^{\mathcal{G}^{(t)}}.$$

(ii) Let $C \subseteq U^{(t-1)}$.

For the first inclusion, let $x \in \underline{C}^{\mathcal{G}^{(t)}}$. Then there exists $\pi \in \Pi_t$ such that

$$x \in \mathcal{G}^{(t)}(\pi) \quad \text{and} \quad \mathcal{G}^{(t)}(\pi) \subseteq C.$$

In particular $x \in C$, so

$$\underline{C}^{\mathcal{G}^{(t)}} \subseteq C.$$

For the second inclusion, let

$$x \in C \cap \left(\bigcup_{\pi\in\Pi_t} \mathcal{G}^{(t)}(\pi)\right).$$

Then $x \in C$ and $x \in \mathcal{G}^{(t)}(\pi_0)$ for some $\pi_0 \in \Pi_t$. Thus

$$\mathcal{G}^{(t)}(\pi_0) \cap C \neq \emptyset,$$

and by Definition 26we have

$$x \in \mathcal{G}^{(t)}(\pi_0) \subseteq \overline{C}^{\mathcal{G}^{(t)}}.$$

Therefore every element in the intersection $C \cap \left(\bigcup_{\pi} \mathcal{G}^{(t)}(\pi)\right)$ belongs to $\overline{C}^{\mathcal{G}^{(t)}}$, which yields the desired inclusion.

Iterated MetaRough sets

Iterated MetaRough Sets extend rough approximations to higher levels by applying the Meta Rough construction repeatedly, now over families of rough objects themselves. This yields a hierarchy of rough universes together with meta-indiscernibility relations at each depth.

Definition 27 (Hierarchy of rough universes and meta-indiscernibilities). Let (X, R) be a Pawlak rough approximation space, and let $\mathsf{Rough}(X, R)$ denote the set of all rough objects $(\underline{U}, \overline{U})$ determined by R.

Define the level-0 universe by

$$\mathsf{Rough}^{\langle 0\rangle}(X, R) := \mathsf{Rough}(X, R).$$

For each $t \geq 1$, define the level-t universe inductively by

$$\mathsf{Rough}^{\langle t\rangle}(X, R) := \mathcal{P}\left(\mathsf{Rough}^{\langle t-1\rangle}(X, R)\right) \times \mathcal{P}\left(\mathsf{Rough}^{\langle t-1\rangle}(X, R)\right).$$

Thus a level-t rough object is a pair

$$\boldsymbol{r}^{(t)} = \left(\mathcal{L}^{(t)}, \mathcal{U}^{(t)}\right)$$
$$\text{with} \quad \mathcal{L}^{(t)}, \mathcal{U}^{(t)} \subseteq \mathsf{Rough}^{\langle t-1\rangle}(X, R),$$

interpreted as lower and upper approximations inside the universe of level-$(t-1)$ rough objects.

For each $t \geq 1$, fix an equivalence relation

$$\mathcal{E}^{(t)} \text{ on } \mathsf{Rough}^{\langle t-1\rangle}(X, R),$$

called the level-t meta-indiscernibility. For $r \in \mathsf{Rough}^{\langle t-1\rangle}(X, R)$ we denote its $\mathcal{E}^{(t)}$-equivalence class by $[r]_{\mathcal{E}^{(t)}}$.

Definition 28 (Iterated MetaRough Set of depth t). Let $t \geq 1$ and let

$$\mathcal{C} \subseteq \mathsf{Rough}^{\langle t-1\rangle}(X, R)$$

be any family of level-$(t-1)$ rough objects.

The meta-lower and meta-upper approximations of $\mathcal{C}$ with respect to $\mathcal{E}^{(t)}$ are defined by

$$\underline{C}^{\mathcal{E}^{(t)}} := \{ r \in \mathsf{Rough}^{\langle t-1 \rangle}(X,R) \mid [r]_{\mathcal{E}^{(t)}} \subseteq \mathcal{C} \},$$

$$\overline{C}^{\mathcal{E}^{(t)}} := \{ r \in \mathsf{Rough}^{\langle t-1 \rangle}(X,R) \mid [r]_{\mathcal{E}^{(t)}} \cap \mathcal{C} \neq \emptyset \}.$$

The pair

$$\mathbf{R}^{(t)}(\mathcal{C}) := \left(\underline{\mathcal{C}}^{\mathcal{E}^{(t)}}, \overline{\mathcal{C}}^{\mathcal{E}^{(t)}} \right) \in \mathsf{Rough}^{\langle t \rangle}(X,R)$$

is called the Iterated Meta Rough Set of depth t generated by $\mathcal{C}$. For $t = 1$ this coincides with the Meta Rough Set from Definition 18, where $\mathcal{E}^{(1)}$ plays the role of the meta-indiscernibility on $\mathsf{Rough}(X,R)$.

Example 11 (Iterated MetaRough Set (depth 2): course pass-status aggregated by classes and by a school-level summary). Let $X = \{s_1, s_2, s_3, s_4\}$ be students in two homerooms (indiscernibility relation R):

$$[s_1]_R = [s_2]_R = \{s_1, s_2\},$$
$$[s_3]_R = [s_4]_R = \{s_3, s_4\}.$$

Consider two observed pass-sets for a mock exam:

$$U_1 = \{s_1\}, \qquad U_2 = \{s_3, s_4\}.$$

We first compute their rough approximations in (X,R).

For $U_1 = \{s_1\}$:

$$\underline{U_1} = \{x \in X \mid [x]_R \subseteq U_1\}.$$

The R-classes are $\{s_1, s_2\}$ and $\{s_3, s_4\}$. Neither $\{s_1, s_2\} \subseteq \{s_1\}$ nor $\{s_3, s_4\} \subseteq \{s_1\}$ holds, so no class is fully contained in U_1. Hence

$$\underline{U_1} = \emptyset.$$

The upper approximation is

$$\overline{U_1} = \{x \in X \mid [x]_R \cap U_1 \neq \emptyset\}.$$

Here $[s_1]_R = \{s_1, s_2\}$ meets U_1, so both s_1 and s_2 are included, while $[s_3]_R = \{s_3, s_4\}$ does not meet U_1. Thus

$$\overline{U_1} = \{s_1, s_2\}.$$

So the rough object associated to U_1 is

$$r_{U_1} = (\underline{U_1}, \overline{U_1}) = (\emptyset, \{s_1, s_2\}).$$

For $U_2 = \{s_3, s_4\}$:

$$\underline{U_2} = \{x \in X \mid [x]_R \subseteq U_2\}.$$

Now $[s_3]_R = [s_4]_R = \{s_3, s_4\} \subseteq U_2$, so both s_3 and s_4 are in the lower approximation:

$$\underline{U_2} = \{s_3, s_4\}.$$

The upper approximation is again

$$\overline{U_2} = \{x \in X \mid [x]_R \cap U_2 \neq \emptyset\}.$$

The class $\{s_3, s_4\}$ meets U_2 and is the only such class, hence

$$\overline{U_2} = \{s_3, s_4\}.$$

Thus the rough object for U_2 is

$$r_{U_2} = (\underline{U_2}, \overline{U_2}) = (\{s_3, s_4\}, \{s_3, s_4\}).$$

Level 1 (MetaRough over class-level rough objects). Form the level-1 family

$$\mathcal{C} := \{r_{U_1}, r_{U_2}\} \subseteq \mathsf{Rough}^{\langle 0 \rangle}(X,R) = \mathsf{Rough}(X,R),$$

and choose the level-1 meta-indiscernibility $\mathcal{E}^{(1)}$ on $\mathsf{Rough}(X,R)$ to be equality:

$$r \; \mathcal{E}^{(1)} \; r' \quad \Leftrightarrow \quad r = r'.$$

For this choice, each equivalence class is a singleton:

$$[r]_{\mathcal{E}^{(1)}} = \{r\} \quad (\forall r \in \mathsf{Rough}(X,R)).$$

The level-1 meta-lower approximation is

$$= \{ r \mid \{r\} \subseteq \mathcal{C} \} = \mathcal{C}.$$

Similarly, the level-1 meta-upper approximation is

$$\overline{\mathcal{C}}^{\mathcal{E}^{(1)}} = \{ r \in \mathsf{Rough}(X,R) \mid [r]_{\mathcal{E}^{(1)}} \cap \mathcal{C} \neq \emptyset \}$$
$$= \{ r \mid \{r\} \cap \mathcal{C} \neq \emptyset \} = \mathcal{C}.$$

Hence the MetaRough Set of $\mathcal{C}$ at depth 1 is

$$\boldsymbol{R}^{(1)}(\mathcal{C}) = \left(\underline{\mathcal{C}}^{\mathcal{E}^{(1)}}, \overline{\mathcal{C}}^{\mathcal{E}^{(1)}} \right)$$
$$= (\mathcal{C}, \mathcal{C}) \in \mathsf{Rough}^{\langle 1 \rangle}(X,R).$$

Informally, this is a rough summary of class-level pass-statuses.

Level 2 (MetaRough over class-summary patterns). Now move up one level. The level-1 universe is

$$\mathsf{Rough}^{\langle 1\rangle}(X,R) = \mathcal{P}(\mathsf{Rough}(X,R)) \times \mathcal{P}(\mathsf{Rough}(X,R)),$$

so $\boldsymbol{R}^{(1)}(\mathcal{C}) = (\mathcal{C},\mathcal{C})$ is a single level-1 rough object.

Consider the level-2 family consisting of this single object:

$$\mathcal{D} := \{\boldsymbol{R}^{(1)}(\mathcal{C})\} = \{(\mathcal{C},\mathcal{C})\} \subseteq \mathsf{Rough}^{\langle 1\rangle}(X,R).$$

Choose the level-2 meta-indiscernibility $\mathcal{E}^{(2)}$ on $\mathsf{Rough}^{\langle 1\rangle}(X,R)$ again to be equality. Then for any $\boldsymbol{r} \in \mathsf{Rough}^{\langle 1\rangle}(X,R)$ we have $[\boldsymbol{r}]_{\mathcal{E}^{(2)}} = \{\boldsymbol{r}\}$ and therefore

$$\underline{\mathcal{D}}^{\mathcal{E}^{(2)}}$$

$$\underline{\mathcal{C}}^{\mathcal{E}^{(1)}} = \{\, r \in \mathsf{Rough}(X,R) \mid [r]_{\mathcal{E}^{(1)}} \subseteq \mathcal{C} \,\} = \{\, \boldsymbol{r} \mid [\boldsymbol{r}]_{\mathcal{E}^{(2)}} \subseteq \mathcal{D} \,\} = \mathcal{D},$$

$$\overline{\mathcal{D}}^{\mathcal{E}^{(2)}} = \{\, \mathbf{r} \mid [\mathbf{r}]_{\mathcal{E}^{(2)}} \cap \mathcal{D} \neq \emptyset \,\} = \mathcal{D}.$$

Thus the depth-2 Iterated MetaRough Set generated by $\mathcal{D}$ is

$$\mathbf{R}^{(2)}(\mathcal{D}) = \left(\underline{\mathcal{D}}^{\mathcal{E}^{(2)}}, \overline{\mathcal{D}}^{\mathcal{E}^{(2)}}\right) = (\mathcal{D},\mathcal{D}) \in \mathsf{Rough}^{\langle 2\rangle}(\mathrm{X},\mathrm{R}).$$

Interpretation: level 1 records rough summaries at the class level (two homerooms), while level 2 treats identical class-summary patterns as indiscernible from the viewpoint of a higher aggregation unit (such as a school or exam board). In this simple example the school-level family happens to consist of a single such pattern.

Proposition 2 (Sandwich property at every depth). Let $\mathrm{t} \geq 1$ and let $\mathcal{C} \subseteq \mathsf{Rough}^{\langle \mathrm{t}-1\rangle}(\mathrm{X},\mathrm{R})$ be any family of level-$(\mathrm{t}-1)$ rough objects. Then $\underline{\mathcal{C}}^{\mathcal{E}^{(\mathrm{t})}} \subseteq \mathcal{C} \subseteq \overline{\mathcal{C}}^{\mathcal{E}^{(\mathrm{t})}}$.

Proof. We show the two inclusions separately.

First inclusion, $\underline{\mathcal{C}}^{\mathcal{E}^{(\mathrm{t})}} \subseteq \mathcal{C}$. Let $\mathrm{r} \in \underline{\mathcal{C}}^{\mathcal{E}^{(\mathrm{t})}}$. By definition,

$$[\mathrm{r}]_{\mathcal{E}^{(\mathrm{t})}} \subseteq \mathcal{C}.$$

Since $\mathrm{r} \in [\mathrm{r}]_{\mathcal{E}^{(\mathrm{t})}}$ (every element lies in its own equivalence class), it follows that $\mathrm{r} \in \mathcal{C}$. Hence $\underline{\mathcal{C}}^{\mathcal{E}^{(\mathrm{t})}} \subseteq \mathcal{C}$.

Second inclusion, $\mathcal{C} \subseteq \overline{\mathcal{C}}^{\mathcal{E}^{(\mathrm{t})}}$. Let $\mathrm{r} \in \mathcal{C}$. Then the intersection

$$[\mathrm{r}]_{\mathcal{E}^{(\mathrm{t})}} \cap \mathcal{C}$$

contains r and is therefore nonempty:

$$[\mathrm{r}]_{\mathcal{E}^{(\mathrm{t})}} \cap \mathcal{C} \supseteq \{\mathrm{r}\} \neq \emptyset.$$

By the definition of $\overline{\mathcal{C}}^{\mathcal{E}^{(\mathrm{t})}}$ we conclude that $\mathrm{r} \in \overline{\mathcal{C}}^{\mathcal{E}^{(\mathrm{t})}}$. Hence $\mathcal{C} \subseteq \overline{\mathcal{C}}^{\mathcal{E}^{(\mathrm{t})}}$.

Combining both inclusions yields

$$\underline{\mathcal{C}}^{\mathcal{E}^{(\mathrm{t})}} \subseteq \mathcal{C} \subseteq \overline{\mathcal{C}}^{\mathcal{E}^{(\mathrm{t})}},$$

as claimed.

Theorem 31 (Generalization of MetaRough and Iterated MetaStructure). For each $\mathrm{t} \geq 1$ set $\mathrm{U}^{(\mathrm{t})} := \mathsf{Rough}^{\langle \mathrm{t}\rangle}(\mathrm{X},\mathrm{R})$, $\mathrm{U}^{(0)} := \mathsf{Rough}^{\langle 0\rangle}(\mathrm{X},\mathrm{R}) = \mathsf{Rough}(\mathrm{X},\mathrm{R})$.

(a) For $\mathrm{t} = 1$, the assignment $\mathcal{C} \mapsto \mathbf{R}^{(1)}(\mathcal{C}) = \left(\underline{\mathcal{C}}^{\mathcal{E}^{(1)}}, \overline{\mathcal{C}}^{\mathcal{E}^{(1)}}\right)$ is exactly the MetaRough Set construction of Definition 18applied to subsets $\mathcal{C} \subseteq \mathsf{Rough}(\mathrm{X},\mathrm{R})$.

(b) For each $\mathrm{t} \geq 1$, consider the operations $\Phi^{(\mathrm{t})}_{\mathrm{low}}, \Phi^{(\mathrm{t})}_{\mathrm{up}}\colon \mathcal{P}\left(\mathrm{U}^{(\mathrm{t}-1)}\right) \to \mathrm{U}^{(\mathrm{t})}$, $\mathcal{C} \mapsto \left(\underline{\mathcal{C}}^{\mathcal{E}^{(\mathrm{t})}}, \overline{\mathcal{C}}^{\mathcal{E}^{(\mathrm{t})}}\right)$. If level-$(\mathrm{t}-1)$ isomorphisms are required to preserve the meta-indiscernibility $\mathcal{E}^{(\mathrm{t})}$ (that is, $\mathrm{r}\mathcal{E}^{(\mathrm{t})}\mathrm{s}$ iff $\beta(\mathrm{r})\mathcal{E}^{(\mathrm{t})}\beta(\mathrm{s})$ for any level-$(\mathrm{t}-1)$ isomorphism β), then the family $(\mathrm{U}^{(0)}, \mathrm{U}^{(1)}, \ldots, \mathrm{U}^{(\mathrm{t})};\ \Phi^{(1)}_{\mathrm{low}}, \Phi^{(1)}_{\mathrm{up}}, \ldots, \Phi^{(\mathrm{t})}_{\mathrm{low}}, \Phi^{(\mathrm{t})}_{\mathrm{up}})$ forms an Iterated MetaStructure of depth t in the sense of Definition 2.

Proof. (a) At depth $\mathrm{t} = 1$ we have

$$\mathrm{U}^{(1)} = \mathsf{Rough}^{\langle 1\rangle}(\mathrm{X},\mathrm{R})$$
$$= \mathcal{P}(\mathsf{Rough}(\mathrm{X},\mathrm{R})) \times \mathcal{P}(\mathsf{Rough}(\mathrm{X},\mathrm{R})),$$

so elements of $\mathrm{U}^{(1)}$ are pairs of subsets of $\mathsf{Rough}(\mathrm{X},\mathrm{R})$. Given any $\mathcal{C} \subseteq \mathsf{Rough}(\mathrm{X},\mathrm{R})$, the pair

$$\left(\underline{\mathcal{C}}^{\mathcal{E}^{(1)}}, \overline{\mathcal{C}}^{\mathcal{E}^{(1)}}\right) \in \mathrm{U}^{(1)}$$

is exactly the MetaRough Set of $\mathcal{C}$ constructed using the meta-indiscernibility $\mathcal{E}^{(1)}$ as in Definition 18. Hence $\mathbf{R}^{(1)}$ recovers the MetaRough Set construction.

(b) Fix $\mathrm{t} \geq 1$. A level-t object is a pair of subsets

$$\mathbf{r}^{(\mathrm{t})} = (\mathcal{L}^{(\mathrm{t})}, \mathcal{U}^{(\mathrm{t})}) \in \mathrm{U}^{(\mathrm{t})} = \mathcal{P}\left(\mathrm{U}^{(\mathrm{t}-1)}\right) \times \mathcal{P}\left(\mathrm{U}^{(\mathrm{t}-1)}\right).$$

By Definition 28, both $\Phi_{\mathrm{low}}^{(\mathrm{t})}$ and $\Phi_{\mathrm{up}}^{(\mathrm{t})}$ are constructed from the equivalence relation $\mathcal{E}^{(\mathrm{t})}$ on $\mathrm{U}^{(\mathrm{t}-1)}$ via

$$\underline{\mathcal{C}}^{\mathcal{E}^{(\mathrm{t})}} = \{\, \mathrm{r} \in \mathrm{U}^{(\mathrm{t}-1)} \mid [\mathrm{r}]_{\mathcal{E}^{(\mathrm{t})}} \subseteq \mathcal{C} \,\},$$
$$\overline{\mathcal{C}}^{\mathcal{E}^{(\mathrm{t})}} = \{\, \mathrm{r} \in \mathrm{U}^{(\mathrm{t}-1)} \mid [\mathrm{r}]_{\mathcal{E}^{(\mathrm{t})}} \cap \mathcal{C} \neq \emptyset \,\}.$$

Let $\beta\colon \mathrm{U}^{(\mathrm{t}-1)} \to \mathrm{U}^{(\mathrm{t}-1)}$ be a level-$(\mathrm{t}-1)$ isomorphism in the sense of Definition 4, so by assumption β preserves $\mathcal{E}^{(\mathrm{t})}$-equivalence classes: for all $\mathrm{r}, \mathrm{s} \in \mathrm{U}^{(\mathrm{t}-1)}$,

$$\mathrm{r}\ \mathcal{E}^{(\mathrm{t})}\ \mathrm{s}$$
$$\Leftrightarrow \quad \beta(\mathrm{r})\ \mathcal{E}^{(\mathrm{t})}\ \beta(\mathrm{s}).$$

Take any $\mathcal{C} \subseteq U^{(t-1)}$. Consider the image $\beta[\mathcal{C}] \subseteq U^{(t-1)}$. For the lower approximation we have

$$\underline{\beta[\mathcal{C}]}^{\mathcal{E}^{(t)}} = \left\{ u \in U^{(t-1)} \mid [u]_{\mathcal{E}^{(t)}} \subseteq \beta[\mathcal{C}] \right\}.$$

By substituting $u = \beta(r)$ and using preservation of equivalence classes,

$$[u]_{\mathcal{E}^{(t)}} = [\beta(r)]_{\mathcal{E}^{(t)}} = \beta\left([r]_{\mathcal{E}^{(t)}}\right),$$

so

$$[u]_{\mathcal{E}^{(t)}} \subseteq \beta[\mathcal{C}]$$
$$\Leftrightarrow \quad \beta\left([r]_{\mathcal{E}^{(t)}}\right) \subseteq \beta[\mathcal{C}]$$
$$\Leftrightarrow \quad [r]_{\mathcal{E}^{(t)}} \subseteq \mathcal{C},$$

because β is a bijection. Hence

$$u \in \underline{\beta[\mathcal{C}]}^{\mathcal{E}^{(t)}}$$
$$\Leftrightarrow \quad u = \beta(r) \text{ for some } r \in \underline{\mathcal{C}}^{\mathcal{E}^{(t)}}.$$

Therefore

$$\underline{\beta[\mathcal{C}]}^{\mathcal{E}^{(t)}}$$
$$= \beta\left[\underline{\mathcal{C}}^{\mathcal{E}^{(t)}}\right].$$

A completely analogous elementwise argument shows

$$\overline{\beta[\mathcal{C}]}^{\mathcal{E}^{(t)}}$$
$$= \beta\left[\overline{\mathcal{C}}^{\mathcal{E}^{(t)}}\right].$$

Consequently, the action of β on $U^{(t-1)}$ lifts to an action on $U^{(t)}$ that commutes with the maps

$$\mathcal{C} \mapsto \left(\underline{\mathcal{C}}^{\mathcal{E}^{(t)}}, \overline{\mathcal{C}}^{\mathcal{E}^{(t)}}\right)$$
$$= \Phi_{\mathrm{low}}^{(t)}(\mathcal{C}) = \Phi_{\mathrm{up}}^{(t)}(\mathcal{C}).$$

This is precisely the naturality (isomorphism-invariance) condition required in Definition 4. Since this holds at each level t, the tower

$$(U^{(0)}, U^{(1)}, \ldots, U^{(t)};$$
$$\Phi_{\mathrm{low}}^{(1)}, \Phi_{\mathrm{up}}^{(1)}, \ldots,$$
$$\Phi_{\mathrm{low}}^{(t)}, \Phi_{\mathrm{up}}^{(t)})$$

constitutes an Iterated MetaStructure of depth t.

Theorem 32 (Monotonicity at every meta-level). Let $\mathrm{t} \geq 1$ and let $\mathcal{E}^{(\mathrm{t})}$ and $\mathsf{Rough}^{\langle \mathrm{t}-1\rangle}(\mathrm{X},\mathrm{R})$ be as in Definition 27. For all families $\mathrm{C}, \mathrm{D} \subseteq \mathsf{Rough}^{\langle \mathrm{t}-1\rangle}(\mathrm{X},\mathrm{R})$ with $\mathrm{C} \subseteq \mathrm{D}$ we have $\underline{\mathrm{C}}^{\mathcal{E}^{(\mathrm{t})}} \subseteq \underline{\mathrm{D}}^{\mathcal{E}^{(\mathrm{t})}}$, $\overline{\mathrm{C}}^{\mathcal{E}^{(\mathrm{t})}} \subseteq \overline{\mathrm{D}}^{\mathcal{E}^{(\mathrm{t})}}$.

Proof. Let $\mathrm{C} \subseteq \mathrm{D}$.

For the meta-lower approximation, take $\mathrm{r} \in \underline{\mathrm{C}}^{\mathcal{E}^{(\mathrm{t})}}$. By Definition 28,

$$[\mathrm{r}]_{\mathcal{E}^{(\mathrm{t})}} \subseteq \mathrm{C}.$$

From $\mathrm{C} \subseteq \mathrm{D}$ it follows that

$$[\mathrm{r}]_{\mathcal{E}^{(\mathrm{t})}} \subseteq \mathrm{D},$$

so $\mathrm{r} \in \underline{\mathrm{D}}^{\mathcal{E}^{(\mathrm{t})}}$. Hence $\underline{\mathrm{C}}^{\mathcal{E}^{(\mathrm{t})}} \subseteq \underline{\mathrm{D}}^{\mathcal{E}^{(\mathrm{t})}}$.

For the meta-upper approximation, let $r \in \overline{C}^{\mathcal{E}^{(t)}}$. Then by Definition 28

$$[r]_{\mathcal{E}^{(t)}} \cap C \neq \emptyset.$$

Since $C \subseteq D$, we have

$$[r]_{\mathcal{E}^{(t)}} \cap D \supseteq [r]_{\mathcal{E}^{(t)}} \cap C \neq \emptyset,$$

hence $r \in \overline{D}^{\mathcal{E}^{(t)}}$. Therefore $\overline{C}^{\mathcal{E}^{(t)}} \subseteq \overline{D}^{\mathcal{E}^{(t)}}$.

Theorem 33 (Idempotence of iterated meta-approximations). Let $\mathrm{t} \geq 1$ and let $\mathcal{E}^{(\mathrm{t})}$ be as above.

For every $C \subseteq \mathrm{Rough}^{\langle t-1\rangle}(X,R)$ we have $\underline{\left(\underline{C}^{\mathcal{E}^{(t)}}\right)}^{\mathcal{E}^{(t)}} = \underline{C}^{\mathcal{E}^{(t)}}$, $\overline{\left(\overline{C}^{\mathcal{E}^{(t)}}\right)}^{\mathcal{E}^{(t)}} = \overline{C}^{\mathcal{E}^{(t)}}$.

Proof. We prove idempotence for the meta-lower approximation; the argument for the meta-upper approximation is analogous.

Set $L := \underline{C}^{\mathcal{E}^{(t)}}$. By Proposition 2,

$$L = \underline{C}^{\mathcal{E}^{(t)}} \subseteq C.$$

Applying Theorem 78 with $L \subseteq C$ yields

$$\underline{L}^{\mathcal{E}^{(t)}} \subseteq \underline{C}^{\mathcal{E}^{(t)}} = L.$$

Thus

$$\underline{L}^{\mathcal{E}^{(t)}} \subseteq L.$$

For the converse inclusion, let $r \in L = \underline{C}^{\mathcal{E}^{(t)}}$. Then by definition

$$[r]_{\mathcal{E}^{(t)}} \subseteq C.$$

For any $s \in [r]_{\mathcal{E}^{(t)}}$ we have $[s]_{\mathcal{E}^{(t)}} = [r]_{\mathcal{E}^{(t)}}$, so

$$[s]_{\mathcal{E}^{(t)}} \subseteq C.$$

Hence $s \in \underline{C}^{\mathcal{E}^{(t)}} = L$. Since this holds for all $s \in [r]_{\mathcal{E}^{(t)}}$, we obtain

$$[r]_{\mathcal{E}^{(t)}} \subseteq L.$$

Therefore $r \in \underline{L}^{\mathcal{E}^{(t)}}$. As $r \in L$ was arbitrary, we conclude

$$L \subseteq \underline{L}^{\mathcal{E}^{(t)}}.$$

Combining the two inclusions gives

$$\underline{L}^{\mathcal{E}^{(t)}} = L = \underline{C}^{\mathcal{E}^{(t)}},$$

i.e.,

$$\underline{\left(\underline{C}^{\mathcal{E}^{(t)}}\right)}^{\mathcal{E}^{(t)}} = \underline{C}^{\mathcal{E}^{(t)}}.$$

For the meta-upper operator, define $U := \overline{C}^{\mathcal{E}^{(t)}}$. By Proposition 2,

$$C \subseteq U = \overline{C}^{\mathcal{E}^{(t)}},$$

and by Theorem 34,

$$\overline{C}^{\mathcal{E}^{(t)}} \subseteq \overline{U}^{\mathcal{E}^{(t)}}.$$

Since $U = \overline{C}^{\mathcal{E}^{(t)}}$, this gives $U \subseteq \overline{U}^{\mathcal{E}^{(t)}}$.

Conversely, let $r \in \overline{U}^{\mathcal{E}^{(t)}}$. Then

$$[r]_{\mathcal{E}^{(t)}} \cap U \neq \emptyset.$$

Take $s \in [r]_{\mathcal{E}^{(t)}} \cap U$. As $s \in U = \overline{C}^{\mathcal{E}^{(t)}}$, we have

$$[s]_{\mathcal{E}^{(t)}} \cap C \neq \emptyset.$$

But $[s]_{\mathcal{E}^{(t)}} = [r]_{\mathcal{E}^{(t)}}$, so

$$[r]_{\mathcal{E}^{(t)}} \cap C \neq \emptyset,$$

which implies $r \in \overline{C}^{\mathcal{E}^{(t)}} = U$. Hence $\overline{U}^{\mathcal{E}^{(t)}} \subseteq U$.

Together with $U \subseteq \overline{U}^{\mathcal{E}^{(t)}}$ we obtain

$$\overline{U}^{\mathcal{E}^{(t)}} = U = \overline{C}^{\mathcal{E}^{(t)}}.$$

Theorem 80 (Exactness and unions of meta-indiscernibility classes). Let $t \geq 1$ and let $\mathcal{E}^{(t)}$ be an equivalence relation on $\mathrm{Rough}^{\langle t-1\rangle}(X,R)$. For $C \subseteq \mathrm{Rough}^{\langle t-1\rangle}(X,R)$ the following are equivalent.

1. C is meta-exact: $\underline{C}^{\mathcal{E}^{(t)}} = \overline{C}^{\mathcal{E}^{(t)}}$.
2. C is a union of $\mathcal{E}^{(t)}$-equivalence classes: there exists an index set I and $\mathcal{E}^{(t)}$-classes $\{B_i\}_{i\in I}$ such that $C = \bigcup_{i\in I} B_i$.

Proof. (i)⇒(ii). Assume $\underline{C}^{\mathcal{E}^{(t)}} = \overline{C}^{\mathcal{E}^{(t)}}$. By Proposition 2,

$$C \subseteq \overline{C}^{\mathcal{E}^{(t)}} = \underline{C}^{\mathcal{E}^{(t)}}.$$

Hence

$$C \subseteq \underline{C}^{\mathcal{E}^{(t)}} \subseteq C,$$

so $C = \underline{C}^{\mathcal{E}^{(t)}}$.

Let $r \in C$. Then $r \in \underline{C}^{\mathcal{E}^{(t)}}$ and therefore

$$[r]_{\mathcal{E}^{(t)}} \subseteq C.$$

Thus C contains the entire $\mathcal{E}^{(t)}$-class of each of its elements. Consequently,

$$C = \bigcup_{r\in C} [r]_{\mathcal{E}^{(t)}},$$

which is a union of equivalence classes (possibly with repetitions, which do not affect the union). This shows (ii).

(ii)⇒(i). Assume $C = \bigcup_{i\in I} B_i$ where each B_i is an $\mathcal{E}^{(t)}$-equivalence class. We first show that $\underline{C}^{\mathcal{E}^{(t)}} \subseteq C$ and $C \subseteq \overline{C}^{\mathcal{E}^{(t)}}$ hold by Proposition 2. It remains to show $C \subseteq \underline{C}^{\mathcal{E}^{(t)}}$ and $\overline{C}^{\mathcal{E}^{(t)}} \subseteq C$.

Let $r \in C$. Then $r \in B_{i_0}$ for some $i_0 \in I$, and $B_{i_0} = [r]_{\mathcal{E}^{(t)}}$ is fully contained in C because C is a union of the classes B_i. Hence

$$[r]_{\mathcal{E}^{(t)}} \subseteq C,$$

so $r \in \underline{C}^{\mathcal{E}^{(t)}}$. Thus $C \subseteq \underline{C}^{\mathcal{E}^{(t)}}$. Together with $\underline{C}^{\mathcal{E}^{(t)}} \subseteq C$ we obtain

$$\underline{C}^{\mathcal{E}^{(t)}} = C.$$

Now let $r \in \overline{C}^{\mathcal{E}^{(t)}}$. Then

$$[r]_{\mathcal{E}^{(t)}} \cap C \neq \emptyset,$$

so there exists $s \in [r]_{\mathcal{E}^{(t)}} \cap C$. As C is a union of $\mathcal{E}^{(t)}$-classes, $s \in C$ implies $[s]_{\mathcal{E}^{(t)}} \subseteq C$. But $[s]_{\mathcal{E}^{(t)}} = [r]_{\mathcal{E}^{(t)}}$, so $[r]_{\mathcal{E}^{(t)}} \subseteq C$ and therefore $r \in C$. Hence $\overline{C}^{\mathcal{E}^{(t)}} \subseteq C$, and together with $C \subseteq \overline{C}^{\mathcal{E}^{(t)}}$ we obtain

$$\overline{C}^{\mathcal{E}^{(t)}} = C.$$

Thus

$$\underline{C}^{\mathcal{E}^{(t)}} = C = \overline{C}^{\mathcal{E}^{(t)}},$$

so C is meta-exact and (i) holds.

Conclusion

In this paper, we introduce the concepts of MetaFuzzy Sets, MetaNeutrosophic Sets, MetaSoft Sets, and MetaRough Sets by extending classical Fuzzy Sets, Neutrosophic Sets, Soft Sets, and Rough Sets through the application of MetaStructure and Iterated MetaStructure.

Future work

This work is currently restricted to finite domains, where naive constructions incur high combinatorial costs. Future research should therefore explore measure-theoretic extensions, scalable algorithms, and principled normalization schemes tailored to diverse application settings and robustness requirements. In addition, future studies may investigate whether similar extensions can be developed for other classes of sets, such as Plithogenic Sets, Vague Sets, and Near Sets. We also anticipate further developments involving extensions based on graphs, hypergraphs, superhypergraphs, hyperstructures, and hyper-algebra.

Acknowledgment

We extend our sincere gratitude to everyone who provided valuable insights, inspiration, and assistance throughout this research. We particularly thank our readers for their interest and acknowledge the authors of the cited works for laying the foundation that made this study possible. We also appreciate the support of the individuals and institutions that provided the resources and infrastructure needed to complete and disseminate this work. Finally, we are grateful to all those who supported us in various ways during the course of this project.

Conflict of interest

The authors declare that there are no conflicts of interest associated with this research or its publication.

Disclaimer (Regarding manuscript formatting)

In this paper, we converted the LaTeX source into a Word document using tools such as Pandoc. While every effort has been made to ensure accurate formatting, minor errors may have been introduced during the conversion process. We kindly ask for your understanding.

References

Atagün AO and Kamacı H. Strait fuzzy sets, strait fuzzy rough sets and their similarity measures-based decision making systems. *Int. J. Syst. Sci.*2023; 54(12): 2519-2535.

Broumi S, Talea M, Bakali A and SmarandacheF. Single valued neutrosophic graphs.*J. New Theory*, 2016; 10: 86-101.

Fujita T. MetaHyper graphs, meta superhyper graphs, and iterated meta graphs: modeling graphs of graphs, hypergraphs of hypergraphs, superhypergraphs of superhypergraphs, and beyond. *Curr. Res. Interdiscip. Stud.*2025a; 4(5): 1-23.

Fujita T. Meta structure, meta-hyperstructure, and meta-superhyperstructure. *J. Comput. Appl.*2025b; 1(1): 1-22.

Fujita T. A study on hyperfuzzy hyperrough sets, hyperneutrosophic hyperrough sets, and hypersoft hyperrough sets with applications in cybersecurity.*Artificial Intell. Cyb.*2025c;2: 14-36.

Fujita T. Advancing uncertain combinatorics through graphization, hyperization, and uncertainization: Fuzzy, neutrosophic, soft, rough, and beyond. *Biblio Publishing*, 2025d. pp. 1-229.

Hadi HM and Al-SwidiL. The neutrosophic axial set theory. Neutrosophic *Sets and Systems, Int. J. Infor. Sci. Eng.*, 2022; 51:295-302.

He T, Chen Y and Shi K. Weighted rough graph and its application. In: *Proceedings of the sixth international conference on intelligent systems design and applications,*16-18 October, Jinan, China, 2006; pp. 486-491.

Hsiao C-C, Chuang C-C, Jeng J-T and Su SF. A weighted fuzzy rough sets based approach for rule extraction. In:*The 52nd annual conference of the society of instrument and control engineers of Japan*. *SICE*. 2013, pp. 104-109.

Jech T. Set theory: The third millennium edition, revised and expanded. *Bull. Symb. Log*.2003;11(02): 243-245

Lenz UO, Cornelis C and Peralta D. Fuzzy-rough-learn 0. 2: A python library for fuzzy rough set algorithms and one-class classification. *Int. Confer. Fuzzy Syst.* July, 2022.

Maji PK, Biswas R and Roy AR. Soft set theory. *Comput. Math. Appl.* 2003; 45(4-5): 555-562.

Molodtsov D. Soft set theory-first results. *Comput. Math. Appl.*1999;37(4-5):19-31.

Own HS, AalNAA and Abraham A. A new weighted rough set framework for imbalance class distribution. In: *Proceedings of the 2010 international conference of soft computing and pattern recognition*, SoCPaR,2010; pp. 29-34.

Pawlak Z and Skowron A. Rudiments of rough sets. *Inf. Sci.* 2007. 177(1): 3-27.

Pawlak Z. Rough sets. *Int. J. Comput. Inf. Sci.*1982. 11: 341-356.

Pawlak Z. Rough set theory and its applications to data analysis. *Cyber. Syst.* 1998; 29(7): 661-688.

Pawlak Z. *Rough sets: Theoretical aspects of reasoning about data*. Springer Sci. Bus. Media, 2012; Vol. 9.

Smarandache F. Plithogenic set, an extension of crisp, fuzzy, intuitionistic fuzzy, and neutrosophic sets-revisited. *Inf. study*, 2018; 21: 153.

Torra V. Hesitant fuzzy sets. *Int. J. Int. Syst.* 2010; 25(6): 529-39.

Wang H, Smarandache F, Sunderraman R and Zhang Y-Q. Interval neutrosophic sets and logic: Theory and applications in computing. *Inf. Study*. 2005; 5: 87.

Wang H, Smarandache F, Zhang Y and Sunderraman R. Single valued neutrosophic sets. *Inf. study*, 2010.

Zadeh LA. Fuzzy sets. *Inf. Cont.* 1965; 8(3): 338-353.

Zadeh LA. Fuzzy logic, neural networks, and soft computing. In:*Fuzzy Sets, Fuzzy Logic, and Fuzzy Systems: Selected Papers by Lotfi a Zadeh*. World Sci. 1996. pp. 775-782.

J. Bangladesh Acad. Sci. 50(1); 147-151: March 2026 DOI:https://doi.org/10.3329/jbas.v50i1.82696

Journal of Bangladesh Academy of Sciences

Journal homepage: http://www.bas.org.bd/publications/jbas.html

Short Communication

The first record of *Neptis cartica* (Insecta: Lepidoptera: Nymphalidae) from a northeastern forest of Bangladesh

Akash Mojumdar, Rasel Debbarma[1] and Tania Akhter[2*]

Department of Environmental Science, Stamford University Bagnladesh, Dhaka, Bangladesh

RTICLE INFO

Article History

Received: 02 July 2025
Revised: 05 October 2025
Accepted: 02 November 2025

Keywords: Butterfly, *Neptis cartica*, Plain Sailer, New record, Madhabkunda Eco-Park, Bangladesh.

ABSTRACT

Neptis cartica (Moore, 1872), commonly known as the Plain Sailer and belonging to the family Nymphalidae, is reported here for the first time from Madhabkunda Eco-Park (MEP) (24°38′25″N, 92°13′06″E) in Moulvibazar District, northeastern Bangladesh. To species was identified based on the following key diagnostic characteristics: the upperside exhibits whitish to sullied-white markings; the basal streak extends to the origin of vein 8; the forewing upperside shows a prominent spot in space 3, a non-extended cell streak, and a zigzag outer margin; the hindwing upperside bears a distinct whitish discal band; and the discal fascia is dark, while the underside is dark ochreous brown with white markings. The photographed specimen of *Neptis cartica* represents the first confirmed record of this species in Bangladesh, highlighting the importance of conserving the biodiversity of MEP and updating its butterfly checklist.

Introduction

Butterflies are scaly-winged insects of the order Lepidoptera, which serve as indicators of biodiversity and pollinators (Chowdhury et al., 2014; Hasan et al., 2018). In Bangladesh, a total of 421 butterfly species have been recorded across different regions (Hossain, 2023). Among them, the northeast region of Bangladesh included the Sylhet division (covering about 8.5% of Bangladesh's landscape), with four districts namely, Habiganj, Moulvibazar, Sunamganj, and Sylhet with 10 forest patches (Siddique et al., 2024; Ahmed et al., 2020), which represents mixed evergreen forest habitats and reported a dense landscape for butterfly species (IUCN, 2015), while a total of 231 butterflies encountered from the Satchari National Park (Hasan et al., 2018; Akhter et al., 2023; Akhter et al., 2026), 159speciesfrom LawacharaNational Park: (Khandokar et al., 2013), 165 species from Rema-KalengaWildlifeSanctuary (Shihan and Prodhan, 2014; Akhter et al., 2026), and 266 species from Adampur forests (Babu et al., 2024). However, there is limited information on butterfly species in Madhabkunda Eco-Park (MEP). MEP (24°38'25"N 92°13'06"E) is a tropical mixed evergreen forest located in the Moulvibazar district in northeast Bangladesh (IUCN, 2015; Islam et al., 2022) (Fig. 1). Geologically, the study area is the Bhuban rock formation, sandy clay-loam to clay-loam of top soils, and a 61m-high waterfall, and the landscape is dominated by slopes and hillocks that are intersected by several water sources (Islam et al., 2022) (Fig. 2).

*Corresponding author: <taniaaktar733@gmail.com>

[1]*Satchari Tripura Para, Habiganj, Bangladesh*

[2*]*Department of Zoology, Jagannath University, Dhaka, Bangladesh*

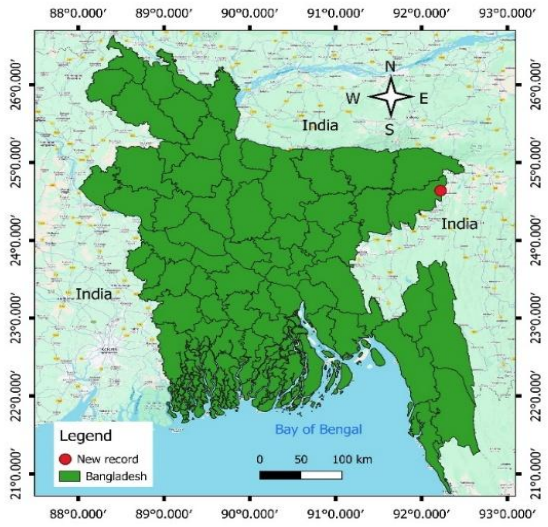

Fig. 1. Map of the study area: New record (*Neptis cartica*) in Bangladesh.

Fig. 2. Habitat of Madhabkunda Eco-Park.

The study spanned three days, from November 27 to November 29, 2024. On the first day at 15:35 hours +06 GMT, we observed an individual of *Neptis cartica* (Moore, 1872) from the nearest stream of MEP at an elevation of 30 meters (location- Fig. 1, species- Fig. 3). The geographic coordinate was taken by GPS (Garmin e-Trex 10). The activity of this species was puddling; it was taking nutrients from the surface of wet rocks along the waterfall (Fig. 3). During this time, the butterfly was systematically observed and documented by following Pollard and Yates (1993). This species was sighted in the morning between 8:00 and 16:30 hours. Butterfly identification was primarily done by direct observation, and we took photos with a Nikon D7200 camera and 70-300mm lens. The average temperature and humidity were 28.7°C and 63% during the observation period. The temperature and humidity were measured using a digital thermometer-hygrometer (HTC-1).

The species *Neptis cartica* is commonly known as the Plain sailer under the family Nymphalidae (Varshney and Smetacek, 2015). This species is widely distributed across northern India (from Uttarakhand to Arunachal Pradesh), Nepal, Bhutan, Myanmar, and Thailand (Kehimkar, 2016; https: //yutaka.it-n.jp/lim1/720300010.html). The upper side markings are white or sullied, and the upper forewing (UPF) has a prominent spot in space 3. The UPF cell streak is not extended from the base of space 3, and it has a highly zigzag marginal line (Kehimkar, 2016).

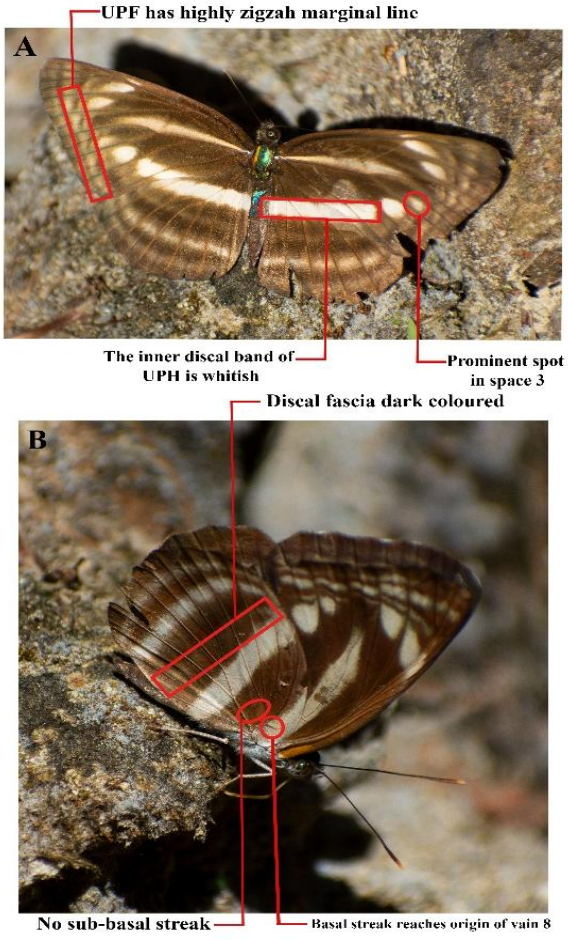

Fig. 3. Paddling behavior of *Neptis cartica* (ventral and dorsal view with identification marking).

Table 1. Major diagnostic differences andecological information of Neptis species in Bangladesh.

Species Name	Major Diagnostic	IUCN Status (Local and Global)	Wingspan, Habitat, Elevation, Flight period
Neptis clinia Moore, 1872	Generally, with wider white bands. From the cell streak UPF and discal band UPH sullied and with diffused edges (wet season) (Sondhi and Kunte., 2018). UPH central band broad and prominent, lower band obscure/absent, UPF streak usually sullied, larger spots below cell streak outwardly square/concave (Kehimher, 2016).	VU, NE	45-60mm, Forest, Up to 1500m, February to December
Neptis harita Moore, 1874	UPF discal spot in 2 crescentic; cilia not prominently white at apex. UPH in discal band only to v5; postdiscal and sub-marginal pale lines wide and close together, encircling the dark area between so as to form a row of dark spots (Evans, 1932). Markings are dusky pale, narrow, and suffused with brown (Kehimher, 2016).	EN, NE	55-60mm, Forest, Low elevations, March to November
Neptis hylas Linnaeus, 1758	Above white markings broad and sharp. Below rather dark ochreous and UNF veins beyond cell prominently black (Evans, 1932). UPF streak short, spot at end cell outwardly sharp. An imaginary line drawn throught spots in spaces 2 and 3 joins outer edge below UPF apex. UPH central band dose not widen towards leading edge (Kehimher, 2016). UPF white spots in 2 and 3 not in line with 5 (Sondhi and Kunte., 2018).	LC, NE	55-60mm, Forests and Gardens, Up to 3000m, January to December
Neptis jumbah Moore, 1857	UPF: white spots in 2 and 3 in line with 5, centers directed to costa below apex (Sondhi and Kunte, 2018). Central white band on UPH could be broad. Dark chestnut streak beyond UNF cell. In row of white spots absent/reduced near UPH (Kehimher, 2016).	LC, NE	60-70mm, Forest, Up to 1900m, February to November
Neptis magadha Felder & Felder, 1867	Marking on UP always white. UPF: cell streak and a spot beyond. 2 larger spots and 1 smaller in middle are in line on UPF. UN light brown (Kehimher, 2016).	EN, NE	55-60mm, Forest, Up to 880m. March to December
Neptis mahendra Moore, 1872	Central band wider at UPH leading edge. End-cell spot well-separated from white cell streak. UPF central spots in spaces 2 and 3 not in line with spot in space 5 (Kehimher, 2016). In UPH, discal white band expands to costa (Sondhi and Kunte, 2018).	NE, NE	55-60mm, Hill forest, 1200-3000m, April to October
Neptis nata adipala Moore, 1872	UPF: white spots in 2 and 3 not in line with 5, centers directed to termen below apex. Cell-end spot sepearated from cell streak (Sondhi and Kunte, 2018). UPH has inner band to conjoined spots. Reddish brown UN, markings slightly blurred, not black-edged (Kehimher, 2016).	NE, NE	58-70mm, Forest, 450 to 2200m, February to November
Neptis pseudovikasi Moore, 1899	In FW, apex cilia prominently white. UPF: discal spot in 3 more/less quadrate. UPH: Post-discal and sub-marginal bands well separated. UNH: markings sullied, narrower (Sondhi and Kunte, 2018). No crescent shaped spot near lower tip of UPF (Kehimher, 2016).	EN, NE	55-70mm, Forest, Up to 1220m, Up to 700m in the Himalaya, March to November
Neptis sappho astola Moore, 1872	Very similer to *N. hylas*, Differ in size and colour. UP markings narrow and often sullied. UN chocolate (Kehimher, 2016). UNF: veins never blackened beyond cell.	NE, NE	44-57mm, Hill forest, Up to 1900m, February to October
Neptis soma Moore, 1858	UPF cell streak narrowly separated from end cell (Kehimher, 2016). Spots in 2 and 3 not in line with 5 and a line joining centers is pointed to termen below apex. 3 sub-marginal spot shifted in and at right angles to costa. UNF: cell spot often joined/close to cell streak. UPH: broad white discal band, entering base of 3 and expending to costa (Sondhi and Kunte, 2018).	VU, NE	47-54mm, Hill forest, 700-2800m, March to December
Neptis cartica (Moore, 1872)	The upper side markings are white or sullied, and the upper forewing (UPF) has a prominent spot in space 3. The UPF cell streak is not extended from the base of space 3, and it has a highly zigzag marginal line (Kehimkar, 2016). The inner discal band of UPH is whitish, with other markings in pale brown. The discal fascia dark coloured. The UNF submarginal pale line at the apex does not align parallel to the apical discal spots. Basal streak reaches origin of vein 8. The underside of it is dark ochreous brown, with markings highlighted in white (Evans, 1932; Eliot, 1969). UNH white costal streak at base broad, and no pale streak at base of cell (Sondhi and Kunte, 2018).	NE, NE	55-70mm, Forest, Up to 1800m, March to December

LC: Least Concern, VU: Vulnerable, EN: Endangered, NE: Not Evaluated, mm: Millimeter, m: Meter, UPF: Upper Forewing, UPH: Upper Hindwing, UNF: Under Forewing, UNH: Under Hindwing, UP: Upper side, UN: Under side, FW: Forewing.

The inner discal band of UPH is whitish, with other markings in pale brown. The discal is fascia dark colored. The UNF submarginal pale line at the apex does not align parallel to the apical discal spots. The basal streak reaches the origin of vein 8. The underside is dark ochreous brown, with markings highlighted in white (Evans, 1932; Eliot, 1969). The UNH white coastal streak at the base is broad, and there is no pale streak at the base of the cell (Sondhi and Kunte, 2018). A total of 10 *Neptis* species in the family Nymphalidae are recorded from Bangladesh (Hossain, 2023; Larsen, 2004; IUCN, 2015). Regarding the species *Neptis cartica* (Moore, 1872), there is no published article, nor is it listed in any published books from Bangladesh. This observation is the first confirmed record for Bangladesh.

The habitat of MEP is not only good for rare mammals (Akhter et al., 2024a) but also for butterflies, while *Mooreana trichoneura* and *Bibasis sena* were reported as new for Bangladesh from this habitat (Khan et al., 2014;Das and Chowdhury, 2016). Therefore, *Ancema blanka*, *Faunis canens*, and *Euthalia anosia* were also reported very recently for the first time as country records from MEP (Akhter et al., 2024b). Afterwards, the photographic evidence of *Neptis cartica* from this location has been documented as the first country record and a new addition to the butterfly fauna of Bangladesh. These findings highlight the significance of this habitat for rare species. Further faunal studies and conservation efforts are needed to better understand species diversity and protect this vital habitat.

Acknowledgment

The authors would like to thank Joy Biswas, Department of Zoology, Jagannath University, for species identification.

Authors contribution

Akash Mojumdar: Conceptualization, original draft, review, editing, and visualization; Rasel Debbarma: Review and editing; Tania Akhter: Investigation, supervision, review, editing, and project administration.

Conflict of interest

The authors declare that there are no potential conflicts of interest regarding the publication of this article.

References

Ahmed N, Mahbub RB, Hossain MM and Sujauddin M. Modelling spatio-temporal changes of tropical forest cover in the north-eastern region of Bangladesh. *J. Trop. For. Sci.* 2020; 32(1): 42-51.

Akhter T, Rahim MA, Tabassum N and Hasan S. Three new records of butterflies from Madhabkundo Eco-Park in Bangladesh. *TAPROBANICA* 2024a; 13(2): 146-147.

Akhter T, Tabassum N and Hasan S. Observations of large-toothed ferret badger (*Melogale Personata*) in Patharia Hill reserve forest at Northeast Bangladesh. *Bangladesh J. Zool.* 2024b; 52(2): 271-275.

Akhter T, Ullah A, Siam MS, Naher H, Biswas S and Mree K. Sightings of the witch (Lepidoptera: *Araotes lapithis*) in Northeast Bangladesh. *TAPROBANICA.* 2023; 12(12): 96-97.

Akhter T, Mojumdar A, Ahammed MS, Hasan MR, Rahman MA, Mahmud MM, Naher H, Debbarma R and Hasan MAU. Forest type as a key driver of butterfly species diversity. *Psyche,* 2026: 9509378:1-21.

Babu MQ, Mojumdar A, Debbarma P, Alom K and Hasan MAU. Unveiling the unknown: a butterfly checklist of the Adampur forest in Bangladesh. *J. Bangladesh Acad. Sci.* 2024; 48(1): 85-97.

Chowdhury S, Aich U and Dash MK. Checklist of butterfly fauna of Dinajpur, Bangladesh. *J. Entomol. Zool. Stud.* 2014; 2(5): 156-159.

Das MK and Chowdhury S. Record of two new butterflies for Bangladesh. *J. Entomol. Zool. Stud.* 2016; 4(3): 32-34.

Eliot JN. An analysis of the Eurasian and Australian Neptini (Lepidoptera: Nymphalidae). *Bull. Br. Mus. (Nat. Hist.) Entomol. Supp.* 1969;15:156.

Evans WH. *The Identification of Indian Butterflies. 2nd ed.* Bombay Natural History Society;1932, p. 454.

Hasan MAU, Neha SA, Baki MA and Babu MQ. An inventory of butterfly species in relation to food sources and climatic factors influencing their diversity and richness in a semi-evergreen forest of Bangladesh. *Arthropods*. 2018; 7(3): 53-68.

Hossain MM. A review on the diversity of butterfly (Insecta: Lepidoptera) fauna from Bangladesh. *Bangladesh J. Zool.* 2023; 51(1): 3-34.

Islam KK, Hoque MA, Rahman NAIMUR, Sarker MAA and Uddin SN. A checklist of the vascular flora of Madhabkundo Eco-Park, Moulvibazar, Bangladesh. *Bull. Bangladesh National Herb*. 2022; 8: 1-31.

IUCN Bangladesh. *Red List of Bangladesh. Volume 7: Butterflies.* IUCN, International Union for Conservation of Nature; 2015, p. 400.

Kehimkar I. *Butterflies of India.* Bombay Natural History Society; 2016, p. 505.

Khan AKMMA, Khan T and Khan MK. Three new records of butterfly from the northeast region of Bangladesh. *The Festschrift on the 50th Anniversary of The IUCN Red List of Threatened Species™*. 2014; pp. 35-38.

Khandokar F, Rashid M, Das DK and Hossain M. Species diversity and abundance of butterflies in the Lawachara national park, Bangladesh. *Jahangirnagar Univ. J. Biol. Sci*. 2013; 2(2): 121-127.

Larsen TB. *An annotated checklist of the butterflies of Bangladesh (Lepidoptera, Rhopalocera). Dhaka, Bangladesh.* IUCN (International Union for Conservation of Nature);2004, p. 158.

Pollard E and Yates V. *Monitoring Butterflies for Ecology and Conservation.* Springer Dordrecht; 1993, p. 292.

Shihan TR and Prodhan MAH. Butterflies of Rema-Kalenga wildlife sanctuary, Habiganj, Bangladesh. *Int. J. Fauna Biol.* 2014; 1(6): 96-100.

Siddique AB, Rayhan E, Sobhan F, Das N, Fazal MA, Riya SC and Sarker S. Spatio-temporal analysis of land use and land cover changes in a wetland ecosystem of Bangladesh using a machine-learning approach. *Front. Water*. 2024; 6: 1394863.

Sondhi S and Kunte K. *Butterflies of Uttarakhand A Field Guide.* M/s Bishen Singh Mahendra Pal Singh (Dehradun), Titli Trust (Dehradun), National Centre for Biological Sciences (Bengaluru) and Indian Foundation of Butterflies (Bengaluru); 2018, pp. 310.

Varshney RK and Smetacek P. *A Synoptic Catalogue of the Butterflies of India.* Butterfly Research Centre, Bhimtal and Indinov Publishing; 2015, p. 261.

J. Bangladesh Acad. Sci. 50(1); 153-155: March 2026 DOI:https://doi.org/10.3329/jbas.v50i1.85021

Journal of Bangladesh Academy of Sciences

Journal homepage: http://www.bas.org.bd/publications/jbas.html

Short Communication

Feeding behaviour of Tawny Asian Cat Snake *Boiga multomaculata ochracea* (Theobald 1868) from Southeast Bangladesh

Md. Mizanur Rahman* and Sajid Al Rafi[1]

Venom Research Centre, Chittagong Medical College, Chattogram, Bangladesh

ARTICLE INFO

Article History

Received: 17 October 2025
Revised: 02 February 2026
Accepted: 05 February 2026

Keywords: *Boiga multomaculata ochracea*, *Calotes versicolor*, Feeding behaviour, Ecology, Bangladesh.

ABSTRACT

The Tawny Asian Cat Snake (*Boiga multomaculata ochracea*) is a rear-fanged colubrid that inhabits the mixed evergreen forests of northeast and southeast Bangladesh. The feeding behaviour of this opportunistic predator remains poorly understood. This study presents the first documented observation of *B. m. ochracea* preying on the Oriental Garden Lizard (*Calotes versicolor*) in southeastern Bangladesh and highlights the limited research on the species' feeding ecology.

Introduction

The Tawny Asian Cat Snake (*Boiga multomaculata ochracea*) is a rear-fanged, mostly arboreal, crepuscular and nocturnal colubrid snake which is distributed across most of Myanmar (except for the northern portion of the country), north-eastern India (Mizoram), Bangladesh, north of 18° N latitude of Thailand, and northern Laos (Köhler et al., 2023). The species known to prey on lizards, birds and their eggs, and small mammals (Whitaker and Captain, 2004). Its ophiophagous nature, as described by Pradhan (2021), includes the Black-belly Worm-eating Snake (*Trachischium fuscum*) found in its diet list. However, specific details regarding the species' diet remain scarce. Here, we report on the feeding behaviour of *B. m. ochracea* observed while consuming a garden lizard from south-east Bangladesh.

On 27th December 2024, at 1905 h, an adult *B. m. ochracea* was observed preying on an adult male Oriental Garden Lizard (*Calotes versicolor*) in the rural, hilly plains of Fatikchari upazila under Chattogram district of Bangladesh (22.70638, 91.71972, 18 m elevation). The location was near a small village market along Baroiyadhala-Haidchakia Road and adjacent to Hazarikhil Wildlife Sanctuary, the oldest and richest reserved forest of Bangladesh. The *B. m. ochracea* was perched on the stem of a small Charcoal Tree (*Trema orientale*), while the *C. versicolor* rested on a small branch of Golden Dewdrop (*Duranta erecta*). These two plant species were next to each other. The snake approached the lizard slowly before launching a swift attack, biting the lizard on the neck. Initially, the lizard attempted to escape but was soon tightly constricted by the snake, which coiled around it, leaving only the lizard's head and tail exposed (Fig. 1). The snake exerted pressure on the lizard until it succumbed approximately 30 minutes later. Following the lizard's death, the snake attempted to swallow it multiple times, starting at various points including mid-body, neck and hind limbs before finally beginning at the head (Fig. 2). The ingestion process was slow. After swallowing the body and most of the lizard's long tail, the snake rested briefly for 2-3

*Corresponding author: <op.mizanepu@gmail.com>

[1]*Central Medical College, Paduar Bazar Bishaw Road, Cumilla-3500, Bangladesh.*

minutes (Fig. 3) before consuming the remainder. The entire feeding process lasted for an hour (one and a half hours after grasping). Once the meal was complete, the snake hungmomentarily from the Golden Dewdrop tree of 0.75 m high before falling to the ground. After a while, the snake moved to the nearest scrubland and disappeared into the leaf litter, likely seeking cover.

Fig. 1. The *B. m. ochracea* tightly coiled to kill the prey. Photo- Sajid Al Rafi.

Fig. 2. The *B. m. ochracea* started to engulf the prey from the head. Photo- Sajid Al Rafi.

Fig. 3. The *B. m. ochracea* in brief rest before engulfing the remainder of the tail. Photo- Sajid Al Rafi.

To our knowledge, this is the first documented report of *B. m. ochracea* preying on *C. versicolor*. Although Patra et al. (2021) previously observed the foraging behaviour of *B. m. ochracea* in a similar context, where the snake approached a *C. versicolor*. In that case, the lizard managed to escape by jumping away just as the snake's tongue touched it. We hope this observation will provide insights into the snake's hunting strategies and its role as a predator, feeding ecology, habitat use, as well as conservation and management efforts.

Acknowledgment

We extend our heartfelt gratitude to Dr. Tanvir Jubair of Cumilla Popular Hospital and Md. Nahidul Islam, a local guide at Hazarikhil Wildlife Sanctuary, for their invaluable support during our field visit. We are grateful to our co-photographers for their passion in capturing this moment of the snake in the act of preying and feeding. Additionally, we are deeply thankful to Kazi Fayzatul Zannat for her insightful comments on the manuscript.

Authors contribution

Md. Mizanur Rahman: Conceptualization, data collection, writing original draft, editing, and reviewing the manuscript. Sajid Al Rafi: Data collection and resources, review manuscript.

Conflict of interest

The authors declare that they have no conflicts of interest regarding the publication of this article. There are no financial, personal, or professional relationships that could be perceived as influencing the research, analysis, authorship, or publication of this article.

References

Köhler G, Charunrochana PT, Mogk L, Than NL, Kurniawan N, Kadafi AM, Das A, Tillack F and O'Shea M. A taxonomic revision of *Boiga multomaculata* (Boie, 1827) and *B. ochracea* (Theobald, 1868), with the description of a new subspecies (Squamata, Serpentes, Colubridae). *Zootaxa.* 2023; 5270(2): 151-193.

Patra A, Lalremsanga HT,Malhotra A, Kartik A and Santra V. *Boiga ochracea* (Tawny Cat Snake). Foraging Behavior. *Herp. Rev.* 2021; 52(1): 147-148.

Pradhan A. *Boiga ochracea* (Tawny Cat Snake). Diet. *Herp. Rev.* 2021; 52(1): 147.

Whitaker R and Captain A. Snakes of India. The Field Guide. Draco Books, Chennai, India. 2004; p. 280.

INSTRUCTION FOR AUTHORS

The Journal of Bangladesh Academy of Sciences is published four times a year in March, June, September and December. Original research articles, review articles, and short communications of high standards of all branches of Science and Technology are considered for publication in this journal. Review articles are generally by invited authors; however, the Editor welcomes suggestions of potential topics and potential authors.

The following instructions must be followed while preparing the manuscript intended for publication in this journal:

1. **Research Article:** Manuscripts should be concise and consistent with the style of the journal. The manuscript must be typed using Times New Roman font, size 12 on A4 size page, and wide (1 inch) margins on all four sides. The main text must be typed in a two-column format with 1.5 spacing, and for full papers, it should not exceed 10-20 typed pages, including figures, tables, and references. In general, an article may contain the following sub-titles in sequence: **Title, Abstract, Keywords, Introduction, Materials and Methods, Results and Discussion, Acknowledgement (**if any), and **References.**

A. Title: The first page of the paper, the title page, should have the title and the names of the authors. The title should be brief and specific. Abbreviations and formulae should be avoided where possible. The next line in italics should be the authors' affiliation addresses (where the actual work was done) below the names. Indicate all affiliations with a lowercase superscript letter immediately after the author's name and in front of the appropriate address. The corresponding author, along with email address, should be indicated at the footnote with a proper asterisk.

B. The second page should carry the Title of the paper, Abstract, and Keywords. Author(s) name must not be typed on this page.

(i) Abstract: It should not exceed 150 words and should briefly state the purpose of the research, the significant results, and meaningful conclusions. Nonstandard or uncommon abbreviations should be avoided, but if essential, they must be defined at their first mention in the abstract itself.

(ii) Keywords: Immediately after the abstract, provide a maximum of 6 keywords.

C. The next pages (a maximum of 15 printed pages), will contain the main text of the paper.

(i) Introduction: It should be concise and relevant to the objectives of the study. The importance of the research work described should be pointed out. An appropriate review of the current literature should be made to identify the frontier of existing knowledge and point out the need for further work. The knowledge contributed to the study should be mentioned.

(ii) Materials and Methods: Materials used should be mentioned precisely along with their sources and any pre-treatment undertaken.

The description of methods must be brief but clear enough to enable a reader to reproduce the results. References must be considered sufficient for methods described in earlier publications: only relevant modifications should be described.

It is recommended that authors use the nomenclature and symbols adopted by IUPAC document UIFII (S.U.N. 65-3) 1965, symbols, units, and nomenclature in Physics or by IUPAC Manual of Physiochemical symbols,

Terminology and similarly for other disciplines.

(iii) Results and Discussion: This section should include descriptions of results obtained with the help of figures, tables, graphs, and photographs as may be necessary. Tables should have a descriptive title. Large and cumbersome tables should be avoided. Figures and graphs should be prepared and should be properly labelled with bold solid lines such that no further size reduction will be necessary. The paper should contain a minimum number of **Tables, Graphs,** and **Figures.** The same data should not be depicted using both tables and figures. The photographs are to be submitted in JPEG format.

The discussion should include thorough analysis and interpretation of results, and comparison with existing relevant published results, if any, and self-evaluation of the new knowledge contributed, avoiding extensive citations and discussion of published literature.

(iv) Conclusions

The study's main conclusions may be presented in a short Conclusions section, which may stand alone or form a part of the Results and Discussion section.

(v) Acknowledgment: The following support for the research work should be acknowledged:

- Funding by any agency;
- The use of instruments in a laboratory other than those of the authors;
- Individual's help during the research (e.g., providing an interpretation of results, language help, writing assistance, or proofreading, etc.).

(vi) Author contributions

For transparency, we encourage authors to submit an author contribution statement outlining each author's contributions to the paper. The authors should have participated sufficiently in the work to take public responsibility for appropriate portions of the content.

(vii) References and Text Citations:

In the text, references should be cited within brackets quoting the first author's surname followed by et al. if necessary and the year of publication in the appropriate place, e.g. (Bhuiyan, 2020), Khan et al. (2021) or (Khan et al., 2021). In the case of only two authors, surnames of both need to be mentioned, e.g., (Khan and Rahman, 2021). A semi colon should separate two or more references when putting within the same bracket. At the end of the manuscript, references should be listed and arranged alphabetically according to the first author's surname according to the style described below:

(a) Journal article:

In each reference, names of all authors' will have to be given in the same style, e.g., surname followed by initials, lumped together without using a full stop. The names will be followed by the full title of the article and the journal's abbreviated title (in italics). The year of publication will be given next, followed by volume number (issue number) and page ranges. For abbreviations of the names of journals, authors are advised to follow the *World List of Scientific Periodicals.* For online publications, the URL address must be given. Note: Please list ALL authors' names in the list of references, do not use (et al.). **Examples:**

Islam S. The Induced Morphological and Root Anatomical Changes in Lentil. *J. Bangladesh Acad. Sci.* 2019; 43(2):107-112.

James BD and Bennett DA. Causes and Patterns of Dementia: An Update in the Era of Redefining

Alzheimer's Disease. *Annu. Rev. Public Health;* 2019; 40: 65-84.

Moniruzzaman M, Khatoon R and Qamruzzaman AKM. Influence of Plant growth Regulators on Vegetative Growth, Sex Expression and Yield of Summer Bottle Gourd. *Bangladesh J. Agril. Res*. 2019; 44(4): 577-590.

(b) Book or Chapter in a Book:

The place and name of the publisher, year of publication, will have to be given in addition to the name of the author(s), the title of the book (in italics), edition number (if not first), and the number of pages. In the case of an article or chapter in a book or proceedings of a conference, author(s) name and the title of the article or chapter will be followed by the title of the book (in italics), the names of the editors of the book, edition number (if not first), the place and name of the publisher, year of publication and page or page numbers of chapter. **Examples:**

Book:

Carlson BM. *Human Embryology and Developmental Biology*. 4th ed. St. Louis: Mosby; 2009. p. 541.

Cassese A, Acquaviva G, Fan M and Whiting A. *International Criminal Law: Cases and Commentary*. Oxford University Press; 2011, p. 600.

Chapter in an edited book:

Muhammad HFL and Dickinson KM. Nutrients, energy values and health impact of conventional beverages, Chapter 3. In: *The Science of Beverages, Volume 12: Nutrients in Beverages*. Grumezescu AM, Holban AM, eds., Elsevier Science; 2019; pp. 77-109.

Balsam KF, Martell CR, Jones KP, Safren SA. Affirmative cognitive behavior therapy with sexual and gender minority people. In: *Culturally Responsible Cognitive Behavior Therapy: Practice and Supervision*. Iwamasa GY, Hays PA, eds., 2nd edition, American Psychological Association. 2019; p. 287-314.

(c) Proceedings of a Conference:

Luca J and Tarricone P. Does emotional intelligence affect successful teamwork? In: *Meeting at the Crossroads*. Kennedy G, Keppell M, McNaught C (eds.), Proceedings of the 18th Annual Conference of the Australasian Society for Computers in Learning in Tertiary Education, 2001 Dec 9-12; Melbourne: Biomedical Multimedia Unit, The University of Melbourne; 2001. pp. 367-376.

(d) Reports:

Bangladesh Bureau of Statistics (BBS). Population census - 2011. Preliminary report. Bangladesh Bureau of Statistics, Ministry of Planning, Government of the People's Republic of Bangladesh, Dhaka, 2011.

Rowe IL and Carson NE. *Medical manpower in Victoria. East Bentleigh (AU)*: Monash University, Department of Community Practice; 1981. p. 35. Report No.: 4.

2. **Short communication:** Important research findings that may initiate further research in the relevant field may be published in the form of a short communication. This should not exceed three printed pages (900 words), including Graphs, Tables, and Figures. The presentation should be continuous and paragraphed, i.e., without headings like Introduction, Materials, and Methods, etc. A short communication paper should have an **Abstract** containing the gist of the article and should not exceed 60 words, followed by **Keywords.**

3. **Declarations:** While submitting, the corresponding **a**uthor will have to make a declaration mentioning the laboratory/laboratories in which the work was carried out and certifying that the contents of the paper were not published before or submitted for publication in any other journal and that all the co-authors have given their consent for the article to be considered by the Editorial Board for publication in the Journal of Bangladesh Academy of Sciences.

Declaration of conflicting interests

The corresponding author must provide a formal conflict of interest statement for all authors disclosing any financial and personal relationships with other people or organizations that could inappropriately influence (bias) their work. If no conflict exists, please state that 'The author(s) declare(s) that they have no conflicts of interest regarding the publication of this article.'

4. The manuscript should be submitted in pdf or MS Word or LaTex files through online at www.bas.org.bd/publications/jbas.html. Equations generated by using Math Type or Math ML should be incorporated in the text.

   Soft copies of manuscripts with tables, graphs, illustrations, and photographs placed correctly in a printable format are to be submitted. Authors wishing to publish coloured schemes/diagrams/ sketches/photographs in their papers need to pay for the printing charges of one format. This will be charged only after the acceptance of the manuscripts for publication in the JBAS.

   The manuscript submitted should also contain a separate list of tables, figures, illustrations, photographs, and sketches with appropriate captions.

5. Electronic versions of final galley proofs will be sent to authors. No alteration in the title or additions in the text is desirable at this stage.

6. All correspondence for publication should be made on www.bas.org.bd/publications/jbas.html to the **Editor, Journal of Bangladesh Academy of Sciences, National Science and Technology Complex, Agargaon, Dhaka 1207.**

N.B.: No paper will be accepted for publication if it does not conform to the style specified for the journal and approved by the Editorial Board, which has the authority to accept or reject the manuscript of a paper submitted without showing any reason.

JOURNAL OF
BANGLADESH ACADEMY OF SCIENCES

Volume 50 | Issue 1 | March 2026

ISSN: 2224-7270 (Online), 0378-8121 (Print)

Bangladesh Academy of Sciences, National Science & Technology Complex
Agargaon, Dhaka-1207, Bangladesh